SPIN-ORBIT INTERACTION AND SPINTRONICS EFFECTS IN SEMICONDUCTOR STRUCTURES

V. Kantser

LISES, Institute of Applied Physics ASM, Chisinau, Republic of Moldova,
kantser@lises.asm.md

Abstract

A review of the recent results concerning the new concepts and achievements in the area of semiconductor spintronics (or spin-electronics) is presented. Because spin-orbit interactions (SOI) couple electron spins to electric fields and allow electrical manipulation of electron spins and electrical detection of spin dynamics they form the fundamental mechanisms of new effects and the basis of different proposals for new spintronic devices. In addition to known channels of SOI in semiconductor materials and heterostructures, new terms of SOI, induced by interband interaction through the electrical polarization or atomic displacement like optical phonons are proposed and analyzed in the paper. These SOI mechanisms have the physical nature in the relativistic quantum mechanics with Lorentz boosts and this aspect is highlighted. Some particularities of the electronic states of semiconductor quantum wells (QW) related to the intrinsic Rashba SOI and Rashba like SOI induced by the electrical polarization (EP) are studied. Size quantization states are shown to transform into interface ones at some value of the in-plane QW wave vector under SOI effect. Tunneling characteristics of single barrier heterostructure are analyzed in the conditions of both types of SOIs and are established to be spin-dependent under SOI induced by the EP. Several aspects dealing with the new discovered intrinsic spin and angular momentum Hall effects (SHE and AMHE) are revealed. The SHE is investigated in a two dimensional electron system with the SOI of both intrinsic and EP induced types. New peculiarities of SHE and AMHE , induced by interband interaction of heavy and light holes are studied in p-doped semiconductors with band degeneracy in the framework of generalized Luttinger Hamiltonian. Spin-conductivity induced by the EP is shown to proportional to difference of the inverse values of the hole wave vectors.

1. General aspects of spintronics

Spintronics is the acronym of spin-dependent electronics and it combines the intrinsic fundamental attributes of solid-state carriers – charge and spin [1]. As rapid progress in the miniaturization of semiconductor electronic devices leads toward chip features smaller than 100 nanometers in size, device engineers and physicists are inevitably faced with the looming presence of quantum mechanics - that counterintuitive and sometimes mysterious realm of physics wherein wavelike properties dominate the behavior of electrons. It is generally accepted that in the near future device dimensions are going to approach their physical limits. Figure 1 illustrates the anticipated technology nodes for the semiconductor industry development following the Semiconductor Industry Association and International Technology Roadmap for Semiconductors [2]. The dashed wall in Fig.1 is the boundary at which there are no known solutions for further development of semiconductor industry and therefore a cardinal research breakthrough is expected.

In such circumstances the new concepts and principles in electronic device architectures are a major challenge of solid-state physics. One of such concepts is the spintronic one, which is based on the quantum property of the electron known as spin, which is closely related to magnetism. Devices that rely on an electron's spin to perform their functions form the foundation of spintronics, also known as magnetoelectronics. Thus the basic concept of spintronics is the manipulation of spin currents, in contrast to mainstream electronics in which the spin of the electron is ignored. Adding the spin degree of freedom provides new effects, new capabilities and new functionalities.
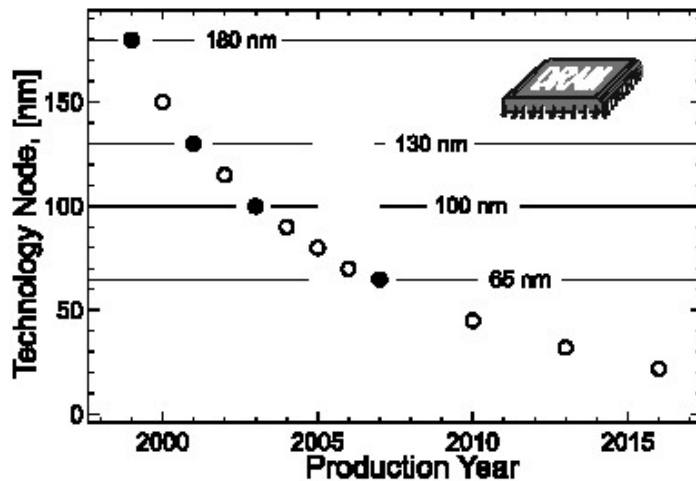

Fig. 1. Evolution of technology miniaturization for the traditional electronic devices [1].

The main goals of spintronics can be generalized in two major tasks:

- *to understand the interaction between the particle spin and its solid-state environments*
- *to make useful devices using the acquired knowledge.*

Fundamental studies of spintronics include:

- *investigations of spin transport*
- *understanding of spin dynamics and spin relaxation.*

In an ordinary electric current, the spins point at random and play no role in determining the resistance of a wire or the amplification of a transistor circuit. Spintronic devices, in contrast, rely on differences in the transport of "spin up" and "spin down" electrons. In a ferromagnetic material, such as iron or cobalt, the spins of certain electrons on neighboring atoms tend to line up. In a strongly magnetized piece of iron, this alignment extends throughout much of the metal. When a current passes through the ferromagnet, electrons of one spin direction tend to be obstructed. The result is a spin-polarized current in which all the electron spins point in the other direction. Naturally, one could try exploiting this intrinsic spin imbalance present in ferromagnetic materials to provide an extra degree of freedom to be used in semiconductor electronic devices. However, although the fundamental concepts needed to understand spin transport have been available for a longer time [3], a dramatic growth in the research in this field took place the last few years [4]. The name of spintronics is nowadays used to describe the field of research on electronic devices in which the electron spin plays the role of the active element [4]. Presently the research drive in the field of spin-dependent transport is two-fold: both commercial application and fundamental research driven. Practical spintronics incorporates existing microelectronic manufacturing techniques. It involves the development of many electronic devices that include ferromagnetic materials. It is enabling to note the development of ultra-fast switches and fully programmable all-spintronics microprocessors that can combine logic, storage and communications on a single chip. The applied side is based on the very rapid commercial success of giant and tunneling

magnetoresistance (GMR and TMR), others tunneling devices as magnetic field sensors in the read-heads of hard disks, entering large-scale production within ten years from discovery. Moreover, magnetic random access memories (MRAM) have the potential of replacing CMOS based non-volatile FLASH memories in the future [5]. On the other side, the physics of spin is interesting for the field of quantum computation [6]. The intrinsic binary nature of electronic spin suggests it could be used as the basic unit, the qubit, for quantum information storage and processing.

However, despite these practical achievements of metal magnetoelectronics semiconductor spintronics has at present the most emerging development. Why semiconductor spintronics is interesting? There are two main reasons for this

- Semiconductor-based spintronics could combine storage, detection, logic and communication capabilities on a single chip to produce a multifunctional device that could replace several components.

- Semiconductors offer a greater wealth of possibilities to create and to manipulate the nonequilibrium spin by transport, optical, and resonance methods (as well as their combination).

The basic advantages of semiconductor spintronics cover:

- long electron spin lifetime (100 ns)

- diverse types of interactions between electron spin and environment

- possibilities to tune these interactions

- controllable optical properties and the ability to amplify both optical and electrical signals

Fifteen yeas ago yet Datta and Das [7] have proposed a design for a spin-polarized field-effect transistor, or spin FET. In a conventional FET, a narrow semiconductor channel runs between two electrodes named the source and the drain. When voltage is applied to the gate electrode, which is above the channel, the resulting electric field drives electrons out of the channel (for instance), turning the channel into an insulator. The Datta-Das spin FET (Fig. 2) has a ferromagnetic source and drain so that the current flowing into the channel is spin-polarized. When a voltage is applied to the gate, the spins rotate as they pass through the channel and the drain rejects these anti-aligned electrons.

A spin FET would have several advantages over a conventional FET. An electron's spin flipping takes much less energy and can be done much faster than an electron

Fig. 2. Scheme of the Datta-Das spin field-effect transistor [7]

pushing out of the channel. One can also imagine changing the orientation of the source or drain with a magnetic field, introducing an additional type of control that is not possible with a conventional FET: logic gates where functions can be changed on the fly.
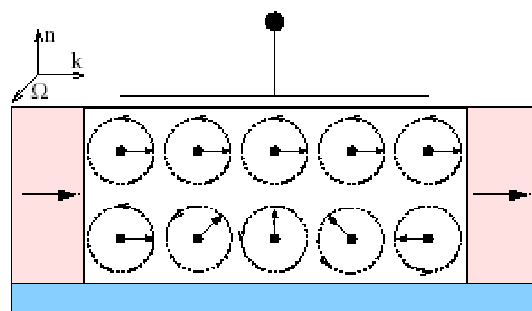
The last years many quantum structures that provide the spin-polarized states and transport were proposed and designed [1]. They can be classified in: layered magnetic structures, hybrid layered ferromagnetic/superconductor structures, hybrid ferromagnetic/semiconductor structures and pure semiconductor structures. A direct approach to obtain spin polarization of the carriers in the structure is the injection of spin-oriented carriers from the magnetic component of the structure. However for such hybrid structures it has recently pointed out a fundamental problem inherent in the electrical injection of spin currents from metal into semiconductors, the so-called conductivity mismatch. Therefore the pure non-magnetic semiconductor structures remain the more attractive systems for the spintronics.

At present fundamental studies of semiconductor spintronics include:

1. Time-resolved optical experiments
2. Spin dynamics in magnetic semiconductors
3. Spin dynamics in quantum dots
4. Spin injection
5. The Datta-Das spin transistor
6. Spin-dependent tunneling
7. Spin-related currents.
8. Nuclear spin effects in optics and electron transport.

In semiconductor spintronics the concept of spin brings an amazing new functionality into mainstream of charge-based electronics. Moreover, the spin of electron or photon can be used to store and process information locally, on the nanoscale. Though, semiconductors offer the most functional advantages (very long carrier scattering time and low noise, for example), the fabrication of semiconductor-based spintronic device and structures up to now remains a challenge despite enormous interest to this field. The lack of efficient ways to create and manipulate spin-polarized charge ensemble in a semiconductor materials or structures by electrical and optical means, spin injection, leaves semiconductor spintronics still on the level of fundamental investigations.

The purpose of this paper is to present a review of the recent results concerning the new concepts and achievements in the area of semiconductor spintronics, which has emerged last years and which includes the principles and effects of the manipulation and control of the electronic spin degree of freedom. The ability to control the electron spin requires finding the corresponding mechanisms of the spin splitting of the electronic states as well as of the spin dependent transport characteristics. The spin-orbit interactions (SOI) for carriers in semiconductor nanostructures form the basis of different proposals for new spintronic devices and this aspect is reviewed in Section 2. In particular, in addition to known channels of SOI (Rashba and Dresselhause terms, for example) in semiconductor materials and heterostructures, new terms of SOI, induced by interband interaction through the electrical polarization or atomic displacement like optical phonons are proposed and analyzed. These SOI mechanisms have the physical nature in the relativistic quantum mechanics with Lorentz boosts and this aspect is highlighted.

In Section 3 some particularities of the electronic states of semiconductor quantum well (QW) related to the intrinsic Rashba SOI and Rashba like SOI induced by the electrical polarization (EP) are studied. The intrinsic SO coupling is shown to conserve spin degeneracy of a symmetric QW in accordance with the results of other papers. However, it influences considerably QW size quantization states transforming the latter into interface states at some

value of the in-plane wave vector. The interface states are shown to occur even in tunnel barrier structure at finite value of the in-plane wave vector. The evolution of such interface states under EP induced SOI are studied for different QWs, and it is established that they become strongly spin-splitted as well as size quantization states.

Several aspects of spin-dependent tunneling characteristics of single barrier heterostrucrure generated by the intrinsic Rashba SOI and Rashba like SOI induced by the electrical polarization (EP) are investigated in Section 4. In particular by the transmission coefficient and the tunneling time investigation of a symmetric barrier structure it is show that EP induced SO coupling leads to sufficient spin-dependent tunneling characteristics of such structure.

Section 5 includes some results dealing with the new discovered recently spin Hall effect (SHE). The SHE is investigated in a two-dimensional electron system with the SOI of both intrinsic and EP induced types. A spin current perpendicular to the electric field is generated by both SOI. The direction of spin current is controllable by tuning the magnitude of the surface electric field perpendicular to the two dimensional plane via adjusting the traditional Rashba coupling and EP SOI coupling. Some new peculiarities of SHE, induced by interband interaction of heavy and light hole bands through electrical polarization or atomic displacement like optical phonon are revealed in p-doped semiconductors with band degeneracy in the framework of Luttinger Hamiltonian.

2. Spin-orbit interactions and semiconductor spintronics

In semiconductor spintronic structures the spin dynamics of carriers in general aspects can be controlled by different types of magnetic interactions - dipole-dipole interaction, spin-orbit interaction, exchange interaction, hyperfine interaction with nuclear spins. Spin-orbit interaction is considered to be the main channel for carrier spin manipulation [1,8] due to its comparatively large magnitude and due to the possibilities of using the electrical fields and optical phenomena for modification of spin states.

The spin-orbit interaction (SOI) arises as a result of the magnetic moment of the spin coupling to its orbital degree of freedom. It is actually a relativistic effect, which was first found in the emission spectra of hydrogen. SOI is a relativistic effect that occurs when a quantum mechanical particle with a non-zero spin moves in a region with a non-zero electric field. When an electron is moving with relativistic velocities in a static electric field, in the rest frame of the electron the original static electric field transforms into a field that has also a magnetic field component, its magnitude is given by the standard Lorentz transformation

$$\vec{B}_{eff}(x) = \left(\vec{v} \times \vec{E}(x)\right)/c \qquad (2.1)$$

The presence of this effective magnetic field that the electron feels in its rest frame affects both the dynamics of the spin and the total energy of the electron. This interaction is called spin-orbit interaction.

The Hamiltonian describing traditional SOI in quantum mechanics of a slow electron in a vacuum, derived from the four-component Dirac equation [9], has the form

$$H_{SO}(\vec{r}) = \frac{e\hbar}{4m_0 c^2} \vec{\sigma}\left(\vec{E}(\vec{r}) \times \vec{v}\right) \qquad (2.2)$$

where m_0 is the free electron mass, $\vec{\sigma}$ is the Pauli matrix vector and $\vec{E}(\vec{r})$ is an electric field.

Presence of the field $\vec{E}(\vec{r})$ in Eq. (1) suggests that an electron possesses a dipole moment [10]

$$\vec{P}(\vec{v}) = \frac{e\hbar}{4m_0c^2}\left(\vec{\sigma} \times \vec{v}\right) \tag{2.3}$$

Thus even for an electron in a vacuum $H_{SO}(\vec{r})$ reveals two important aspects. One is related to the fact that its magnetic moment μ of an electron is proportional to its spin $\vec{s} = \hbar\vec{\sigma}/2$ and H_{SO} is like Zeeman interactions, and the other is connected to its dipole moment, which involves electron velocity $\vec{v}$, and H_{SO} is like electro-polarization interaction.

In crystal structures due to symmetry properties of materials, band structure effects and other various factors influencing the motion of the carriers, the SOI becomes stronger and has diverse channels of manifestation [8]. The static electric field causing the spin-orbit interaction can have different physical origins, for example being the electric field of the atomic nucleus, or related to the crystal or band structure of the solid.

Enhancement of SOI in crystals occurs from two basic sources. The first part appears as a result of fast electron motion in a strong electric field near nuclei through the band structure effects. For example, the equations of the two-band scheme of narrow gap semiconductors are similar to a Dirac equation but with the forbidden gap E_g instead of the Dirac gap $2m_0c^2$. Therefore H_{SO} after the reduction to one band model becomes

$$H_{SO} = \frac{1}{2m_0}\left[\vec{p}\times\hbar\vec{\nabla}\left(\frac{V_{ext}}{2E_g}\right)\right]\vec{\sigma} \tag{2.4}$$

The difference in equations (2.2) and (2.4) reflects enormous increase in SOI in narrow gap semiconductors as compared to a vacuum.

Second type of enhancement and diversification comes from the symmetry of materials and of solid-state structures, which is essentially lower than the symmetry of a vacuum. This leads to new terms in SOI that critically change spin dynamics appearing in carrier Hamiltonians. In the area of semiconductor spintronics several types of SOI terms are considered. The specific Dresselhaus and Rashba mechanisms are more frequently explored for different spintronics applications [1,8]. The Dresselhaus SOI in bulk semiconductors [11] appears as a result of the asymmetry present in certain crystal lattices, e.g., the zinc blende structures. For a two-dimensional electron gas in semiconductor structures with appropriate growth geometry, the Dresselhaus SOI has the form [8]

$$H_D = \alpha_D\left(\sigma_x\hat{k}_x - \sigma_y\hat{k}_y\right) \tag{2.5}$$

where α_D is the Dresselhaus coupling constant, which ranges from about $2 \cdot 10^{-10}$ eV cm to $2 \cdot 10^{-9}$ eV cm and decreases rapidly with the quantum well width.

The Rashba SOI [12] arises due to the asymmetry associated with the confinement potential in z-direction of the structure and reads as

$$H_R = \alpha_R\left(\sigma_x\hat{k}_y - \sigma_y\hat{k}_x\right) \tag{2.6}$$

Being related to the structure confinement potential Rashba SOI is of interest because of the ability to electrically control the strength of this interaction.

The above mentioned mechanisms of SOI stem from the electron orbital motion and are related to the 3D spatial angular momentum. At the same time there are angular momenta related to the generators of so-called Lorentz boost, which traditionally have always been ignored because their infinitesimal generators are not conserved and their eigenvalues can not be used to label physical states [13]. However, recently [14] it was shown that the generators of Lorentz boost have a nontrivial physical significance in quantum mechanics, and they do have interactions (including SOI) related to the generators of Lorentz boost. It was shown [14] that in a charged system the nonzero space-time components of 4D angular momentum tensor (i.e. the generators of Lorentz boost) correspond to an electric moment similar as nonzero purely spatial components of 4D angular momentum tensor (i.e. the generators of 3D spatial rotation) correspond to a magnetic moment.

In this generalized case, the infinitesimal generators of the Lorentz transformation are

$$\Sigma^{\mu\nu} = \frac{i}{4}\left[\gamma^{\mu}, \gamma^{\nu}\right] \tag{2.7}$$

i.e., the 4D spin tensor of electron, which is written in (2.7) through Dirac γ matrices. Using the totally anti-symmetric tensor ε^{ijk} with $\varepsilon^{123} = 1$ (i,j,k = 1,2,3) it is easy to show that

$$\vec{\Sigma} = \left(\Sigma_1, \Sigma_2, \Sigma_3\right) \text{ with } \Sigma_i = \frac{1}{2}\varepsilon_{ijk}S^{jk}$$

is the usual spin matrices (as the generators of 3D spatial rotations). In addition to that they're appearing the generators

$$\vec{K} \equiv \left(S^{01}, S^{02}S^{03}\right)$$

of Lorentz boosts related to space-time rotations and called [14] spin-like matrices.

In terms of the Pauli's matrix vector σ, the spin matrices Σ and *spin-like* matrices K

are expressed as

$$i\frac{\partial}{\partial t}\psi' = \left[\frac{(\hat{p} - e\vec{A})^2}{2m} + e\Phi - g_s\frac{e}{2m}\vec{\Sigma}\vec{B} + g_s\frac{e}{2m}\vec{K}\vec{E}\right]\psi' \qquad (2.12)$$

This equation illustrates that. the electron in vacuum will behave as though it has a magnetic moment operator

$$\frac{e}{2m}\vec{\Sigma}$$

and an electric moment operator

$$\frac{e}{2m}\vec{K}$$

The magnetic moment related to the spin matrices Σ. , is nonzero in the rest frame of electron (the magnetic moment is *intrinsic*); whereas the electric moment, related to *spin-like* matrices K, is the relativistic effect of the magnetic moment (the electric moment is *induced*). Thus, just as that the spin degrees of freedom related to the infinitesimal generators of spatial rotation (i.e., the spin matrices Σ .) bring an *intrinsic* magnetic moment for electron, the *spin-like degrees of freedom* related to the infinitesimal generators of Lorentz boost (i.e., the *spin-like* matrices K) bring an *induced* electric moment for electron. The physical nature of the latter is related to the aspect that an electron with spin degrees of freedom has also the *spin-like* degrees of freedom, which belong to *the particle-antiparticle space. This space is* spanned by the positive- and negative-energy states of electron and a superposition of plane waves of positive- as well as of negative-energy is necessary to obtain a wave packet of electron. In result an *induced* electric moment for the electron occurs.

This new fundamental quantum attribute of the electron in vacuum [14] - *induced* electric moment must have a lot of richer manifestations in crystals, in particular in semiconductor materials and structure. One such new channel of interaction of the carriers in semiconductor materials and heterostructures is related to electrical polarization appearing in spontaneous way due to the atomic displacement of two sublattices of semiconductors or due to piezoelectric effect induced by strain. In the two band model of semiconductors with similar conduction and valence bands (like PbTe) a variant of such effect of the electrical polarization on the electronic states of semiconductor heterostructures has been considered in papers [15, 16]. Such term was introduced by symmetry considerations in order to describe the relative displacements of two sublattices of the semiconductor compound of lead telluride type. Being the displacement of cationic and anionic sublattices it is accompanied by electrical polarization [16]. Thus in this simplest two band model the equations of the electronic states with incorporated electrical polarization or displacement are written

$$\begin{pmatrix} h_c & h_{cv} \\ h_{vc} & h_c \end{pmatrix}\begin{pmatrix} F_c \\ F_v \end{pmatrix} = \begin{pmatrix} E_g(\vec{r})/2 + Q(\vec{r}) & \vec{\sigma}\,\vec{p} - i\vec{\sigma}\,\vec{U}(\vec{r}) \\ \vec{\sigma}\,\vec{p} + i\vec{\sigma}\,\vec{U}(\vec{r}) & -E_g(\vec{r})/2 + Q(\vec{r}) \end{pmatrix}\begin{pmatrix} F_c \\ F_v \end{pmatrix} = E\begin{pmatrix} F_c \\ F_v \end{pmatrix}, \qquad (2.13)$$

where $E_g(\vec{r})$ is position dependent band gap of the semiconductor. In the case of heterojunction $Q(\vec{r})$ is the external applied potential, $\vec{p} = ip\vec{\nabla}$ is the momentum operator (p being momentum interband matrix elements), $U(\vec{r})$ is the term related to the above-mentioned electrical polarization or displacement. F_v and F_c are the components of the spin wave function.

Equation (2.12) is of Dirac type which includes the term $\vec{\sigma}\ \vec{U}(\vec{r})$. Its quantum mechanical nature in connection with Lorentz boots [14] on the one side, has been discussed above, but on the other side it represents the interaction of conduction and valence bands through optical phonons. In this aspect we mention that the interband interaction through acoustic phonons in the context of SOI and SHE has been analyzed recently [17].

In order to identify the SOI terms following traditional procedure of the transformation of Dirac-like equation in the Schrodinger ones we reduce the corresponding set of four-coupled first order differential equations. These can be written as:

$$H_c F_c = \left\{ [h_c + h_v][E - h_v]^{-1} h_{vc} \right\} F_c = E F_c$$

where $F_c = (f_+, f_-)$ is the conduction band envelope function spinor with the component for each spin orientation and E is the electron energy measured from the semiconductor midgap.

Following the outlined procedure and using the relation

$$\left(\vec{\sigma}\ \vec{a} \right)\left(\vec{\sigma}\ \vec{b} \right) = \left(\vec{a}\ \vec{b} \right) + i\,\vec{\sigma}\ \vec{a}\ \vec{b}$$

the Hamiltonian is H_c getting the form:

$$H_c = h_c + \vec{p}(E - h_v)^{-1}\,\vec{p} + P\vec{\sigma}\left[\vec{\nabla}(E - h_v)^{-1} \times \vec{p} \right] + + U^2(E - h_v)^{-1} + P\vec{\nabla}\left[\vec{U}(E - h_v)^{-1} \right] -$$
$$- 2\vec{\sigma}\left[\vec{U}(E - h_v)^{-1} \times \vec{p} \right] - iP\vec{\sigma}\left[\vec{\nabla}(E - h_v)^{-1} \times \vec{U} \right] - iP\vec{\sigma}\,\text{rot}\left(\vec{U}(E - h_v)^{-1} \right)$$

(2.15)

From this expression we observed that even in the two band model with included spin like degree of freedom through the mechanism of electrical polarization or atomic displacement, new SOI terms appearing in the reduced Schrodinger like Hamiltonian. The term $U^2(E - h_v)^{-1}$ is the operator related to the energy of polarization, while the terms $P\vec{\nabla}\left[\vec{U}(E - h_v)^{-1} \right]$ express the hydrostatic and shear deformations induced by optical like displacement of the sublattices. This term is similar to the strain term that appears in the result of usual interband acoustic hydrostatic and shear deformation [17]. However in the context of the problem analyzed in the present paper the two last terms of Eq. (2.14), which describes SOI induced by electrical polarization or displacement are more important. The term $2\vec{\sigma}\left[\vec{U}(E - h_v)^{-1} \times \vec{p} \right]$ looks like traditional SOI term $P\vec{\sigma}\left[\vec{\nabla}(E - h_v)^{-1} \times \vec{p} \right]$, where the electric field related to $\vec{\nabla}(E - h_v)^{-1}$ is replaced by electrical polarization. The last term looks more unusual. The term $iP\vec{\sigma}\,\text{rot}\left(\vec{U}(E - h_v)^{-1} \right)$ describes the SOI induced by the vector of local rotation of the lattices $\vec{\Omega} = \dfrac{1}{2}\text{rot}\,\vec{U}$ [18] which together with symmetric tensor of deformation is the antisymmetric part of the general distortion tensor.

Also a part of analyzed term $iP\vec{\sigma}\left[\vec{\nabla}(E - h_v)^{-1} \times \vec{U} \right]$ describes the term of SOI induced by rotation like interaction of electrical and polarization fields. Following [19] and introducing the effective masses of the two band model

$$m(\vec{r}, E) = \frac{\hbar^2}{2P^2}\left(E + \frac{E_g(\vec{r})}{2} + Q(\vec{r}) \right)$$

the Hamiltonian is rewritten

$$H_c = \frac{E_g(\vec{r})}{2} + Q(\vec{r}) - \frac{\hbar^2}{2}\vec{\nabla}\frac{1}{m}\vec{\nabla} + \frac{\hbar^2}{2}i\vec{\nabla}\frac{1}{m}\left(\vec{\sigma}\times\vec{\nabla}\right) + \frac{\hbar^2 U^2}{2P^2 m} + \frac{\hbar^2}{2P}\left(\vec{\nabla}\frac{\vec{U}}{m}\right) +$$

$$+ \frac{i\hbar^2}{P}\vec{\sigma}\left(\frac{\vec{U}}{m}\times\vec{\nabla}\right) - \frac{i\hbar^2}{2P}\left(\vec{\sigma}\,\mathrm{rot}\left[\frac{\vec{U}}{m}\right]\right) \tag{2.16}$$

In the case of two dimensional layered heterostructure with variation of the parameters in one z direction and polarization vector $\vec{U}$ oriented in the same direction $\vec{U} = \{0,0,U(z)\}$ the Hamiltonian H_c takes the form.

$$H = -\frac{\hbar^2}{2}\frac{d}{dz}\frac{1}{m(z)}\frac{d}{dz} + \frac{\hbar^2 k_\perp^2}{2m(z)} + \frac{\hbar^2 U^2}{2P^2 m(z)} + \frac{\hbar^2}{2P}\frac{d}{dz}\left(\frac{U}{m(z)}\right) +$$

$$+ \left[\frac{\hbar^2}{2}\frac{d}{dz}\left(\frac{1}{m(z)}\right) + \frac{\hbar^2}{P}\frac{U}{m(z)}\right]\cdot\left(k_x\hat{\sigma}_y - k_y\hat{\sigma}_x\right) \tag{2.17}$$

where k_x and k_y are the wave vectors in the plane of the heterostructure $k_\perp^2 = k_x^2 + k_y^2$.

In this case the energy is measured from the bottom of the band. From (2.17) it follows that in this case the SOI induced by electrical polarization is Rashba like [8,12]

3. Electronic states in semiconductor quantum well structures

One of the main issues of the physics of quantum well structures in the context of spintronic investigations is the formation of spin-split states. Concerning the spin-orbit splitting of the electronic states in quantum well (QW) structures there exists a vast lot of investigations. In particular, spin splitted electronic states have been obtained in an asymmetric quantum well on the basis of Rashba mechanism and the standard envelope-function formalism starting from the eight-band Kane model for the bulk semiconductors [19]. Simpler two-band Kane model has been used later to study the spin splitting of the states in the IV-VI semiconductor QWs [20], although in the analysis of the states of symmetric variants of the QW the effect of spin-orbit coupling has been neglected. However, as will be shown below although the effect of Rashba SOI does not lead to spin splitting in the symmetric QW (as well as to spin dependent tunneling in the symmetric barrier structure) it can considerably modify the states of size quantization in QW (as well as the tunneling transmission of the barrier structure). In particular, due to Rashba SOI size quantization electronic states in the QW at finite values of the in-plane wave vectors transform into interface like states. Moreover such interface states will be shown to appear in the barrier structure yet at finite values of the in-plane wave vectors [21, 22].

The electronic states and their energy spectrum are investigated on the basis of one band Schrodinger like Hamiltonian (2.17) taking into account that reduced electrical polarization Q(z)= U(z)/m(z) is oriented along axis z. The last non-diagonal term (2.17) in spin variable can be reduced to the diagonal form using the following
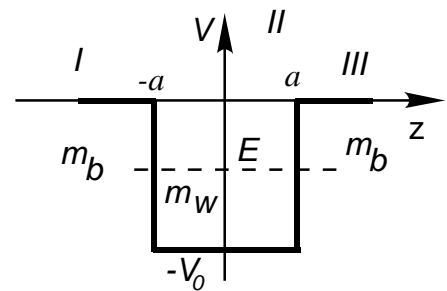

Fig. 3. The symmetric quantum well with width $2a$ and depth V_0. Electron energy is smaller than well borders

unitary transformation

$$U = \begin{pmatrix} -e^{i\varphi} & e^{i\varphi} \\ 1 & 1 \end{pmatrix},$$

(3.1)

where φ is the angle between $\vec{k}_\perp$ and the axis x. The result can be explained as $(k_x \sigma_y - k_y \sigma_x) \rightarrow k_\perp \sigma_z$

On the basis of (2.17) it is convenient for further calculation to write bulk Hamiltonian (in the region with constant mass, far from junction interface)

$$H = -\frac{\hbar^2}{2m}\nabla_z^2 + V(z) + \frac{\hbar^2}{2m}\left(k_\perp^2 + \frac{u^2}{p^2}\right) + \frac{\hbar^2 u}{2mp}k_\perp\lambda,$$

(3.2)

and boundary conditions such as

$$\frac{1}{m}\left[\nabla_z - \frac{u}{p} + k_\perp\lambda\right]\psi = const$$

(3.3)

where $\lambda = \pm 1$ is the quantum number that describes the states with spin "up" and spin "down" in the new spin-coordinate systems (3.1).

Considering potential profile for electrons as shown in Fig. 3 we can treat the problem using the Hamiltonian (3.2). The Schrodinger equation gives for each region the following wave functions

$$\psi_I = C_1 e^{q(z+a)}$$ (3.4.I)

$$\psi_{II} = C_2 e^{i\kappa(z+a)} + C_3 e^{-i\kappa(z+a)}$$ (3.4.II)

$$\psi_{III} = C_4 e^{-q(z-a)}$$ (3.4.III)

where

$$q = \sqrt{-\frac{2m_b E}{\hbar^2} + (k_\perp + \lambda Q_b)^2}$$ is the

wave vector in the barrier region and

$$\kappa = \sqrt{\frac{2m_w(E+V_0)}{\hbar^2} - (k_\perp + \lambda Q_w)^2}$$ is the

wave vector in the well region.

The notations $Q = \dfrac{U}{p}$ were used

and the index "b" notes the quantities corresponding to barrier layer (region I and III) and index "w" corresponds to well region (region II)

Using at the interface of wave functions continuity and condition (3.3) gives the relation of dispersion for size quantized electronic states [22].
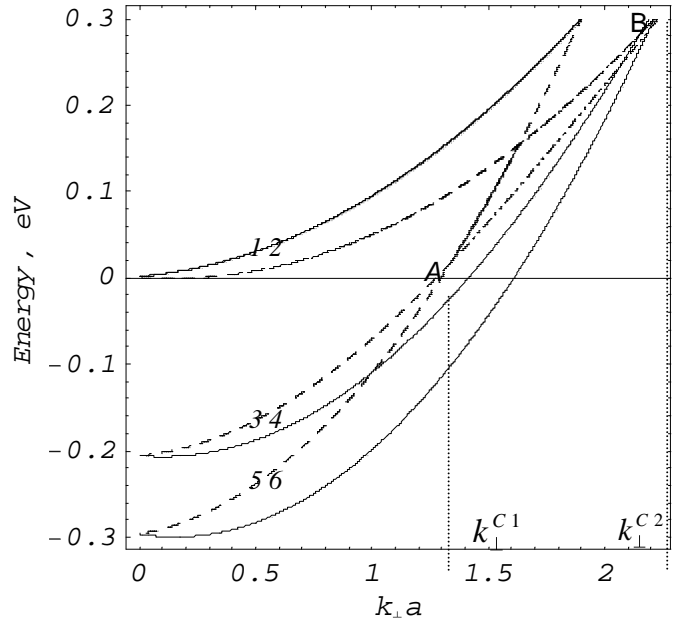
Fig. 4. Quantum well structure
1, 2, 5 and 6 are the bulk dispersion curves; 3 and 4 are an energy level for spin-up (solid line) and spin-down (dotted line) electrons.

$$2\gamma q\kappa \, \cos 2\kappa a + \left\{q^2 - \gamma^2\kappa^2 - [(Q_b + k_\perp\lambda) - \gamma(Q_w + k_\perp\lambda)]^2\right\}\sin 2\kappa a = 0$$

(3.5)

where $\gamma = \dfrac{m_b}{m_w}$ is the mass rapport. It is important to outline the appearance of spin-orbit coupling contributions in dispersion equation (3.5) for a symmetric QW without electrical polarization $Q = 0$ of the layers yet.

The interface states are described by a exponential behavior in the region I and III near the interface (no oscillatory as in the case of quantum dimensional states) and the change of wave function (3.1.II) with

$$\psi_{II} = C_2 e^{\kappa(z+a)} + C_3 e^{-\kappa(z+a)} \qquad (3.6)$$

gives

Fig. 5. Variation of the potential energy in the direction normal to the barrier. The potential energy is zero in regions I and III.

$$2\gamma q\kappa \cosh 2\kappa a + \left\{ q^2 + \gamma^2\kappa^2 - \left[(Q_b + k_\perp\lambda) - \gamma(Q_w + k_\perp\lambda) \right]^2 \right\} \sinh 2\kappa a = 0 \qquad (3.7)$$

Relations (3.2) and (3.4) give the energy for both size quantization and interface states.

To be more explicit we present in Fig. 4 the numerical results for a quantum well with width 40 A and depth 300 meV. The effective mass in the well structure is about 0,07 electron mass and the mass rapport is equal to 2. Electrical polarization is equal in magnitude but opposite in sign for well and its borders. Thus $Q_b = -Q_w = 4 \ 10^{-3} \ A^{-1}$.

The interface states for spin down electrons appear from $k_\perp^{C1}$ to $k_\perp^{C2}$ in the domain where bulk dispersions intersect (curve AB). For spin up, the situation has mirror symmetry relative to energy axis.

The discussed situation is in accordance with results obtained by Kolesnikov and Silin for single heterojunction [16, 23].

4. Spin dependent tunneling in barrier heterostructure

The new field of spintronics exploits especially the ability of conduction electrons in metals and semiconductors to carry spin-polarized current. In the context of spin injection and filtering different variants of tunnelling barrier structures have been investigated the last years. In [24, 25], in particular, an asymmetric barrier was proposed to generate spin-dependent tunnelling due to interface-induced Rashba spin-orbit coupling. The tunnelling transmission was shown to become spin-dependent in the result of spin-dependent reflection by inequivalent interfaces. Recently the Dresselhaus term in the effective Hamiltonian of bulk semiconductor of symmetric barrier was shown to result in a dependence of the tunnelling transmission on the carrier spin orientation [26]. However, the difference of the transmission probability for opposite spin orientations can achieve several percents as well as in the structures with Rashba mechanism of spin polarisation. In order to illustrate the possibilities of combined intrinsic SOI and extrinsic SOI, induced by the electrical polarization, to form spin polarized tunnel current a simple barrier semiconductor structure is analyzed taking in account only the conduction band, variation of the potential energy in the direction normal to the barrier is shown in fig. 3.
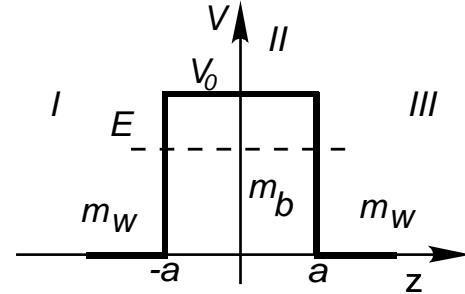
Solutions of one-dimensional Scrhodinger equation for each region with Hamiltonian given by (3.2) read

$$\psi_I = C_1 e^{iq(z+a)} + C_2 e^{-iq(z+a)} \tag{4.1.1}$$

$$\psi_{II} = C_3 e^{\kappa(z+a)} + C_4 e^{-\kappa(z+a)} \tag{4.1.2}$$

$$\psi_{III} = C_5 e^{-iq(z-a)} \tag{4.1.3}$$

where $q = \sqrt{\dfrac{2m_w E}{\hbar^2} - \left(k_\perp + \lambda Q_w\right)^2}$ and $\kappa = \sqrt{\dfrac{2m_b\left(V_0 - E\right)}{\hbar^2} + \left(k_\perp + \lambda Q_b\right)^2}$ are the wave

vectors in the well an in the barrier.

After application of boundary conditions presented in section 2 the relation between emergent and incident amplitudes of electron beam takes the form

$$\frac{C_5}{C_1} = G \exp[i\alpha] \tag{4.2}$$

The transmission coefficient T_C and the tunnelling time T_T are given in terms of G and α by the relations [27]

$$T_C = GG^* \tag{4.3}$$

and

$$T_T = \frac{m_w}{\hbar q} \frac{\partial \alpha}{\partial q} \tag{4.4}$$

Explicit relations for the mentioned quantities are

$$T_C = \frac{B^2}{A^2 \sinh^2 2\kappa a + B^2 \cosh^2 2\kappa a} \tag{4.5}$$

$$T_T = \frac{m_w}{\hbar q \kappa} \frac{\left[\frac{1}{2}B^2(\gamma+1) + A\gamma\left(\gamma q^2 - \kappa^2\right)\right]\sinh 4a\kappa - 4aA\gamma^2 q^2 \kappa}{A^2 \sinh^2 2\kappa a + B^2 \cosh^2 2\kappa a} \quad , \tag{4.6}$$

where

$$A = \gamma^2 q^2 - \kappa^2 + \left[\gamma\left(Q_w + \lambda k_\perp\right) - \left(Q_b + \lambda k_\perp\right)\right]^2 \text{ and } B = 2\gamma\kappa q$$

Relations (4.5) and (4.6) correspond to relations obtained by Paranjape [27] for $Q = 0$, and $\lambda = 0$ i.e. in the absence of polarization for spinless electrons.

The important characteristics for tunneling of electron with spin are the polarizability

$$P = \frac{T_C^+ - T_C^-}{T_C^+ + T_C^-} \tag{4.7}$$

and tunneling current

$$I^\pm = \frac{2}{\pi} \int_0^{\pi/2} T_C^\pm d\theta \tag{4.8}$$

where $\pm$ means the quantities for spin up or spin down($\lambda = 1$ or $\lambda = -1$)

Relations (4.5) – (4.8) take into account the space dependent electron effective mass, the motion in the perpendicular and parallel direction to the barrier, the spin of incident electrons and the electrical polarization due to the stress of layers. We have plotted the transmission coefficient via angle of incidence (see Fig. 6) for a symmetric barrier with height $V_0 = 300\ meV$ and width $2a = 40\ A$ for different energy of incident electrons. The effective mass of incident electrons is $0,067\ m_0$ and mass ratio $\gamma = 2$. From graphic it is clear that there is a great difference for transmission probability of electrons with up or down spin orientation. This fact can be used to obtain a spin polarization current. Although the last three terms in expression (2.17) modify potential (decreasing the height of the barrier and increasing the levels of the borders) the curves B, C and D presented in Fig. 6 plot the under barrier transmission and curve A is for on barrier electrons.
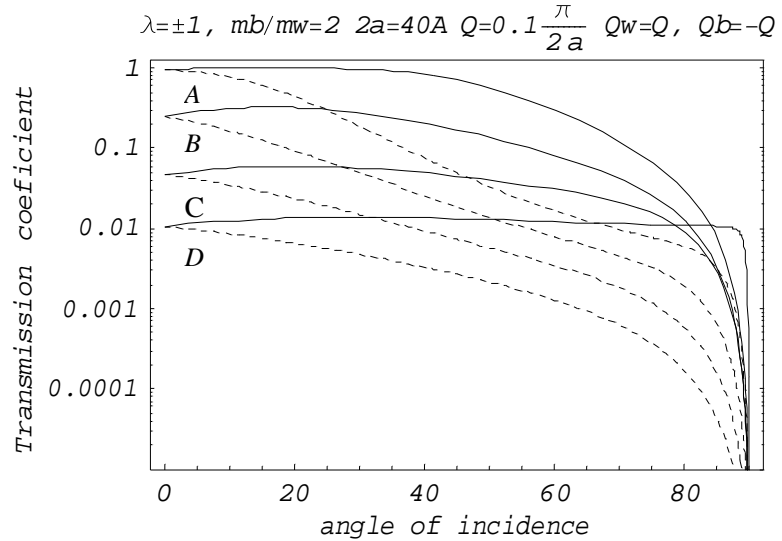
Fig. 6. Variation of the transmission coefficient via angle of incidence of electron beam for barrier structure with height $V_0 = 300\ meV$ and width $2a = 40\ A$. Curves A, B, C and D are plotted for incident energy $E = 450, 350, 250, 150\ meV$ respectively. Dotted lines are for spin down and solid lines for spin up.

5. Spin and orbital momentum Hall effect

In the area of emerging field of semiconductor spintronics one of the difficult obstacles is an efficient spin injection into semiconductors. One way is to make last ferromagnetic, such as (Ga, Mn)As [28],.However its Curie temperature is still lower than the room temperature, and there are still rooms for improvement towards practical use. Among other variants of spin injection during the last years spin Hall effect (SHE) was analyzed, which in its extrinsic form has been discovered more than two decades ago [29]. The extrinsic SHE is related to skew-scattering mechanism [29] and is based on asymmetric scattering of spin-up and spin-down electrons from a random impurity potential that includes a SOI term. However, the real practical interest to this approach of spin current generation has appeared recently after the discovery of intrinsic SHE [3h,4h], when Murakami, Nagaosa, and Zhang [30] proposed it in hole doped semiconductors like p-GaAs, and Sinova et al. [31] proposed the SHE in n-type two-dimensional semiconductor heterostructures. After this, two seminal experiments on the SHE have been done. Kato et al. [32] observed spin accumulation in n-type GaAs by means

of Kerr rotation, and Wunderlich et al. [33] observed a circularly polarized light emitted from a light-emitting diode (LED) structure, confirming the SHE in p-type semiconductors.

The geometrical structure of the intrinsic SHE is such that for an electric field applied, for example, on the z direction, a y-polarized dissipationless spin current will flow in the x direction (Fig.7). The electric field induced spin current can be summarized by the following macroscopic relation

$$J_j^i = \sigma_s \varepsilon_{ijk} E_k \tag{5.1}$$

Where σ_s is the spin conductance, ε_{ijk} is antisymmetric tensor.

At the same time, at the microscopic level the spin current is defined by the velocity times the spin, which is a rank two tensor. However, the velocity operator in general does not commute with the spin operator in a model with spin-orbit coupling. In order to define the spin current tensor as Hermitian operator that is symmetrized as:

$$J_j^i = \frac{1}{2}\left(S_i \frac{\partial H}{\partial P_j} + \frac{\partial H}{\partial P_j} S_i \right) \tag{5.2}$$

where S_i is the projection of the spin.

The induced spin current is considered to be dissipationless and unlike the anomalous Hall effect can be realized even in non-magnetic systems. Murakami et al.[30] and Sinova et al [31]. have argued, in contexts of p-doped semiconductors and 2D Rashba coupled systems, that spin-Hall conductivity can be dominated by an intrinsic contribution that follows from distortion of Bloch electrons by the electric field and therefore approaches a disorder independent value in high mobility systems. The

Fig. 7. Schematic illustration of the traditional Hall effect and spin Hall effect geometries with the evolution of Fermi level

aspect of dissipationless is one of the central issues of SHE both from fundamental and practical point of view. Although papers [30,31] dedicated to the topics of intrinsic SHE have appeared just at the same time
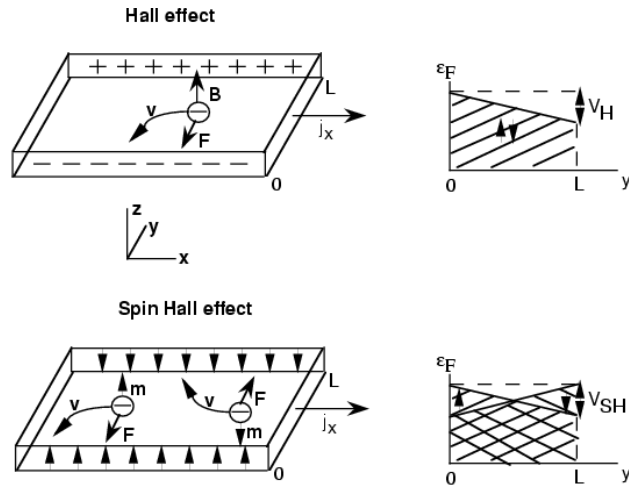
In the first papers the analysis of intrinsic SHE was done on the basis of semiclassical approach. In two-dimensional n-type systems, studied in [31], the Hall conductivity σ_{xy} in a clean limit is calculated from the Kubo formula as

$$\sigma_{xy} = -\frac{e^2}{2\pi\hbar} \sum_n \int_{BZ} d^2\vec{k}\, n_F(\varepsilon_n(\vec{k})) B_{nz}(\vec{k}) \tag{5.3}$$

where n is the band index, and integral is over the entire Brillouin zone. $B_{nz}(\vec{k})$ is defined as a z component of $\vec{B}_n(\vec{k}) = \nabla_{\vec{k}} \vec{A}_n(\vec{k})$, where

$$\vec{A}_n(\vec{k}) = -i \left\langle nk \left| \frac{\partial}{\partial k_i} \right| nk \right\rangle \equiv -i \int_{unit\ cell} u_{nk}^+ \frac{\partial u_{nk}}{\partial k_i} d^2x \qquad (5.4)$$

and u_{nk} is the periodic part of the Bloch wave function $\phi_{nk}(x) = e^{jkx} u_{nk}(x)$. This $B_{nz}(\vec{k})$ represents the effect of Berry phase momentum space. $n_F(\varepsilon_n(\vec{k}))$ is the Fermi distribution function for the n-th band.

By incorporating the effect $B(k)$, the Boltzman-type semiclassical equation of motion (SEOM) acquires an additional term [34]:

$$\dot{x} = \frac{1}{\hbar} \frac{\partial E_n(k)}{\partial k} + \dot{k} \times B_n(k) \qquad \hbar \dot{k} = -e(E + \dot{x} \times B(x)) \qquad (5.5)$$

The term $\dot{x} \times B(x)$ represents the effect of Berry phase, and it is called an anomalous velocity. Under the external electric field, the anomalous velocity becomes perpendicular to the field, and gives rise to the Hall effect. This Hall current is distinct from the usual Ohmic current, which comes from the shift of the Fermi surface from its equilibrium. This Hall effect comes from all the occupied states, not only from the states on the Fermi level. Sinova et al. [31] applied the Kubo formula to this Rashba Hamiltonian (2.6). For this procedure, they defined the spin current J_{zy} to be a symmetrized product of the spin Sz and the velocity

$$v_y = \frac{\partial H}{\partial k_y}. \qquad (5.6)$$

By assuming no disorder, the resulting spin Hall conductivity

$$\sigma_{sH} = \frac{-e}{16 \pi \lambda m}(p_{F+} - p_{F-}) \qquad (5.7)$$

where p_{F+} and p_{F-} are the Fermi momenta of the majority and minority spin Rashba bands. However, when $n_{2D} > m^2 \lambda^2 / \pi \hbar^4 \equiv n_{2D}^*$, $p_{F+} - p_{F-} = 2m\lambda/\hbar$ and the spin Hall conductivity is

$$\sigma_{sH} = -\frac{j_{sy}}{E_z} = \frac{e}{8\pi} \qquad (5.8)$$

independent of both the Rashba coupling strength and the 2DES density.

The origin of the SHE in this model is the following. The Rashba term (2.6) can be regarded as a k- dependent effective Zeeman field $B_{eff} = \alpha(z \times k)$. In equilibrium the spins are pointing either parallel or antiparallel to B_{eff} for the lower and upper bands, respectively. An external electric field $E \| x$ changes the wave vectors k of Bloch wave functions, and B_{eff} also changes accordingly. The spins will then precess around B_{eff}, and tilt to the $\pm z$-direction, depending on the sign of k_y. This appears as the SHE, and the spin Hall

conductivity is calculated to be $\dfrac{e}{8\pi}$, in agreement with the Kubo formula. The Dresselhaus term (2.5) can also be incorporated and if this SOI is stronger than Rashba ones spin Hall conductivity changes the sign.

By straightforward calculation following [31] it is easy to incorporate the influence of Rashba like SOI induced by electrical polarization, oriented normal to the 2D systems. As follows from (2.17) in this case the electrical induced SOI leads only to renormalization of Rashba constant.

In the general case both Rashba and Dresselhaus like terms are generated by electrical polarization appearing, and its effect is similar to established effect of intrinsic ones.

Initially the intrinsic SHE in p-type systems has been studied [30] in bulk semiconductors on the basis of isotropic effective Luttinger Hamiltonian of the two-fold degenerate valence bands of conventional semiconductors such as Si, Ge, GaAs et al

$$H_L = \frac{1}{2m}\left[\left(\gamma_1 + \frac{5}{2}\gamma_2\right)P^2 - 2\gamma_2(PS)^2\right] \tag{5.9}$$

where $S = (S_x, S_y, S_z)$ are spin 3/2 matrices, γ_1 and γ_2 are the Luttinger constants.

Following [35] in semiclassical approximation is straightforward to get the relation for spin Hall conductivity. The semiclassical equations of motion for holes under an electric field E read as

$$\dot{x} = \frac{1}{\hbar}\frac{\partial E_\lambda(k)}{\partial k} + \dot{k} \times B_\lambda(k) \qquad \hbar\dot{k} = -eE \tag{5.10}$$

Here $E_\lambda(k) = \dfrac{\hbar^2 k^2}{2m}\left(\gamma_1 + \left(5/2 - 2\lambda^2\right)\gamma_2\right)$ is an eigenenergy for the band with helicity λ. The Berry curvature is given by

$B_\lambda(k) = \lambda\left(2\lambda^2 - 7/2\right)\vec{k}/k^3$, which depends on the helicity.

If there is no anomalous velocity, the holes will move parallel to $\vec{k}$. The Berry curvature gives rise to an anomalous velocity perpendicular to both $\vec{k}$ and $\vec{E}$. This anomalous velocity is opposite for opposite helicity, i.e. for opposite

Fig. 8
(a) Schematic of the spin Hall effect for p-type semiconductors [35].
(b) Semiclassical trajectories for the wavepackets with helicity λ, projected onto the plane perpendicular to the electric field E. The thick arrows represent the spins.

spin orientation. This anomalous velocity from the motion along $\vec{k}$, when summed over all $\vec{k}$ of occupied states, amounts to a spin current. At the zero temperature, by applying an electric
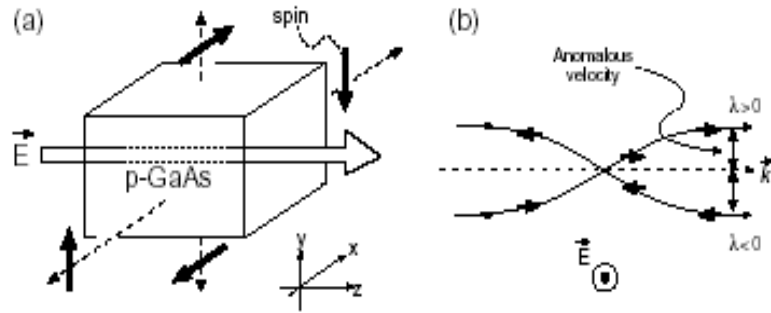
field along the l-direction, the spin current in which spins along the i-axis will flow along the j-direction is calculated as

$$j_j^i = \frac{e}{12\pi^2}\left(3k_F^H - k_F^L\right)\varepsilon_{ijl}\,E_l \tag{5.11}$$

Here, k_F^H and k_F^L are the Fermi wavenumbers for the HH and the LH bands, respectively.

A schematic of this effect is shown in Fig. 8 (a).

Taking into account the interband interaction through optical phonons [36] the SOI induced by electrical polarization or optical like displacement can be incorporated into effective Luttinger Hamiltonian in the following form

$$\begin{pmatrix} 0 & iu_y + u_x & -iu_z & 0 \\ -iu_y + u_x & 0 & 0 & -iu_z \\ iu_z & 0 & 0 & -iu_y - u_x \\ 0 & iu_z & iu_y - u_x & 0 \end{pmatrix} \tag{5.12}$$

Thus the generalized effective Luttinger Hamiltonian including both induced SOI and the anisotropy terms of the holes is written as

$$\hat{H} = \frac{\hbar^2}{2m^*}\left[\left(\gamma_1 + \frac{5}{2}\gamma_2\right)k^2 - 2\gamma_2\left(k_x^2 S_x^2 + k_y^2 S_y^2 + k_z^2 S_z^2\right) - \right.$$
$$\left. - 4\gamma_3\left(\{k_x, k_y + u_z\}\{S_x, S_y\} + \{k_y, k_z + u_x\}\{S_y, S_z\} + \{k_z, k_x + u_y\}\{S_z, S_x\}\right)\right] \tag{5.13}$$

where $\left[S_i, S_j\right] = \frac{1}{2}\left(S_i S_j + S_j S_i\right)$.

Taking into account that Luttinger like Hamiltonian (1) has two eigenvalues of light and heavy hole states following the recently proposed approach [37] terms in the anisotropic Luttinger Hamiltonian can be transformed in terms of a Clifford algebra of Dirac Γ matrices $\{\Gamma_a, \Gamma_b\} = a\delta_{ab}I_{4x4}\ \hat{H} = \gamma_1 k^2 + 2\gamma_3 d_a \Gamma_a$

Where

$$d_1 = -\sqrt{3}k_z k_y + \sqrt{3}u_x$$
$$d_2 = -\sqrt{3}k_z k_x + \sqrt{3}u_y$$
$$d_3 = -\sqrt{3}k_x k_y + \sqrt{3}u_z$$
$$d_4 = -\frac{\sqrt{3}}{2}\frac{\gamma_2}{\gamma_3}\left(k_x^2 - k_y^2\right)$$
$$d_5 = -\frac{1}{2}\frac{\gamma_2}{\gamma_3}\left(2k_z^2 - k_x^2 - k_y^2\right)$$

and $\frac{\hbar^2}{2m^*}\gamma_j \to \gamma_j$

The eigenvalue of the operator $d_a\Gamma/d$, where $d^2 = d_a d_a$ are ± 1 so that, the eigenvalues of $\hat{H}$ are:

$$E(k) = \gamma_1 k^2 \pm 2\gamma_3 d(k)$$

where

$$d^2(k) = \left(\frac{\gamma_2}{\gamma_3}\right)^2 k^4 + 3\left(1 - \left(\frac{\gamma_2}{\gamma 1}\right)^2\right)\left(k_x^2 k_y^2 + k_y^2 k_z^2 + k_z^2 k_x^2\right) + 3u^2 + 6\left(k_x k_y u_z - k_y k_z u_x - k_z k_x u_y\right)$$

The terms with polarization SOI lead to the spin splitting of heavy and light holes as illustrated in the Fig, 9,

Following the approach [37] in spherical approximation and keeping only terms linear in u_j the expression for spin conductance is obtained: in analytical form:

$$\sigma_{ij}^l = \sigma_{ij}^l 0) + \sigma_{ij}^l(u) = \frac{1}{6\pi^2}\varepsilon_{ijl}\left(k_F^H - k_F^L\right) + \frac{1}{6\pi^2}\varepsilon_{ijl}u_l\left(\frac{1}{k_F^L} - \frac{1}{k_F^H}\right)$$

(5.14)

where k_F^H и k_F^L are the Fermi wave vector of heavy and light holes of bulk semiconductors respectively, ε_{ijl} is the antisymmetric tensor.

The obtained formula (5.14) for spin-conductivy shows that the part $\sigma_{ij}^l(u)$ of conductivity induced by the polarization u in comparison with intrinsic part $\sigma_{ij}^l(0)$, considered in [30] is proportional to difference of the inverse values of the hole wave vectors. In result $\sigma_{ij}^l(u)$ for low doped semiconductors can exceed $\sigma_{ij}^l(0)$. $\sigma_{ij}^l(0)$.

Fig.. 9 Band splitting.by optical phonon like interband coupling in hole semiconductors.

The induced spin currents in the SHE are considered to be dissipationless. Murakami et al.[31] in the first paper have argued, that spin current approaches a disorder independent value in high mobility systems. The aspect of dissipationless is one of the central issues of SHE as well as recently proposed orbital angular momentum Hall effect (OAHE) from both fundamental and practical points of view. Although first papers [30,31], dedicated to the topics of intrinsic SHE, have appeared just at the same time, the proposed mechanisms of SHE are of different nature as follows from the above short analysis. In the Luttinger spin orbit coupling systems, a beautiful physical interpretation of the nature of intrinsic SHE was done. The origin of the spin- current comes from the existence of a monopole structure in momentum space, which is directly derived from the Berry phase in spin orbit coupling systems when Hamiltonian is projected to double degenerated helicity bands. Due to this topological nature, the conserved spin Hall current in general can be called as topological spin Hall current.

Recently [38], an orbital angular momentum Hall effect was proposed for two-dimensional systems with both Rashba and Dresselhaus SOI. It was demonstrated, that the orbital Hall current is different from the spin Hall current [31] and has a topological origin related to the existence of the magnetic flux in momentum space, while there is no such topological nature for the spin Hall current. In this context it is argued that the orbital Hall
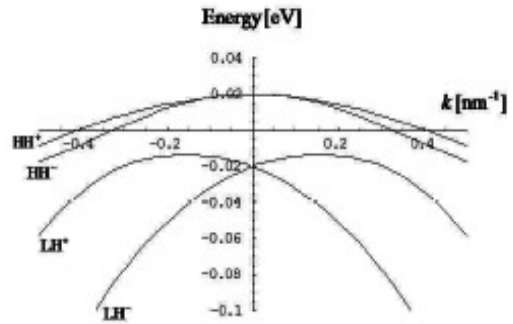
current dominates the transport properties in such systems, especially in disordered limit. The amprents of SHE are suggested to be only measurable in the ballistic regime.

References

[1] I. Zutic, J. Fabian and S. Das Sarma, Rev. Mod. Phys.76, 323 (2004).

[2] International Technology Roadmap for Semiconductors, http://public.itrs.net.

[3] M. Johnson and R. H. Silsbee, Phys. Rev. B **35**, 4959 (1987)

[4] G.A. Prinz, Science **282**, 1660 (1998)

[5] J. De Boeck and G. Borghs, Physics World, **12**, 27 (1999)

[6] D. P. DiVincenzo, Science, 270, 255 (1995)

[7] S. Datta and B. Das, Appl. Phys. Lett. 56, 665 (1990)

[8] R. H.Silsbee, J.Phys. Condens. Matter. 16, R179, (2004)

[9] D. Bjorken, S. D. Drell, Relativistic Quantum Mechanics (Mc Graw Hill, New York (1964).

[10] E.I. Rashba, Phys. Rev. B 68, 241315(R) (2003).

[11] Dresselhaus G 1955 Phys. Rev. 100 580

[12] Rashba E I and Sheka V I 1991 Landau Level Spectroscopy (Amsterdam: North-Holland) p 131

[13] S. Weinberg, Quantum Field Theory, Vol. 1, Foundations, Cambridge University Press, 1995. p.61.

[14] Z. Y. Wang and C. D. Xiong, Cond. mat. 0504049

[15] O.A.Pankratov, JETP Lett, 45, 82, (1987).

[16] V.Kantser and N.M.Malkova, JETP Lett, **54**, 388 (1991)

[17] B.A. Bernevig and O. Vafek, Cond. mat. 0408476

[18] A.M.Kosevich, Teoria kristalicheskoi reshetki, Kiev, 1988, p.35

[19] E.A.de Andrada e Silva *et al*, Phys.Rev.B, 55, 16293, (1997)

[20} E.A.de Andrada e Silva *et al*, Phys.Rev.B 60, 8859, (1999)

[21] G.Birliba, S.Carlig and V.Kantser, Proc. General Conference BPU-5 Vrnjaиka Banja, Serbia and Montenegro, p.567-572, (2003).

[22] S.Carlig and V.Kantser Mold.Journ Phys. Sci., Vol.2, 212, 2003

[23] A. V. Kolesnikov and A. P. Silin, Phys. Rev. B 59, 7596 (1999)

[24] A.Voskoboynikov et al, Phys.Rev.B 58, 15397, (1998)

[25] E.A.de Andrada e Silva *et al*, Phys.Rev.B 50, (1994)

[26] V.I.Perel *et al*, Phys.Rev.B **67** 201304 (2003).

[27] V. V. Paranjape, Phys. Rev. B **52**, 10740 (1995)

[28] H. Ohno, Science 281, 951 (1998)

[29] M. I. D'yakonov and V. I. Perel', JETP Lett. 13, 467 (1971).

[30] S. Murakami, N. Nagaosa, and S. C. Zhang, Science 301, 1348 (2003).

[31] J. Sinova, D. Culcer, Q. Niu, N. A. Sinitsyn, T. Jungwirth, and A. H. MacDonald, Phys. Rev. Lett. 92, 126603 (2004).

[32] Y. K. Kato, R. C. Myers, A. C. Gossard, D. D. Awschalom, Science, 306, 1910,(2004).

[33] J. Wunderlich, B. Kaestner, J. Sinova, T. Jungwirth, Phys. Rev. Lett. 94, 047204 (2005).

[34] G. Sundaram and Q. Niu, Phys. Rev. B 59, 14915 (1999).

[35] Shuichi Murakami, Cond. mat. 0405003

[36] B. Laikhtman, R.A. Kichl, Phys. Rev B, 47, 10515. (1993)

[37] Shuichi Murakami, Naoto Nagaosa, and Shou-Cheng Zhang, Phys. Rev B, 69, 235206. (2004)

[38] Jiangping Hu, Cond. mat. 0503149

ROLE OF ORBITALLY DEGENERATE Mn(III) IONS IN MAGNETIC BISTABILITY OF Mn$_5$-CYANIDE CLUSTER: NEW PROSPECTS FOR DESIGN OF SINGLE MOLECULE MAGNETS WITH HIGH BLOCKING TEMPERATURES

A.V. Palii [a#], S.M. Ostrovsky [a#], S.I. Klokishner [a, b], B.S. Tsukerblat [c], J.R. Galan-Mascaros [d], C.P. Berlinguette [d], K.R. Dunbar [d]

[a] *Institute of Applied Physics, Academy of Sciences of Moldova, Academiei Str. 5, MD 2028 Kishinev, Moldova*
[b] *State University of Moldova, Mateevich Str. 60, MD 2009 Kishinev, Moldova*
[c] *Chemistry Department, Ben-Gurion University of the Negev, Beer-Sheva 84105, Israel*
[d] *Department of Chemistry, Texas A&M University, PO Box 30012, College Station, Texas 77842-3012 (USA)*

[#] *Corresponding authors, e-mails: Andrew.Palii@uv.es, sm_ostrovsky@yahoo.com*

Abstract

In this paper we report a new model aimed at the explanation of the magnetic properties of the trigonal bipyramidal cyanide cluster $\{[Mn^{II}(tmphen)_2]_3[Mn^{III}(CN)_6]_2\}$ (tmphen = 4,5,7,8-tetramethyl-1,10-phenantroline). The model explicitly takes into account the strong single-ion anisotropy associated with the unquenched orbital angular momenta of two Mn(III) ions, and satisfactory explains the observed temperature dependence of dc magnetic susceptibility. At the same time the model is compatible with firmly confirmed fact that the system represents single molecule magnet and provides the theoretical background for the design of new cyanide-based single molecule magnets with higher blocking temperatures.

1. Introduction

Molecules that exhibit magnetic bistability, commonly referred to as Single-Molecule Magnets (SMM), are of high interest due to their unusual physical properties and potential importance for high-density data storage and quantum computing[1]. To date, almost all the molecules firmly established as displaying SMM behavior incorporate oxide-based bridging ligands that mediate the magnetic exchange coupling between metal centers. A remarkable feature of these systems is that in them all orbital angular momenta are completely quenched by the local low-symmetry crystal fields, so the oxo-bridged SMMs can be referred to as spin systems. Such molecules possess a large total spin ground state (S) formed by the isotropic Heisenberg magnetic exchange, which, when combined with a negative axial zero-field splitting ($D_S < 0$), leads to the appearance of the energy barrier for spin reversal.

Recently in the interest of producing clusters with larger spin reversal barriers, much attention has been focused on developing cyano-bridged cluster systems, for which the strength of the magnetic anisotropy is more readily changed via substitution of various metal ions. Particularly, the trigonal bipyramidal cyano-bridged cluster $[Mn^{III}(CN)_6]_2[Mn^{II}(tmphen)_2]_3$ (tmphen = 4, 5, 7, 8 – tetramethyl–1, 10–phenanthroline) was synthesized and characterized[2]. This system (hereunder abbreviated as Mn$_5$-cyanide cluster) contains three equatorial Mn(II) and two apical Mn(III) ions. The obtained temperature dependence of the static magnetic susceptibility exhibits interesting peculiarities, and at the

same time the ac-susceptibility signal clearly indicates that this cluster represents a new SMM.

The Mn(III) ions in the Mn$_5$-cyanide cluster occupy almost perfect octahedral sites. As a result the strong cubic crystal field produced by six carbon ions leads to the orbitally degenerate $^3T_1(t_2^4)$ ground term of the Mn(III) ion. This state carries first order orbital magnetism. This observation shows that the system under consideration is drastically different from the oxo-bridged spin systems consisting of orbitally non-degenerate ions possessing weak (second order) single ion anisotropy described by the zero-field splitting Hamiltonian $D_S S_Z^2$. On the contrary, in the Mn$_5$-cyanide one can expect a significant local (single ion) anisotropy associated with the unquenched orbital angular momenta of the Mn(III) ions. From this point of view the Mn$_5$-cyanide can be regarded as the first representative of a new class of SMMs based on cyanide clusters containing metal ions with unquenched orbital angular momenta.

In this paper we endeavor to develop the model able to explain the magnetic properties of the Mn$_5$-cyanide cluster and its magnetic anisotropy that is required for the SMM behavior. This model takes into account the first order single ion anisotropy associated with the Mn(III) ions and includes also the antiferromagnetic superexchange (mediated by the cyanide bridges) between Mn(III) and Mn(II) ions. The temperature dependence of the dc magnetic susceptibility is discussed in the context of the SMM behavior of the Mn$_5$-cyanide cluster.

2. Model

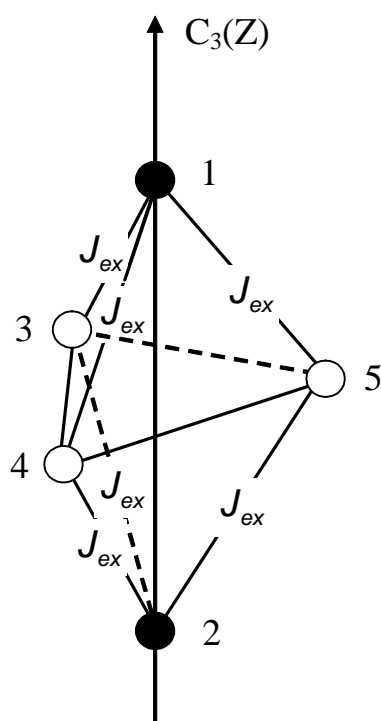The molecular geometry of the Mn$_5$-cyanide is shown in Fig. 1 of Ref. 2. Each Mn(III) ion forms three linear cyanide bridges to the Mn(II) centers and is capped by three terminal cyanide ligands. Five Mn ions form a trigonal bipyramid in which two Mn(III) occupy the apical positions and are surrounded by six carbon atoms, three Mn(II) ions reside in the equatorial plane and are coordinated by the nitrogen atoms. Due to strong cubic crystal field produced by carbon atoms, the ground term of the Mn(III) ion in a cubic field is expected to be the low-spin ($s=1$) orbital triplet $^3T_1(t_2^4)$. On the contrary, weak crystal field induced by the nitrogen atoms gives rise to a high-spin ($s=5/2$) ground term $^6A_1(t_2^3 e^2)$ of each Mn(II) ion. Since the closest intermolecular Mn-Mn distance is 8.77 A [2] we will neglect the intercluster interactions and consider a single-cluster problem. The adopted enumeration of the Mn ions is shown in Fig.1, where the numbers 1 and 2 are assigned to two Mn(III) ions, three Mn(II) ions are marked by the numbers 3, 4, 5.

The model includes the following interactions:

(i) *The spin-orbit (SO) coupling* operating within the ground cubic $^3T_1(t_2^4)$ term (state with fictitious orbital angular momentum $l=1$) of i-th Mn(III) ion ($i=1,2$) is described by the Hamiltonian

Fig.1. Metalic skeleton of the Mn$_5$-cyanide cluster: 1, 2 – Mn(III); 3, 4, 5 – Mn(II)

$H^i_{SO} = -\kappa\lambda \, s_i l_i$, where $\lambda \approx -180 \, \text{cm}^{-1}$ and $\kappa \approx 0.8$ are the many-electron SO coupling parameter for $^3T_1(t_2^4)$ term, and corresponding orbital reduction factor, respectively [3]. The SO coupling splits the $^3T_1$ term into three levels with $j=0$ (A_1), $j=1$ (T_1) and $j=2$ (E, T_2), where j is the total angular momentum of the Mn(III) ion in the ground state.

(ii) *Trigonal crystal field.* The site symmetry of the Mn(III) ions is $C_{3\upsilon}$. The trigonal component of the crystal field acting on i-th Mn(III) ion is described by the operator $H^i_{trig} = \Delta\left(l^2_{iz} - 2/3\right)$. This interaction splits the $^3T_1$ $(l=1)$ term into $^3A_2$ ($m_l = 0$) and ^3E ($m_l = \pm 1$). The parameter Δ is defined in such a way that for $\Delta > 0$ the $^3A_2$ term becomes the ground one.

(iii) *Magnetic exchange.* We assume that only the superexchange interaction between Mn(II) and Mn(III) ions through the cyanide bridges affects the magnetic properties, meanwhile the interactions between Mn(II) ions are expected to be negligible due to the large intermetallic distances. The typical values of the parameters of exchange coupling between cyanide bridged metal ions are of the order of several wave numbers [4], i.e. they are two orders of magnitude smaller than the parameters of the SO coupling and trigonal crystal field. We will use a simplification similar to that proposed by Lines in his study of the magnetic exchange between high spin Co(II) ions[5] and retain only the isotropic part of the exchange Hamiltonian. Within this approximation the exchange Hamiltonian for Mn$_5$-cyanide cluster is given by $H_{ex} = -2J_{ex}(s_1 + s_2)(s_3 + s_4 + s_5)$, where the parameter J_{ex} is assumed to be the same for all Mn(II) – Mn(III) pairs in accordance with the geometry of the complex. One can prove that the magnetic orbitals involved in the exchange interaction are non-orthogonal, so the exchange parameter J_{ex} is expected to be negative.

The full Hamiltonian of the system looks as follows:

$$H = \sum_{i=1,2}\left(H^i_{SO} + H^i_{trig}\right) + H_{ex} + \beta\, H\left[-\kappa(l_1 + l_2) + g_e(s_1 + s_2) + g(s_3 + s_4 + s_5)\right], \qquad (1)$$

where the last term is the Zeeman interaction, that includes orbital and spin parts, β is the Bohr magneton, H is the applied magnetic field. The g-factor for Mn(II) ions is allowed to be slightly different from 2.

To find the matrix representation of the Hamiltonian (1) we use the basis

$$\left|s_1 l_1(j_1) s_2 l_2(j_2)(J_{12})\, s_3 s_4 (S_{34}) s_5 (S_{345}) J M_J\right\rangle \equiv \left|(j_1)(j_2)(J_{12})(S_{34})(S_{345}) J M_J\right\rangle, \qquad (2)$$

where J and M_J are the angular momentum and its projection for the entire system, the meaning of the remaining quantum numbers is clear from eq. (2). For the sake of brevity the details of calculation of the matrix elements of the Hamiltonian (1) are omitted.

3. Results and discussion.

Figure 2 displays the temperature dependence of χT measured for crushed single crystal at 1000 G in a wide temperature range (1.8-300 K) [2], and the theoretical curve calculated for the set of the best fit parameters. The observed room temperature χT value is about 13.70 emu·K·mol^{-1}; the χT value decreases as the temperature is lowered to 10.413 emu·K·mol^{-1} at 45 K, after which point, χT increases to a maximum of 15.685 emu·K·mol^{-1} at 4.0 K. The best fit is achieved for $\Delta = -251 \, \text{cm}^{-1}$, $J_{ex} = -3.8 \, \text{cm}^{-1}$ and $g = 1.95$, with the

agreement criterion $(1/N)\sum\left[(\chi T)_{\text{exp}}-(\chi T)_{\text{calc}}\right]^2\big/(\chi T)^2_{\text{exp}}$ being equal to $2.9\cdot10^{-3}$ ($N=52$ is the number of the experimental points). One can see that the theoretical curve calculated with this set of parameters is in a satisfactory agreement with the experimental data well reproducing the magnetic behavior at low temperatures, the minimum at 45 K, and the slope of the curve in the high temperature region. The obtained relatively small value of the trigonal crystal field parameter is in line with the structural data revealing almost perfect octahedral positions of the Mn(III) ions. The best fit J_{ex} value falls into the range of the typical values for the parameters of superexchange mediated by the cyanide bridges [4].
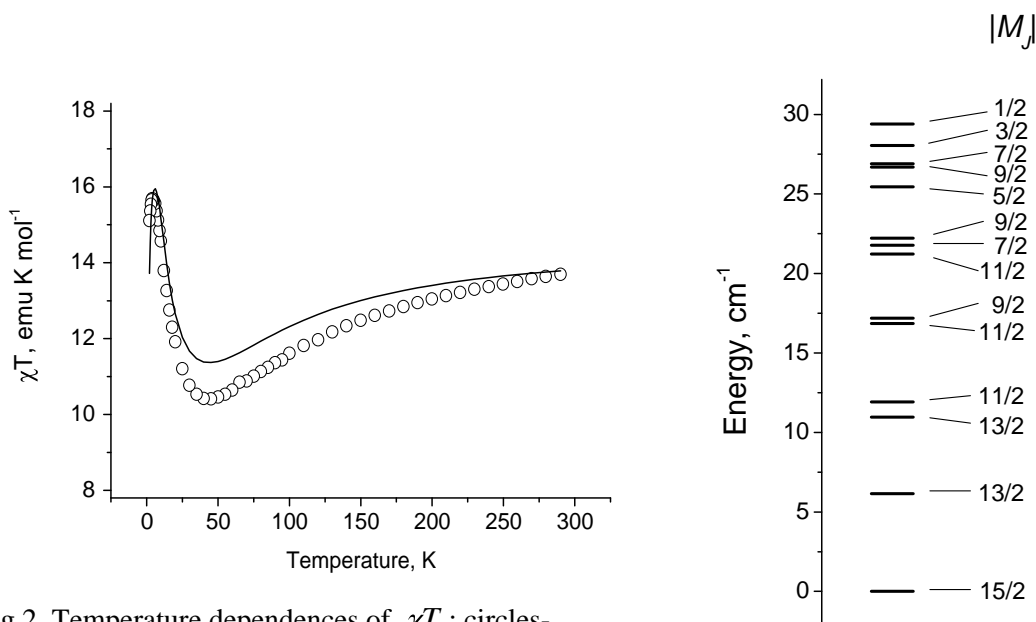
Fig.2. Temperature dependences of χT : circles-experimental data, solid line – theoretical curve calculated with the best fit parameters $J_{ex}=-3.8\,cm^{-1}$, $\Delta=-251\,cm^{-1}$, $g=1.95$

Fig.3. Low-lying energy levels calculated with $J_{ex}=-3.8\,\text{cm}^{-1}$, $\Delta=-251\,\text{cm}^{-1}$

The scheme of the low-lying energy levels (up to 30 cm^{-1}) calculated with the set of the best fit parameters is shown in Fig.3. The energies are dependent on $|M_J|$ in accordance with the axial magnetic symmetry of the system. The ground state of the cluster possesses $|M_J|=15/2$, and the energies of the low-lying levels tend to increase with the decrease of $|M_J|$ giving rise to a positive magnetic anisotropy defined as $\Delta\chi=\chi_{//}-\chi_{\perp}$. These features of the energy pattern clearly indicate the presence of appreciable barrier ($\approx$ 30 cm^{-1}) for the reversal of magnetization that is compatible with the observed SMM behavior of the Mn$_5$-cyanide cluster. Some irregularities in the disposition of the excited levels vs. $|M_J|$ are unable to change this conclusion.

References

[1] D. Gatteschi, R. Sessoli, Angew. Chem. Int. Ed. 42 (2003) 269-297.

[2] C. P. Berlinguette, D. Vaughn, C. Cańada-Vilalta, J.-R. Galan-Mascaros, K. R. Dunbar. Angew. Chem. Int. Ed. 42 (2003) 1523-1526.

[3] A. Abragam, B. Bleaney, Electron Paramagnetic Resonance of Transition Ions, Clarendon, Oxford, England, 1970.

[4] H. Weihe, H. Gudel, Comments Inorg. Chem. 22 (2000) 75.

[5] M. E. Lines, J. Chem. Phys. 55 (1971) 2977.

IMPACT OF NONLINEAR ELECTRON-PHONON COUPLING IN MgB$_2$ ON HIGH T$_C$ SUPERCONDUCTIVITY

V. Eremeev

Center of Optoelectronics, Institute of Applied Physics, Academy of Sciences of Moldova, Department of Engineering and Computer Science, Free International University of Moldova

"True laws of Nature cannot be linear" - Albert Einstein

The processes of nonlinear electron-phonon coupling in superconductors with two-band electronic structure are considered. It is shown that the mechanism of two-phonon exchange between the carriers has a considerable impact on increasing of T$_C$ of superconductivity in MgB$_2$ compound.

1. Introduction

The recent discovery of superconductivity at 40 K in magnesium diboride MgB$_2$ [1] has provoked a keen interest in the structural and electronic properties of this binary inter-metallic compound. Particularly the high T$_C$ caused a lot of interest in this compound and its physical properties. For example the authors of paper [2] have carried out inelastic neutron scattering measurements of the phonon density of states and compared these results with detailed first-principle calculations of the lattice dynamics (and electronic) calculations for MgB$_2$. Thus they conclude that the electron-phonon coupling is nonlinear, providing the essential ingredient to explain the high T$_C$ and boron isotope effect in MgB$_2$ [3]. Another research group considers in [4] that the E$_{2g}$ modes in MgB$_2$ have a significant nonlinear coupling with electrons and suggests that it is stronger than the linear coupling, which signify substantial contribution to the Cooper pairing from the two-phonon exchange.

Also the high T$_C$ superconductivity of MgB$_2$ has stimulated a strong interest on the role of band-filling in phonon-driven superconductivity when the charge carriers stem from low electron or hole density in the conduction band. There is an agreement among theorists that there are two qualitatively different systems of bands in MgB$_2$: quasi-2D σ-bands, and 3D π-bands, and that the former strongly couple to optical E$_{2g}$ phonon at $\approx$ 600 cm^{-1} [5]. This phonon mode is calculated to be highly anharmonic, and it also has significant nonlinear contributions to the electron-phonon coupling. Thus the puzzle of superconductivity in MgB$_2$ is hidden in it two-gap, nonlinear electron-phonon coupling mechanism (two-phonon in particular) on E$_{2g}$-mode related with in-hexagonal-plane vibrations of boron ions. This mechanism lays off a bridge for the novel joint model of a *nanotubular* multi-phonon multi-gap room-T$_C$ superconductivity (RTSC) on base of gallery of whispering circular zero-point phonon modes (twistons, rotons), in particular E$_{2g}$-mode, resulting in resonant electron-phonon coupling. Suggested model is in accordance with some recent experimental data confirming the effect of nanotubular superconductivity and indicating possible RTSC in 2D bundles of carbon nanoscale tubes [6].

In this paper the superconducting properties of magnesium diboride considering the mechanism of nonlinear phonon exchange between the carriers have been studied. The two-band structure of this compound in processes of interband two-phonon scattering of electrons is considered. Taking into account the nonlinear mechanism of electron-phonon interaction as

preponderant in the process of formation of superconducting phase the sophisticated temperature dependence of the order parameter is found, comparatively with the one-phonon BCS-like model. The anomalous behavior of the order parameter as a function of temperature is observed due to the fact that the electron-phonon interaction "constant" in case of two-phonon exchange between the carriers increases as a temperature function. One expects that the nonlinear exchange effects can explain the high T_C superconductivity of MgB_2.

2. The effect of nonlinear electron-phonon interaction in multi-band superconductors: case of two-phonon exchange

The experimental and theoretical results indicate that the compound MgB_2 has a two-band electronic structure [7]. Presence of two bands near the Fermi energy in the electron spectrum of cuprates has stimulated the application of various models with interband interactions to explain their superconductivity, for example see [8]. In framework of these results one can consider the simple case of two-band electronic system which interacts with the phonon subsystem through the two-phonon exchange mechanism. In this model the Columbian interaction between electrons is not taken into consideration without losing of physical essence of this process in superconductors. Therefore the interacting electron-phonon system is governed by the following Hamiltonian, dropping spin indexes

$$H = H_{el} + H_{ph} + H_{int} \tag{1}$$

where $H_{el} = \sum_m \sum_{\mathbf{k}} \varepsilon_m(\mathbf{k}) a_{m,\mathbf{k}}^+ a_{m,\mathbf{k}}$; $H_{ph} = \sum_{\mathbf{q}} \hbar\omega_{\mathbf{q}} b_{\mathbf{q}}^+ b_{\mathbf{q}}$; $H_{int} = \frac{1}{\sqrt{V}} \sum_{m,n} \sum_{\mathbf{k},\mathbf{q}} \left(g_{mn}(\mathbf{q}) a_{m,\mathbf{k}+\mathbf{q}}^+ a_{n,\mathbf{k}} b_{\mathbf{q}} + H.c. \right)$

Here V is the volume of the crystal $b_{\mathbf{q}}^+ (b_{\mathbf{q}})$ is the creation (annihilation) operator of the phonon with $\mathbf{q}$ wave-vector and $a_{n,\mathbf{k}}^+ (a_{n,\mathbf{k}})$ is the electron creation (annihilation) operator in n-band (n=1,2) with the quasi-wave vector $\mathbf{k}$. The matrix elements of the electron-phonon interaction constant can be approximated by following expressions

$$g_{11}(\mathbf{q}) \approx i\mathbf{q}\varepsilon_F \sqrt{\frac{\hbar}{2\rho\omega_{\mathbf{q}}}} , \quad g_{21}(\mathbf{q}) \approx i\varepsilon_{21}\sqrt{\frac{m^*\varepsilon_{21}}{\hbar\rho\omega_{\mathbf{q}}}} \tag{2}$$

where ρ is the density of the material, ε_F is the energy of the Fermi level, ε_{21} is the energetic distance between bands, m^* is the effective mass of carriers.

Taking into account the proprieties of the local symmetry of Bloch wave functions for the down and upper bands, it is not difficult to demonstrate that in many cases when the second and the first bands arise from the atomic local levels with different symmetries (for example P and S atomic states) the interband matrix element of the electron-phonon interaction g_{12} is larger than the intraband matrix elements g_{11} ($g_{12} \gg g_{11}$) and g_{22}=0. Also it is considered the symmetric form of matrix g, i.e. $g_{12} = g_{21}$.

In the framework of detailed model discussed in [9] the two-phonon cooperative processes between the electrons of the lowest band through the virtual states of the second band are considered (see Fig.2 in [9]). The case of overlapped bands [10] is not taken into account in the proposed model. Thus, it is necessary firstly to eliminate the operators of the second band from Hamiltonian (1). If the second band is situated at the energetic distance larger than $\kappa_B T$, we can eliminate the electronic operators of this band from Hamiltonian (1). After elimination of electronic operators belonging to second band of superconductor the effective electron-electron interaction Hamiltonian resulting from two-phonon exchange

mechanism is obtained [9]. Thus one can write the kinetic equation for any operator *A(t)* of electronic subsystem [6].

$$\left\langle \frac{dA(t)}{dt} \right\rangle = \frac{i}{\hbar} \left\langle \left[H'_{el}; A(t) \right] \right\rangle + \frac{i}{\hbar} \left\langle \left[H^{eff}_{e-e}; A(t) \right] \right\rangle \tag{3}$$

Here $H'_{el} = \sum_{\mathbf{k}} \varepsilon'_1(\mathbf{k}) a^+_{\mathbf{k}} a_{\mathbf{k}}$ and

$$H^{eff}_{e-e} = -\frac{1}{V^2} \sum_{\mathbf{k}\mathbf{k}'} \sum_{\mathbf{q}_1, \mathbf{q}_2} \frac{(1+2N_{q_1})|g_{21}(\mathbf{q}_1)|^2 |g_{21}(\mathbf{q}_2)|^2 \phi_1(\mathbf{k})\phi_1(\mathbf{k}')(\hbar\omega_{\mathbf{q}_1} + \hbar\omega_{\mathbf{q}_2}) a^+_{\mathbf{k}+\mathbf{q}_1+\mathbf{q}_2} a^+_{\mathbf{k}'} a_{\mathbf{k}'+\mathbf{q}_1+\mathbf{q}_2} a_{\mathbf{k}}}{(\hbar\omega_{\mathbf{q}_1} + \hbar\omega_{\mathbf{q}_2})^2 - (\varepsilon_1(\mathbf{k}'+\mathbf{q}_1+\mathbf{q}_2) - \varepsilon_1(\mathbf{k}'))^2}$$

$$-\frac{2}{V^2} \sum_{\mathbf{k}\mathbf{k}'} \sum_{\mathbf{q}_1, \mathbf{q}_2} \frac{N_{q_1}|g_{21}(\mathbf{q}_1)|^2 |g_{21}(\mathbf{q}_2)|^2 \phi_2(\mathbf{k})\phi_2(\mathbf{k}')(\hbar\omega_{\mathbf{q}_1} - \hbar\omega_{\mathbf{q}_2}) a^+_{\mathbf{k}+\mathbf{q}_1-\mathbf{q}_2} a^+_{\mathbf{k}'} a_{\mathbf{k}'+\mathbf{q}_1-\mathbf{q}_2} a_{\mathbf{k}}}{(\hbar\omega_{\mathbf{q}_1} - \hbar\omega_{\mathbf{q}_2})^2 - (\varepsilon_1(\mathbf{k}'+\mathbf{q}_1-\mathbf{q}_2) - \varepsilon_1(\mathbf{k}'))^2} \tag{4}$$

where

$$\phi_1(\mathbf{k}) = \frac{\varepsilon_2(\mathbf{k}+\mathbf{q}_1) + \varepsilon_2(\mathbf{k}+\mathbf{q}_2) - \varepsilon_1(\mathbf{k}+\mathbf{q}_1+\mathbf{q}_2) - \varepsilon_1(\mathbf{k})}{\left[\varepsilon_2(\mathbf{k}+\mathbf{q}_1) - \varepsilon_1(\mathbf{k}+\mathbf{q}_1+\mathbf{q}_2) + \hbar\omega_{\mathbf{q}_2}\right]\left[\varepsilon_2(\mathbf{k}+\mathbf{q}_2) - \varepsilon_1(\mathbf{k}) - \hbar\omega_{\mathbf{q}_2}\right]}$$

$$\phi_2(\mathbf{k}) = \frac{\varepsilon_2(\mathbf{k}+\mathbf{q}_1) + \varepsilon_2(\mathbf{k}-\mathbf{q}_2) - \varepsilon_1(\mathbf{k}+\mathbf{q}_1-\mathbf{q}_2) - \varepsilon_1(\mathbf{k})}{\left[\varepsilon_2(\mathbf{k}+\mathbf{q}_1) - \varepsilon_1(\mathbf{k}+\mathbf{q}_1-\mathbf{q}_2) - \hbar\omega_{\mathbf{q}_2}\right]\left[\varepsilon_2(\mathbf{k}-\mathbf{q}_2) - \varepsilon_1(\mathbf{k}) + \hbar\omega_{\mathbf{q}_2}\right]}$$

In expression (4) $N_q = \left(\exp[\hbar\omega_q/(\kappa_B T)] - 1\right)^{-1}$ is the mean number of phonons in the **q** state.

   Thus the effective interaction Hamiltonian (4) of the electrons from the first band through the two-phonon exchange is obtained. From Exp.(4) it results that the interaction is attractive when the difference between the energies of electrons is smaller as $2\hbar\omega_D$ (Debay cutoff). The cooperative interaction between the electrons through the biphonon field is reduced not only to the simple processes of simultaneous absorption or emission of two phonons. As a consequence of effective interaction Hamiltonian, here are possible the scattering processes, i.e. the transitions between two states of the first band can take place with the one-phonon absorption with $\mathbf{q}_1$ wave-vector and the emission of the other phonon with $\mathbf{q}_2$ wave-vector. This cooperative exchange between the electrons increases with increasing of the temperature. In other words the effective Hamiltonian is proportional with the temperature through the mean number of phonons, N_q. This is one of the main differences between the one-phonon Bardeen-Cooper-Schrieffer exchange (BCS, [11]) and the effective electron-electron interaction in case of two-phonon exchange mechanism. Also the temperature dependence of superconductive energy gap in presence of this exchange integral can be modified essentially, as consequence the critical temperature will increase. Thus the two-phonon exchange mechanism can explain the increasing of critical temperature in many-band superconductors.

3. Superconducting properties of MgB$_2$ considering the two-phonon exchange between electrons

   The influence of the second virtual band position on the creation of the two-phonon Cooper effect in the first band plays an important role in this model. For example, if the virtual states of second band are situated near the Fermi level of the first band, the two-phonon scattering effects with the absorption of one phonon from the thermostat and the

generation of another phonon can play a more important role as processes with the simultaneous generation or absorption of phonon pairs.

Considering some approximations in the effective interaction Hamiltonian from Exp.(3) the Hamiltonian of system is obtained taking into consideration spin indexes:

$$H = \sum_k \varepsilon_1'(\mathbf{k}) a_k^+ a_k - \frac{G(T)}{V} \sum_{k,k'} a_{k'}^+ a_{-k'}^+ a_{-k} a_k \ , \tag{5}$$

where $k = (\mathbf{k}, \frac{1}{2})$ and $G(T) = \frac{4}{V} \sum_{\mathbf{q}_1} \frac{|g_{21}(\mathbf{q}_1 - \mathbf{q}_2)|^2 |g_{21}(\mathbf{q}_2)|^2}{\varepsilon_{21}^2} \left\{ \frac{1}{\hbar\omega_{\mathbf{q}_1-\mathbf{q}_2}} + 4N_{q_1} \frac{\hbar\omega_{\mathbf{q}_1-\mathbf{q}_2}}{(\hbar\omega_{\mathbf{q}_1-\mathbf{q}_2})^2 - (\hbar\omega_{\mathbf{q}_2})^2} \right\}.$

Defined the superconductive energy gap $\Delta(T) = \frac{G(T)}{2V} \sum_{k'} \langle a_{k'}^+ a_{-k'}^+ \rangle$, we can approximate the Hamiltonian (5) in the following form:

$$H = \sum_k \varepsilon_1'(\mathbf{k}) a_k^+ a_k - \sum_k \left(\Delta(T) \langle a_{-k} a_k \rangle + H.c. \right) \tag{6}$$

The diagonalization of Exp.(6) using the Bogoliubov transformations [12] gives us the following relation for the order parameter as a temperature function

$$\Delta(T) = \frac{4\pi\kappa_B T}{\sqrt{14\xi(3)}} \left[\ln \frac{T_c}{T} + \frac{1}{\lambda} \left(\frac{\sigma T^2}{1+\sigma T^2} - \frac{\sigma T_c^2}{1+\sigma T_c^2} \right) \right]^{1/2}, \tag{7}$$

where $\xi(3)$ is the value of Riemann zeta-function ($\xi(3) \approx 1.2$), λ, σ are the model parameters and T_C is critical temperature that is calculated in the framework of two-phonon exchange approximation used in proposed model [9].

In Fig.1 the comparison of one-phonon BCS-like model and proposed two-phonon superconductivity model (with $\sigma \neq 0$) is represented. The decreasing of $\Delta(T)$ as a temperature function in the proposed model is slower than in one-phonon BCS-like model. This follows from numerical results and analytic dependence (7). The slow decreasing of $\Delta(T)$ gives us the higher critical temperature than in conventional superconductivity theory with constant exchange integral when $\sigma=0$.
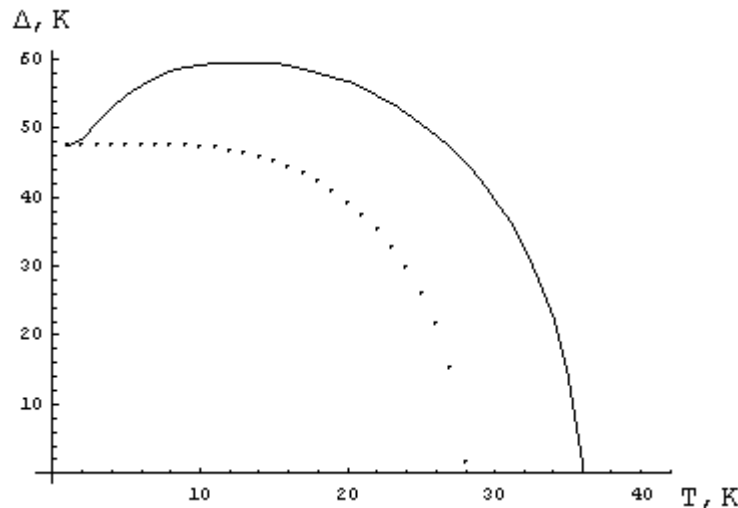

Fig.1 The temperature dependence of the superconductivity order parameter Δ(T). Comparison of one-phonon BCS-like (dotted curve) and two-phonon (solid curve) superconductivity models.

4. Conclusions

In this paper it is shown briefly that the exchange integral between the electrons increases with temperature due to the fact that the two-phonon exchange mechanism stimulates the coherence formation of Cooper-pairs in the two-band superconductors. One of similar superconductor material is MgB_2 and we applied the two-phonon cooperative mechanism of superconductivity [9] for this compound to study its thermodynamic properties. Basing on numerical calculations we plotted the dependence of superconductive energy gap as a temperature function and found the critical temperature of analyzed material. The results of these calculations are in a good agreement with experimental calculations. Thus the two-phonon (nonlinear in general) mechanism of superconductivity opens a new concept on the formation of Cooper-pairs in the processes of multi-phonon exchange between the carriers in multi-band superconductors. The non-traditional temperature dependence of the order parameter (see Fig.1) is described by a complicated two-phonon exchange mechanism between the electrons. Also, from Eq.(7) it results that the temperature of phase transition is higher if the two-phonon interaction is more intensive.

References

[1] J. Nagamatsu, N. Nakagawa, T. Muranaka, Y. Zenitani and J. Akimitsu, Nature **410**, 63, (2001).
[2] T.Yildirim et al, Phys.Rev.Lett. **87**, 037001 (2001).
[3] S. L. Bud'ko, G. Lapertot, C. Petrovic, et al, Phys.Rev.Lett. **86**, 1877 (2001).
[4] Amy Y. Liu, I. I. Mazin and Jens Kortus, Phys.Rev.Lett. **87**, 167003 (2001).
[5] A. B. Kuz'menko et al, cond-mat/0107092 (2001)
[6] V. Pokropivny, *Physica C* **351**, 71 (2001).
[7] K.D.Belashchenko et al., cond.-mat./0102290 (2001); J.M.An, W.E.Pickett, cond.-mat./0102391 (2001).
[8] N.Kristoffel, P.Konsin and T. Ord, Rivista Nuovo Cim. **17**, 1 (1994); N.Kristoffe1 and T. Ord, cond-mat/0103536 (2001).
[9] N. Enaki and V. Eremeev, New J.of Physics **4**, 80 (2002).
[10] V.A. Moskalenko, Fiz.Mettal. Mettaloved **8**, 503 (1959).
[11] J.Bardeen, L.Cooper and J.Schrieffer, Phys. Rev. **108**, 1175, (1957).
[12] E.M.Lifshits, L.P.Pitaevski, *Statistical Physics* V.2, (Nauka), Moscow, 1978.

CRITICAL TEMPERATURE AND ISOTOPE EFFECT IN NONADIABATIC SYSTEMS WITH "EXTENDED" SADDLE POINT SINGULARITY IN ENERGY SPECTRUM

M.E. Palistrant and V. Ursu

Institute of Applied Physics, Academy of Sciences of Moldova, 5 Academiei str. 2028, Chisinau,

Republic of Moldova

The experimental studies of electronic structure of $YBa_2Cu_3O_{6,9}$ and $YBa_2Cu_4O_8$ [1] show the existence of a "extended" saddle point singularity in the band defined by the plane CuO_2. In paper [1] it is introduced a simple model for the appearance of this singular point.Under certain conditions, applied to the parameters of the theory, one could obtain a one-dimensional density of electronic states that diverges like the square root of energy

$$N(\varepsilon) = N_0 \sqrt{\frac{E}{\varepsilon - \varepsilon_0}}, \tag{1}$$

where E is value of the order of electronic energy, ε_0 is the critical point. The existence of an "extended" distinctive feature permits to obtain high T_c regardless of the superconductivity mechanism (phonon or non-phonon). In [1] the theory is built on the basis of BCS – Migdal model, which is used for the description of superconductivity in metals, where the relationship $\varepsilon_F \gg \omega_o$ is respected (ε_F is Fermi energy, ω_o is the characteristic phonon frequency). The compounds marked about, where this distinctive feature was observed, are neadiabatic systems. This inequality is not respected, and the relationship $\varepsilon \sim \omega_o$ takes place. In this case the theorem Migdal is violated [2] and it is necessary to build a theory of superconductivity for the systems that have an "extended" point singularity disregarding the framework of Migdal theorem and taking into consideration the additional multiparticle processes.

The objective of this paper is to build the theory of superconductivity for systems that are characterised by non-adiabatic features ($\varepsilon \sim \omega_o$ or $\varepsilon_F \ll \omega_o$) and contain in the energetic spectrum the "extended" saddle point singularity; i.e. a one-dimensional density of electronic states (1).

We start from the Hamiltonian that describes the electron-phonon system and apply the theory of perturbations [3] to determine the matsubarian Grin functions (normal and abnormal). The series from the theory of perturbation for self-energetic operators (diagonal $\Sigma_N(\vec{p}\Omega)$ and non-diagonal $\Sigma_S(\vec{p}\Omega)$) considers the diagrams of all the orders of the theory of perturbations by the electron-phonon interaction, as it is done in the case of adiabatic systems, and additional diagrams that contain the vertex corrections and correspond to the intersection of two lines of an electron-phonon interaction. In this way we obtain the following for the operators Σ_N and Σ_S

$$\Sigma_N(\vec{p}\Omega) = \frac{1}{\beta V} \sum_{\vec{p}_1\Omega_1} V_N(pp_1) G(\vec{p}_1\Omega_1),$$

$$\Sigma_S(\vec{p}\Omega) = \frac{1}{\beta V} \sum_{\vec{p}_1\Omega_1} V_S(pp_1) F(\vec{p}_1\Omega_1), \tag{2}$$

where

$$V_N(\vec{p}\vec{p}_1) = -g^2 D(\Omega - \Omega_1)[1 + \lambda_0 P_V(\vec{p}\vec{p}_1 \Omega\Omega_1)], \qquad (3)$$

$$V_S(\vec{p}\vec{p}_1) = -g^2 D(\Omega - \Omega_1)[1 + 2\lambda_0 P_V(\vec{p}\vec{p}_1 \Omega\Omega_1) + \lambda_0 P_C(\vec{p}\vec{p}_1 \Omega\Omega_1)], \quad (4)$$

Here D $(\Omega-\Omega_1)$ correspond to the phonon Grin function

$$D(\omega) = -\frac{\omega_0^2}{\omega^2 + \omega_0^2}, \qquad (5)$$

g^2 is the constant of electron-phonon interaction, $\lambda_0 = N_0 g^2$, P_V and P_C are the vertex and the intersecting functions respectively (see [4] for the definitions of these functions).

By starting with the relationship in (1) and applying the method of direct calculation in the same manner as in [2] and [4] (regarding the one-dimensional movement of electrons) the following expression is obtained for the vertex function

$$P_V(0\Omega_1) = P_C(0\Omega_1) = \frac{\omega_0\sqrt{E}}{2\Omega_1}[\varphi_+ + \varphi_-], \qquad (6)$$

where

$$\varphi_+ = \frac{A_+}{A_+^2 + B_+^2}\left[arctg\frac{B_+}{A_+ - \sqrt{\mu_1}} - arctg\frac{B_+}{A_+ + \sqrt{\mu_1}}\right] - \frac{B_+}{A_+^2 + B_+^2}\frac{1}{2}\ln\frac{(A_+ - \sqrt{\mu_1})^2 + B_+^2}{(A_+ + \sqrt{\mu_1})^2 + B_+^2},$$

$$\varphi_- = \frac{B_-}{A_-^2 + B_-^2}\left[\frac{1}{2}\ln\frac{(W^{1/2} + A_-)^2 + B_-^2}{(W^{1/2} - A_-)^2 + B_-^2} - \frac{1}{2}\ln\frac{(\sqrt{\mu_1} + A_-)^2 + B_-^2}{(\sqrt{\mu_1} - A_-)^2 + B_-^2}\right] - \frac{A_-}{A_-^2 + B_-^2} \times$$

$$(7)$$

$$\times\left[arctg\frac{B_-}{W^{1/2} - A_-} + arctg\frac{B_-}{W^{1/2} + A_-} - arctg\frac{B_-}{\sqrt{\mu_1} + A_-} + arctg\frac{B_-}{A_- - \sqrt{\mu_1}} - \pi\,\Theta(A_- - \sqrt{\mu_1})\right],$$

$\Theta(x) = 1$ for x > 0 and 0 for x < 0.
The values of $A_\pm, B_\pm$, are determined by the following expressions:

$$A_\pm = \frac{1}{\sqrt{2}}\left[\sqrt{(\mu_1 \pm \omega_0)^2 + \Omega_1^2} + (\mu_1 \pm \omega_0)\right]^{1/2},$$

$$(8)$$

$$B_\pm = \frac{sign\Omega_1}{\sqrt{2}}\left[\sqrt{(\omega_0 \pm \mu_1)^2 + \Omega_1^2} - (\mu_1 \pm \omega_0)\right]^{1/2}.$$

On base of (2) – (5), and considering (1) as well, we obtain the equation for the determination of the temperature of the transition in superconductive state the system under study

$$1 = \lambda_0 \int\limits_{-\mu_1}^{W-\mu_1} d\varepsilon_{p1}\frac{\sqrt{E}}{\sqrt{\varepsilon_{p1} + \mu_1}}\frac{1}{\beta}\sum_{\Omega_1}\frac{\omega_0^2}{(\Omega_1^2 + \omega_0^2)}\left[1 - \frac{\Omega_1^2}{\Omega_1^2 + \omega_0^2}\right]\frac{1}{\tilde{\varepsilon}_{p1}^2 + Z^2\Omega_1^2}. \qquad (9)$$

where

$$\lambda_\Delta^0 = \lambda_0\left[1 + 3\lambda_0 P_V(0\omega_0)\right] \qquad (10)$$

$$Z = 1 - \lim\frac{1}{\Omega}\mathrm{Im}\,\Sigma_N(\Omega)\big|_{\Omega\to0} = 1 + \frac{\omega_0\sqrt{E}\lambda_Z^0}{2}\left\{-\frac{\sqrt{W}}{(\mu_1-\omega_0)(W-\mu_1+\omega_0)}+\right.$$

$$+\frac{\sqrt{\mu_1}}{\omega_0}\left(\frac{1}{\mu_1+\omega_0}+\frac{1}{\mu_1-\omega_0}\right) - \frac{1}{2(\mu_1+\omega_0)^{3/2}}\ln\frac{\sqrt{\mu_1-\omega_0}-\sqrt{\mu_1}}{\sqrt{\mu_1-\omega_0}+\sqrt{\mu_1}} -$$

$$-\frac{1}{2}\frac{1}{(\mu_1-\omega_0)^{3/2}}\left[\ln\frac{\sqrt{W}-\sqrt{\mu_1-\omega_0}}{\sqrt{W}+\sqrt{\mu_1-\omega_0}} - \ln\frac{\sqrt{\mu_1}-\sqrt{\mu_1-\omega_0}}{\sqrt{\mu_1}+\sqrt{\mu_1-\omega_0}}\right]\Theta(\mu_1-\omega_0)+$$

$$\left. +\frac{1}{(\omega_0-\mu_1)^{3/2}}\left[arctg\sqrt{\frac{W}{\omega_0-\mu_1}} - arctg\sqrt{\frac{\mu_1}{\omega_0-\mu_1}}\right]\Theta(\omega_{01}-\mu)\right\}, \qquad (11)$$

$$\lambda_Z^0 = \lambda_0\left[1+3\lambda_0 P_V(0\omega_0)\right] \qquad (12)$$

In the approximation of a weak coupling ($T_c \ll \omega_o$) the equation that defines T_c could be presented as

$$\frac{Z}{\lambda_\Delta^0}\sqrt{\frac{\mu_1}{E}} = \frac{\sqrt{\mu_1}}{2}\int\limits_{-\bar\mu_1}^{\overline{W}-\bar\mu_1}\frac{d\bar\varepsilon_{p1}\,th\dfrac{\beta_C\bar\varepsilon_{p1}}{2}}{\bar\varepsilon_{p1}\sqrt{Z\bar\varepsilon_{p1}+\tilde\mu_1}} - \Phi(\omega_0\tilde\mu_1 W), \qquad (13)$$

$$\Phi(\omega_0\tilde\mu_1 W) = \frac{1}{4}\left[\frac{\tilde\mu_1}{\tilde\mu_1+Z\omega_0}+\frac{\tilde\mu_1}{\tilde\mu_1-Z\omega_0}\right] - \frac{\omega_0\sqrt{W\tilde\mu_1}}{4(\omega_0+\overline{W}-\tilde\mu_1)(\tilde\mu_1-Z\omega_0)}+$$

$$+\frac{1}{2}\left[1+\frac{Z\omega_0}{4(\tilde\mu_1+Z\omega_0)}\right]I_1 + \frac{1}{2}\left[1-\frac{Z\omega_0}{4(\tilde\mu_1-Z\omega_0)}\right]I_2, \qquad (14)$$

$$I_1 = -\frac{\sqrt{\tilde\mu_1}}{\sqrt{\tilde\mu_1+Z\omega_0}}\ln\frac{-\sqrt{\tilde\mu_1}+\sqrt{\tilde\mu_1+Z\omega_0}}{\sqrt{\tilde\mu_1+Z\omega_0}+\sqrt{\tilde\mu_1}},$$

$$I_2 = -\frac{\sqrt{\tilde\mu_1}}{\sqrt{\tilde\mu_1-Z\omega_0}}\left[\ln\frac{\sqrt{W}-\sqrt{\tilde\mu_1-\omega_0}}{\sqrt{W}+\sqrt{\tilde\mu_1-\omega_0}} - \ln\frac{\sqrt{\tilde\mu_1}-\sqrt{\mu_1-Z\omega_0}}{\sqrt{\tilde\mu_1}+\sqrt{\mu_1-Z\omega_0}}\right]\Theta(\tilde\mu_1-Z\omega_0)+$$

$$+\frac{2\sqrt{\tilde\mu_1}}{\sqrt{Z\omega_0-\tilde\mu_1}}\left[arctg\sqrt{\frac{W}{Z\omega_0-\tilde\mu_1}} - arctg\sqrt{\frac{\tilde\mu_1}{Z\omega_0-\tilde\mu_1}}\right]\Theta(Z\omega_0-\tilde\mu_1). \qquad (15)$$

The analytical equation for the value of T_c that results from (13) could be obtained in two extreme limited cases, as follows: $\overline{W}$; $\mu_{1\gg}T_c$ and in the singular point $\mu_1=0$.

After highlighting the logarithmic feature by T_c in (13) at W; $\mu_1\gg T_c$, we obtain

$$T_C = \frac{8\tilde{\mu}_1 \gamma}{\pi}\left[\frac{\sqrt{W}-\sqrt{\tilde{\mu}_1}}{\sqrt{W}+\sqrt{\tilde{\mu}_1}}\right]^{1/2}\exp\left\{-\frac{Z}{\lambda_\Delta^0}\sqrt{\frac{\tilde{\mu}_1}{E}}-\Phi(\omega_0\tilde{\mu}_1 W)\right\}. \qquad (16)$$

In the point $\mu_1=0$ on the basis of (13) there is

$$T_C = \frac{A^2}{2Z_0}\left[\frac{Z_0}{\lambda_{\Delta_0}^0}\frac{1}{\sqrt{E}}+\frac{1}{\sqrt{W}}+\frac{\sqrt{W}}{4(Z_0\omega_0+W)}+\frac{5}{4}\frac{1}{\sqrt{\omega_0 Z_0}}arctg\sqrt{\frac{W}{Z_0\omega_0}}\right]^{-2}, \qquad (17)$$

where

$$A = \int_0^\infty \frac{dx}{\sqrt{x}ch^2 x} = 1,906; \qquad Z_0 = Z\big|_{\mu_1=0}; \qquad \lambda_{\Delta_0}^0 = \lambda_\Delta^0\big|_{\mu_1=0}.$$

In the limits of $W \to \infty$, $P_V = 0$, $\omega_0 \to \infty$ we obtain on the basis of (16) and (17) while $T_c \ll \mu_1$ and $\mu_1 = 0$ respectively, the relationships that correspond to the results from [1].

The existence of a root feature singularity in the density of electronic states (1), related to the one-dimensional law of dispersion of the electrons' energy in the non-adiabatic systems, plays a double role in the issue of appearance of superconductivity under high temperatures. First of all, this feature on its own leads to high T_c close to the distinctive singular point $\mu_1=0$. Second, due to the one-dimensional movement of the electrons and their dispersion scattering "forward" the impulse transmitted during the electron-phonon interaction is small. This circumstance results in high positive values of the vertex function and therefore in increase of the value for the constant of electron-phonon interaction and the critical temperature T_c.
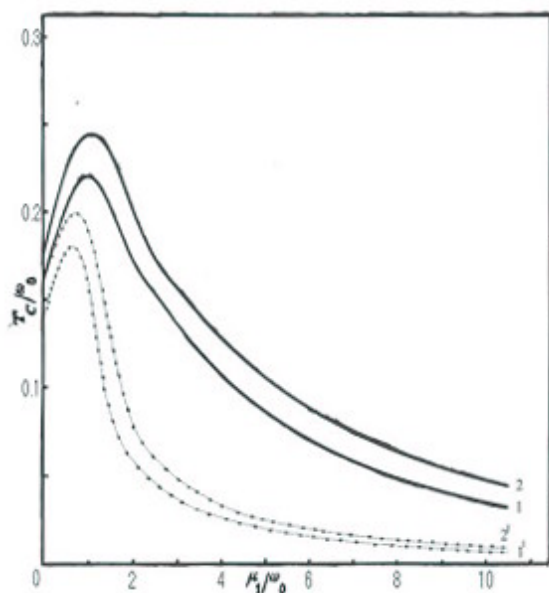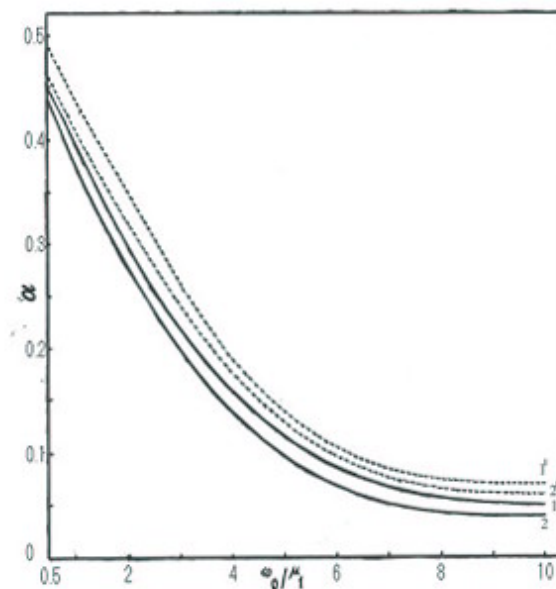

Fig.1.   Fig.2.

The solution of equation (13) for the temperature of the transition to superconductivity T_c as a function of μ_1/ω_0 is represented in fig 1. In the process of calculations the analytical

formulas (16) and (17) are used as well. The maximum value of T_c , as in the case of non-adiabatic systems (lines 1,2), as in the case of adiabatic systems (lines 1', 2') is achieved at $\mu_1 \approx \omega_0$.

The contribution of the non-adiabatisity to the value of T_c to a great extent depends on the parameters of the theory and is considerable for all the values of the relationship μ_1/ω_0, increasing as the distance from the singular point $\mu_1=0$ gets bigger. As results from fig 1 the values for T_c that are characteristic of the materials with high temperature superconductivity are easily obtained in the non-adiabatic systems under study.

The relationship between the coefficient of the isotopic effect $\alpha = -\dfrac{d \ln T}{d \ln M}$ and the values of ω_0/μ_1 is represented in fig 2. A significant decrease of the isotopic effect is observed as we get closer to point $\mu_1=0$ (in the adiabatic systems described by curves 1' - 2'). The qualitative picture in this case agrees with the results of paper [1]. An additional decrease due to the non-adiabatic effect is observed at the same time (curves 1,2).

Thus we conclude that the small value of the isotopic effect coefficient in the mentioned about compounds could be explained by the joint influence of the "extended" distinctive feature in the energetic spectrum of the electrons and the non-adiabatic characteristics of these systems.

References

[1] A.A. Abrikosov, Y.C. Campuzano and K. Gofron, *Physica C* **214**, 73 (1993).
[2] A.B. Migdal, *Zh. Eksp. Teor. Fiz.*, **34**, 1438 (1958).
[3] A.A. Abrikosov, L.P. Gor'kov and I.E. Dzyalosinskii, *Methods of Quantum Field Theory in Statistical Physics* (New York: Dover).
[4] M.E. Palistrant, *Fiz. Niz. Temp.,* **29**, 1173 (2003).

UPPER CRITICAL FIELD IN MgB$_2$ SYSTEM ON BASE OF TWO - BAND MODEL

M.E. Palistrant, V. Ursu, A.V. Palistrant

Institute of Applied Physics, Academy of Sciences of Moldova, 5 Academiei str.2028, Chisinau, Republic of Moldova

The discovery of the high temperature of transition in superconducting state T$_c$ ~ 40K in the simple intermetallic compound MgB$_2$ [1] has stimulated researches of this material properties both in the experimental and theoretical plans. The significant result of these researches is the discovery of two energetic gaps in the spectrum of the elementary excitations [2] and the possibility of theoretical describing of this compound on the base of the two-band model [3].

This two-band model and its generalization for the anisotropic value of the energetic gaps Δ_1 and Δ_2 case, [4, 5] confirm the experimental results for the thermal capacity C$_s$ dependence on temperature, the penetration depth of the magnetic field and other characteristics in the MgB$_2$ compound.

As it is known, the superconductive metals undergo the transition from the superconductive phase into normal in the magnetic field at its certain value. This transition which is relevant to the full penetration of the magnetic field into the superconductor, occurs in the moment when the field achieves the value of the upper critical field H$_{c2}$.

The main purpose of the work is researching of pure two-band superconductor of the secondary type for arbitrary temperatures close to the upper critical field and the definition of temperature dependence of the H$_{c2}$ value. The calculations are based on the fundamental equations of the electrodynamics of two-band superconductors [6], which are valid both for pure and doped superconductors.

If the exterior magnetic field is great enough the order parameters Δ_m (m = 1, 2) of two-band superconductor are small, and we can use equations ref. [6] for pure two-band superconductor:

$$\Delta_m^*(\vec{x}) = \frac{1}{\beta} \sum_\omega \sum_{nn'} V_{nm} \int d\vec{y}\, g_{n'n}(\vec{y}, \vec{x}/\omega) \Delta_{n'}^*(\vec{y}) g_{n'n}(\vec{y}, \vec{x}/-\omega). \qquad (1)$$

We restricted here by linear terms on Δ_n quantities in comparison with reduced in [6] because in the H=H$_{c2}$ point solutions with the infinitely small values Δ_m occur. Green function is defined by equation at presence of the magnetic field [7]:

$$g_{nn'}(r, r'/\omega) = e^{i\varphi(r,r')} g_{n'n}^0(r, r'/\omega), \qquad \varphi(r, r') = e\int_{r'}^{r} A(\vec{l})\, d\vec{l}. \qquad (2)$$

where $g_{n'n}^0$ is Green function of an electron in normal metal without magnetic field. The presence of the magnetic field is taken into account by the phase multiplier.

We decompose in equation (1) the normal metal function $g_{n'n}^0$ into the row by the Bloch functions $\Psi_{n\vec{k}}(\vec{x}) = e^{i(\vec{k}\vec{x})} U_{n\vec{k}}(\vec{x})/\sqrt{N}$ ($U_{n\vec{k}}$ is the Bloch amplitude):

$$g_{n'n}^0(\vec{y}, \vec{x}/\omega) = \sum_{\vec{k}\,\vec{k}'} g_{n'n}^0(\vec{k}', \vec{k}/\omega) \Psi_{n'\vec{k}'}(\vec{y}) \Psi_{n\vec{k}}^*(\vec{x}) \qquad (3)$$

and use approaching of the diagonal Green functions. Magnetic field is guided along the z axis. Besides we choose the vector potential as $A_x = A_z = 0$; $A_y = H_0 x$.

On the base of (1) - (3) after calculating the integral by impuls $\vec{k}$, averaging by elementary cells, applying   Maki and   Tsuzuki metodic [7]   and assuming $\Delta_m (x) = \Delta_m \exp\{- H_0 x^2\}$, we obtain:

$$\Delta_m^* = \sum_n V_{nm} N_n \rho_n^{-1/2} \Delta_n^* \int_1^\infty \frac{du}{u} \int_{\delta_n'}^\infty d\zeta \exp\left[-\frac{\zeta^2}{4}(u^2+1) \right] \frac{I_0\left[\frac{\zeta^2}{4}(u^2-1) \right]}{sh\left[u\zeta \rho_n^{-1/2} \right]}, \qquad (4)$$

where v_n and N_n are accordingly electron speed and electron density of state on n-th cavity of the Fermi surface,

$$\delta_n' = (eH_0)^{1/2} \frac{v_n}{2\gamma e_0 \omega_D^{(n)}}; \qquad\qquad \rho_n = \frac{v_n^2 e H_0}{(2\pi T)^2}. \qquad (5)$$

γ Is the Euler constant , $\omega_D^{(n)}$ is the cutoff frequency.

Basing on (5) it is easy to obtain the equation for the upper critical field definition in the following form:

$$-\Delta_m^* + \sum_n V_{nm} N_n \Delta_n^* \ln\frac{2\gamma\omega_D^{(n)}}{\pi T_c} + \sum_n V_{nm} N_n \Delta_n^* \left[\ln\frac{T_c}{T} - f(\rho_n) \right] = 0, \qquad (6)$$

where

$$f(\rho_n) = \rho_n^{-1/2} \int_0^\infty d\zeta \int_1^\infty \frac{du}{u \, sh \, [u\zeta \rho_n^{-1/2}]} \times$$

$$\times \left\{ 1 - \exp\left[-\frac{\zeta^2}{4}(u^2+1) \right] I_0\left[\frac{\zeta^2}{4}(u^2-1) \right] \right\} \qquad (7)$$

Equality to zero of the system (6) determinant corresponds to the presence of non-zero solutions, that is the connected pairs forming. The field, in the presence of which such solutions can appear, is the upper critical field H_{c2}. So the H_{c2} value is determined from the condition of the system (6) solvability:

$$a f(\rho_1) f(\rho_2) + B_1 f(\rho_1) + B_2 f(\rho_2) + C = 0 , \qquad (8)$$

where

$$B_n = N_n V_{nn} - \alpha \, \xi_c^{(n)} \quad ; \quad (n = 1,2)$$

$$C = 1 - N_1 V_{11} \xi_T^{(1)} - N_2 V_{22} \xi_T^{(2)} + a \, \xi_T^{(1)} \xi_T^{(2)} ; \quad a = N_1 N_2 \left(V_{11} V_{22} - V_{12} V_{21} \right);$$

$$\xi_T^{(n)} = \ln\frac{2\gamma\omega_D^{(n)}}{\pi T}; \qquad \xi_c^{(n)} = \ln\frac{2\gamma\omega_D^{(n)}}{\pi T_c}.$$

The analytic solutions to equation (8) could be computed for two limit cases as follows:
a. $\rho_n \ll 1$ ($T_c - T \ll T_c$) ;   **b.** $\rho_n \gg 1$ ($T \ll T_c$) ,
for which functions $f(\rho_n)$ are defined in works [7]:

$$f(\rho_n) = \frac{7}{6}\zeta(3)\rho_n - \frac{31}{10}\zeta(5)\rho_n^2 + \frac{381}{28}\zeta(7)\rho_n^3 , \qquad \rho_n \ll 1 \qquad (9)$$

$$f(\rho_n) = \ln \frac{2(2\gamma\rho_n)^{1/2}}{e_0} - \frac{1}{\pi^2 \rho_n}\left[\zeta'(2) + \frac{\zeta(2)}{2}\ln\frac{2}{\pi^2\gamma\rho_n}\right], \quad \rho_n \gg 1. \quad (10)$$

In the case of $(T_c - T \ll T_c)$ applying the formulas in (10) and (11) we obtain the following expression for the H_{c2} value

$$H_{c2}(T) = \frac{4\pi^2 T_c^2}{e}\left[v_1^2\eta_1 + v_2^2\eta_2\right]^{-1}\frac{6}{7\zeta(3)}\Theta \cdot$$

$$\cdot\left[1 + \Theta\left\{\frac{\frac{v_1^2}{v_2^2}\eta_1 + \frac{v_2^2}{v_1^2}\eta_2}{\left(\frac{v_1}{v_2}\eta_1 + \frac{v_2}{v_1}\eta_2\right)}\frac{31}{10}\xi(5)\left(\frac{6}{7\xi(3)}\right)^2 - \frac{3}{2}\right\}\right], \quad (11)$$

$$\theta = 1 - \frac{T}{T_c}, \quad \eta_1 = \frac{1}{2}(1+\eta), \quad \eta_2 = \frac{1}{2}(1-\eta);$$

$$\eta = \frac{N_1 V_{11} - N_2 V_{22}}{\sqrt{(N_1 V_{11} - N_2 V_{22})^2 + 4N_1 N_2 V_{12} V_{21}}}. \quad (12)$$

In the **b** case (T close to zero) we obtain:

$$\frac{H_{c2}(T)}{H_{c2}(0)} = \left[1 + \frac{16\gamma}{e_0^2\pi^2}\left(\frac{T^2}{T_c}\right)^2 e^{Sv(\lambda) - Sv(1)}\left\{\left(\lambda\gamma^+ + \frac{1}{\lambda}\gamma^-\right) + \left[\zeta©(2) + \zeta(2)\ln\frac{4T}{e_0\pi T_c} + \right.\right.$$

$$\left.\left. + \frac{S}{2}v(\lambda) - \frac{S}{2}v(1)\right] + \frac{\zeta(2)}{2}\left(\lambda\gamma^+ - \frac{1}{\lambda}\gamma^-\right)\ln\lambda\right\}, \quad (13)$$

where

$$v(\lambda) = \sqrt{(\ln\lambda - \eta^{(-)})^2 + \frac{4N_1 N_2 V_{12} V_{21}}{a^2}}, \quad S = \pm 1$$

$$\gamma\pm = \frac{1}{2}\left[1 \pm \frac{\eta^- - \ln\lambda}{Sv(\lambda)}\right], \quad H_{c2}(0) = \frac{\pi^2 T_c^2 e_0^2}{2\gamma e v_1 v_2}\exp[v(1) - v(\lambda)]. \quad (14)$$

We obtained equation (8), on the base of which the value of the upper critical field in the two-band model can be calculated on the whole temperature interval $0 \le T \le T_c$. The analytic solutions of this equation were obtained for $T \to T_c$ (11) and $T \to 0$ (13). It is easy to notice that H_{c2} depends on the correlations of the speeds v_1 and v_2 of the electrons on the Fermi surface, and on the constants of the electronic-phonon interaction λ_{nm}.

If $H_{c2}^0(0)$ and T_{c0} are introduced (upper critical field and critical temperature of the one-band low-temperature superconductor), on the base of (14) we obtain:

$$H_{c2}(0) / H_{c2}^0(0) = (T_c / T_{c0})^2 \frac{v_1}{v_2}\exp(v(1) - v(\lambda)) \quad (15)$$

The numerical estimations let us make the conclusion, that the upper critical field of two-band superconductors for T=0 can exceed the value of $H_{c2}^0(0)$ for usual superconductors by two-three orders. These big values $H_{c2}(0)$ are provided by high T_c and by ratio $v_1/v_2 > 1$ or $v_1/v_2 \gg 1$.

We put the goal to research the dependence from the temperature of the value H_{c2} for the connection MgB$_2$ in the whole temperature interval $0 < T < T_c$. For this it is necessary to

estimate the parameters of the two band theory λ_{nm}, using the experimental data obtained by researching this substance [8], [9] :

$$\Delta_1(0)=6,8 mev;\ Z(0)=\frac{\Delta_1(0)}{\Delta_2(0)}=3,8,\ \frac{N_1}{N_2}=0,8,\ \ \ \left.\frac{C_S-C_N}{C_N}\right|_{T=T_c}=0,78. \tag{16}$$

In corresponding with the two band theory of superconductors we have [10]

$$\Delta_1(0)=2\hbar\omega_D e^{-\varsigma(0)};\ \Delta_2(0)=\Delta_1(0)/Z(0), \tag{17}$$

where

$$\varsigma(0)=\frac{N_2 V_{22}-N_2 V_{12}/Z(0)}{a},$$

$$a\ln Z(0)=N_1 V_{11}-N_2 V_{22}+\frac{V_{12}N_2}{Z(0)}-N_1 V_{12}Z(0). \tag{18}$$

Let's consider that $N_2 V_{22}=0$, which corresponds to the passivity of the second zone in forming of the Cooper pairs. On the base of data (16) and equations (18) we get: for $\omega_D^{(1)}=\omega_D^{(2)}=700$ K - $N_1 V_{11}=0,3$, $N_2 V_{12}=0,12$; for $\omega_D^{(1)}=500K$, $N_1 V_{11}=0,33$, $N_2 V_{12}=0,13$ for $\omega_D=300K$, $N_1 V_{11}=0,42$, $N_2 V_{12}=0,16$.

the heat capacity jump at T = T_c is determining by the relation [10]

$$\frac{C_S-C_N}{C_N}=1,43\ \frac{\left(N_1+N_2/Z_c^2\right)^2}{\left(N_1+N_2\right)\left(N_1+N_2/Z_c^4\right)},\ \ \ \ \ Z_c=\frac{\Delta_1\left(T\to T_c\right)}{\Delta_2\left(T\to T_c\right)}=\frac{1-N_2 V_{22}\xi_c}{N_1 V_{12}\xi_c}. \tag{19}$$

The estimate of the ratio Z_c on the base of experimental data (16) and on the base of the first formula (19) gives the value $Z_c = 3,19$. The second formula (19) gives the value $Z_c = 3,26$. So we conclude that $\Delta_1(T)/\Delta_2(T)$ isn't a constant value since $Z(0) > Z_c$.
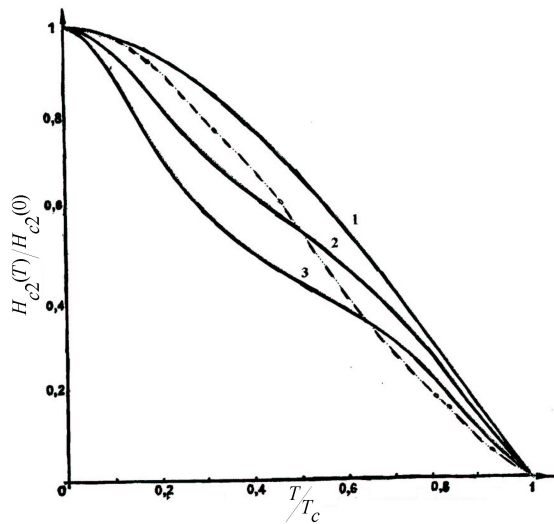
Fig.1 presents the dependence of the upper critic field H_{c2} from the temperature, which is obtained by numerical method of solving equation (8) and using its analytic solutions when $T \ll T_c$ (13) and $T \sim T_c$ (11). The used parameters are $N_1 V_{11} = 0,3$, $N_2 V_{12} = 0,12$, $N_1/N_2 = 0,8$.

The case $\dfrac{v_1}{v_2}= 1$ (curve 1); $\dfrac{v_1}{v_2}= 2$ (curve 2); $\dfrac{v_1}{v_2}= 3$ (curve 3).

The interrupted curve is corresponding to the experimental dependence [11].

Fig.1

Using other parameters of theory obtained for $\omega_D^{(1)}=\omega_D^{(2)}=500\ K$ and *300 K* we do not get an essential new result. A more important role belongs to the values of ratios v_1/v_2 .

It is easy to see that with growth of v_1/v_2 , the curvature in this dependence changes.

The obtained above results let us make the conclusion about qualitative describing of the experimental data by the behavior of the ratio H_{c2} (T)/ H_{c2} (0) as a function of temperature [11] in the intermetallic compound MgB_2, and also about big values of H_{c2} (0) in this compound in comparison with one-band system case.

References

[1] J. Nagamatsu. N. Nakagowa at al. *Natura* 410 , 63 (2001) .
[2] S. Tsuda, T. Yokoya at al , *Phys. Rev. Lett.* **87**, 177006 - 1 (2001).
[3] V. A. Moskalenko , *Fiz. Met. Metalloved* , 503 (1959) ; *Phys. Met. and Metallog*. **8** , 25 (1959).
[4] V. A. Moskalenko, M. E. Palistrant and V. M. Vakalyuk, *Usp. Fiz. Nauk*, 161, 155 (1991); *Sov. Phys. Usp*. **34** , 717 (1991); *arXiv : cond-mat* / 0309671.
[5] T. Mishonov , S. Drechsler and E.Penev, *Modern Physics Letters B*, **17**, 755 (2003).
[6] V.A. Moskalenko *Zh. Eksp. Teor. Fiz.* **51**, 1163 (1966).
[7] K. Maki and T. Tsuzuki, *Phys. Rev. A* **139,** 868 (1965).
[8] H.J. Choi , M. L. Cohen , S. G. Louie, *Physica C* 385, 66 (2003).
[9] F. Bouquet , Y. Wang at all , *Physica C* 385 , 192 (2003) , *Cond. mat*. 0210706.
[10] V. A. Moskalenko, L. Z. Kon , M. E. Palistrant , Low - *Temperature Properties of Metals with Band Spectrum Singularities* , Shtiinta , Kishinev, 1989.
[11] P.C. Confield , S. L. Bud'ko, D. K. Finnemore , *Physica C* , 385 , 1 (2003).

CRYSTAL STRUCTURE AND OPTICAL PROPERTIES OF SYSTEMS LnF$_3$-CeF$_3$ (Ln-Sm, Eu, Yb) AND EuF$_3$-TbF$_3$

V. Zinchenko[1], O. Eryomin[1], N. Efryushina[1], I. Stoyanova[1], V. Markiv[2], N. Belyavina[2]

[1]*O.V. Bogatsky Physico-Chemical Institute of NAS of Ukraine, 86, Lustdorfska doroga, 65080 Odesa, Ukraine*
[2]*Taras Shevchenko National University, 60, Volodymyrska Str., 01003 Kyiv, Ukraine*

The interaction and structure of phases in systems LnF$_3$-Ln'F$_3$ (Ln-Sm, Eu, Yb Ln'-Ce, Tb) are studied at 700-1100°C. Formation of solid solutions on the basis of binary fluorides of lanthanides is established. Appearance of fluorite-like phases of a structure LnF$_{2+x}$ beginning from 1000°C is observed. The content of the latter notably increases at heat treatment in vacuum. The formation of Ln(II) in systems LnF$_3$-Ln'F$_3$ is confirmed by appearance of intensive bands of absorption in UV range of a spectrum. They are caused by 4f-5d electronic transitions in ions Ln(II) and charge transfer Ln'(IV) → Ln(III). The intensity of bands of absorption increases with temperature rise and in a series Sm-Yb-Eu and Tb-Ce, that is in agreement with strengthening of interaction in the studied systems.

Samarium, Europium, Ytterbium, Cerium and Terbium fall to elements of a lanthanide series, for which the variable valence Sm(III) and Sm(II), Eu(III) and Eu(II), Yb(III) and Yb(II), Ce(III) and Ce(IV), Tb(III) and Tb(IV) is peculiar. This feature gives a definite originality to interaction between fluorides of the indicated lanthanides. The initial compounds of systems are obtained by a fluorization of oxides of lanthanides by a hydrofluoric acid (H$_2$F$_2$) or ammonium hydrofluoride (NH$_4$HF$_2$) with the subsequent dehydration and refusing in inert atmosphere [1]. The powders of systems were extruded in tablets and sintered at temperatures 700-1100°C in inert gas (He). A part of last sample was incinerated at 1100°C in vacuum 10^{-1}Pa. One of the tablets was evaporated in the vacuum installation VU1A at residual pressure ~10^{-3}Pa with subsequent deposition of thin-film coating. The optical and operational parameters of coating were determined by a standard technique [1]. The X-ray diffraction and X-ray phase analysis were conducted on the automated vehicle DRON-3 with application of filtrated radiation CuK$_\alpha$ by a specially designed technique [2]. The spectra of a diffuse reflection of powders were measured with the help of the spectrophotometer Lambda 9 in the range 200-2700 nm [3].

The outcomes of the X-ray phase analysis testify that the hyperthermal interaction between fluorides of lanthanides results in formation of solid solutions on the basis of each of components, and, in some cases, the formation of one continuous solid solution (Tab. 1). In the systems SmF$_3$-CeF$_3$ and EuF$_3$-CeF$_3$ at high temperatures only high-temperature modification (β-LnF$_3$) takes place. The temperature rise results in stronger change of a phase structure and parameters of lattices of solid phases in comparison with the initial components. At rather high temperatures - 1000°C for a system EuF$_3$-CeF$_3$ and 1100°C for a system YbF$_3$-CeF$_3$ the appearance of new phases - solid solutions of fluorite-like structure of composition LnF$_{2+x}$ - is observed, the basis of which is formed by ions Ln(II). At hyperthermal processing in vacuum the content of such phases in the indicated systems essentially increases, and also results in appearance of admixture of a similar phase in the system SmF$_3$-CeF$_3$. The data of spectroscopy of a diffuse reflection confirm availability of ions Ln(II) in the studied systems.

Table 1. Structure of phases and parameters of their crystal lattices
in the systems LnF_3-CeF_3 (Ln - Sm, Eu, Yb) and EuF_3-TbF_3

System, 50 mol. %	Conditions of thermal treating	Structure of phases and their parameters, nm
SmF_3–CeF_3	Annealing in He, 1100°C	CeF_3, hex. (88%), a=0.7020, c=0.7187 β-SmF_3, hex. (12%); a=0.7020, c=0.7187
	Annealing in vacuum, 1100°C	SmF_{2+x}, cub.(<1%), a=0.5680 CeF_3, hex. (>99%), a=0.7036, c=0.7196
EuF_3–CeF_3	Annealing in He, 1100°C	β-EuF_3, hex. (37%); a=0.7039, c=0.7179 EuF_{2+x}, cub. (33%), a=0.5829 CeF_3, hex. (30%); a=0.7167, c=0.7297
	Annealing in vacuum, 1100°C	β-EuF_3, hex. (36%); a=0.7004, c=0.7151 EuF_{2+x}, tetr.(44%), a=0.3968, c=0.7282 CeF_3, hex. (20%); a=0.7107, c=0.7282
YbF_3–CeF_3	Annealing in He, 1100°C	α-YbF_3, rhomb.(52%), a=0.6263, b=0.6820 YbF_{2+x},cub. (8%), a=b=c=0.5471 CeF_3, hex. (40%); a=0.7032, c=0.7185
	Annealing in vacuum, 1100°C	α-YbF_3, rhomb.(21%), a=0.6261, b=0.6830, c=0.4458 YbF_{2+x} cub. (19%), a=b=c=0.5460 CeF_3, hex. (60%); a=0.7012, c=0.7150
EuF_3–TbF_3	Annealing in He, 1100°C	α-EuF_3, rhomb.((Eu, Tb)F_3) (100%), a=0.6579, b=0.6993, c=0.4393

Really, besides weak-intensive peaks of absorption characteristic of ions Ln(III) in visible and near IR range of a spectrum (fig.1), in UV range of a spectrum appearance of broad and high-intensive bands of absorption (fig.2) for annealed samples is observed. Their intensity increases in a series of systems Eu-Tb, Sm-Ce, Yb-Ce, Eu-Ce. The interesting fact is the shift of band maxima in short-wave range at decreasing of a range of symmetry of lattices of the formed phases (Tab.2).

Table 2 - Positions of extrema on the diffuse reflection spectra in the UV interval of powders
of the systems LnF_3 - CeF_3 (Ln - Sm, Eu, Yb) and EuF_3 - TbF_3, annealed in He at 1100°C

System	λ_{max}, nm	$F(R)_{max}$	$\Delta H^0_{298, r}$, kJ/mole
SmF_3 - CeF_3	312	1.372	269
EuF_3 - CeF_3	304	3.445	129
YbF_3 - CeF_3	249	2.254	209
EuF_3 - TbF_3	243	1.145	302

These bands are caused by the 4f-5d electronic transitions in ions Ln(II) [4], and also processes of a charge transfer Ln(II)→ Ln(III) and Ln'(III) → Ln'(IV). At rise of heat treatment temperature and effect of vacuum the intensity of bands increases.
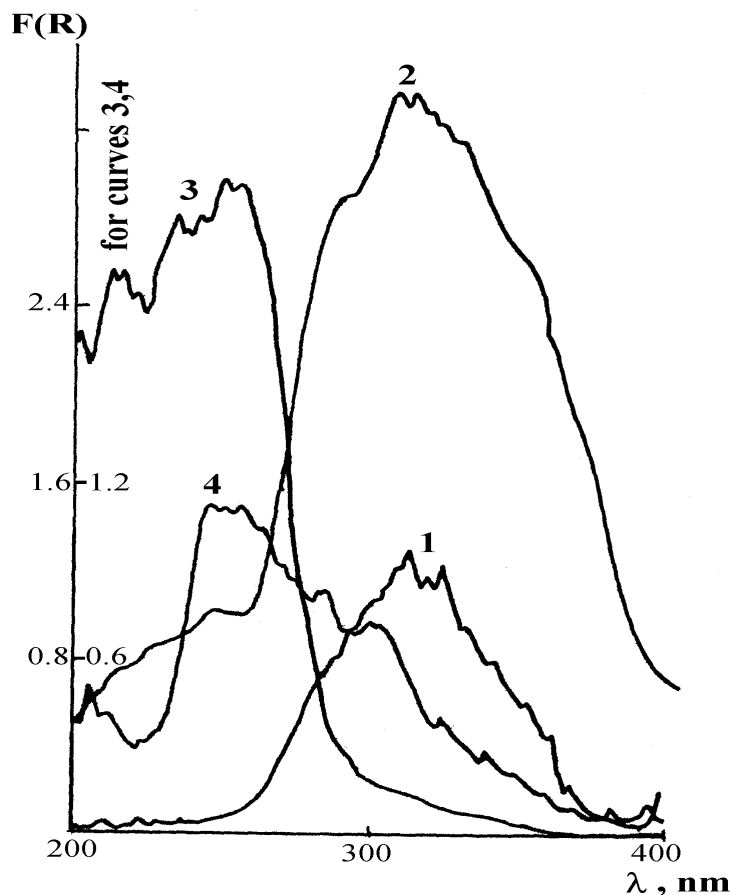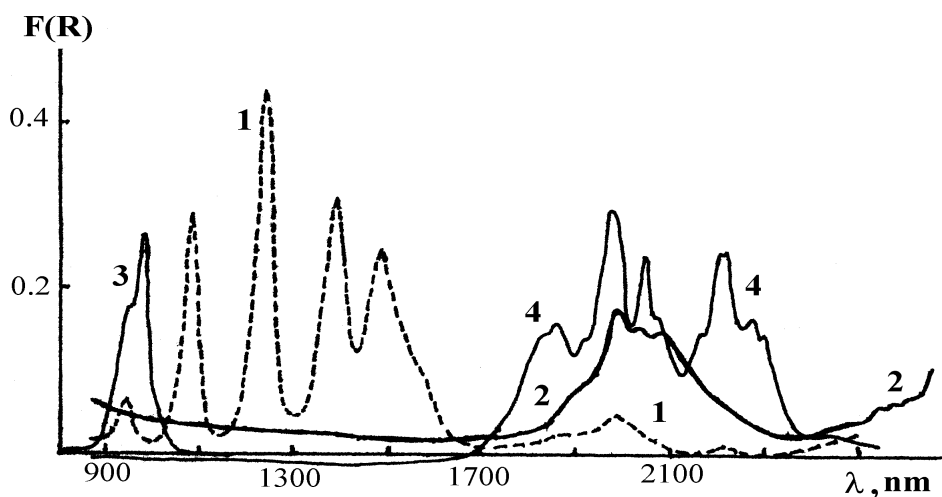

Fig. 1. Diffuse reflection spectra in the UV interval of spectrum for powders of the systems (1100°C, He): 1- SmF_3-CeF_3, 2 - EuF_3-CeF_3, 3 - YbF_3-CeF_3, 4 - EuF_3-TbF_3.

Fig. 2. Diffuse reflection spectra in the near IR interval of spectrum for powders of the systems (1100°C, He): 1- SmF_3-CeF_3, 2 - EuF_3-CeF_3, 3 - YbF_3-CeF_3, 4 - EuF_3-TbF_3.

The possible causes of origin of ions Ln(II) and Ln'(IV) in systems can be redox processes in the indicated systems:

$$LnF_3 + Ln'F_3 \rightarrow LnF_2 + LnF_4$$
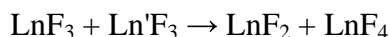
As the thermodynamic estimation demonstrates on the basis of the data [5], the probability of such processes is not so high ($\Delta H^0_{298,r} > 0$). However, the temperature rise should essentially move equilibrium of reaction in the side of formation of LnF_2 and $Ln'F_4$. This also is promoted by formation of solid solutions and compounds on the basis of the mentioned fluorides, and also evaporation of Ln'(IV) fluorides, which are rather volatile compounds at high (>1000°C) temperatures [6]. Symptomatic is the availability of inverse relationship of intensity of bands of absorption (as well as content of phases such as LnF_{2+x} from value of $\Delta H^0_{298,r} > 0$) (Tab.2).

Thin-film coatings obtained by vacuum evaporation of samples of systems EuF_3-CeF_3 and YbF_3-CeF_3, have essentially different optical and operational parameters. So, the scattering coefficients have values 0.07-0.1% and 0.4-0.45%, respectively, and their mechanical durability - 17000-19000 and 1000 rotations before wiping of coating, respectively. Apparently the degree of interaction favours improvement of properties of coatings.

References

[1] V.F. Zinchenko, N.P. Efryushina, O.G. Eryomin, V.P. Sobol', O.V. Mozkova, V.Ya. Markiv, N.M. Bilyavina, Phys. Chem. Solid State 2, 35(2001) (In Ukrainian).
[2] V.Ya. Markiv, N.M. Bilyavina, Proc. 2nd Inf. conf. "Construction and Functional materials" KFM, Lviv, 260(1997) (In Ukrainian).
[3] V.F. Zinchenko, O.G. Eryomin, N.P. Efryushina, I.V. Stoyanova, N.M. Bilyavina, L.V. Sadkovska, O.V. Stamikosto, Ukr.Khim.Jhurn. (Ukr.Chem.Journ.) 70, 18(2004) (In Ukrainian).
[4] G. Ionova, V. Vokhmin, V. Spitsyn Regularities of changes of properties of lanthanides and actinides, Nauka (Science), Moscow, 1990 (In Russian).
[5] D. Brown, Halides of lanthanides and actinides, Atomizdat, Moscow, 1972 (In Russian).
[6] V. Zinchenko, O. Eryomin, N. Efryushina, V. Kozlov, O. Mozkova, B. Gorshtein, Patent Ukraine #60760A *MKI*[7]C03C17/22 Filmforming material for interference coatings Publ. 15.10.2003, Issue №10 (In Ukrainian).

HIGH VOLTAGE BREAKDOWN TESTING OF SOL-GEL MgO-ZrO$_2$ INSULATION COATINGS UNDER VARIOUS COMPRESSIONS AT 298 K AND 77 K

O. Cakiroglu

Istanbul University, Faculty of Education, Bayezit, 34470, Istanbul, Turkey
National High Magnetic Field Laboratory, Florida State University, 1800 E. Paul Dirac Dr.,
Tallahassee, FL 32310, USA

Abstract

High voltage breakdown (HV$_{bd}$) tests was carried out to investigation electrical properties of high temperature MgO-ZrO$_2$ insulation coatings on long-length stainless-steel 304 (SS) tapes under various pressures at room temperature (298 K) and liquid nitrogen temperature (77 K) for applications of HTS/LTS coils and magnets. Solutions are prepared Mg and Zr based precursors and insulated on SS substrates using reel-to-reel sol-gel technique. Thicknesses of coatings (7 and 12 μm for 4 and 8 dips) and stycasted ribbons were determined by using Environmental Scanning Electron Microscope (ESEM). HV$_{bd}$ and dielectric constant of ribbons have been presented graphically.

1. Introduction

Sol-gel ceramic-based insulation coating have been developed at National High Magnetic Field Laboratory (NHMFL) for fabricating turn-to-turn electrical insulation for high temperature superconductor (HTS)/low temperature superconductor (LTS) coils [1]. Sol-gel coatings were prepared using various precursors and solvent so that coatings are processed to apply to both high temperature and cryogenic temperature when needed. The advantages of sol-gel process and applications reported elsewhere [1,2,3]. ZrO2 based coatings have ability of chemical stability, high resistivity, large relative (ε≅20) dielectric constant and good phase transformation [4,5]. Therefore sol-gel MgO-ZrO2 insulation coatings are passionately applicable to HVbd tests for HTS/LTS.

Previous researchers at NHMFL studied electrical properties of MgO-ZrO$_2$ coating without applying pressure at 298 K, while insulating on Ag and AgMg/Bi-2212 superconducting tapes [3,6]. They showed that ZrO$_2$ provided sufficient turn-to-turn insulation after 13 dipping in this process [7]; MgO-ZrO$_2$ does the same with only 8 dipping. We studied electrical properties of sol-gel MgO-ZrO$_2$ insulation coated on SS tapes in our recently published paper [8]. In this work we studied HV$_{bd}$ and dielectric properties of the sol-gel MgO-ZrO$_2$ reel-to-reel insulation coatings as function under various pressures at 298 K and 77 K.

2. Experimental procedure

The MgO-ZrO$_2$ coatings were insulated on commercial 304-SS tapes by using sol-gel precursor dipping technique in air. The prepared solution consists of dilute and normal. The normal coating solution consists of 20 mol % MgO and 80 mol % ZrO$_2$, which was prepared using zirconium tetrabutoxide, isopropanol and acetone. Dilute solution is obtained by adding equal amount of isopropanol to normal solution. Zirconium tetrabutoxide and several Mg based

precursors were used as precursors, which was prepared as clear homogenous by stirring for an 8 h period at 100 rpm. The detail information on solution preparation and coating process can be found in Refs. [1-3]-[6-8].

Conductor substrate SS tapes were cleaned with acetone in air. Then SS tape was coated by MgO-ZrO$_2$ solution and the coating process was repeated 4 and 8 dips. Coating thickness is regulated with dip numbers, viscosity of solution, wetting and withdrawal rate. By cutting the tapes as 10 cm long, two kinds of samples were produced for each 4 and 8 dips. First, ribbons were made without stycast; the second, the gap of the layer was filled with stycast (2850 FT/11 Black, Emerson & Cuming). The thickness of coating and stycast were determined by using ESEM, as seen in Fig 1. Ribbons were placed for testing the experimental set up as shown in Fig.2, in which HV$_{bd}$ and capacitance was measured by Model 200-02R High Voltage Power Supply and 161 Analog Digital Capacitance Meter, respectively. For each measurement, the process was repeated at least three times. The dielectric constant of samples was calculated by using Eq. (1) without taking into account effects of strain.

$$\varepsilon_r = \frac{C(d_i + d_s)}{\varepsilon_0 A}, \tag{1}$$

where ε_r is dielectric constant of insulation coatings, ε_o permittivity of free space (8.854 10^{-12} F/m), A is coated area in the sandwich, d_i is twice the coating thickness, and d_s is the stycast
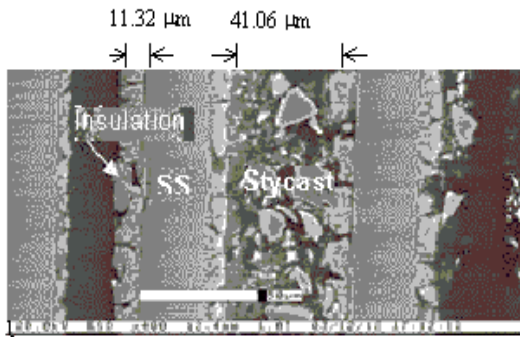
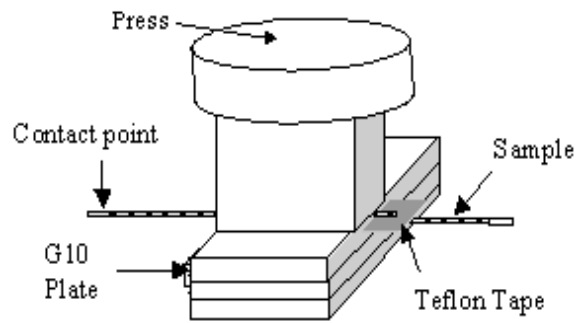Fig.1. The thickness of insulation and Staycast of 8 dips samples.

Fig.2. Experimental set up HV$_{bd}$ tests

Table I.The average values of HV$_{bd}$, electric strength and dielectric constant

	Room Temp. (298K)		Liquid Nitrogen Temp. (77K)	
Dip Number	4	8	4	8
Without stycast (WOS)				
HV$_{bd}$ (kV)	0.18	0.35	0.53	1.21
Electric Strength (kV/mm)	13.2	14.8	38.44	49.4
Dielectric Strength, P=0	3.52	4.6	2.79	3.94
With stycast (WS)				
HV$_{bd}$ (kV)	0.85	0.65	2.72	2.78
Electric Strength (kV/mm)	5.74	4.22	18.24	18.00
Dielectric Strength, P=0	32.90	27.30	27.60	24.60

thickness, which is zero for the cases without stycast ribbons. Under the stress, the epoxy between the layer fills the porosity of the insulation coating of the layers and air is leaked or/and trapped into pores, so that it is extremely hardened; therefore, HV_{bd} may not appreciably change with increasing pressure on them.

2. Results and discussion

As expected, coating thickness, crack in coatings, dopant materials, stycast thickness, pressure and temperature influence electrical, mechanical properties as well as surface morphology and structure of insulations. Also, porosity, coating thickness, cracks; dopant, viscosity, and withdrawal speed influence insulation properties

Table I and Fig.3 show the HV_{bd} of 4 and 8 dips for WS and WOS ribbons at 298 K and 77 K. HV_{bd} values increased with increasing of the coating thickness and temperature. It is clear that the HV_{bd} of WOS samples for 4 dips are lower than that of 8 dips samples, as expected. HV_{bd} values of WOS ribbons are concerning 0.18, 0.53 kV for 4 dips, and 0.35, 1.21 kV for 8 dips for the former at 298 K and the latter 77 K. HV_{bd} practically increases by 3 times for WOS samples, when cooling from 298 K to 77 K. HV_{bd} of samples WS for 4 dips are about 0.85 kV at 298 K and 2.72 kV at 77 K for WS samples. At these temperatures the HV_{bd} values of the ribbons of 8 dips are 0.65 and 2,72 kV, respectively. HV_{bd} values of WS samples increase almost by 3.3 times for 4 dips and by 4.3 times for 8 dips, when cooling from 298 K to 77 K.
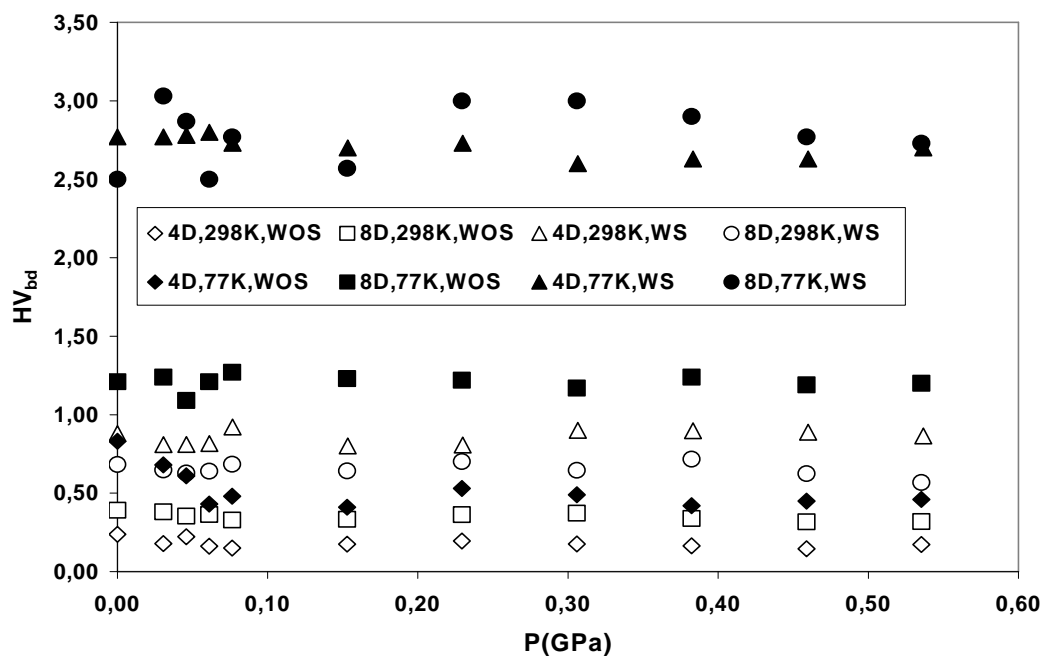
Fig.3. HV_{bd} compression with the ribbons of WS and WOS for 4 and 8 dips at 298 K and 77 K.
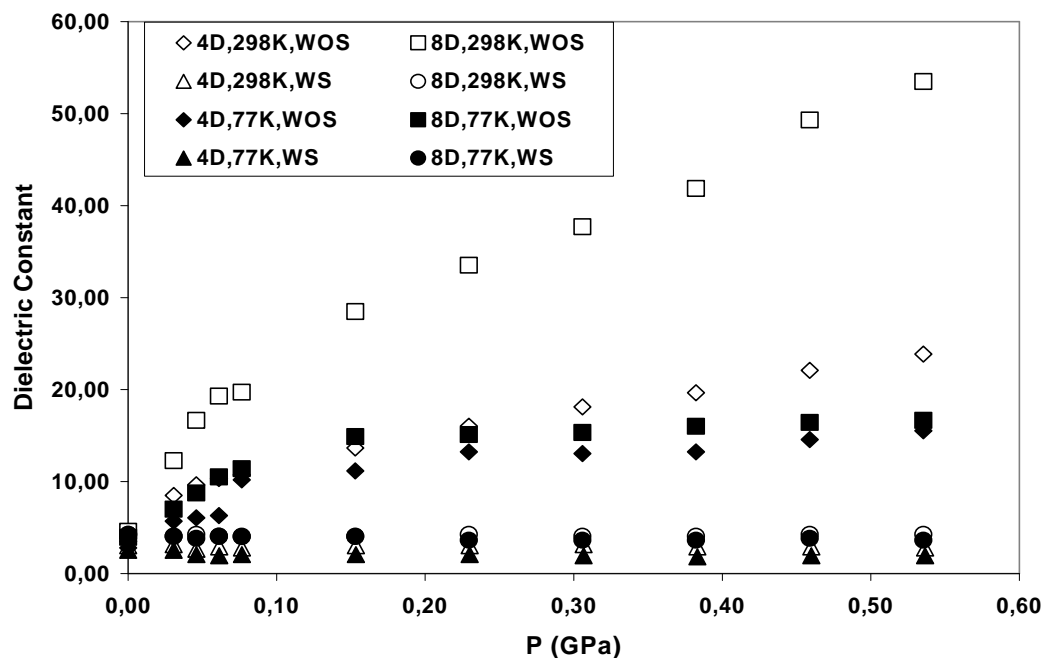
Fig.4. Dielectric constant varies with dip numbers, temperature and pressure with epoxy samples. It is constant with epoxy impregnation.

As shown in Fig.4 dielectric constant values increased with increasing number of dipping and pressure for WOS samples at 298 K. This increase at 77 K is lower than that at 298 K. Dielectric constant values of WS ribbons at 298 K are slightly higher than at 77 K. This is probably due to thicker stycast, increased porosity, pinhole and/or higher value of crack cavity. Dielectric constant values of WS ribbons are about 7.4 and 6.8 times higher than that of WOS at 0 pressure at 298 K and 77 K, respectively. Normally, in spite of the fact that the dielectric constant of ZrO_2 was 20 [5], it was measured to be 32.9 and 27.5 for 4 and 8 dipped WS ribbons at 298 K.

3.Conclusion

MgO-ZrO_2 was coated on SS-304 tapes at 4 and 8 dips by using reel-to-reel sol-gel technique. Test ribbons were formed of WS and WOS. Thickness of insulation was determined by ESEM, which were about 7 and 12 μm for insulation for 4 and 8 dips, respectively. HV_{bd} tests were performed with these samples under various stresses at 298 K and 77 K. HV_{bd} values vary with numbers of dipping. WOS ribbons were cooled from 298 K to 77 K. Depending on this, HV_{bd} values increased by about 3 times. The highest values of HV_{bd} is 2.78 kV for 8 dips for WS at 77 K. Stycast increased the HV_{bd} values by 4.7 and 2 times at 298 K, and by 5 and 2.3 times at 77 K for the former 4 dips and the latter 8 dips in which stycast thickness for 4 dips is thicker than 8 dips. The highest HV_{bd} was 2.78 kV at 8 dips for WS at 77 K.

Dielectric constant depends on capacitance, temperature, pressure, coating and stycast thickness. Dielectric constant values for WOS ribbons gradually increased with increasing numbers of dipping as well as increasing pressure at 298 K. But this trend is considerably lower

and adjacent to each other with the number of dipping at 77 K. On the other hand, the dielectric constant values for WS samples are about constant with increasing pressure, but decreasing with increasing number of dipping, since insulation thickness for 4 dips becomes thicker than that for the other samples. The dielectric constant increased by about 7.4 and 6.8 times with stycast at 298 K and 77 K. Dielectric constant of ZrO_2 is given by about 20 in the literature [5], and in this work, WS ribbons values are found to be 27-32 at 298 K. HV_{bd} and dielectric constant depend on dip number, temperature and epoxy impregnation.

Acknowledgements

References

[1] E. Celik, I.H. Mutlu, Y.S. Hascicek, USA Patent Application Pending, May 1998.

[2] E. Celik, I.H. Mutlu, Y.S. Hascicek, "Electrical Properties of High Temperature Insulation Coatings by Sol-Gel Method for Magnet Technology," IEEE Transactions on Applied Superconductivity **10** (1), 1341 (2000).

[3] E. Celik, I.H. Mutlu, E. Avci, Y.S. Hascicek, "MgO-ZrO_2 Insulation Coatings on Ag and AgMg/Bi-2212 tapes for magnet technology," Scripta Materialia **47,** 315 (2002).

[4] R.H. French, S.J. Glass, F.S. Ohuchi, Y.N. Xu, W.Y. Ching, Physical Review B **49,** 5133 (1994).

[6] E. Celik, I.H. Mutlu, Y.S. Hascicek, Physica C **370**, 125 (2002).

[5] X. Zhao, D. Vanderbilt, "First-principles Study of Electronic and Dielectric Properties of ZrO_2 and HfO_2," arXiv: cod-mat/0301016 V1 2 Jan.2003.

[7] I.H. Mutlu, E. Celik, Y.S. Hascicek, Physica C **370,** 113 (2002).

[8] O. Cakiroglu, L. Arda, Z. Aslanoglu, Y. Akin, O. Dur, A. Kaplan, Y.S. Hascicek, "Insulation Coatings Under Compression for Magnet Technology," Advance Cryogenic Engineering, USA, 22-26 September, 2003, to be published.

LUMINESCENCE SPECTRA AND CRYSTAL FIELD CALCULATION OF Pr³⁺ ION IN CRYSTAL LiYF₄

O. Krachni[1*], L. Guerbous[2] and S. Benabid[3]

[1] *Department of Physics, Faculty of Science, Ferhat Abbas University Setif 19000 Algeria*
[2] *Algiers Nuclear Research Center, 02, bd Frantz Fanon, BP 399, Algiers 16000, Algeria*
[3] *Department of Chemistry, Faculty of Science, Ferhat Abbas University Setif 19000 Algeria*
* Corresponding author: E-mail: omarkrachni@univ-setif.dz
Fax: +213 36 93 04 29

Abstract

Luminescence of LiYF₄: Pr³⁺ in the visible and near ultraviolet region is investigated. In the visible region, the emissions observed were attributed to intra-4f²-configuration transitions. It has been shown that these transitions take place predominantly from ³P₀ level and nonradiative relaxation rate between ³P₀ and ¹D₂ is weak even at room temperature. The emission and excitation bands observed in the ultraviolet region were assigned to 4f²–4f5d interconfigurational transitions. The energy levels of Pr³⁺ 4f² configuration are fitted by using the crystal field method. The set of free-ion and crystal field parameters corresponding to the best fits allow to reproduce satisfactorily the experimental spectra.

1. Introduction

The last few years, the Pr³⁺ doped compounds acquired a particular importance because of the possibilities of application in new scintillator materials [1] or tunable UV lasers [2]. The LiYF₄ crystal is one of the most promising candidates for this last application [3]. The aim of this work is the investigation of LiYF₄: Pr³⁺ luminescence in the visible and near ultraviolet (UV) regions and the calculation of energy levels of Pr³⁺ 4f² configuration in this host matrix by using the crystal field method.

2. Experimental details

The method of preparing the LiYF₄: 0.24 at. % Pr³⁺ crystal has been described in [4]. X-ray diffraction analysis revealed that LiYF₄ is isostructural with the scheelite (CaWO₄) which exhibits a tetragonal structure [5]. The space group of symmetry is C_{4h}^{6} (I4₁/ₐ) with four LiYF₄ molecules by elementary cell. The Li atom is placed in the center of a tetrahedron formed by 4 atoms of fluorine; 8 such tetrahedrons surround each Y³⁺ ion. When the Pr³⁺ ions are embedded in the LiYF₄ matrix they substitute certain Y³⁺ ions, no compensator of charge being then necessary. Only one site of symmetry characterizes the ions Pr³⁺, it is of S₄ type.

We carried out luminescence measurements using a Perkin-Elmer LS 55 luminescence spectrometer at room and liquid nitrogen temperatures. A powder holder was placed at a suitable angle to the excitation and emission beams to achieve maximum emission and minimum scattering. The emission spectra were corrected for wavelength dependent detection efficiency using the correction curve delivered by the spectrometer supplier.

3. Experimental results and discussion

In the visible region, the emissions observed are attributed to the $4f^2$ - $4f^2$ intraconfigurational transitions with low intensities, as they are parity forbidden. Furthermore, as Pr^{3+} site in $LiYF_4$ does not exhibit inversion symmetry, one may except forced electric dipole transitions to play a prominent role.

Figure 1 displays emission spectra of $LiYF_4$: Pr^{3+} measured under $^3P_2$ excitation (440 nm) at room temperature and at 77 K. The most intense peaks correspond to transitions from $^3P_0$ to $^3H_6$, $^3F_2$ and $^3H_4$ levels. However peaks of lower intensity involving $^3P_1$ and $^1D_2$ levels are also observed. It is important to note that transitions which take place starting from $^1D_2$ level located at about 3500 cm^{-1} below $^3P_0$ are of much lower intensity compared to those resulting from $^3P_0$. This indicates that the probability of nonradiative relaxation from $3P_0$ to $^1D_2$ is weak in this compound even at room temperature.
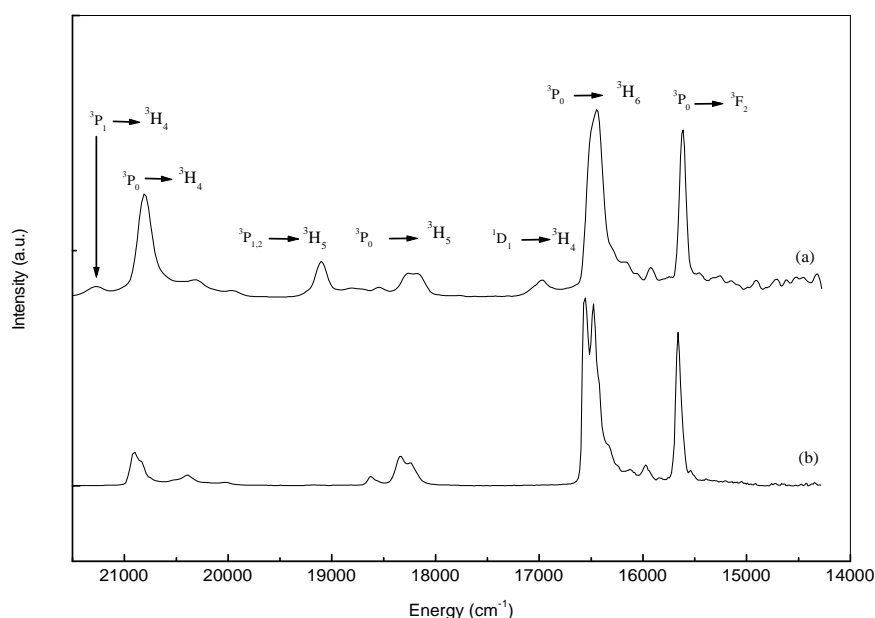
Figure 1 : Emission spectra of $LiYF_4$: Pr^{3+} under $^3P_2$ excitation (440 nm), (a) at room temperature and (b) at 77 K.

This property is common to the fluorides which have rather weak frequencies of lattice vibration (460 cm^{-1} for $LiYF_4$). At 77 K, the transitions starting from $^1D_2$ vanish, as the nonradiative relaxation rate decreases with the lowering of temperature [6]. The transitions $^3P_1$ -$^3H_4$ and $^3P_1$-$^3H_5$ are observed at room temperature but vanish at 77 K, which suggests we are in presence of thermal population of $^3P_1$ from $^3P_0$. The same phenomenon has been reported previously in PrP_5O_{14} [7] and in $BaSO_4$: Pr^{3+} [8]. Our suggestion is supported by the fact that under $^3P_0$ excitation $^3P_1 \rightarrow {}^3H_5$ emission transition is observed at room temperature, but vanishes at 77 K.

Excitation spectra of $LiYF_4$: Pr^{3+} measured for $^3P_0 \rightarrow {}^3H_6$ emission wavelength at room and liquid nitrogen temperatures show excitation transitions from the fundamental level $^3H_4$ to $^3P_0$, $^3P_1 + {}^1I_6$ and $^3P_2$ excited levels.

Figure 2 shows excitation spectra of $LiYF_4$: Pr^{3+} at room temperature between 20000 and 50000 cm^{-1} measured for different emission transitions. All these spectra exhibit a similar

shape and are characterized by two regions of efficient excitation: (i) the low energy region situated between 20000 and 23000 cm^{-1} in the visible part of the spectrum corresponds to intra-$4f^2$-configuration excitation transitions, (ii) the high energy region in the near UV (45000-50000 cm^{-1}) is assigned to $4f^2(^3H_4)$–4f5d interconfigurational transitions. In addition to these two regions, a broad excitation band with weak intensity is observed around 27000 cm^{-1}. It could be related to an unknown intrinsic defect level.

Figure 3 shows that excitation in the lowest level of 4f5d configuration yields in the ultraviolet and blue regions broad emission bands which can be attributed, in order of decreasing energy, to the emission from this level to the following groups of $4f^2$ ground configuration levels: $^3H_4$, $^3H_5$, $(^3H_6, ^3F_2)$, $(^3F_3, ^3F_4)$, $^1D_2$ and $(^3P_J + ^1I_6)$.
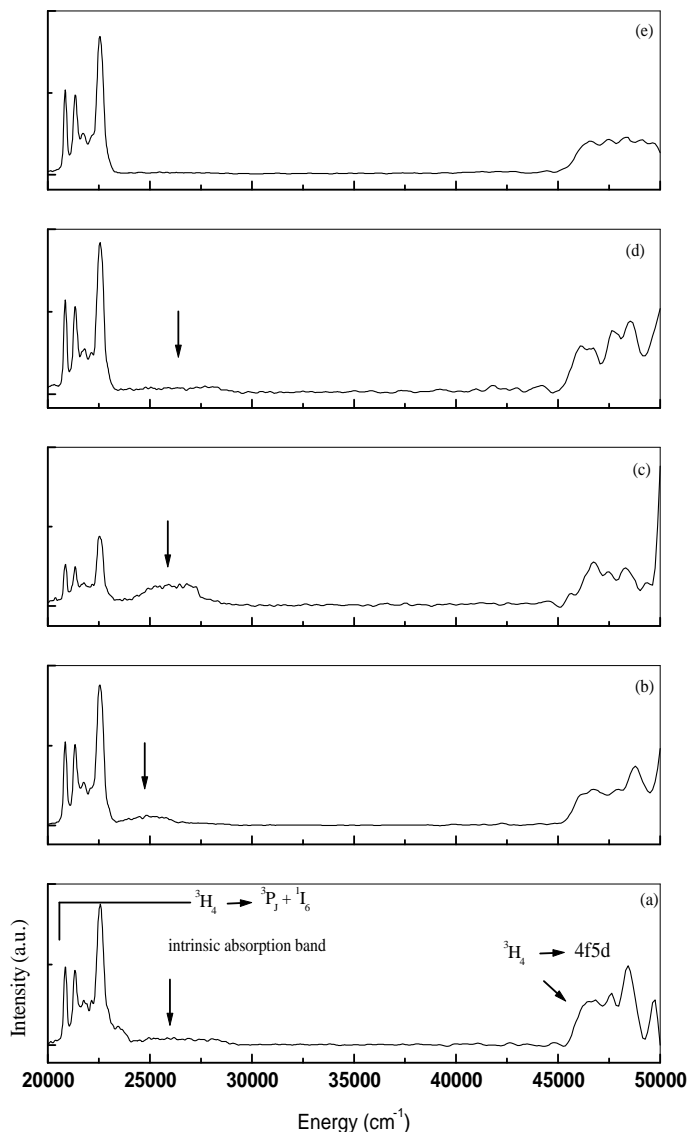
Figure 2: Room temperature excitation spectra of LiYF$_4$: Pr^{3+} measured for the emission transitions: (a) $^3P_0 \rightarrow ^3F_2$ (640 nm); (b) $^3P_0 \rightarrow ^3H_6$ (607 nm); (c) $^1D_2 \rightarrow ^3H_4$ (590 nm); (d) $^3P_0 \rightarrow ^3H_5$ (548 nm) (e) $^3P_1 \rightarrow ^3H_5$ (523 nm)

Thus, following 4f5d excitation, the higher levels of $4f^2$ configuration are populated, in particular ^3P_J triplet. The emission starting from these levels yields spectra identical to those measured by exciting directly towards ^3P_J triplet. It appears that intensity of emission originating from $^3P_0$ is stronger than that of 4f5d $\rightarrow$ ^3P_J + $^1I_6$. The same phenomenon has been reported by Oskam *et al* [9] in CaF$_2$: Pr^{3+} at 6 K and explained by a direct nonradiative relaxation from 4f5d excited state to the ^3P_J, $^1I_6$ levels in addition to population of these levels by radiative decay from 4f5d. This may also explain why in Fig.2, the intensity of the $4f^2(^3H_4)$–4f5d electric dipole transitions is comparable and even weaker than that of the parity forbidden intra-$4f^2$-configuration transitions.

The experimental Pr^{3+} $4f^2$ energy levels of LiYF4: Pr3+ were obtained from [10,11]. The crystal field calculations were carried out using the SPECTRA program available on the Argonne National Laboratory website [12]. This program is based on the standard phenomenological model for a $4f^N$ ion embedded in a crystalline environment. As usual, the

parameters to be adjusted involve the F^2, F^4 and F^6 Slater parameters describing the inter-electronic repulsion between the two electrons of the $4f^2$ configuration, the ζ_{4f} spin-orbit coupling constant ($\varsigma_{4f} = \langle 4f|r|4f \rangle$), the Trees parameters α, β, γ and the $(B_q^k)_{4f}$ crystal field parameters. Values of these parameters obtained for LaF_3: Pr^{3+} were used as starting parameters [13]. In addition, the α, β, γ, M^0 and P^2 parameters were first set at the LaF_3: Pr^{3+} values, $M^{2,4}$ and $P^{4,6}$ being set at zero. The set of free-ion and crystal field parameters corresponding to the best fit allow to reproduce satisfactorily the experimental spectra. The parameters leading to the best fit (standard deviation in the order of 29 cm^{-1}) are (in cm^{-1}): F^2 = 69004, F^4 = 50610, F^6 =33341, ζ = 750, α = 22.642, β = -653, γ = 1371, $M^{0,2,4}$ = (2 ,1.12, 0.76), $P^{2,4,6}$ = (202, 152, 101), $B_0^2 = 458$, $B_0^4 = -948$, $B_0^6 = -21$, $B_4^4 = 1248$, $B_4^6 = 1159$.
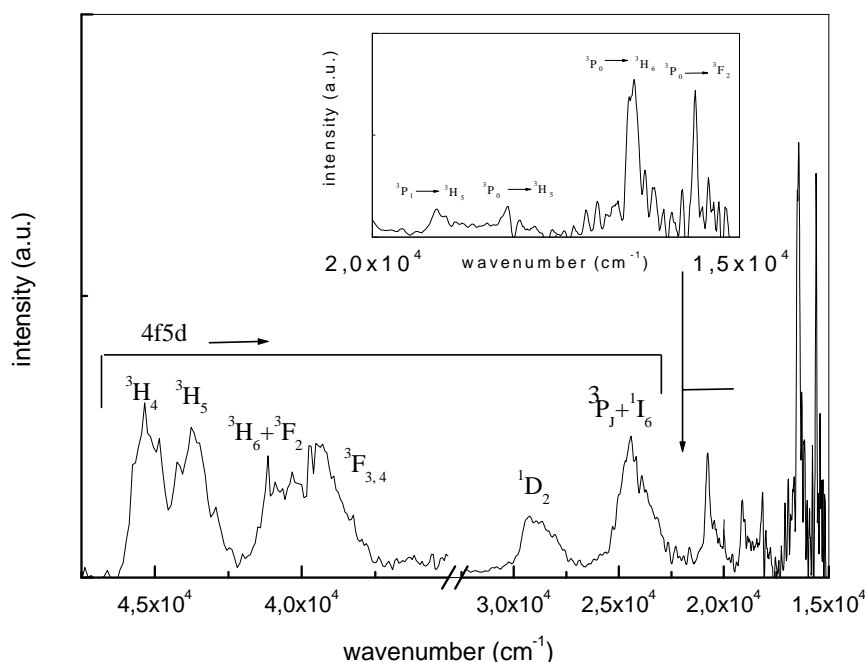

Figure 3: Emission spectrum of $LiYF_4$: Pr^{3+} at room temperature upon 4f5d excitation (207 nm)

References

[1] P. Dorenbos, M. Marsman, C.W.E. van Eijk, M.V. Korzhik, and B.I. Minkov, Radiat. Eff. Defects Solids 135, 325 (1995)

[2] S. Nicolast, M. Laroche, S. Girard, R. Moncorge, Y. Guyot, M.F. Joubert, E. Descroix and A.G. Petrosyan, J. Phys.: Condens. Matter 11, 7937 (1999)

[3] M. Laroche, J.L. Doualan, S. Girard, J. Margerie and R. Moncorge, J. Opt. Soc. Am. B17, 1291 (2000)

[4] M. Malinowski, M.F. Joubert and B. Jacquier, Physical Review B 50 12367 (1994)

[5] E. Garcia and R.R. Ryan, Acta Cryst. C49, 2053 (1993)

[6] G. Blasse, B.C. Grabmaier, Luminescent Materials, Springer-Verlag, Berlin, 1994

[7] W. Strek, C. Szafranski, P. Deren and K. Jablonski, Proceedings of the international symposium of rare earth spectroscopy, Wroclaw, Poland, September 10-15, 1984

[8] A.P. Vink, P. Dorenbos, C.W.E. van Eijk, Physical Review B 66, 075118 (2002)

[9] K.D. Oskam, A. J. Houtepen, A. Meijerink, Journal of luminescence 97, 107 (2002)

[10] L. Esterowitz, F.J. Bartoli, R.E. Allen, D.E. Wortman, C.A. Morrison and R.P. Leavitt, Physical Review B19, 6442 (1979)

[11] C. K. Jayasankar and F.S. Richardson, Physica Status Solidi b155, 221, (1989)

[12] Spectra Web Site: http://chemistry.anl.gov/downloads/spectra.

[13] W.T. Carnall, G.L. Goodman, K. Rajnak, and R.S. Rana, J. Chem. Phys. 90 3443 (1989).

EVIDENCE OF PRESENCE OF Ce^{3+} TRACES IN PRASEODYMIUM DOPED LUTETIUM AND YTTRIUM ORTHOBORATES AND THEIR INFLUENCE ON Pr^{3+} LUMINESCENCE SPECTRA

L. Guerbous[a], O. Krachni[* b], A. Guittoum[a] and S. Tobbeche[a]

[a] *Algiers Nuclear Research Center, 02, bd Frantz Fanon, BP 399, Algiers 16000, Algeria*
[b] *Department of Physics, Faculty of Science, Ferhat Abbas University Setif 19000 Algeria*
* Corresponding author: E-mail: omarkrachni@univ-setif.dz
Fax: +213 36 93 04 29

Abstract

The luminescence of three compounds: LuBO$_3$, with calcite and vaterite structures, and YBO$_3$ (vaterite structure) doped with Pr^{3+} ions has been investigated. The emission was ascribed to four spin-allowed transitions and one spin-forbidden transition from the 4f5d to the 4f^2 configuration. Two additional broad emission bands with very weak intensity at 440 and 580 nm were studied. Evidence of the presence of Ce^{3+} traces is reported and their influence on Pr^{3+} luminescence is discussed.

1. Introduction

The trivalent praseodymium ion is an attractive optical activator since it offers the potential of laser action (both in the visible and infrared region) along with upconversion processes [1-2]. Furthermore, transitions between the opposite parity configurations 4f5d - 4f^2 yield fast and intense broad emission bands in the near ultraviolet useful for scintillator applications [3] or tunable UV lasers [4]. In most host crystals, Pr^{3+} ion yields under 4f5d excitation an emission spectrum that consists of at least four intense bands in the near UV region [5]. These bands can be attributed unequivocally to the emission from the lowest 4f5d level of Pr^{3+} to $4f^2$ ground configuration triplets: $^3H_4, ^3H_5, (^3H_6, ^3F_2)$ and $(^3F_3, ^3F_4)$. However, additional broad bands with very weak intensity can be distinguished at longer wavelengths. In this work, we have focused our attention on the investigation of the origin of these weak broad bands.

2. Experimental details

LuBO$_3$ and YBO$_3$ powder samples doped with Pr^{3+} (1 at. %) were synthesized by means of a solid state reaction method described elsewhere [6]. LuBO$_3$ presents both a low-temperature calcite form and a high-temperature vaterite form, while YBO$_3$ may be obtained in the vaterite type only.

Room temperature excitation and emission spectra were recorded in the 200 - 800 nm range using a Perkin-Elmer LS 55 luminescence spectrometer. A powder holder was placed at a suitable angle with respect to the excitation beam to achieve maximum fluorescence and minimum scattered incident light. The spectra were corrected for wavelength dependent detection efficiency using the correction curve delivered by the supplier.

3. Experimental results and discussion

Figure 1 depicts the emission spectrum of calcite $LuBO_3:Pr^{3+}$ under 4f5d excitation (230 nm). The emission spectra of vaterite $LuBO_3: Pr^{3+}$ and $YBO_3: Pr^{3+}$ present an identical shape to that of calcite $LuBO_3:Pr^{3+}$, but are slightly shifted towards longer wavelengths. In each spectrum, at least four intense bands can be distinguished between 250 and 330 nm, numbered 1-4 in Fig. 1. These bands can be attributed, in order of decreasing energy, to the emission from the lowest crystal field component of the 4f5d excited configuration to the following groups of $4f^2$ ground configuration levels: $^3H_4, ^3H_5, (^3H_6, ^3F_2)$ and $(^3F_3, ^3F_4)$.
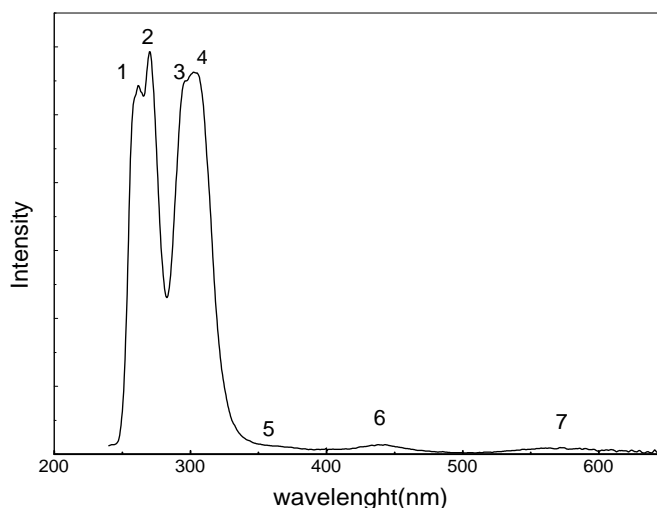
Figure 1. Emission spectrum of $LuBO_3:Pr^{3+}$ calcite under 4f5d excitation (230 nm)

In addition, broad bands with very weak intensity can be distinguished around 350 nm (band 5) and 582 nm (band 7) for all the three compounds, 440 nm for calcite $LuBO_3$, 460 nm for vaterite $LuBO_3$ and 455 nm for YBO_3 (band 6). The weak intensity of band 5 relative to bands 1-4 suggests that we are in presence of a spin-forbidden transition. It could be attributed to a transition from the lowest $4f5d$ level of Pr^{3+} to the $4f^2$ configuration singlet level $^1G_4$. It has been assumed before that the lowest 4f5d level is a triplet state in Pr^{3+} doped orthoborates [5]. This assumption could explain the fact that the transitions from the lowest 4f5d level to the spin triplets ^3H_J and ^3F_J are more intense than those to the spin singlet multiplets. The excitation spectrum of the band situated at 350 nm is identical to those measured for the intense bands 1-4, which indicates that it has a purely 4f5d - $^1G_4$ nature. However, the situation is more complex for the two bands situated around 440 – 460 nm and 580 nm as shown by figures 2 for the former and 3 for the latter.

3.1. Investigation of the emission band situated around 440-460 nm:

The excitation spectrum of calcite $LuBO_3:Pr^{3+}$ for 440 nm monitored emission wavelength exhibits two efficient excitation regions (Fig. 2a). The first region between 200 and 260 nm is characterized by a broad complex band that could be assigned to $4f^2$–4f5d interconfigurational transitions in Pr^{3+}. The second region situated between 260 and 380 nm consists of a broad band with a maximum at 345 nm. In order to unravel the nature of this

band, we have measured the emission spectrum excited by 350 nm wavelength (Fig. 2b) which consists of two overlapping bands with a splitting around 2000 cm^{-1}.

The band positions and the characteristic value of the splitting are in good agreement with interconfigurational transitions from the lowest $^2T_{2g}$ level of 5d configuration to the $^2F_{5/2}$, $^2F_{7/2}$ spin-orbit components of 4f ground configuration observed previously in these compounds doped with trivalent cerium [6]. Excitation spectrum of these emission bands is displayed in Fig. 2c. The structure and the positions of these excitation bands are also in good agreement with those of trivalent cerium.
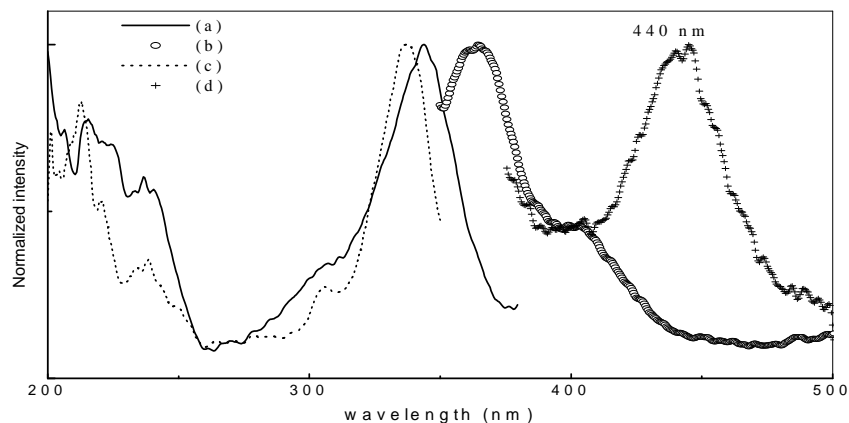
Figure 2. a) Normalized excitation spectrum of calcite LuBO$_3$ for 440 nm monitored emission wavelength
b) Normalized emission spectrum of calcite LuBO$_3$ under 345 nm excitation wavelength
c) Normalized excitation spectrum of calcite LuBO$_3$ for 5d - $^2F_{7/2}$ emission in Ce^{3+}
d) Normalized 440 nm emission band under 230 nm excitation wavelength

It is important to note that emission and excitation spectra attributed to Ce^{3+} ions exhibit a very weak intensity relatively to those of Pr^{3+}, thus it is reasonable to assume that in our samples doped with trivalent praseodymium, some traces of trivalent cerium are present. It is well known that rare earths are often found in the same ores and are difficult to separate because of their similar chemical properties. The presence of traces of Ce^{3+} ions may be prejudicial for Pr^{3+} UV emission as excitation energy may be transferred from Pr^{3+} 4f5d levels to 5d levels of neighboring Ce^{3+} ions. In our case, despite the overlapping of Pr^{3+} UV emission bands and Ce^{3+} excitation bands, we did not observe clearly the characteristic emission of trivalent cerium under 4f5d excitation of Pr^{3+}. This excitation yields, in addition to bands 1-5, the emission band under study situated around 440-460 nm. Instead, the excitation at 345 nm yields clearly the characteristic Ce^{3+} emission spectrum, but with a very weak intensity. The band peaking at 345 nm overlaps with the low energy bands of Ce^{3+} excitation spectrum. Thus, it could be concluded that the 440-460 nm emission band stems from two distinct contributions: (i) a spin-forbidden transition from the lowest crystal field component of Pr^{3+} 4f5d configuration to the 4f^2 configuration singlet level $^1D_2$, as its excitation spectrum shows clearly the 4f^2 ($^3H_4$) – 4f5d excitation band of Pr^{3+} in the near UV region, (ii) the tail of Ce^{3+} emission spectrum, as its excitation spectrum contains also the band peaking at 345 nm which overlaps strongly with Ce^{3+} excitation bands. The band peaking at 345 nm could be related to some structure defect or impurity center present in these orthoborates. It is responsible for the transfer of a small amount of excitation energy

from Pr^{3+} to Ce^{3+}. Because of the small portion of Ce^{3+} ions existing in the samples, only a small amount of excitation energy can be transferred to them from Pr^{3+}.

3.2. Investigation of the emission band situated at 580 nm:

We have measured the excitation spectra for the three compounds by monitoring the emission wavelength corresponding to the maximum of the broad band with very weak intensity situated around 582 nm. The spectrum of calcite $LuBO_3$ is shown in Fig. 3a, in which two regions of efficient excitation may be clearly distinguished. The first region situated in the near UV between 200 and 300 nm, consists of one intense broad complex band, identical in shape and position to the excitation bands measured for the intense emission bands 1-4 and even 5 (figure 1) and consequently could be assigned to $4f^2(^3H_4) - 4f5d$ interconfigurational transitions in Pr^{3+}.
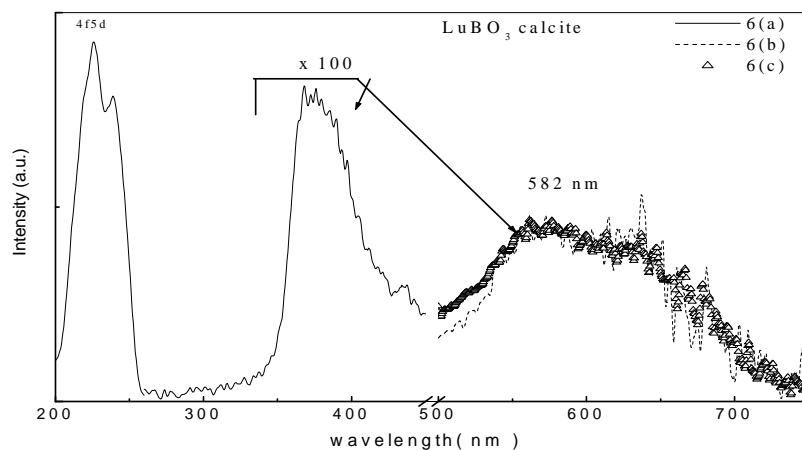

Figure 3. a) Excitation spectrum of calcite $LuBO_3$ for 582 nm monitored emission wavelength with enlarged intensity between 300 and 450 nm
b) 582 nm emission band of calcite $LuBO_3$ under 4f5d excitation (230 nm) with enlarged intensity
c) 582 nm emission band of calcite $LuBO_3$ under 375 nm wavelength excitation with enlarged intensity

The second region appears as a broad band with very weak intensity relative to the former (enlarged in Fig.3) peaking at around 375 nm for all the three orthoborates. Excitation upon 4f5d wavelength (230-240 nm) yields the 582 nm emission band observed in figure 1 and reproduced in Fig.3b with enlarged intensity. It is important to note that 375 nm excitation wavelength leads to a similar broad weak intensity emission band (Fig. 3c). The origin of the 375 nm excitation band is unclear, it could be related to an unknown defect level that is present in all the three compounds. The fact that both 4f5d and 375 nm excitations yield the same emission band peaking at 582 nm indicates that an energy transfer from Pr^{3+} to this unknown center occurs. The radiative decay of this center gives rise to the 582 nm emission band. Its weak intensity suggests the transfer rate from Pr^{3+} to this unknown center is very low.

References

[1] A.A. Kaminskii, Laser Crystals, 2nd edition, Springer-Verlag, Berlin, 1990

[2] M. Malinowski, M.F. Joubert and B. Jacquier, Physical Review B 50 12367 (1994)

[3] P. Dorenbos, M. Marsman, C.W.E. van Eijk, M.V. Korzhik, and B.I. Minkov, Radiat. Eff. Defects Solids 135, 325 (1995)

[4] S. Nicolast, M. Laroche, S. Girard, R. Moncorge, Y. Guyot, M.F. Joubert, E. Descroix and A.G. Petrosyan, J. Phys.: Condens. Matter 11, 7937 (1999)

[5] G. Blasse, J.P.M. Van Vliet, J.W.M. Verwey, R. Hoogendam and M. Wiegel, J. Phys. Chem. Solids 50, 583 (1989)

[6] L. Zhang, Elaboration et proprietes de luminescence et de scintillation de materiaux denses a base de lutecium dopes aux ions cerium et praseodyme, Ph.D. thesis, Universite Claude Bernard-Lyon I, France, 1997

ROENTGEN IMAGE RECORDING ON SILLENITE-TYPE ELECTROOPTICAL CRYSTALS BY ELECTROPHOTOGRAPHIC METHOD

Ig. Dementiev, E. Maximov, E. Pocotilov, L. Tarakanova

Moldavian State University, Department of Physics,
E-mail: EP@pokatilov.moldline.net

Abstract

To record Roentgen image on sillenite-type crystals while charging in a corona discharge field, a device has been performed. The resolution not less than 10 pairs of lines per mm, the sensitivity of 25 reciprocal Roentgens, the contrast coefficient not less than 2 at the exposure length of 0.6 s were obtained using $Bi_{12}GeO_{20}$ crystal. The device survives more than 10^4 of writing-erase cycles. From the sensitivity point of view, the considered registration is just as good as X-Ray films used for radiography and dosimetry.

1. Introduction

Currently the interest in X-ray technique does not relax owing to its more expanding use in practice. A brief survey of X-ray registration directions allows us to mark out the following main methods [1]:

-   photography – utilizing X-ray sensitive photographic materials, necessary for further chemical processing;
-   electrostatic photography – based on charging of X-ray sensitive layers in a corona discharge field followed by liquid or powdered visualization of an X-ray scene;
-   Lumiprinting – converting the X-ray radiation to visible light with the wavelength caused by a luminescent material;
-   Television method – using vidicons sensitive to X-rays;
-   Methods based on the employment of semiconductor layers sensitive to X-rays.

Investigations done earlier have shown that by analogy with xeroradiography Roentgen image recording by the sillenite-type crystals ($Bi_{12}SiO_{20}$, $Bi_{12}GeO_{20}$) while charging their surfaces in the field of a corona discharge may be realized [2, 3]. This circumstance allows us to simplify the Roentgen image recording procedure and improve the responsiveness of the recording process in comparison with the conventional electrographic method. Physical principle of the developed method is based on the fact that sillenite-type crystals possess both the Roentgen sensitivity and electrooptic properties at the same time.

2. X-ray recording

X-ray image recording process is carried out by means of a small-sized unit the scheme of which presented in Fig. 1 illustrates well this process in automatic regime. The process itself can be divided into four consequent stages: charging of crystal surfaces in the corona discharge field; the Roentgen exposure of the crystal; readout of the formed image; erasure of the image prior to a following registration cycle. High-voltage bloc 19 controlled by the voltage ramp generator 18 feeds corona-forming filaments located in the charging device 4 which gives rise to working element 5 charging. An appearing field of a corona discharge

gives rise of a potential at the crystal surfaces according to a near –linear low. In the process of charging, the crystal is illuminated by the plain-polarized light with the wavelength $\lambda = 700 \div 750$ nm which is inactive for the crystal. This probe parallel beam is formed by the light source 21 (projector lamp КГМ), system of filters 22, lens 23, and polarizer 24 and it is directed on the sample by the stationary 1 and movable 3 mirrors.While charging the crystal, bloc 20 and the program-simulated unit 16 control a rotation gear 7 which sets up the movable mirror 6 horizontally so that the probe beam passes through the analyzer 8. A part of the light beam is diverted by the semitransparent mirror 9 on the photodiode 13 forming feedback.

Figure 1: The scheme of the small-sized device for Roentgen image recording.

During the charge accumulation process, the rising potential modifies the crystal refraction index that, in turn, changes the polarization characteristics of the whole optical system making it "blooming" on the output of the crossed analyzer 8. In accordance with Pockels' law

$$I = I_0 \sin^2 \frac{\pi}{2} \frac{U}{U_{\lambda/2}},$$

where I is the light intensity passed through the system "polarizer – crystal - analyzer" at the voltage difference U on the crystal; I_0 is the maximal intensity of light passing through the system under analyzer oriented parallel to polarizer in the no-voltage condition; $U_{\lambda/2}$ is the half-wave voltage of the crystal.

When the intensity *I* reaches a magnitude close to its maximal one, the photodiode signal entering the derivator 14 and, hereinafter, comparator 15 disconnects the charging. A potential close to the half-wave voltage $U_{\lambda/2}$ arises between the crystal surfaces. High values of the specific resistance ($\rho \sim 10^{14}$ Ω cm) and permittivity ($\epsilon \sim 40$) provide sufficiently long time (more than 10 minutes) of the surface potential relaxation, i.e. being in the darkness the charged crystal is ready for the exposure quite a long time. When charging is carried out, the executive unit 20 turns the mirror 3 by means of the rotation gear 2 into the horizontal position overlaying the probe beam and opening the crystal for the exposure of X-ray radiation passed beforehand through the object "0" under investigation. At the same time, the command switching on the X-ray radiation power supply is given. X-ray quanta passing through the object fall onto the crystal generating non-equilibrium charge carriers in it, which are drifted to the crystal surfaces with the opposite sign of charge with a successive recombination. As a result, the charge relief is formed with corresponding distribution of the refractive index being stipulated by the electrooptic effect.

After the exposure ending, the X-ray radiation source supply turns off and the mirror 3 is rotated into its initial inclined position so that it might direct the beam of the inactive reading-out light on the crystal. Passing through the crystal and analyzer 8 crossed with polarizer 24 this beam contains information regarding the refractive index distribution, i.e. the Roentgen imagery data. The irradiated areas are reproduced as a dark background, but radiation-free ones remain light-colored. The beam passed through the analyzer is focused by the objective 10 at the recording instrument 11. As a recorder, digital video camera, camera with TV-monitor, or photo camera connected to computer may be used. Being observed and recorded, the actual image is erased by intensive, active for the crystal blue-green light from the source 21 after the command rotating the mirror 6 in inclined position.

3. Results and discussion.

Fig. 2 shows the Roentgen image photographs for some objects registered by means of the method worked out.
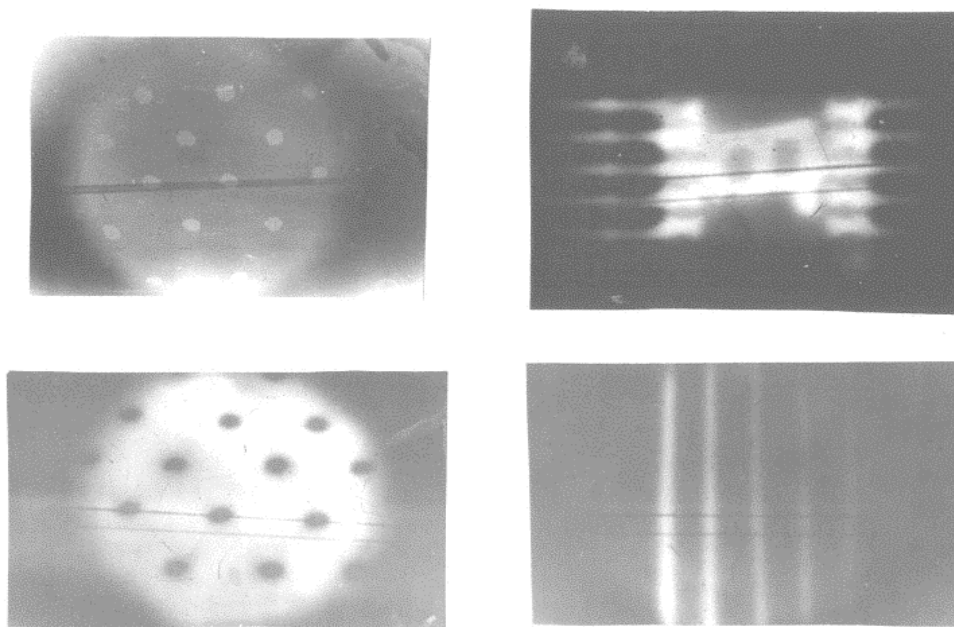

Figure 2: Samples of the obtained Roentgen images.

The negative (upper) and positive X-ray patterns of 3 mm – metal plates with holes of 1 mm across diameters are at the left. Dark dots in the positive photograph (below) comply with the holes through which Roentgen radiation falls onto the crystal.

The right-hand lower photograph offers X-ray pattern for a test-object, which consists of a system of the copper wires with different diameters (0.1, 0.15, 0.2, 0.33, and 0.44 mm). The places, where the wire model shields the X-ray radiation, keep the field created on the crystal and are recorded as light bands in the photograph. The given test allows us to estimate the value of the resolution capability of recording medium. As an illustration, the X-ray pattern of the seven-segmented opaque to visible light indicator is presented in the right-hand upper photograph.
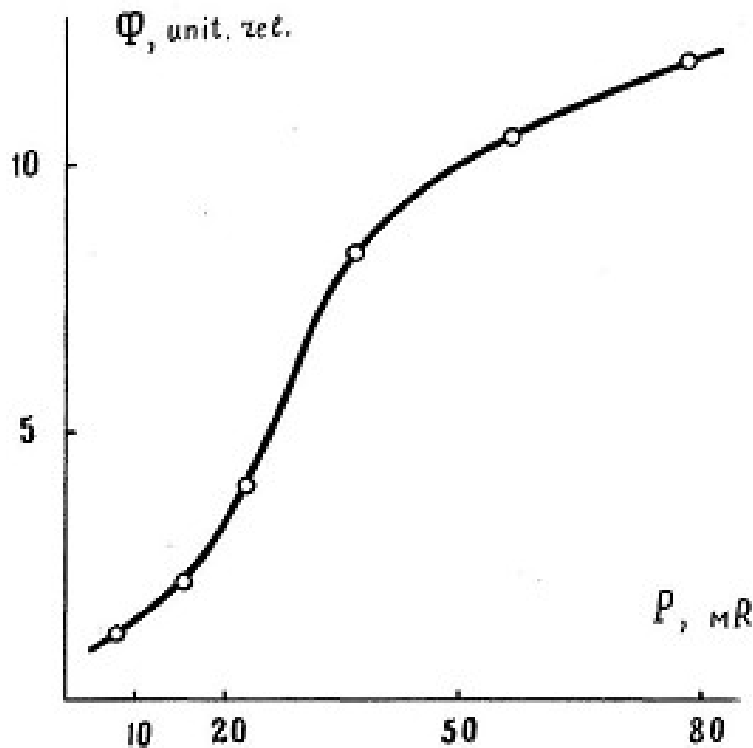
Figure 3. Probing light contrast versus the Roentgen radiation energy.

The main parameters specifying recording material properties are: Roentgen sensitivity, contrast ratio, photographic latitude, and resolution capability. Contrast of the line-process bloc image recorded on the crystal as a function of the X-ray radiation intensity is presented in Fig. 3. As the contrast value there was used $\Phi = I_{rf} / I_{ir}$, i.e. the ratio of intensities of the readout light passed through the crystal in a radiation-free position to irradiated one. It is possible to estimate the sensitivity by the formula $S = 1/(P_{exp.}\, C)$, i.e. the reciprocal to the product of the X-ray intensity and the exposure time C. The radiation power was measured by means of the calibrated standard instrument DRG 3-03. If we carry out the calculation of sensitivity proceeding from the plot $\Phi = f(lgP)$ at the value of Φ estimated for 0.85 of maximal $\Phi = 12$.data, the sensitivity is equal to $S_{0.85} = 25\ PR^{-1}$.

The contrast ratio is determined by the angle of the characteristic curve straight-line portion slope,

$$\gamma = tg\,\alpha = \frac{\Phi_2 - \Phi_1}{\lg P_2 - \lg P_1}\,.$$

This coefficient characterizes the recording material capability to reproduce different brightness (intensities) of the object under investigation. Photographic latitude $L = \lg(P_2 - P_1)$ defines a range of the object intensities reproduced in the image with the same contrast ratio. Metering conducted allows us to conclude that X-ray image recording method proposed here on the base of X-rays sensitive sillenite-type electrooptic crystals ensures the following parameters:

the sensitivity to X-rays, $S_{0.85} = 25\,R^{-1}$;

the contrast ratio, $\gamma \to 2$;

the photographic latitude, $L = 0.6$;

the resolution capability, $N \sim 10$ мм$^{-1}$;

the recording cycling -no less 10^4.

By the sensitivity, the developed method is just as good as photographic one using X-ray films employed for defectoscopy and radiation monitoring. The developed method can be successfully used in such fields of application as welded part checking (defectoscopy), express radiation monitoring, the definition of Roentgen particle tracks and their wave propagation (crystallography).

References

[1] A.M. Gurvich, *Fizicheskie osnovy radiatsionnogo kontrolia I diagnostiki, Energoatomizdat, Moskova, 1989.*

[2] V. Gladilin, I. Dementiev, E. Maximov, L. Tarakanova, and K. Sherban. "X-Radiation recording by sillenite – type electrooptic crystals while charging surface in corona discharge field", Optoelectronica, 3, nr. 3, pp. 71-73, 1995.

[3] Ig. Dementiev, E. Maximov, "*Instalaţie pentru roentgenografie*". Brevet de invenţie MD 928, G2, 28.02.1998.

INFLUENCE OF DEFECT COMPOSITION ON OPTICAL ACTIVITY OF Mn^{2+} IONS IN ZnS CRYSTALS

V. Korotkov, R. Sobolevskaya, L. Bruk, K. Sushkevich, P. Ketrush, A. Dubrovin

State University of Moldova,
Mateevich str. 60, Dep. of Phys., USM, Chisinau, Moldova, MD2009,
vitaliikorotkov@yahoo.com

The Mn_{Zn}^{2+} ion intracentred luminescence in ZnS crystal (λ_{max}=590nm, FWHM=160-210meV) and its relation to the native, impurity (the background and aluminum) defects formed at the crystal annealing in the bismuth melt at 950^oC during 100hrs was studied. The luminescence of the aluminum doped and undoped ZnS single crystals , before and after annealing, were studied. The aluminum presence on the one hand creates sensitizing centers (the radiation bands close to 400nm and 450nm) and on the other hand makes difficult Mn doping of the crystal. It is supposed that the temperature influence on the Mn_{Zn}^{2+} ion is determined by the position of the electron and hole Fermi cuazi-levels relative to the deep levels, acting as recombination radiative and noneradiative centers the nature of which is determined by the type of crystal lattice defects. The relation between blue centers of recombinative radiation and Mn bands was shown

In the optical absorption and luminescence spectra of II-VI compound crystals doped with the atoms having uncompleted 3d-shell the intracentered transitions in the impurity atoms reveal themselves. The study of such ions and, particularly, of two-valence manganese ions is of practical interest, as $ZnS:Mn^{2+}$ luminophor is the most efficient electroluminescent phosphorous [1-5]. Two types of the electron excitation: band to band and intracentered one bring their contribution to the luminescence, often considerably interacting with one another. The main subject of the given paper is the investigation of the optically excited (PL) and intracentered luminescence (IL) of the Mn_{Zn}^{2+} ions and its relation with the inherited and imputity (the background and aluminum) defects in ZnS crystals after their annealing in bismuth melts. On the formation of photoluminescence (PL) spectra of $ZnS:Mn^{2+}$ a considerable influence is exercised by the local symmetry of the crystalline field [1,6,7]. In the PL process the Mn^{2+}ions absorb the radiation from the manganese characteristic absorption region. For to enhance the luminescence efficiency a sensitization impurity is introduced into the crystal the radiation of which leads to the resonance excitation of Mn^{2+} ions due to dipole-quadrupole interaction. The use of Mn^{2+} as a sonde impurity at ZnS PL studies allows us to get information about the peculiarities of the inherited and impurity defects leading to the appearance of self-activated luminescence (SAL).The effect of sondage using Mn^{2+} ions is determined by the fact that manganese is a paramagnetic impurity. The ion intracentred transitions reveal themselves in ZnS as a characteristic radiation close to 590nm, depending on the symmetry of the local crystalline field. The radiation from this region of spectrum related to the other known inherited and impurity defects reveals itself rather weakly. Proceeding from this the ZnS single crystals with the background impurities and aluminum doped, before and after the annealing were investigated. The annealing was carried out in the silica ampoules at 950^oC during 100 hrs in the Bi melts and bismuth melts with the addition of 5at.% of Mn or 6.10^{-3} and $a10^{-2}at\%$ Al with the subsequent tempering outside the furnace. The temperature variation of the PL spectra from a crystal cleavage perpendicular

to the surfaces contacting with the melt during the annealing was studied both in the crystal volume and subsurface region as well in the temperature range from77 up to 300K.

At 77K the luminescence spectrum of the parent crystal with the background impurities is represented by two bands with the maxima situated at 390nm and 650nm accordingly. At 300K the spectrum consists of a single band with the maximum situated close to 470nm. In the PL spectra of the starting samples, containing aluminum the two radiation bands with the maxima at 445nm, 650nm (77K) and 480nm, 660nm (300K) accordingly were observed.

After the annealing of the both types of starting crystals in the Bi without any additions in their Pl spectra at 77K the PL spectrum consists of two bands with the maxima situated at 400nm (SAL) and 650nm. At 300K a band centered at 595nm with the FWHM of 160meV predominates.
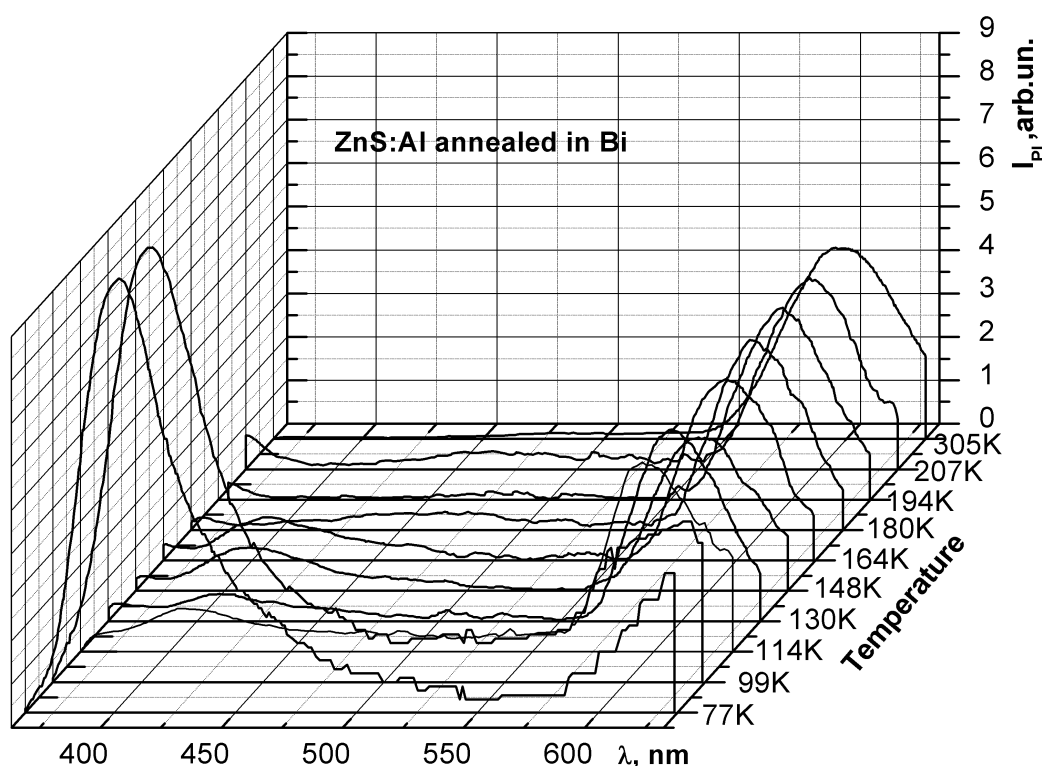
Fig.1. The PL spectra at different temperatures of ZnS: AL crystal annealed in Bi melt.

The analysis of PL spectra temperature evolution had shown that beginning from approximately 105K a peculiarity close to 590nm reveals itself, which at about 115K is formed into a predominant band. At 300K this band remains as a single one in the PL spectrum (Fig1). This band FWHM temperature dependence in the $T^{?}$ scale (Fig.2) is linear, which along with the preservation of its maximum position in the temperature interval 100K…300K can indicate the intracentred character of the radiative electron transitions responsible for its appearance in the PL spectrum.

So the PL band with the maximum close to 590nm in the studied crystals can be attributed to the manifestation of the radiation on Mn^{2+} ions. The bursting of the band at 590nm is accompanied by the quenching of the SAL violet radiation at 390nm (Fig1). The last fact can indicate the participation of the given radiation in the excitation of the manganese

band, i.e. the given centre is a sensitization one and its radiation energy corresponds to the Mn_{Zn}^{2+} characteristic radiation $\approx 3,20eV(393nm)$ at 300K) [1,7].

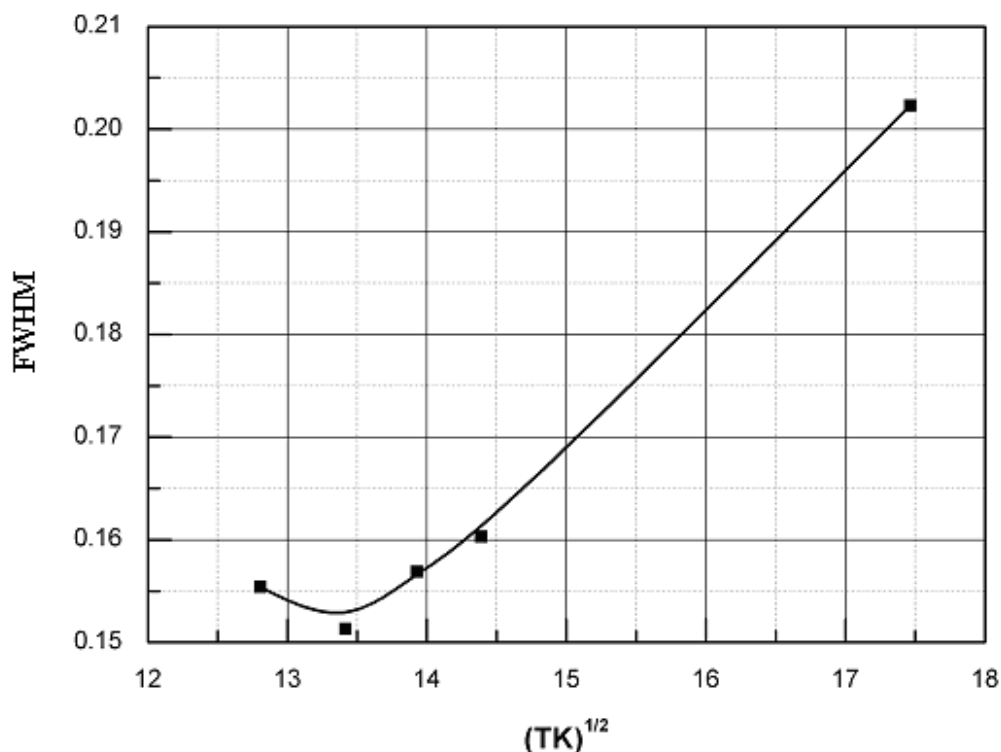

Fig2. The band FWHM temperature dependence in the $T^?$ scale.

After the ZnS annealing in (Bi+10^{-2} at.%Al) melt the PL spectrum at 77K consists of two bands with the maxima situated at 460nm and 540nm. Beginning with the temperatures of 105K (Fig3) the formation of the radiation band with the maximum close to 590nm is observed. At 127K this band predominates in the PL spectrum and then in the temperature range of 210-305K sharply quenches and remains only as a peculiarity on a long wavelength slope of the fundamental band with the maximum at 540nm. One should observe the fact of the absence at 77K of the radiation with the maximum situated close to 400nm. The appearance of the manganese radiation is accompanied by the decrease of the radiation intensity with the maximum close to 460nm.

After ZnS: Al crystals annealing in the Bi melt with the addition of 6.10^{-3}at.%Al the PL spectrum at 77K consists of a wide band with the maximum at 400nm and a shoulder close to 450nm. At the measurement temperature increase at 133K the band with the maximum at 590K emerges which at 245K disappears almost entirely.

After ZnS:Al crystals annealing in the Bi melt with the addition of 0,5at.%Mn in the whole measurement temperature range the predominating radiation with the maximum close to 590nm and a FWHM of $\approx 210eV$ is observed (Fig.4). This value is higher than for a sample where Mn centers were formed at the crystal fabrication and the manganese is uniformly distributed in the whole volume. So, one can suppose, that in the subsurface region the lattice defectness is higher than in the second case

According to the temperature behavior of this band and its spectral position, one can relate its appearance to the intracentered transitions in the manganese ion. The considerable increase of this band FWHM comparable with the previous case, when in the bismuth melt the manganese was not added, is related, apparently, to the fact that the tempering after

annealing with the manganese additions increases the crystal defectness, and, hence, local disorder of the crystal field, which enlarges the Mn^{2+} ion radiation band occurs.
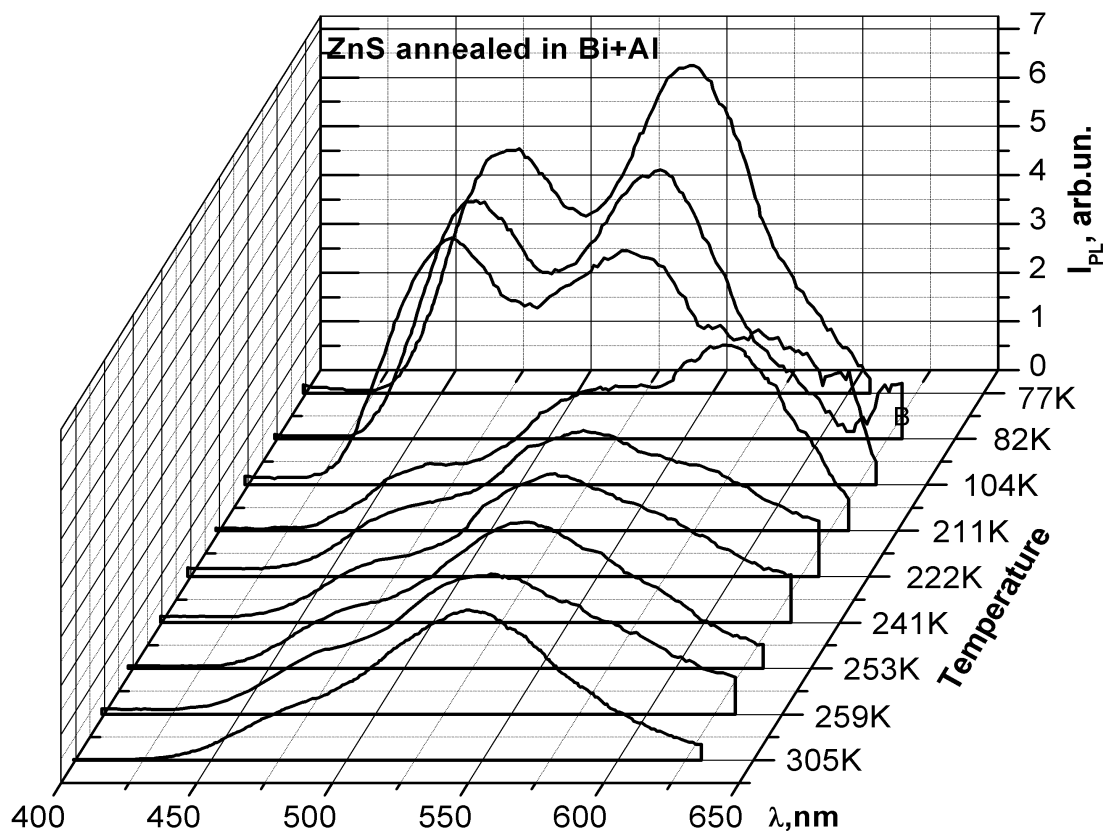

Fig3. The PL spectra at different temperatures of ZnS crystal annealed in Bi+Al melt.

Along with this, due to the high concentration of the manganese centers the formation of Mn-Mn pairs is possible [8]. The appearance of the manganese pairs in the crystal lattice leads to the decrease of PL intensity in the Mn_{Zn}^{2+} ions radiation band in the luminescence spectra, i.e. to its quenching. The same influence on the PL spectrum will have the radiative and none-radiative centers appearing at the atoms recharging, through which a competing with intracentred dissipation of the energy, excited by the ZnS crystal electron subsystem occurs. The named centers recharging at the temperature variation are related to the electron and hole Fermi cuazi-levels displacement, A transformation of the deep levels, which are sensitizers of the intracentred transitions, from recombination levels into the non-equilibrium carrier capture levels and vice-versa, occurs. In its turn this manifests itself in the appearance in the Pl spectra at certain temperatures of the Mn band and its quenching. Earlier [9] we established that interphase interaction at the bismuth melt – ZnS crystal interface generates Zn vacancies. In the subsurface region this enhances the Mn inculcation with the ion formation, occurring according to the bipolar vacancy-hopping diffusion and leads to the impediment of the further manganese doping of the ZnS crystal, due to the formation of, apparently, immobile local charged regions in the dislocation vicinity appearing at the tempering after annealing in bismuth melts. The aluminum presence in the melt, possibly, decreases the efficiency of the manganese doping, as aluminum also occupies the zinc knots of the crystal lattice and from this point of view is competing with the manganese.

It was shown that the starting set of the background, impurity and native defects before the annealing determines the possibilities and the level of ZnS crystal doping from the
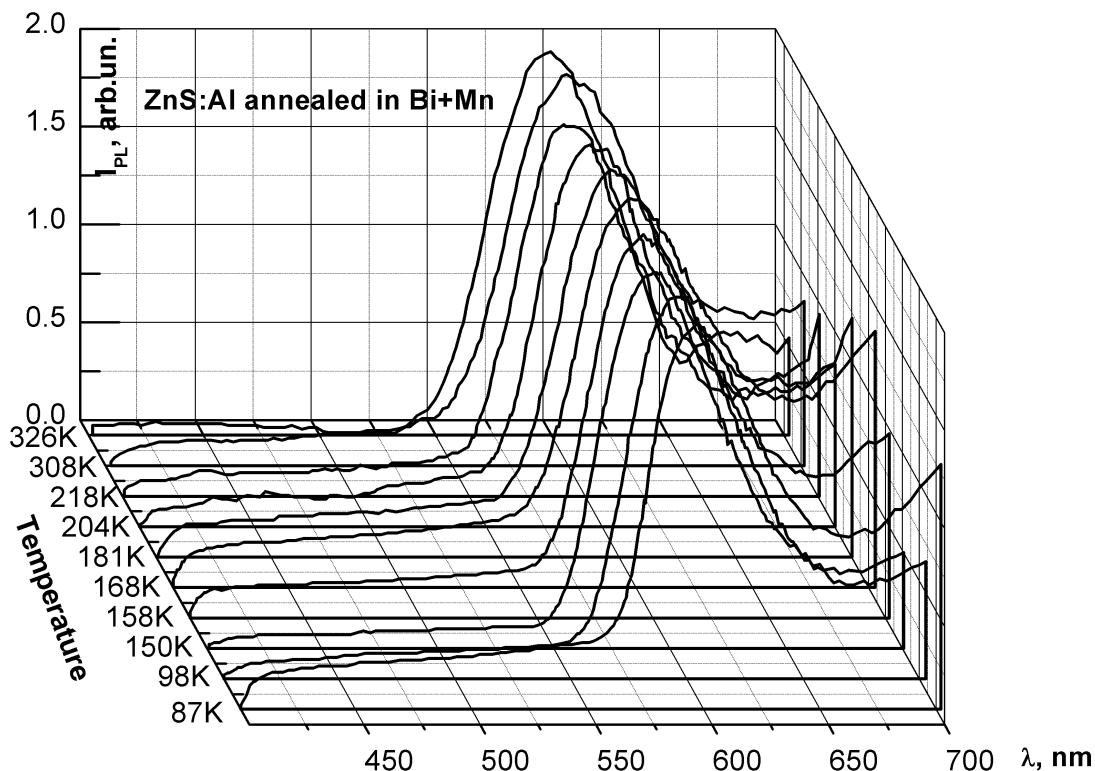

Fig.4. The PL spectra at different temperatures of ZnS:AL crystal annealed in Bi+Mn melt.

bismuth melt. The aluminum presence on the one hand creates sensitizing centers, and on the other hand makes difficult Mn doping of the crystal. The intracentred radiation of Mn $_{Zn}^{2+}$ ion, after crystal doping from Bi melt, is concentrated at the crystal surface and due to the formation of the immobile local regions in the defect vicinity. It is supposed that the temperature influence on the Mn $_{Zn}^{2+}$ ion is determined by the position of the electron and hole Fermi cuazi-levels relative to the deep levels, acting as recombination radiative and nonradiative centers.

References

[1] М.Ф. Буланый, Б.А. Полежаев, Т.А. Прокофьев. ФТП, 32, 673 (1998).

[2] Milind D. Bhise and Monica Katiyar, Adria H. Kitai. J. Appl Phys., 67, 1492 (1990).

[3] P.S.Choudhary, M.S.Sisodia, N.Goswami and P.S;Kamara. Indian J. Of Pure and Aplied Physics, 22, 43 (1984).

[4] В.Ф. Агекян ФТТ, 44, 1921 (2002).

[5] А.М. Гурвич, Введение в физическую химию кристаллофосфоров: ВШ, Москва, 1982.

[6] П.А. Берлов, М.Ф. Буланый, С.А. Омельченко, Кристаллография, 43, 457 (1998).

[7] R.N. Bhargava and D. Gallargher, X. Hong and A. Nurmikko. Phys. Rev. Let., 72, 416 (1994).

[8] Milind D. Bhise and Monica Katiar, Adrian H. Kitai. J. Appl. Phys., 67, 1492 (1990).

[9] В.А. Коротков, Л.И. Брук, Р.Л. Соболевская, К.Д. Сушкевич. Поверхн. Рентген., синхротрон. и нейтрон исследования, 10, 29 (1999).

ELECTRONIC AND MAGNETIC PROPERTIES OF CUBIC LAVE PHASE COMPOUNDS

E. Burzo

Faculty of Physics, Babes-Bolyai University, 400084 Cluj-Napoca, Romania

Abstract

Band structure calculations and magnetic measurements were performed on RM_2-based compounds, where R is a rare-earth or yttrium and M = Fe, Co or Ni. The exchange enhanced paramagnets as $Y(Co_xNi_{1-x})_2$, at $T \leq 10$ K, show a T^2 type dependence of magnetic susceptibilities. Above a characteristic temperature, T^*, a Curie-Weiss behaviour was evidenced. The computed mean square amplitude of spin fluctuations, at high temperatures, describes well the experimentally determined effective moments. The transition of cobalt atoms from nonmagnetic to magnetic state was analysed. A small nickel moment is induced in RNi_2 compounds with magnetic rare-earths. The exchange interactions influence little iron moments. The different contributions to the R5d bands polarizations are also analyzed.

1. Introduction

The RM_2 (M=Fe,Co,Ni) compounds crystallize in a cubic $MgCu_2$-type structure. In this structure the M atoms occupy $\overline{3}m$ sites and R atoms are located in $\overline{4}3m$ positions. Due to their simple structure these systems were intensively investigated, particularly concerning the magnetic behaviour of M atoms [1]. The YCo_2 and $LuCo_2$, at low temperatures, are paramagnetic. A magnetic moment is induced on Co atoms when nonmagnetic Y or Lu are replaced by a magnetic rare-earth [2]. In RNi_2 system it was generally accepted that nickel is nonmagnetic. The RFe_2 compounds have technical applications in magnetostrictive devices [3]. On the support of R-Fe exchange interactions the high magnetostrictions characteristic of rare-earth, at 4.2 K, are translated at room temperature. In addition, the Fe atoms show a rather localized magnetic behaviour.

The magnetic moments of light rare-earths and transition metals are parallel aligned while in case of heavy rare-earths an antiparallel orientation was shown. In earlier publications [1,4], the exchange interactions between R and M atoms were considered to be of RKKY type [5]. Some researches have been done in order to reverse the antiparallel coupling of R and M elements by changing the electron concentration and distances between magnetic atoms [6]. No results have been obtained. The magnetic coupling between R and M atoms can be well described by the Campbell model [7]. The model suggests that the R–M exchange interactions are mediated by R5d band polarization.

In this paper we analyse the magnetic behaviour of RM_2-based compounds. We discuss, at the beginning, the exchange enhanced paramagnets as $LuCo_2$ or $Y(Co_xNi_{1-x})_2$. Then, the transition from nonmagnetic to magnetic state of cobalt atoms is analysed. The effect of exchange interactions on R5d band polarizations is correlated with the number and magnetic moments of neighbouring transition metal atoms to a R atom as well the R4f moment.

2. Experimental and computing methods

The samples were prepared by melting the constituent elements in an arc furnace. The compounds were thermally treated at $\cong 900^oC$ for one week. The X-ray analyses show the presence of the $MgCu_2$ type structure. No other phases were evidenced, in limit of experimental errors of 1 %.

Magnetic measurements were performed in the temperature range 1.7 – 1000 K and fields up to 9 T. The saturation magnetizations were determined from magnetization isotherms, according to approach to saturation law, $M = M_s (1-a/H) + \chi_o H$. By χ_o we denoted a field independent susceptibility and a is the coefficient of magnetic hardness. In the paramagnetic range, the magnetic susceptibilities, χ, were determined from their field dependences, according to the relation $\chi_m = \chi + cM_s'/H$, by extrapolation of measured values, χ_m, to $H^{-1} \to 0$. By c a pressumed impurity content is denoted and M_s' is their saturation magnetization. By this method any possible alteration of the magnetic susceptibilities, as a result of the presence of small quantities of magnetic ordered phase is avoided. For all compounds, the estimated impurity content, if it exists, is smaller than 0.1 %.

Band structure calculations were carried out by using the ab initio tight binding linear muffin tin orbitals method (TB-LMTO) [8-10] both in LDA and LDA+U approaches. In the framework of the local density approximation (LDA), the total electric potential is the sum of the external, Coulomb and exchange correlation potentials [4]. The frozen core approximation was employed in the generation of the potential and parametrization of the Von Barth and Hedin [12] was used for the exchange correlation part of the effective one electron potential, obtained within the local spin density approximation of the density functional theory. The LDA+U scheme [13] is based on the Anderson impurity model in mean field approximation that analyses the s and p electrons as non-correlated, described by an orbital independent potential and d electrons as described by an orbital dependent potential [14].

3. Magnetic behaviour of RCo_2 with R=Lu,Y and $Y(Co_xNi_{1-x})_2$ compounds

The thermal variations of magnetic susceptibilities for RCo_2 (R = Lu, Y) compounds are plotted in Fig. 1. The magnetic susceptibilities increase up to a temperature T_{max} and then decrease continuously. Above a temperature T^*, a Curie-Weiss type behaviour was evidenced. In the low temperature range (T $\leq$ 10 K), a T^2 dependence of the magnetic susceptibilities can be shown – Fig.2.
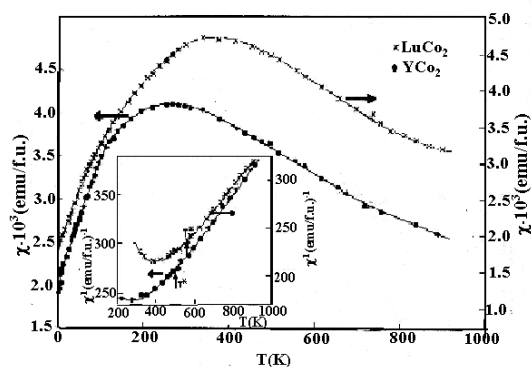

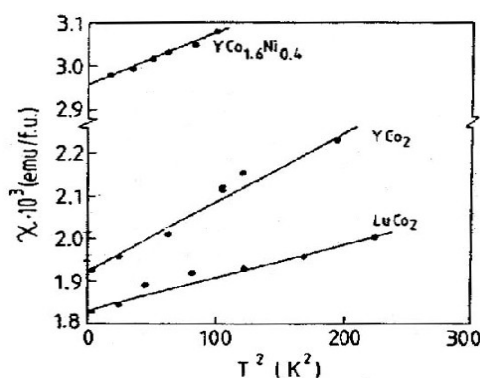Fig. 1 Thermal variations of magnetic susceptibilities for YCo_2 and $LuCo_2$ compounds.

Fig. 2 Thermal variations of magnetic susceptibilities at T $\leq$ 10 K for $Y(Co_xNi_{1-x})_2$ with x = 1.0 and 0.8 and $LuCo_2$

The same behaviour can be evidenced in $Y(Co_xNi_{1-x})_2$ system - Fig.3. The temperatures at which maxima in susceptibilities are shown, decrease when increasing nickel content, from $T_{max} \cong 240$ K ($x = 1.0$) up to $\cong 20$ K ($x = 0.2$). For $Y(Co_{0.2}Ni_{0.8})_2$ compound the magnetic susceptibilities decrease in the whole temperature range [15]. As already stated, the Curie-Weiss dependence is shown above temperatures T^*, which also decrease when increasing nickel content. The effective cobalt moments determined at $T > T^*$, supposing that nickel has no magnetic contribution, vary only little in the studied composition range from 3.87 μ_B/atom ($x = 1.0$) to 3.72 μ_B/atom ($x = 0.1$) – Fig.4. The YNi_2 shows mainly a Pauli type paramagnetism.
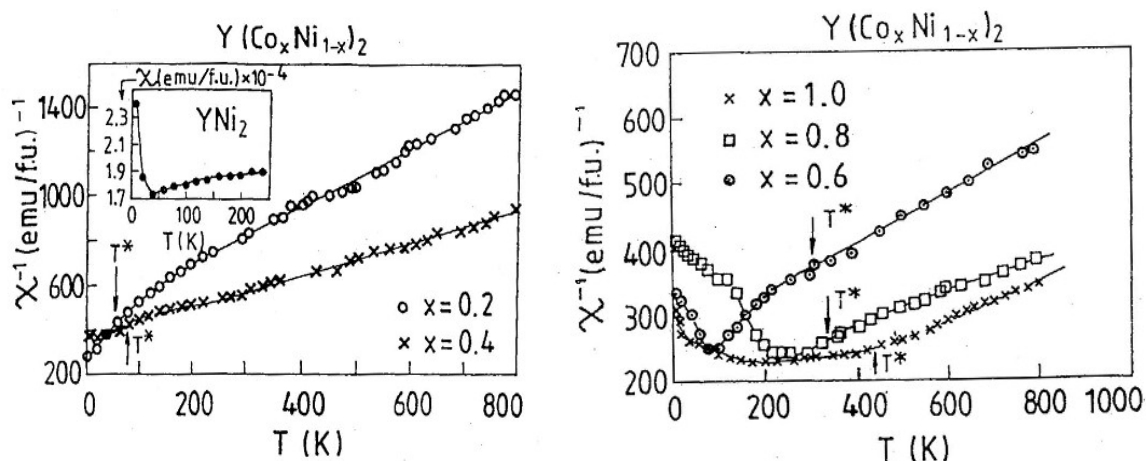

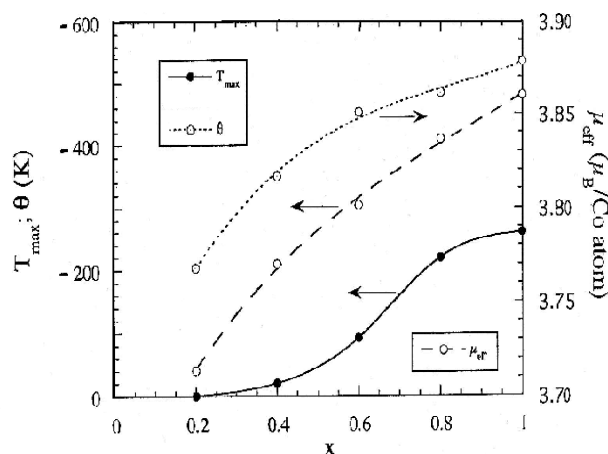Fig. 3 Thermal variations of reciprocal susceptibilities for $Y(Co_xNi_{1-x})_2$ compounds.

Fig. 4 Composition dependences of the effective cobalt moments, paramagnetic Curie temperatures and T_{max} values in $Y(Co_xNi_{1-x})_2$ system.

The projected band structures for YCo_2 and YNi_2 are plotted in Fig. 5. For YCo_2, as well as $LuCo_2$, the Fermi level lies just above a sharp peak in density of states (DOS). By alloying with nickel, the Fermi level in shifted gradually towards a region with lower density of states.
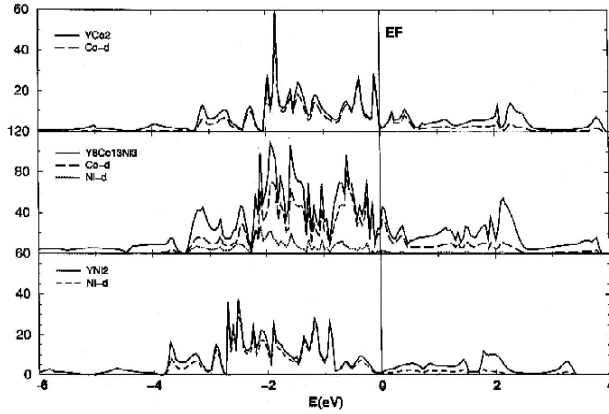
Fig. 5 Projected DOS curves, computed for YCo_2, $YCo_{1.625}Co_{0.375}$ and YNi_2 compounds.

The magnetic behaviour of the above systems can be analysed in the spin fluctuation model. The model considers the balance between the frequencies of longitudinal spin fluctuations, which are determined by their lifetime and that of transverse fluctuations that are of thermal origin. These effects lead to the concept of temperature induced moments. From a strong exchange exchanced paramagnet, as RCo_2 (R=Lu,Y,Hf), the wave number dependent susceptibility, χ_q, has a large enhancement due to electron-electron interactions for small q values. The χ_q shows significant temperature dependence only for the above mentioned q values. The average amplitude of spin fluctuations, ξ^2, increases with temperature and finally reaches an upper limit, at a characteristic temperature T^*. For $T > T^*$, a Curie-Weiss behaviour is predicted, as for systems having local moments. In this model, the moments are localized in q-space.

The temperature dependence of the mean square amplitude of spin fluctuations can be analysed considering the effects of spin fluctuations, for a general model of itinerant electron paramagnetism in the classical Gaussian statistics [16-18]. The contributions to the susceptibilities from the spin fluctuations, in terms of the density of states can be expressed as:

$$\chi_s^{-1} = a_1 - \alpha + (5/3)a_3\xi^2 + (35/9)a_5\xi^4 + (35/3)a_7\xi^6 + ... \tag{1}$$

where the mean square value of the fluctuating magnetization, ξ^2, is given by

$$\xi^2 = \frac{3}{2\pi^2} k_B T q_m A^{-1} \left[1 - \frac{tg^{-1}(q_m\sqrt{A\chi})}{q_m\sqrt{A\chi}} \right] \tag{2}$$

By a_1, a_3, a_5 and a_7 are denoted the expansion coefficients of the free energy with respect to the square of magnetization density and α, q_m and A denote the molecular field coefficient, the cut-off wave vector of spin fluctuations and the exchange stiffness constant, respectively.

By limiting the series expansion development up to terms in ξ^2,we retained in relation (1) only terms in a_1 and a_3, expressed as [17, 18]:

$$a_1 = \frac{2}{Ng^2\mu_B^2} \left\{ 1 + \frac{1}{6}(\pi k_B T)^2 \left[\left(\frac{N'}{N}\right)^2 - \frac{N''}{N} \right] + ... \right\} \tag{3}$$

$$a_3 = \frac{g^2\mu_B^2}{2^2 3!} a_1^3 \left\{ 3\left(\frac{N'}{N}\right)^2 - \frac{N''}{N} + \frac{1}{6}(\pi k_B T)^2 \left[6\left(\frac{N'}{N}\right)^4 - 13\frac{N''N'^2}{N^3} + \left(\frac{N''}{N}\right)^2 + 7\left(\frac{N'''N'}{N^2}\right) - \frac{N''''}{N} + ... \right] \right\} \tag{4}$$

We denoted by N the state density at the Fermi level and N', N'', N''' and N'''' are their derivatives of the order of one to four.

By fitting the experimental data with relation (1) we determined the α, q_m and A values and, as a result, the temperature dependences of the mean square amplitude of spin fluctuations – Fig.6. Generally speaking, the ξ^2 values are not fully saturated in the studied temperature range (T < 750 K) but approach very much to saturation at highest saturation. There is a more evident tendency to saturate, at higher temperatures, as the nickel content increases. This behaviour is in agreement with the decrease of T^* temperatures when nickel content is higher. The lack of full saturation can be connected with the approximation used in determining q_m and A values. We limited the series development for χ up to terms in a_3. In addition, we neglected the Pauli-type contributions to the susceptibilities, due to mainly the fraction of YNi_2 present in a given compound as well of the core diamagnetism. In spite of the approximation used, the differences between $<\xi^2>^{1/2}$ values, experimentally determined, and the computed ones, at highest temperatures, where nearly saturation was attained, are rather small – Fig.7.
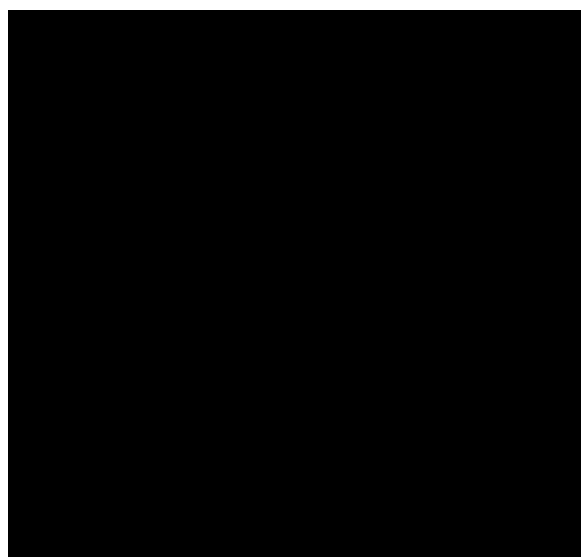

Fig. 6 Temperature dependences of the mean square amplitude of spin fluctuations.
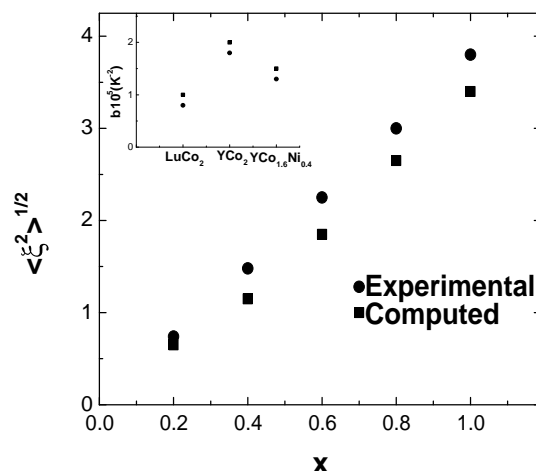

Fig. 7 The computed and experimentally determined values of the mean square amplitude, $<\xi^2>^{1/2}$, of the spin fluctuations. In inset the computed and experimentally determined b values are given.

As above mentioned, in the low temperature range (T ≤ 10 K) – Fig. 2 - the χ values follow a T^2 type dependence.

$$\chi = \chi_0 (1+bT^2)$$ (5)

Since the maximum in χ vs T values is shifted to low temperatures when increasing the nickel content, no accurate determination of χ values was possible for compounds with x ≤ 0.3. In the paramagnon model [19] the b coefficient is given by

$$b = \frac{\pi^2}{6}\left[2\frac{N''}{N}-1.2\left(\frac{N'}{N}\right)^2\right]_{E_F} s^2$$ (6)

where s is the exchange enhanced parameter.

In order to compute the b values we selected a symmetric energy interval around the self-consistent value of the Fermi level in DOS and we used a mean square interpolation scheme in order to analytically analyse the energy dependence of the DOS. This approach allowed us to evaluate the first and second derivative of the DOS at the Fermi level. The b values, computed according to relation (6), describe rather well the experimental data – Fig.7 inset.

The external [20-22] or internal [23,24] fields determine a partial quenching of spin fluctuations. This is reflected by the decrease of the specific heat coefficient γ or of the effective moments. If the magnetic field is sufficiently large so that the Zeeman splitting energy of opposite spin states is comparable to, or larger than the characteristic spin fluctuation energy, then the paramagnons no longer have sufficient energy to flip spins and therefore, the inelastic spin flip scattering in quenched. A magnetic field, H_{eff}, of the order of the characteristic spin fluctuation temperature, $H_{eff} \propto T_{sf}$, is requested to quench the spin fluctuations. A partial quenching of spin fluctuations by external fields was evidenced by specific heat measurements on YCo_2 or $LuCo_2$ [22] The decrease of the electronic specific heat constant, γ, in field of 10 T, was 4 % for YCo_2 and 10 % for $LuCo_2$. A partial quenching of spin fluctuations can be observed by magnetic measurements, when replacing Y or Lu in RCo_2 compounds, by a magnetic rare-earth. The effective cobalt moments decrease as the Curie temperatures, exchange interactions, respectively are greater. In Fig.8 we plotted the effective cobalt moments in RCo_2 compounds as function of the reciprocal exchange field H_{exch}^{-1}, at 4.2 K. There is a linear dependence, $M_{eff}(Co) = d + e\,H_{exch}^{-1}$, with $e = 2.2 \cdot 10^2$ $\mu_B T$. For a variation of the internal (exchange) field of 10 T, the changes in the effective cobalt moments are of $\cong 6$ %. This value is close to the diminution of the electronic specific heat constants, as above mentioned, in the same range of external fields, in YCo_2 or $LuCo_2$ compounds [22].
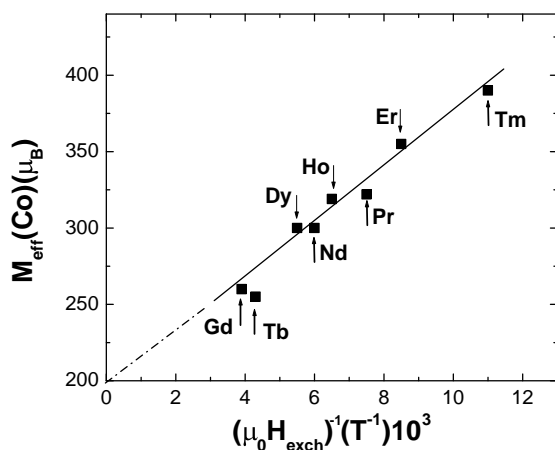

Fig. 8 The effective cobalt moments determined in RCo_2 compounds as function of the inverse exchange fields

4. The effects of exchange interactions on transition metal moments

The substitution of Y or Lu, in RCo_2 compounds, by a magnetic rare-earth induces an order magnetic moment at cobalt site. A magnetic moment of 1.03 μ_B/atom was obtained by magnetic measurements at 4.2 K in $GdCo_2$. This suggests that the cobalt moments are

determined by exchange interactions [2,25]. There seems to be a critical field for the appearance of a moment on cobalt atom.

Previously [26,27], we proposed a model for induced magnetism (or epamagnetism) in which there is a sudden increase of the cobalt moment for a critical field. Then, the magnetic moments increase linearly with exchange fields and finally saturate. The model has been confirmed experimentally by analyzing the magnetic properties of RCo_4B [28] or some RCo_2 [29]–based compounds. In the following we discuss the effect of exchange interactions on the cobalt moments in $Gd_xY_{1-x}Co_2$, $Gd(Co_xNi_{1-x})_2$ and $Gd(Co_xAl_{1-x})_2$ systems in which magnetic atoms as Gd or Co, are replaced by Y or Ni(Al), respectively. In this way the exchange interactions are modified.

The composition dependence of the transition metal moments (CoNi) in $Gd(Co_xNi_{1-x})_2$ system are plotted in Fig.9. There is a great decrease of the transition metal moments for $x \geq 0.8$. Since gadolinium content is not changed, the variation of the magnetizations may be attributed only to the substitution of Co with Ni. In order to have information on Co and Ni magnetic behaviour, band structure calculations were performed [30] – Fig.10. The magnetic moments, thus determined, are listed in Table 1. The cobalt moments, as well as nickel ones, are little dependent on composition. We note that a magnetic moment of 0.12 μ_B was determined in $GdNi_2$ although previous studies stated that nickel is not magnetic [1]. A value of Ni moment of 0.20 μ_B/atom ($\mu^L = 0.06$ μ_B and $\mu^S = 0.14$ μ_B) was recently obtained by magnetic circular dichroism measurements [31]. Since in computing Ni moment only the spin value was obtained, this it is in very good agreement with that experimentally determined.
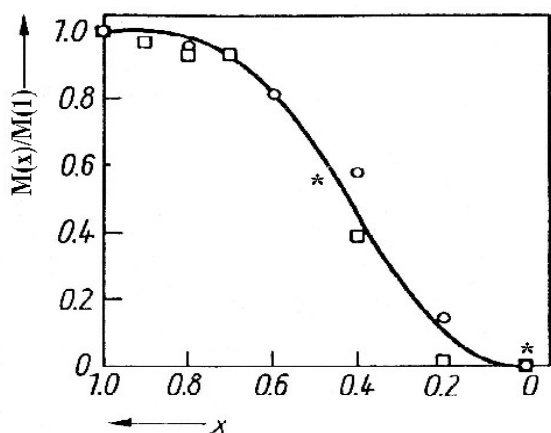

Fig. 9 The composition dependence of the transition metal moments in $Gd(Co_xNi_{1-x})_2$ system. By $*$ the computed values are plotted. Solid line describes the prediction of relation (7) with $n_c \geq 3$.
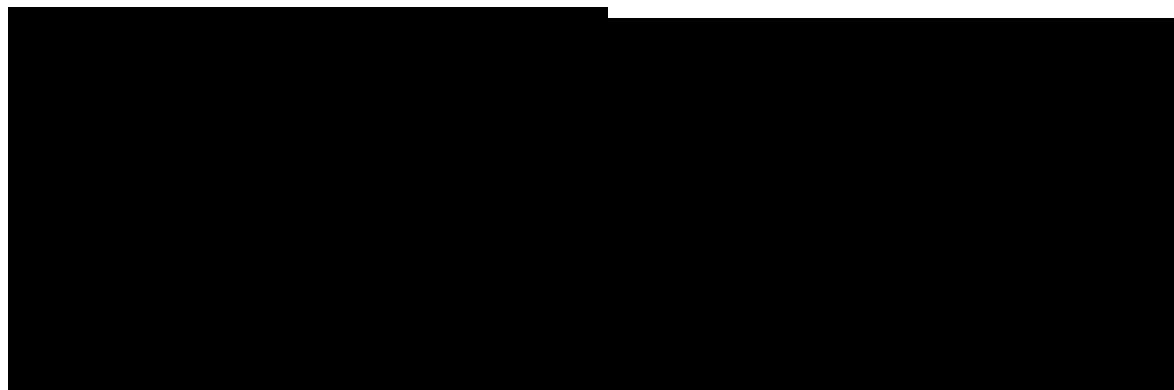

Fig. 10   Projected DOS curves for $GdCo_2$ and $GdCoNi$ compounds.

The analysis of the data from Table 1 suggests that cobalt and nickel moments, as already stated, are little dependent of composition. Thus, the high decrease of the transition metal moments at $x \geq 0.8$ can be attributed only to the loss of cobalt moments at sites where the exchange interactions are smaller than a critical value. This can be correlated with a minimum number of cobalt atoms coupled by exchange interactions. Thus, a statistical model can be used in order to determine the critical exchange field. In this model [32] the magnetic moment of cobalt is lost if there is a smaller number of cobalt atoms as nearest neighbours than a critical value, n_c. The mean magnetic moment for a composition x can be described by:

$$\langle M_{Co} \rangle = \sum_{n > n_c} M_{Co}(x) P_n(x) \tag{9}$$

Table 1. Magnetic moments of Co and Ni determined from band structure calculations in $Gd(Co_xNi_{1-x})_2$ compounds.

Compound	M_{Co} (μ_B/atom)	M_{Ni} (μ_B/atom)	$M_{5d}(Gd)$ (μ_B)	M_{Gd} (μ_B/atom)
$GdCo_2$	1.22	–	-0.53	-7
$GdCoNi$	1.11	0.14	-0.43	-7
$GdNi_2$	–	0.12	-0.30	-7

We denoted by $P_n(x)$, the probability for a cobalt atom to have n nearest neighbour similar atoms. Considering a random distribution of Co and Ni atoms on $\bar{3}m$ sites, we have

$$P_n(x) = \frac{6! \, x^n (1-x)^{6-n}}{(6-n)! \, n!} \tag{10}$$

Relation (9) describes well the composition dependence of (Co,Ni) moments, supposing that cobalt has a magnetic moment M_{Co} (x=1) if there are $n \geq 3$ Co nearest neighbours and is nil if this number is smaller than $n_c = 3$. From these data we can estimate the critical field for the appearance of cobalt moment. By using paramagnetic measurements we evaluate the molecular field coefficients characterizing the interactions between cobalt atoms. A value $J_{Co-Co} = 3.3 \cdot 10^{-22}$ J was obtained. This corresponds to a critical field $H_c = 70$ T for the appearance of cobalt moment, when considering the presence of three atoms in a cluster. This value agrees with that suggested previously by our studies [27, 28] or other data from literature [29].

The critical field for the appearance of cobalt moment can be also estimated in $Gd_xY_{1-x}Co_2$ compounds. For this purpose, the molecular field coefficients were determined by using paramagnetic measurements or by fitting the temperature dependence of the magnetization, by using a two sublattices model, in the molecular field approximation [33]. The cobalt moments as function of the exchange fields, thus determined, are plotted in Fig. 11. In the same figure the data obtained in case of $Gd(Co_xAl_{1-x})_2$ and $Gd(Co_xNi_{1-x})_2$ systems are also included. A transition from nonmagnetic to magnetic state of cobalt is shown also at $H_{crit} \cong 70$ T. The cobalt moments then increase linearly with a slope of $(3 \cdot 10^2)^{-1}$ μ_B/T and above $\cong 150$ T saturate.
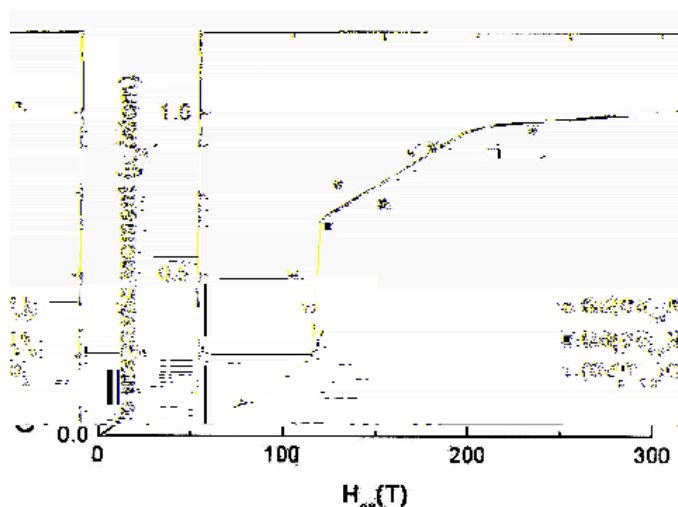
Fig. 11   The variation of cobalt moments, at 4.2 K, as function of the exchange fields.

The dependence of the iron moments on the exchange fields in $(Gd_xY_{1-x})Fe_2$ compounds is plotted in Fig.12 inset. A linear variation, in all the composition range, was shown, described by the relation $\Delta M_{Fe}(\mu_B) = (18.10)^{-2}\Delta H_{exch}(T)$. This suggests that the iron moments are not so sensitive as cobalt to the exchange interactions, showing a more localized behaviour. We also analysed the variations of iron moments in $(Gd_xY_{1-x})Fe_n$ and $Gd(Fe_xAl_{1-x})_n$ series with n = 2,3, where Gd is replaced by Y or Fe by Al. In this way the exchange interactions are modified. We note that in $GdFe_3$-based compounds the iron atoms occupy different sites in lattice, having different magnetic contributions. In this case we considered only the mean iron moments. The composition dependences of iron moments experimentally determined and those computed are plotted also in Fig. 12. There is a rather good agreement between the two sets of data showing that the proportionality relation between the variation of the magnetic moments and of exchange fields is valuable also for other types of structures than Laves phase.

Fig. 12 The dependence of the iron moments on the exchange fields in $(Gd_xY_{1-x})Fe_2$ system (inset) and the computed and experimentally determined variations of the iron moments in $(Gd_xY_{1-x})Fe_n$ and $Gd(Fe_yAl_{1-y})_n$ compounds with n = 2 and 3.

The present band structure calculations show that small magnetic moments are also induced on nickel atoms in RNi_2 compounds with magnetic rare-earths. These values are by nearly two order of magnitude smaller than those of rare-earth moments and cannot be

determined by magnetic measurements since are of the order of experimental errors. Experimental evidence of Ni moment was shown only by magnetic circular dichroism in $GdNi_2$ compound [31].

5. R5d band polarization

The gadolinium 5d band polarization, M_{5d}, in GdM_2 (M=Fe,Co,Ni) Laves phase compounds are plotted in Fig.13 inset, as a function of the transition metal contributions to the magnetization, M_d. There is a linear increase of M_{5d} vs M_d. The extrapolation at $M_d \rightarrow 0$ leads to a value of 5d band polarization, $M_{5d}(R)$, which can be attributed only to local 4f-5d interactions. The above data suggest that the R5d band polarizations are determined both by local 4f-5d and 5d-3d short range exchange interactions. Thus:

$$M_{5d} = M_{5d}(R) + M_{5d}(0) \tag{11}$$

The contributions to 5d band polarization from local 4f-5d exchange interactions can be determined in compounds where M elements are not magnetic or by the extrapolation procedure mentioned above. In case of gadolinium compounds a value $M_{5d}(R) \cong 0.27 \ \mu_B$ was obtained, parallel oriented to the rare-earth moment. The study of 5d band polarizations in RCo_2 compounds with heavy rare-earths suggests that this contribution is proportional to De Gennes factor, $G = (g_J-1)^2 J(J+1)$, $M_{5d}(R) = \alpha G$ with $\alpha = 2.1 \times 10^{-2} \ \mu_B$. Supposing that the above two contributions described by relation (11) are additive, the effects of 5d-3d short range interactions on the 5d bands polarizations, $M_{5d}(0)$, were determined. The exchange interactions of given R atoms with neighbouring M ones are described by the Hamiltonian:

$$H = JS_{5d} \sum_i S_{3di} \tag{12}$$

where J is the exchange integral and i is the number of neighbouring 3d atoms having S_{3di} spin.

Due to high symmetry of the structure, the M and R atoms occupy only one type of site in lattice and thus only one $M_{5d}(0)$ value is expected for all sites in a given compound. The 5d-3d exchange interactions act as an internal field, H_{exch}, on 5d bands and induce an additional polarization to that determined by 4f moment. By using the molecular field approximation, the internal field can be writhen as $H_{exch} = N_{5d-3d}M_d$ where N_{5d-3d} is the molecular field coefficient describing the exchange interactions between R and M atoms. We showed already that above the critical field, which determines appearance of magnetic M moment, the M_d values are proportional to the exchange field. Thus, it results that $M_{5d}(0) = \gamma M_d$. The analysis of the magnetic properties of $Gd_xY_{1-x}Co_2$ system showed that the molecular field coefficients describing the exchange interactions between Gd and Co are $N_{GdCo} = 110 \pm 10$ and not dependent on composition. By using this value and supposing that the 5d band polarization can be described by the same relation, as a function of exchange field, as for Co 3d moments, $M_{5d} = (3 \cdot 10^{-2})^{-1} \ \mu_B/T$, we obtained that $M_{5d} \cong 0.19 \ M_d$. This relation, in spite of used approximation, is in rather good agreement with that experimentally determined, $M_{5d} = 0.12 \ M_d$ – Fig.13. This suggests that sensitivity of 5d band polarization to the exchange interactions is of the order of induced cobalt moments.
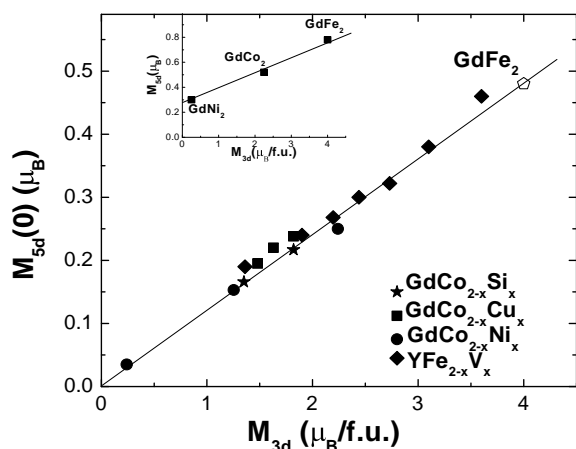
Fig. 13 The $M_{5d}(0)$ band polarizations in some Laves phase compounds as a function of the transition metal moments. In the inset, the total M_{5d} band polarizations are plotted as a function of 3d magnetic moments for RM_2 (M=Fe,Co,Ni) compounds.

6. Conclusion

The exchange enhanced paramagnets $Y(Co_xNi_{1-x})_2$ and $LuCo_2$, at $T \leq 10$ K show a T^2 dependence of the magnetic susceptibility. Above a characteristic temperature, T^*, a Curie-Weiss type behaviour was shown. The determined cobalt effective moments are close to that of Co^{2+} ion. The above behaviour is well described by the spin fluctuations model [35]. By using band structure calculations we computed the contributions of (CoNi) to the mean square amplitude of spin fluctuations. The values thus obtained, agree rather well with those experimentally determined.

A critical exchange field, $H_{crit} = 70$ T, was estimated, as necessary to induce an ordered magnetic moment on cobalt, at 4.2 K. The presence of small nickel moments in RNi_2 compounds, with heavy rare-earths, was shown by band structure calculations. Iron shows a more localized behaviour. The effect of exchange interactions on M_{Fe} values is nearly one order of magnitude smaller than for cobalt.

The effect of local 4f-5d and range 5d-3d exchange interactions on the R5d band polarizations were evaluated. The induced 5d band polarization by 4f-5d local interactions is proportional to the De Gennes factor while that due to 5d-3d short range interactions is proportional to transition metal moments of neighbouring atoms to a given R.

References

[1] E.Burzo, A.Chelkovski and H.R.Kirchmayr, Landolt Bornstein Handbuch, vol. 19d2, SpringerVerlag, Berlin, 1990 and references
[2] E.Burzo, Solid State Commun. 20, 1569 (1976)
[3] A.E.Clark, Handbook on the Physics and Chemistry of the Rare-Earths, vol. 2, Ed. R.A Gschneidner, L.Eyring, North Holland, Amsterdam, 1979, p.231
[4] KH.J.Buschow, Phys. Stat Solidi (a) 7, 199 (1971)
[5] M.A.Ruderman and C.Kittel, Phys. Rev. 96, 99 (1954): T.Kasuya, Progr. Theor. Phys. 16, 45 (1956); K.Yoshida, Phys. Rev. 106, 893 (1957)
[6] W.E.Wallace and J.T.Swearingen, J.Solid State Chem. 8, 37 (1973): W.E.Wallace, E.P.Ganaphaty and R.S.Craig, J. Appl. Phys. 50, 2327 (1979)
[7] I.A.Campbell, J Phys. F: Metal Phys. 2, L 47 (1972)

[8] O.K.Andersen, Phys. Rev. B 12, 3060 (1975)

[9] O.K.Andersen and O.Jepsen, Phys. Rev. Letters 53, 2571 (1974)

[10] O.K.Andersen, O.Jepsen and O.Glotzel, in Highlights of Condensed Matter Theory, Eds. F.Bassani, F.Fumi and M.P.Tossi, North Holland, New York, 1985

[11] R.O.Jones and O.Gunarson, Rev. Mod. Phys. 61, 689 (1989)

[12] U. von Barth and L.Hedin, J. Phys. C5, 1629 (1972)

[13] V.Ansimov, J.Zannen and O.K.Andersen, Phys. Rev. B 44, 943 (1991): A.I.Lichtenstein, J.Zannen and V.I.Ansimov, Phys. Rev. B 52, R 5467 (1995)

[14] V.I.Ansimov, F.Aryasetiavan and A.I.Lichtenstein, J. Phys.: Condens Matter. 9, 967 (1997)

[15] E.Burzo, D.Givord and L.Chioncel, J. Appl. Phys. 83, 1779 (1998)

[16] L.Chioncel, E.Burzo, R.Tetean and V.Pop, Mol. Cryst. Liq. Cryst. 415, 107 (2004)

[17] M.Shimizu, Phys Letters 81 A, 87 (1981)

[18] M.Shimizu, Rep. Progr. Phys. 44, 21 (1989)

[19] M.T.Beal-Monod, Physica B 109, 1837 (1982); M.T.Beal-Monod and J.M.Lawrence, Physica B 21, 5400 (1980)

[20] M.T.Beal-Monod, S.K.Ma and D.R.Fredkin, Phys. Rev. Letters 22, 928 (1968)

[21] W.F.Brinkman and S.Engelsberg, Phys. Rev. 169, 417 (1968)

[22] K.Ikeda, K.A.Gschneidner, R.J.Stiermann, J.W.E.Tsang and O.D.Mc Masters, Phys. Rev. B 29, 5039 (1984)

[23] E.Burzo and R.Lemaire, Solid State Commun. 84, 1145 (1992)

[24] E.Burzo, Rom. J. Phys. 43, 319 (1998)

[25] E. Burzo, Phys. Rev. B 17, 1414 (1978)

[26] E. Burzo,Rev. Roum. Phys. 23, 689 (1978)

[27] E.Burzo, J. Less Common Met. 77, 251 (1981)

[28] E.Burzo, N.Plugaru, I.Creanga and M.Ursu, J. Less Common Met. 155, 281 (1989)

[29] N.N.Duc, T.D.Hien, P.E.Bromer and J.J.Franse, J. Magn. Magn. Mater.104-107, 1252 (1992)

[30] E.Burzo and L.Chioncel, J. Opt. Adv. Mater. (2004), in press

[31] M.Mizumaki, K.Yano, I.Umehara, F.Ishikawa, K.Sato, A.Koizumi, N.Sakai and T.Muro, Phys. Rev. B 67, 132404 (2003)

[32] E.Burzo, D.P.Lazar and M.Ciorascu, Phys. Stat. Solidi (b) 765, K 145 (1974)

[33] L.Neel, Ann. Phys. 3, 137 (1948)

[34] E.Burzo and M.Balanescu, J. Solid State Chem. 37, 1 (1981)

[35] T.Moriya, J.Magn.Magn.Mater. 100, 201 (1991)

TIN DIOXIDE BASED THIN FILM GAS SENSOR OF HYDROGEN

S. Dmitriev

Center of Applied and Environmental Chemistry, Moldova State University
60, A.Mateevici str., Chisinau, MD-2009, Moldova
Tel./Fax: (373-22)-577556; E-mail: serghei_dmitriev@yahoo.com

Abstract

Results of investigation of the SnO_2 thin films sensitivity towards to hydrogen are presented. Films were deposited by chemical spray pyrolysis method on ceramic substrate. Study of electrical characteristics of obtained layers has shown that the latter possess resistance on the level 10^5-10^6 Ohm at the working temperatures 200-250 ^{o}C.

Gas sensitivity S of deposited thin films amounted 95-100 relative units to 0.1 vol.% of hydrogen in air. Optimization of gas sensitive properties of tin dioxide films through bulk and surface doping with Pd and Cu has allowed increasing of hydrogen sensitivity up to 10^3 rel. units. Simultaneously, the considerable shift of the working temperatures of such sensor to the low temperature value (150^oC) was achieved.

Introduction

Metal oxide based thin film gas sensors (TFGS) have found wide application for the control of different industrial processes, including fuel combustion, detection of leakages of toxic and inflammable gases etc due to the power consumption and cost reduction, possibility for further miniaturization and integration in microsystems for air quality monitoring [1].

Most investigated metal oxide semiconductor utilized for gas sensitive element creation is SnO_2. Mechanism of gas impurity sensing through the alteration of surface conductivity of such material at the contact with atmosphere is widely considered in literature [2,3].

SnO_2 demonstrates high thermal and chemical resistivity and stability and sensitivity to different gases but unfortunately possess poor selectivity at that. Obtaining sensor selectivity for a definite gas is difficult and challenging task. Selectivity depends on many parameters [4], such as mechanisms of adsorption and co-adsorption of gas molecules, surface reaction kinetics and electron exchange between adsorbed species and conduction band of semiconductor. For resolving of the selectivity problem, in practice, there are used different methods to improve selectivity through the catalytic and electronic effects with utilization of bulk and surface doping and modification of gas sensitive material.

Different deposition technology like PVD, CVD, sol-gel and other can be used for the fabrication of thin film based gas sensors [5].

In our research there is considered the possibility to produce TFGS by means of spray pyrolysis deposition process. Due to apparatus simplicity and low power consumption this technology is very cheap. Through the modification of deposition process [6] we resolved the technical task of uniform and reproducible deposition of tin dioxide thin films on large area that makes this technology compatible with group technology of microelectronics that will

allow arranging the large-scale manufacturing of TFGS for different application. Earlier we reported [7] on creation of thin film gas sensor with high sensitivity to CO.

In the given report we present results of investigation aimed at the fabrication of TFGS with high sensitivity to hydrogen presence in atmosphere by means of spray pyrolis deposition technology. Topology of developed TFGS and basic operational parameters are presented.

Experimental details

For films deposition by means of spray pyrolysis method on already fabricated through group technology chip of TFGS (Fig.1) there was used 0.2M $SnCl_4 \cdot 5H2O$ water solution. Volume of sprayed solution was equal to 1 ml and time of its spraying was equal to 10 s. Deposition was carried out at pyrolysis temperature $T_{pyr}=425^oC$.
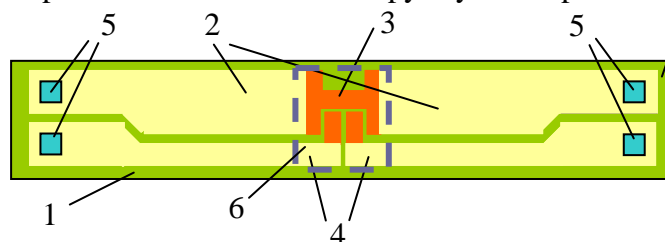

Fig.1. Chip of TFGS: 1-substrate; 2- heating electrodes; 3-resistive heater; 4-measurement electrodes; 5-contact area; 6- SnO_2 gas sensitive film.

For enhancement of SnO_2 films sensitivity to hydrogen the Pd doping was used. Doping was carried out also through spray pyrolysis method with using of $Pd(AcAc)_2$ as a precursor. In order to overcome technical difficulties appearing at the introducing of $Pd(AcAc)_2$ due to its poor dissolving in water there was used specially developed approach [8] based on mixing of two solutions: aquatic, containing 0.2M $SnCl_4 \cdot 5H2O$, and ethanol, containing $Pd(AcAc)_2$. Ratio of tin and palladium atoms in solution Sn:Pd was equal to 100:1. Combined solution was sprayed after homogenization.

The thickness of deposited SnO_2 films was measured using ellipsometer amounted 80-100 nm. Concentration of free electrons determined from Hall effect measurements has amounted $4-6 \cdot 10^{18}$ cm^{-3}.

Gas sensitivity was determined as ratio of SnO_2 film resistance in the pure air and in the presence of gas impurity in atmosphere ($S=R_{gas}/R_{air}$). Values of R were determined through Van-der-Pauw method. Along with study of developed device gas sensitivity to H_2 its sensitivity to some other inflammable gases (CH_4 and C_3H_8) was also tested.

Results and discussion

In Fig.2 there are presented results of experimental study of influence of SnO2 thin films doping with Pd. Here we had used different modes of doping - bulk, surface and combined (simultaneously bulk and surface). The bulk doping of tin dioxide with Pd (curve 2) leads to some growth of sensitivity S to 1 vol.% of H_2 in air but it is not very significant. We connect this with the fact that thin SnO_2 films obtained by means of spray pyrolysis method, are solid (i.e. not porous) and, as a result, atoms Pd introduced in the bulk of film do not participate in the chemosorptional processes on the film surface. So, in this case only atoms of Pd positioned on the film surface can participate in the reaction of catalytic oxidation of CO, giving contribution to sensitivity growth. Simultaneously, it is observed the 100^oC shift of gas sensitivity temperature maximum in the field of lower temperature.

For further improvement of gas sensitivity of tin dioxide thin films we had used additionally surface doping too. The latter has allowed increasing of the sensitivity by order (curve 3, Fig.2) and shifting of S_{max} from 350°C to 150°C. Surface doping was carried out in the same process and doping solution was sprayed onto the as-deposited thin films of SnO_2 already containing Pd in the matrix of film. Such approach is stipulated from the consideration that at the long term exploitation of sensors at elevated (working) temperatures the diffusion of atoms of Pd, concentrated on the film surface, inside the film will be observed. As a result, we can expect the degradation of gas sensitive properties and alteration
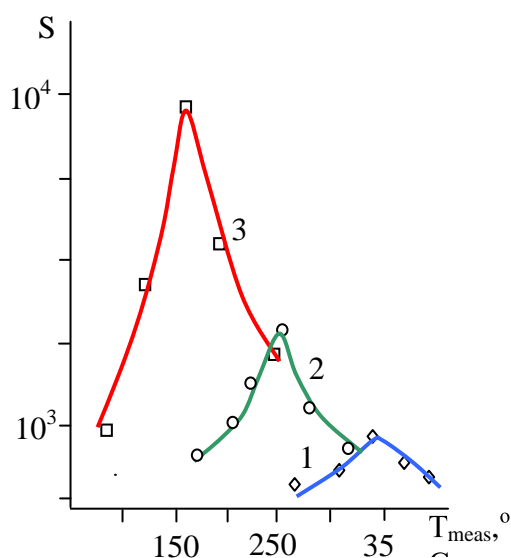

Fig.2.. Dependence $S=f(T_{meas})$ for SnO_2 films:
   1-undoped, 6 vol.% H_2 in N_2;
   2-Pd bulk doped, 1 vol % H_2 в N_2
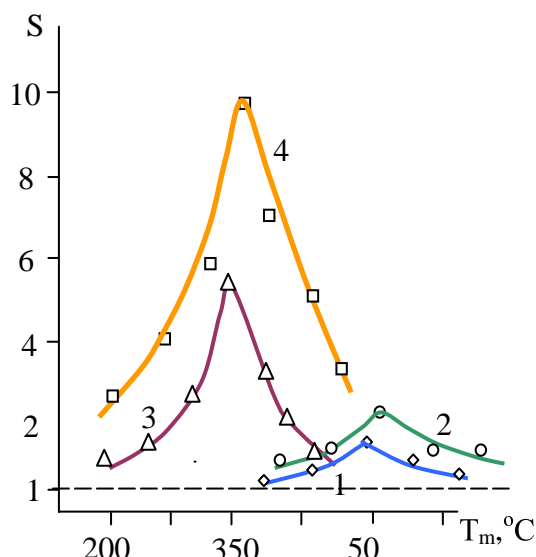   3-Pd bulk and surface doped

Fig.3. Temperature dependence of SnO_2 films sensitivity toward 1 vol% CH_4 in air (curves 2,4) and 1 vol% of C_3H_8 in air (curves 1,3).Curves 1,2-undoped films, curves 3,4- Pd surface doped and Cu bulk doped films

of operational regimes. Preliminary introducing of Pd atoms in the film matrix will prevent the surface Pd diffusion in bulk and provide durability and stability of gas sensitive characteristics of the device.

Along with study and optimization of the gas sensitivity of SnO_2 thin films toward hydrogen we have investigated the possibility to use developed gas sensor for detection of some other explosive gases such as methane and propane. It was established that tin dioxide films deposited through chemical spray pyrolysis process possess very low sensitivity toward these gases. In particular, sensitivity of the obtained films to 1 vol.% of methane or propane in air does not exceed value of 2 relative units. At that, both maxima of gas sensitivity are placed at the temperatures in the interval 500-520°C. Through the series of experiments there was established that combined doping of tin dioxide thin films with copper and palladium allows to increase by some times gas sensitivity of the given films (and, as a result, thin film gas sensors on their base) to methane and propane, widening through that field of application of developed microelectronic devices. Atoms of Cu were introduced in the sprayed solution as $CuCl_2{\cdot}6H_2O$ in ratio Sn:Cu=100:1. Cu was used for bulk doping of tin dioxide films, but Pd for surface doping only.

For the determination of the optimal exploitation parameters of the fabricated TFGS there was carried out a series of experiments, results of which are presented in the Table below.

Table. Parameters of SnO_2 based TFGS with hign sensitivity to H_2.

Parameters	
1. Gas sensitivity to:	
1 vol.% H_2 in N_2	$8\text{-}9 \cdot 10^3$ rel. units
1 vol.%CH_4 in air	8-10 rel. units
1 vol.% C_3H_8 in air	4-6 rel units
2. Threshold sensitivity to H_2	0.01 vol.% in air
3. Temperature in active zone (^{o}C):	
at the detection of H_2	150-180
at the detection of CH_4 and C_3H_8	300-350
4. Sluggishness (s)	<2-3 s
5. Response time (s):	
at the detection of H_2	5-10
at the detection of CH_4 and C_3H_8	15-20
6. Consuming power (mW):	
at the detection of H_2	60
at the detection of CH_4 and C_3H_8	100

Conclusions

In the frame of carried out investigations it was shown that at the correct choice of doping additives and mode of doping the chemical spray pyrolysis deposited thin films of SnO_2 can be used for creation of microelectronic gas detectors with high sensitivity to H_2 as well as other inflammable gases (CH_4, C_3H_8).

References

[1] D.E.Williams, Sensors and Actuators, B57 (1999) 1-16
[2] A.M.Azad, J.Electrochemical Society, 139 (1992) 3690-3704
[3] W.Gopel, Sensors and Actuators, B 18-19 (1994), 1-21
[4] F.Cosandey, G.Skandan, A.Singhal, Journal of Materials, 52 (10) (2000)
[5] G.Sberveglieri, Sensors and Actuators, B 23 (1995), 103-109
[6] G.Korotchenkov, S.Dmitriev, V.Brinzari, Sensors and Actuators, B 54 (1999), 202-209
[7] G.Korotchenkov, S.Dmitriev, V.Brinzari, Mater. Sci. and Eng., B56 (1999) 195-204
[8] S. Dmitriev, I. Dementiev, A. Craciun, Application for Patent Nr. a2004 0067 (MD). Priority from 04.26.2004

MODELING OF TEMPERATURE REGIMES OF THIN FILM GAS SENSITIVE DEVICES

S. Dmitriev

Center of Applied and Environmental Chemistry, Moldova State University
60, A.Mateevici str., Chisinau, MD-2009, Moldova
Tel./Fax: (373-22)-577556; E-mail: serghei_dmitriev@yahoo.com

Abstract

This paper presents results of the modeling of the temperature distribution in a chip of thin film gas sensor, operating at high temperatures ($150\text{-}1000^{o}C$), required to provide high sensitivity and selectivity to target gases. Analysis of thermal regimes of such chip was carried out on the base of model of plate with local source of heat. It was found that substrate heat conductivity is most influencing parameter, determining both temperature distribution in chip and also the electrical power consumption decreasing. The example of realized chips designed in accordance with results of modeling is presented. The results of modeling are compared with experimental data.

Introduction

For the normal functioning of a thin film gas sensor (TFGS) its construction should include heating element, providing the warming of the film up to required working temperature. The latter, in its turn, influences the choice of topology of TFGS chip, substrate material and TFGS construction, in general. As a result, it is needed for TFGS construction optimization with a purpose of increasing of TFGS reliability and durability and decreasing of the power consumption.

In practice, the task of optimization of TFGS construction requires the knowledge of temperature regimes and, in particular, temperature field distribution in a chip of gas sensor on dependence on material substrate, geometry of chip, temperatures in working zone of sensors, etc. In this connection, there was carried out investigation of the given problem through the numerical computer modeling of temperature distribution in a chip of TFGS and experimental testing of the results of modeling on developed structures of TFGS chip.

1. Modeling of the temperature fields in chip of gas sensor

The task of modeling of the temperature regimes of TFGS is sufficiently complicated and for its simplification there was considered the chip of TFGS "isolated" in space. The given approach allows us already at the stage of selection of material of substrate, geometrical sizes and topology of chip to estimate the influence of all the mentioned above factors on temperature distribution in chip.

In our case chip of TFGS represents a thin plate (with thickness $\delta=400\text{-}500$ μm) of dielectric substrate with linear dimensions L_x and L_y, on the surface of which resistive heater (RH) is formed through the group technology methods. Linear sizes of RH are: $2\Delta\xi$, $2\Delta\xi$ and coordinates of center of RH - (ξ,η).

Analysis of the thermal regime of such gas sensitive element can be carried out on the base of model of plate (Fig.1) with local source of heat and heat exchange from surface [1].
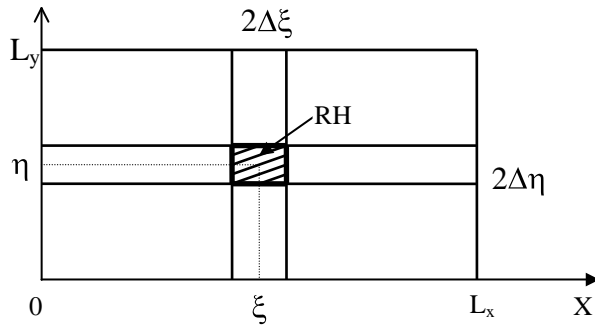
In the frame of the given model it is supposed:

1) the sources of heat of power P are distributed uniformly in the field of RH, surface density of heat flow from local sources with power P is equal to zero out of RH and is constant in its limits;

2) the heat exchange from plate ends is negligible in comparison with heat exchange from basic surfaces;

3) the heat exchange with environment is realized only through irradiation and convection from two basic surfaces;

Fig.1. Plate with local source of heat – the model of chip of TFGS

4) the coefficients of heat exchange from basis surfaces do not depend on temperature and are equal α_1 and α_2 correspondingly.

Then the stationary field of temperatures of such plate can be described by the following differential expression [2]:

$$\frac{\partial^2 \theta}{\partial x^2} + \frac{\partial^2 \theta}{\partial y^2} - a^2 \theta = -g_s, \qquad 1\{U\} \tag{1}$$

where $g_s = \dfrac{P}{4\Delta\xi\Delta\eta\delta\lambda}$, $a = -\dfrac{\alpha_1+\alpha_2}{\lambda\delta}$, $1\{U\}=1$ in the field of U and $1\{U\}=0$ out of this field U; $\theta=T-T_s$ is temperature head, T is temperature of plate in given point, T_E is environment temperature; λ is specific heat conductivity of plate, α_1 and α_2 are coefficients of heat emission. Border conditions for the given equation with account of assumption 2 have the following form:

$$\left.\frac{\partial\theta}{\partial i}\right|_{i=0} = \left.\frac{\partial\theta}{\partial i}\right|_{i=L_i} = 0, \quad (i=x,y) \tag{2}$$

$$\theta = \frac{P}{(\alpha_1+\alpha_2)S_u}\varphi_x\varphi_y \tag{3}$$

where $S_u=4\Delta\xi\Delta\eta$ is surface area of RH (U), a φ_x and φ_y are non-dimensional coordinate functions having bulky form and so will not be presented here.

2. Numerical calculation of temperature distribution in chip

The computer calculation of the temperature fields in TFGS chip by Eq.(3) was carried out for different values of λ, and L_i (i=x,y), coordinates of the field of heating up, environment temperature T_E and average surface temperature T_S.

There were used the following values: $\lambda = 1; 10; 100$ W/(м· K); L_x , $L_y= 5 \cdot 10^{-3}$; $1 \cdot 10^{-2}$; $1,5 \cdot 10^{-2}$; $2 \cdot 10^{-2}$ (m); $\delta = 4^{-4}$ м; $2\Delta\xi = 7,5^{-4}$ м; $2\Delta\eta = 2,5^{-4}$ м; $\xi,\eta = 0$; $L_i/4$; $L_i/2$; $T_E = 20°C$; $T_S = 200; 250; 300; 350; 400°C$. Coordinates x and y were changed with a step $0,1L_i$.

Proceeding from the dependence of the coefficient of heat irradiation on temperature the calculations were carried out in the following order: 1). assignment of average surface temperature of substrate T_S and finding of the coefficients of heat emission α_1 and α_2; 2). finding of the value of dissipating power P; 3). calculation of the temperature as function of coordinate by formula (3).

The value of total dissipated power was estimated by equation:

$$P = \alpha \cdot (T_\Pi - T_c) \cdot L_x \cdot L_y \tag{4}$$

3. Results of modeling of temperature distribution in TFGS chip

In the result of modeling it was established that value of λ plays the key role in the forming of temperature distribution in TFGS chip and power P dissipating (Fig.2-3). Decreasing of λ by two orders leads to the some times growth of temperature T_{RH} in the field of heating at the constant dissipating power. Most significant growth is observed at the λ change in the range from 10 to 1 Wt/m^2K.
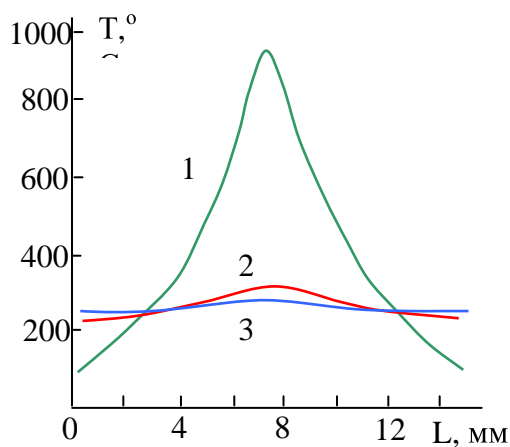

Fig.2. Temperature profile in TFGS chip on
    dependence on substrate λ [Wt/(м²·K]:
    1-1; 2-10; 3-100. (RH in a center of
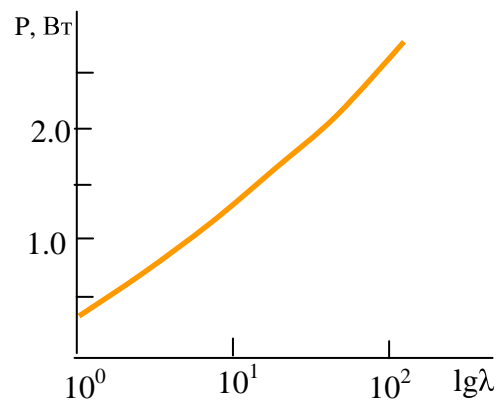   substrate. $P_{RH}=0.87$ Wt)

Fig.3. Dependence of average dissipated power
    P on λ

The second factor by the level of influence on temperature distribution in the chip of TGFGS is the position of resistive heater on substrate. One can see that shift of RH from the position in the center of substrate (Fig.2) to its edge (Fig.4) leads to the twice increase of temperature in the zone of heating up. If the same temperature is kept in a zone of heating up for different values of λ of substrate the temperature in the field of the contacts of gas sensitive elements can be decreased by 200-400°C (Fig5.)

So, the carried out modeling of temperature regimes in TFGS chip allows: 1) to estimate the influence of the heat conductivity of substrate material on the temperature profile in chip;
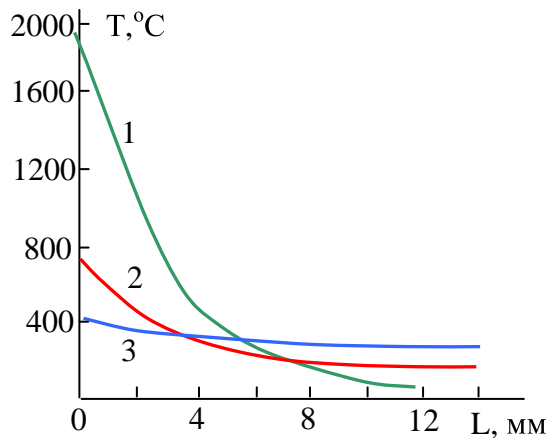

Fig.4. Temperature profile in TFGS chip on dependence on substrate λ [Wt/(м^{2}·K]: 1-1; 2-10; 3-100. (RH at the edge of substrate. P_{RH}=0.87 Wt)
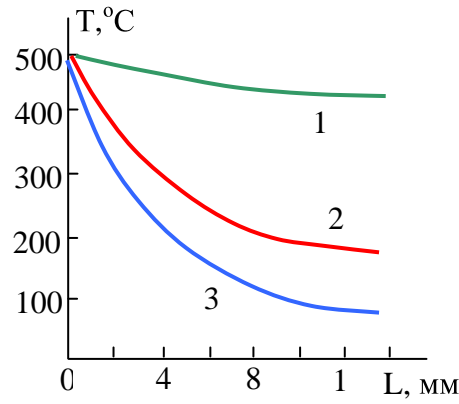

Fig.5. Temperature profile in TFGS chip on dependence on substrate λ [Wt/(м^{2}·K]: 1-100; 2-10; 3-1. (RH at the edge of substrate.)

2) to account the influence of the position of resistive heater on the surface of chip on the temperature distribution and value of consuming power P; 3) to optimize topology of the TFGS chip.

4. Experimental study of temperature distribution in TFGS chip

Results of numerical modeling were tested by means of measurement of temperature profile in real, fabricated by us, TFGS chip. Topology of chip and temperature profile are shown in Fig.6. As a substrate policor (λ=10 Wt/м^{2}·K) with size 6,5x5,5 мм was used. RH was placed in point with coordinates (L_x/4,L_y/2). Resistive heater supply voltage amounted 10 V and current through heater was 150 mA. Temperature was measured by means of Cu-constantan thermocpuple in the cross-section y=L_y/2.
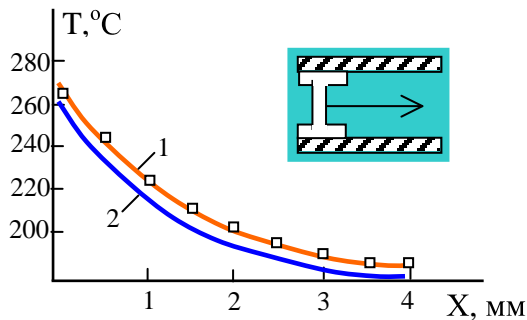

Fig.6. Temeperature profiles in TFGS chip

1-experiment; 2-calculation.

Comparison of the calculated and experimental curves T(x) in Fig.6 demonstrates sufficiently good correspondence of the modeling results to real temperature regimes in TFGS chip that allows us to conclude that the considered model is applicable for TFGS topology design.

References
[1] G.N. Dul'nev, V.G. Parfenov, A.V. Sigalov Metody rascheta teplovogo rezhima priborov. - M.: Radio i sveazi, 1990. - 312 c
[2] G.N. Dul'nev, B.V. Pal'shchikov Temperaturnoe pole plastiny s diskretnym istochnikom energii// Injenerno-fizicheskii zhurnal - 1975. - T.29. - .4.- C.722-727.

CONTACT HTSC – SEMICONDUCTOR FOR DIODE DETECTORS: ROLE OF SURFACE STATES IN QUASI-STATIC REGIME

Ia.I. Kerner

Institute of Applied Physics, Academy of Sciences of Moldova, Academiei str.5, Kishinev, 2028, Moldova. Phone: (37322)543668; Fax: (37322)738149.

The numerical modeling of the electrical potential distribution and current passing in the contacts of the high temperature superconductor (HTSC) with semiconductor InSb had been made. There were analysed the possibilities to create the diode detectors (DD) based on these contacts and working at liquid nitrogen temperature 77.4 K. The influence of the surface states (SSt) densities on the DD parameters was analyzed.

Earlier we had studied the situation, when SSt were in the thermodynamic equilibrium (TE) with HTSC and they had not time to recharge with applied voltage (a "dynamical" regime).

In this article an opposite situation is studied, when SSt are in TE with InSb and they have time to recharge with applied voltage (a "statical" regime).

The comparison with existent literature data shows that the proposed DD can be 10÷100 times better. Therefore these DD are perspective for cryogenic electronics and it is actual to elaborate them.

At present the perspectives of the HTSC technical application are widely studied. The possibilities to create DD with Josephson HTSC junctions are also investigated. According to [1] the best of them revealed the voltage responsibility VR=5000 V/W and noise equivalent power NEP = 2×10^{-12} W/Hz$^?$ at the signal frequency f=31 GHz and temperature T=77 K. We suppose that the elaboration of DD working at T=77.4 K which are based on the HTSC-semiconductor contacts may be done too. At present the contacts of HTSC with semiconducting $SrTiO_3$ [2] and GaAs/AlAs superlattices [3] are already obtained. Taking into account the experimental problems the numerical analysis is actual.

In order to solve this problem the calculation method was elaborated and the numerical analysis of the contacts HTSC-semiconductor (InSb) was made. The [4, 5] results were taken into account. The potential distribution, current-voltage dependences and DD parameters were calculated.

According to [6] it was proposed the SSt energy density to be equal to 2×10^{16} m^{-2} eV^{-1} in the middle of the forbidden band of InSb and one order more at this band edges.

On the other hand taking into account the results in different semiconductors we believe the other SSt densities may be realized too. To make clear the SSt influence two cases were studied: (i) - the above-mentioned SSt energetic density; (ii) - when SSt energetic density is 10 times higher everywhere.

Earlier we studied the situation, when SSt were in the thermodynamic equilibrium (TE) with HTSC and they had not time to recharge with applied voltage (a "dynamical" regime).

In this article an opposite situation is studied, when SSt are in TE with InSb and they have time to recharge with applied voltage (a "statical" regime).

To analyze the possible DD structure a flat contact with a surface 100 μ^2 was considered.

Fig. 1. presents the calculated current responsivity (CR) on the signal frequency (F) - the curve numeration is invariable in this article). In all the figures in this article curves 1 and 2 reflect the cases (i) and (ii) correspondingly. Negative potential is applied to n-InSb and positive one to HTSC.
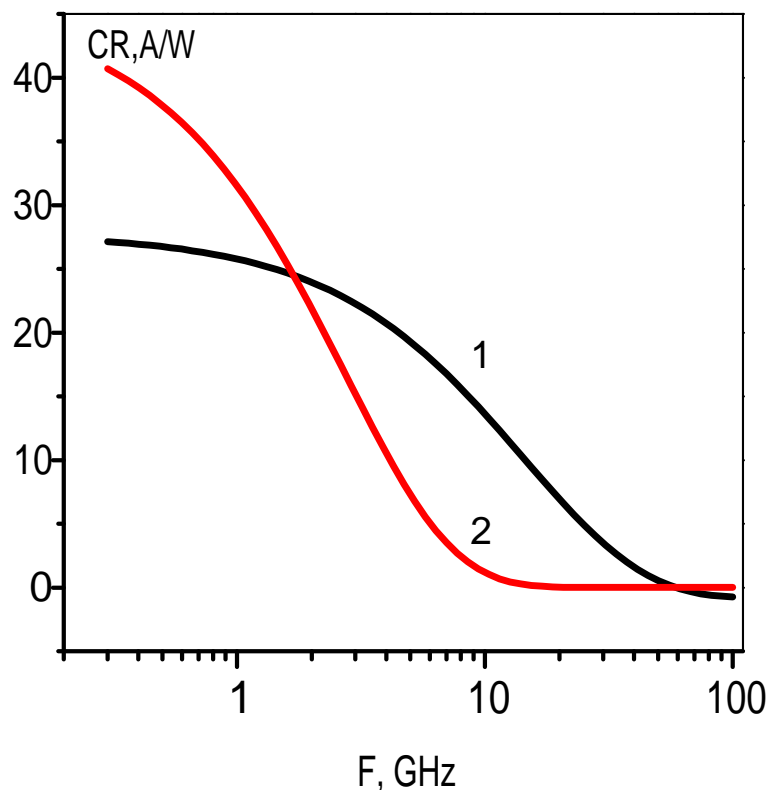

Fig. 1. The calculated current responsivity dependence on the signal
frequency. The logarithmic scale for X-axis is used .

In all cases the current responsivity reduces at high frequencies, because the negative role of the barrier capacity is revealed and the contact capacity resistance becomes comparable with the ohmic resistance of the semiconductor volume. The redistribution of the applied voltage between contact resistance and volume resistance occurs, thus leading to the decrease of the rectified current and DD parameters become worse. In the case (ii) the contact resistance is higher and the change of the potential barrier with applied voltage is more sufficient. This fact provides a bigger current responsivity at low frequencies in the case (ii).

On the other hand in this case a slightly thicker film was considered. And although this circumstance caused the only little increase of the ohmic resistance, but its influence on the DD characteristics was very strong.

At the high frequencies a drastic increase of the current responsivity took place (see fig.1,curve 2). This fact shows the miniaturization importance in examined structures.

The calculated voltage responsivity (VR) dependency on the signal frequency is shown in Fig. 2.
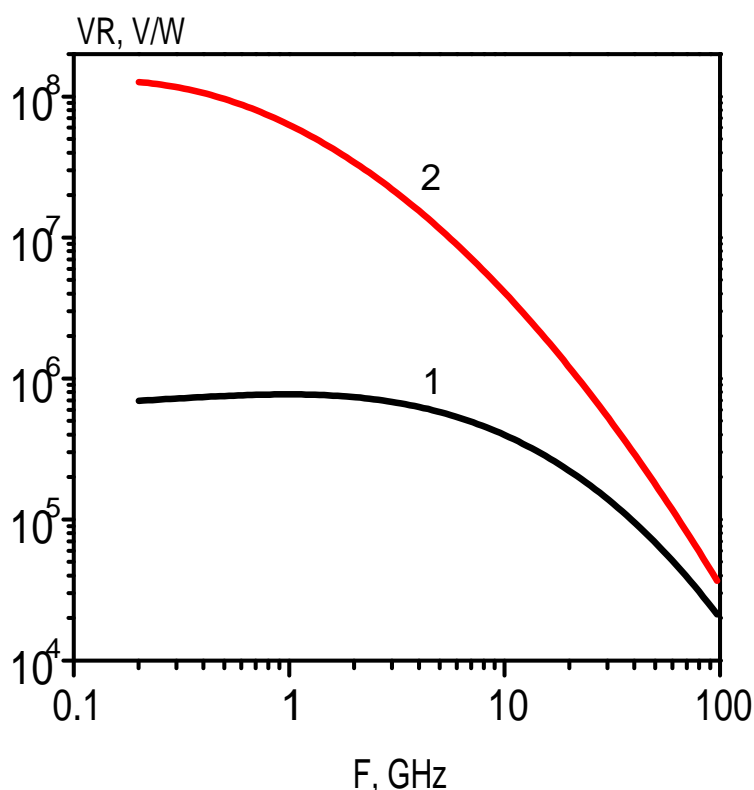

Fig. 2. The calculated voltage responsivity from signal frequency. In fig.
2,3 the logarithmic scale is used for both axes

The explanation of the frequency dependence is similar to one in Fig. 1. The case (ii)– curve 2– is better to achieve the good voltage responsivity, because in this situation we have a big current responsivity and a   contact differential resistance is higher, but the voltage responsivity is approximately determined by the production of these values.

Fig. 3 presents the calculated noise equivalent power (NEP) versus signal frequency (in good DD this value must be minimum).

Noise equivalent power is inversely proportional to the current responsivity. At high frequencies current responsivity decreases and noise equivalent power increases. At lower frequencies (ii) case is better due to its small noise current density . But if the frequency rises the current responsivity reduction becomes more significant and (i) case is better.
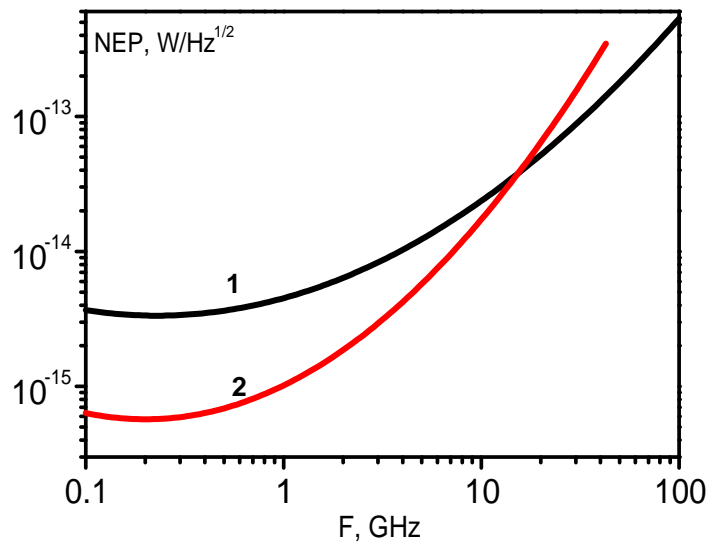
Fig.3 The calculated noise equivalent power dependence on
the signal frequency.

The comparison with [1] data shows that the proposed DD can be 10÷100 times better apart from the SSt density. Therefore these DD are perspective for cryogenic electronics and it is actual to elaborate them.

References

[1] A. K. Kuz`min, V. N. Ohrimenko, E. S. Soldatov, A. N. Tavhelidze The detecting properties of the YBaCuO films microbridges // Sverhprovodimost` (Superconductivity– in Russian). – 1990. –V.3, N.11, P. 2650-2660.

[2] H. Hasegawa, T. Fukazawa, T. Aido, Contact between high-T_c superconductor and semiconducting niobium-doped $SrTiO_3$ //Jap. J. Appl. Phys., Pt. 2. – 1989.– V. 28, N. 12, P. L2210-L2212.

[3] L. D. Chang, M. Z. Tseng, L. A. Sonosca et al. In situ $Yba_2Cu_3O_{7-x}$ superconductor superlattices // Materials Research Society 1991 Spring Meeting. Preliminary Program – USA, Annaheim,1991–P.63.

[4] S. M. Sze Physics of semiconductor Devices.– USA, N. L. : Willey – Interscience Publication,1981-512pp.

[5] V. N. Alfeev, L. N. Neustroev The photo–current in the tunnel contact: high-temperature superconductor-semiconductor-semiconductor // Doclady Akademii Nauk SSSR (Reports of the Soviet Academy of Sciences – in Russian)-1990-V.311-N. 5- P. 1106-1110.

[6] W. Braun, M. Schneider, N. Kubicki, R. Herrman, C-V measurements of anodized InSb MOS structures at 77 and 4.2 K, //Phys. Stat.Sol. (a)- 1984- V. 86, 1- P.427-431.

PLASMA TREATMENT AND SURFACE SENSIBILIZATION OF TIN DIOXIDE FILMS FOR ENHANCEMENT OF GAS SENSITIVITY

V. Brinzari[1], S. Dmitriev[2], G. Korotchenkov[1]

[1]*Microelectronics Laboratory, Technical University of Moldova,*
168 Blv. Stefan cel Mare, Chisinau, 2004, Moldova
[2]*Center of Applied and Environmental Chemistry, Moldova State University,*
60 Mateevich Str.,Chisinau, 2009, Moldova

Abstract

This paper presents result of investigation aimed at the improvement of gas sensitive properties of SnO_2 thin film gas sensors (TFGS) by means of high frequency (HF) oxygen plasma treatment and its surface doping. Used in experiments SnO_2 films were deposited by spray pyrolysis method. It is shown that plasma treatment provides 3-4 times growth of thin film gas sensitivity. Surface doping of SnO_2 films with Pd leads to gas sensitivity increasing by order. It is concluded that combination of HF oxygen plasma treatment and surface sensibilization through surface doping is an effective way to considerable improvement of gas sensitive properties of tin dioxide based TFGS.

Introduction

As follows from the developed earlier model of TFGS [1] and established interrelation between gas sensitive properties and electrophysical parameters of metal oxide film [2] further improvement of gas sensitivity (depending on film thickness d and charge carriers concentration n in film) can be achieved through the decreasing of free electron concentration in the layer and increasing of catalytic activity of SnO_2 surface by means of doping.

The first approach will allow obtaining of thin films with required resistance ($\sim 10^5$-10^6 Ohm·) and correspondingly gas sensitivity at higher values of d that simplifies technological control of this parameter and increases the reproducibility of deposition process. As free electron concentration in thin films of SnO_2 is determined, mainly, by the own stoichiometry defects, connected with oxygen deficient in film matrix the simplest way to decrease free charge carrier concentration in layer could become standard technologies of microelectronics: 1) thermal oxidation in oxygen containing atmosphere (for instance, air) and 2) treatment of layers in oxygen HF plasma.

Second approach allows increasing of the sensitivity of TFGS that is connected with the fact that energies of dissociative adsorption for O_2 and CO on the surface of noble metals (Pd, Pt) are considerably lower than on the surface of SnO_2. As a result, the reaction of CO detection (catalytic oxidation on the surface of SnO_2:(Pd, Pt) will proceed at a lower temperature than in the case of undoped SnO_2.

In this connection we have carried out the investigations aimed at the evaluation of degree of efficiency of the mentioned approaches to improvement of gas sensitive parameters of TFGS fabricated on the base of tin dioxide thin films deposited by means of spray pyrolysis method.

1. Experimental details

For the forming of gas sensitive films on the ceramic substrate there was used method of chemical spray pyrolysis. Details of technology of deposition are described elsewhere [3]. Films were deposited at the temperatures in the interval 400-500°C from alcohol solutions of $SnCl_4 \cdot 5H_2O$. The thickness of films was varied in the range 20-100 nm.

Surface treatment of obtained tin dioxide layers was carried out in pure oxygen plasma at room temperature. Time diapason of treatment had been varied from 5 to 45 minutes, and determined optimal time for such treatment of tin dioxide thin films was found equal to 30 min. For comparison and estimation of efficiency of plasma treatment there was used thermal annealing also. Thermal ageing was carried out in the furnace of open type in atmosphere of air at the temperatures in the range 400-600°C. Time of annealing varied from 1 to 10 min.

For evaluation of plasma treatment and thermal ageing efficiency there was used measurement of resistance and gas sensitivity of tin dioxide thin films towards CO presence in air. Resistance of films was measured by means of Van der Paw method. Sensitivity of thin films to CO was determined as $S = R_{gas}/R_{air}$, where R_{gas} and R_{air} are resistance of film in the presence of detected gas in air and in pure air correspondingly. Stoichiometry of films was controlled by means of SIMS and IR-spectroscopy measurements

For SnO_2 films doping with Pd spray pyrolysis method had been also used.

2. Results

2.1. Oxygen HF plasma treatment and thermal annealing of SnO_2 films

Results of thermal annealing and oxygen HF plasma treatment of SnO_2 are presented in Table and in Fig. 1-2. One can see that utilization of both types of SnO_2 thin film treatment leads to some growth of resistance and sensitivity of films to CO presence in atmosphere.

Table. Influence of HF oxygen plasma treatment and thermal annealing on resistance R and gas sensitivity S of SnO_2 thin films deposited at $T_{pyr}=440°C$ ($T_{treat}=T_{room}$, $t_{treat}=30$ min)

No. of samples		1	2	3	4	5	6	7	8
Before plasma	$R \cdot 10^6$, Ohm	0,06	1,4	0,14	0,08	0,08	0,09	0,08	0,06
After plasma	S, rel.units.	3,6	5,0	5,6	5,1	5,5	4,1	4,4	3,2
Before plasma	$R \cdot 10^6$, Ohm	22	20	4,6	1,4	1,6	1,5	1,0	1,3
After plasma	S, rel.units.	14	12	13	9	11	9	8,5	10
No. of samples		1	2	3	4	5	6	7	8
Before annealing	$R \cdot 10^6$, Ohm	40	2	0,7	0,6	0,3	0,1	0,08	0,3
After annealing	S, rel.units	19	14	12	10	8	4	6	8
Before annealing	$R \cdot 10^6$, Ohm	64	3,3	2,2	1,7	0,6	0,2	0,2	0,7
After annealing	S, rel.units.	43	30	21	19	16	8,0	8,5	11,5

Simultaneously, as follows from the results of SIMS (Fig.2) and IR-spectroscopy (Fig.3) measurements, the content of SnO_2 phase in tin dioxide film is grown noticeably that directly points out improvement of stoichiometry of treated films and the role of the latter in optimization of films characteristics.

Analyzing the obtained results we can conclude that both thermal annealing and HF oxygen plasma treatment possess the similar effect from the point of view of gas sensitivity
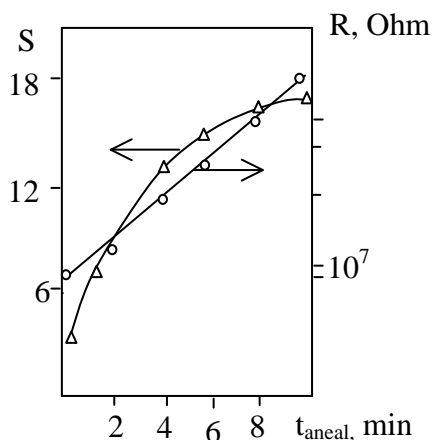
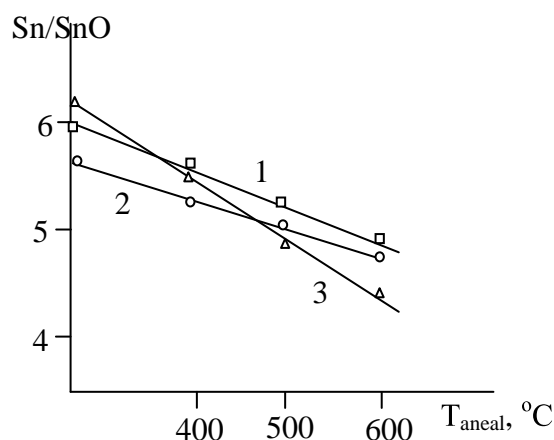Fig.1. Thermal annealing influence on resistance and sensitivity to CO of SnO_2 thin films (T_{aneal}=600°C)

Fig.2. Influence of thermal annealing on ratio Sn/SnO in SnO_2 thin films ($T_{отж}$=600°C; T_{pyr} (^{o}C): 1-500; 2-550;3-450)

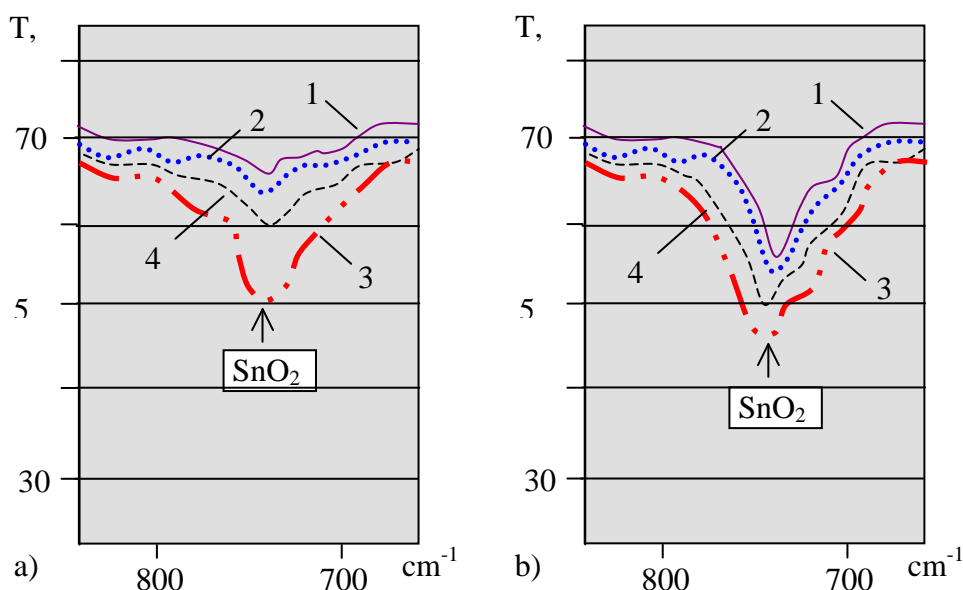
Fig.3. IR transmission spectra of SnO_2/Si, deposited at T_{pyr}(^{o}C): 1-400; 2-450; 3-500; 4-550. (a) -before and (b) after annealing at T=600°C during 10 minutes.

increasing but further it is more advisable to use plasma treatment, which is carried out at room temperature and, as a result, negative influence of high temperatures (enhancing degradation effects) on already ready TFGS chips will be excluded.

2.2. Influence of doping on gas sensitivity and selectivity of tin dioxide thin films

In Fig.4 there are presented results of experiments on SnO2 thin films doped with Pd. Here we had used different modes of doping-bulk, surface and combined (simultaneously bulk and surface). Simple bulk doping of tin dioxide with Pd (curve 2) leads to increase of the resistance of films by order but the growth of sensitivity S to 4vol.% CO in air is not very significant. We connect this with consistence of deposited films. Films obtained by means of

spray pyrolysis method, are continuous (i.e. are not porous) and, as result, atoms Pd introduced in the bulk of film do not participate in the chemosorptional processes on the film surface. So, in this case only atoms of Pd positioned on the film surface can participate in the reaction of catalytic oxidation of CO, giving contribution to sensitivity growth. As one can see from Fig.4 this contribution is sufficiently small – only two times growth of *S* and practically no any shift of temparature maximum of gas sensitivity in the field of lower temperature, although it was expected.
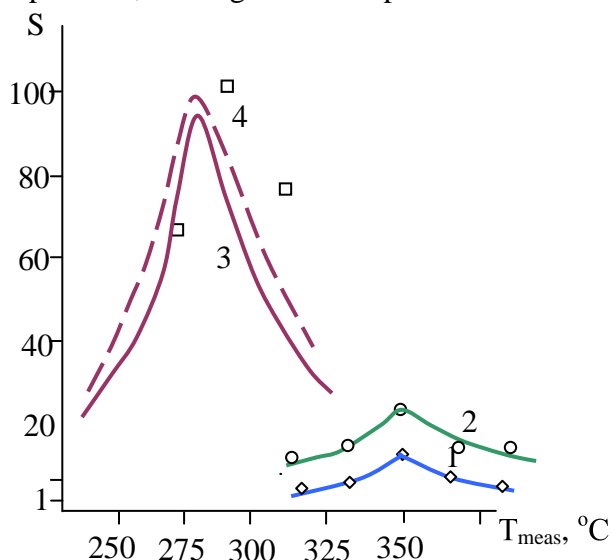

Fig.4. Dependence $S=f(T_{meas})$ of SnO_2 thin films:
1-undoped; 2-bulk Pd doped; 3-surface Pd doped and 4- combined (bulk and surface) doped (4).

Utilization of surface doping has allowed increasing of the sensitivity by order (curve 3, Fig.4) and shifting of S_{max} from 350^oC to 270^oC. However, in spite of achieved progress in sensitivity growth and operating temperature decreasing, such mode of doping also is not ideal because at the long term exploitation of sensors at elevated (working) temperatures the diffusion of atoms of Pd, concentrated on the folm surface, inside the film will be observed. As a result, we can expect the degradation of gas sensitive properties and alteration of operational regimes.

Proceeding from that we had used the combined - bulk and surface-doping of SnO_2 thin films, which allows providing of high sensitivity of the obtained films, decreasing of opera-tional temperatures and maintaining of the gas sensitive characteristics on the required level during long time (curve 4, Fig.4). It is achieved by the presence of sufficient amount of Pd in the bulk of film, which will prohibit the Pd atoms diffusion from surface to bulk.

Conclusion

Carried out study has shown that oxygen plasma treatment can be successfully used for improvement of gas sensitive properties of TFGS fabricated through group technology of microelectronics. Further increasing of gas sensitivity to CO and decreasing of operational temperatures of TFGS can be achieved by means of combination of bulk and surface doping of tin dioxide films in the process of their deposition by spray pyrolysis method.

References

[1] V.Brinzari, S.Dmitriev, G.Korotchenkov, *Proceedings of the 9th Intern. Confer. "Transducers`97",* Chicago, USA, June 16-19, 1997, pp.983-986
[2] S. Dmitriev V.Brynzari, G.Korotchenkov. The Second Intern. Conf. on Ecological Chemistry, Abstract Book, October 11-12, 2002, Chisinau, Republic of Moldova, p.332
[3] S.Dmitriev, V.Brinzari, G.Korotchenkov, *The 6th Intern. Meetings on Chemical Sensors,* Gaithersburg, MD, USA, July 22-25, 1996, p.268

SnO$_2$ THIN FILM PARAMETER INFLUENCE ON GAS SENSITIVE CHARACTERISTICS

S. Dmitriev[1], V. Brynzari[2], G. Korotchenkov[2]

[1]Center of Applied and Environmental Chemistry, Moldova State University,
60 Mateevich Str., Chisinau, 2009, Moldova
[2]Microelectronics Laboratory, Technical University of Moldova, 168 Blv. Stefan cel Mare,
Chisinau, 2004, Moldova

Abstract

In this report we present results of investigation of influence of the parameters of SnO$_2$ thin film on their gas sensitive properties. SnO$_2$ films were deposited by spray pyrolysis method.

The influence of technologic parameters on concentration of free electrons n, stoichiometry, thickness d and gas sensitivity $S=R_{gas}/R_{air}$ was investigated by means of electrophysical, IR-spectroscopy and SIMS measurements. It was established that optimal spray solution's composition is 0.2M, which allows depositing of SnO$_2$ films with required parameters: n-10^{18}-10^{19} cm-3, **R**=10^5-10^6 and **S**>10 correspondently. Obtained results on gas sensitivity are compared with results of theoretical considerations.

Introduction

As follows from the model ideas about thin film gas sensors (TFGS), developed in [1], for the reaching of maximal gas sensitivity SnO$_2$ thin films should have low electron concentration *n* and their thickness should not exceed the value of d=100nm. Both characteristics of these thin films will depend on the technological conditions of film obtaining.

Proceeding from the established task to develop low-cost and low power consuming technology of TFGS manufacturing method of spray pyrolysis deposition was used for formation thin film gas sensitive elements. In this case, the key technology parameters, influencing the formation and electrophysical (n, R) and geometrical (d) parameters of tin dioxide films are: pyrolysis temperature T$_{pyr}$ and sprayed solution composition.

In its turn, electrophysical and geometrical parameters of metal oxide film determine gas sensitive characteristics of spray deposited thin tin dioxide films.

In this connection, the next consequence is considered in the frame of the given report: deposition technology parameters $\Rightarrow$ SnO$_2$ thin film parameters $\Rightarrow$ gas sensitive characteristics.

Experiment

Thin SnO$_2$ films were obtained through spray pyrolysis method (SPM) [1]. SnO$_2$ films were deposited from a starting solution of tin chloride pentahydrate (SnCl$_4$·5H$_2$O) in ethanol or deionized water on the alumna ceramic substrates. The content of SnCl$_4$·5H$_2$O in solution was

varied in a range (0.1-1.0)M. Deposition temperature was in the range 400-550°C. Gas sensitivity was determined as ratio of SnO_2 film resistance in the presence of gas impurity in atmosphere (CO,CH_4, H_2, etc) and in the pure air ($S=R_{gas}/R_{air}$).

Values of R were determined by Van der Paw method and concentration of charge carriers from Hall measurements. SIMS and IR-spectroscopy were used to control stoichiometry of deposited thin SnO_2 films.

Results of study

Fig.1 presents results of experiments carried out for optimization of sprayed solution composition for obtaining of films with required resistance 10^5-10^6 Ohm. It was found that optimal concentration of $SnCl_4 \cdot 5H_2O$ in both alcohol and water solution should amount 0.2M.
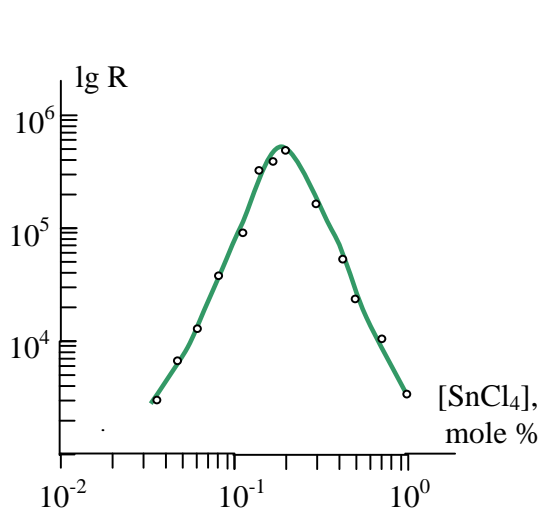

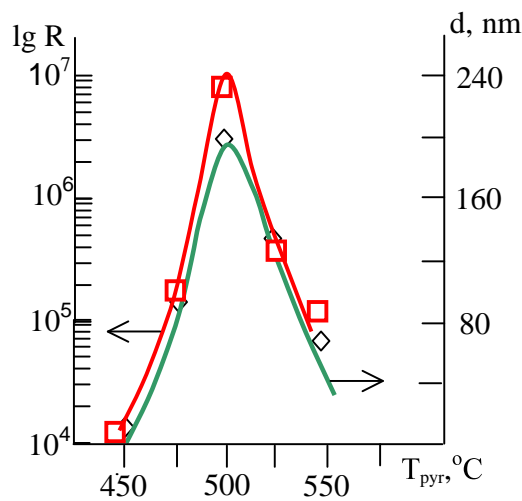Fig.1. Dependence of R on mole concentration of $SnCl_4$ in ethylic alcohol solution

Fig.2. Dependences d=f(T_{pyr}) and R=f(T_{pyr}) for SnO_2 films deposited

Fig.2 shows the influence of deposition temperature on thickness and resistance of tin dioxide films deposited from alcohol solution. One can see that the maximum for both parameters is observed at T_{pyr}=500°C. Apparently this temperature is optimal for providing activation energy of pyrolysis reaction. Deviation from this temperature leads to the decreasing of reaction rate and reaction output (in case if T<T_{pyr}) and re-evaporation of atoms and molecules from the surface of growing film (T>T_{pyr}) and, as result, decreasing of the thickness of deposited layer.

As to dependence R=f(T_{pyr}) the obtained result–dependence trend and maximum presence–is rather unexpected. As follows from the measured dependence R=f(d) (Fig.3) we should expect at the deviation from T_{pyr}=500°C decreasing of d and, correspondingly, growth of R value. However, we observe an opposite situation - value of R is also decreasing. Explaining this fact we supposed that not only reaction output is decreasing but also the alteration of phase composition of SnO_2 in direction of increasing of conducting Sn and SnO phases takes place. The reasons for that are the following: at T<500°C pyrolysis reaction do not proceed in full degree

and the amount of non-reacted atoms of Sn is increasing. Besides that, the amount of intermediate products of pyrolysis reaction (Cl atoms) is also increasing. In accordance with [2] the amount of Cl atoms, acting as donor and, as a result, decreasing value of R, is increasing from 10^{-4} at.% to some atomic % at the T_{pyr} changing from 490 to $380^{o}C$. At the temperatures T_{pyr} higher than $500^{o}C$ the processes of re-evaporation of anions are reinforced [4] and this leads to the growth of Sn and SnO content in the SnO_2 films and, as a result, decreasing of R.

Our further investigation of SIMS and IR spectrum has confirmed the correctness of the given explanation. One can see (Fig.4) that ratio Sn/SnO is minimal at $T_{pyr}=500^{o}C$ that corresponds to the greatest stoichiometry of SnO_2 film composition. The resistance of tin dioxide films is maximal and its value is in the range 10^{5}-10^{6} Ohm corresponding to requirements for TFGS.

Fig.3. Dependence R=f(d) for SnO_2 films deposited at T_{pyr} (^{o}C): 1-450; 2-500; 3-550

Results of IR spectroscopy (Fig5) also confirms our conclusion, demonstrating sharp growth of adsorption at λ characteristic of SnO_2 in the case of films deposited at $T_{pyr}=500^{o}C$.
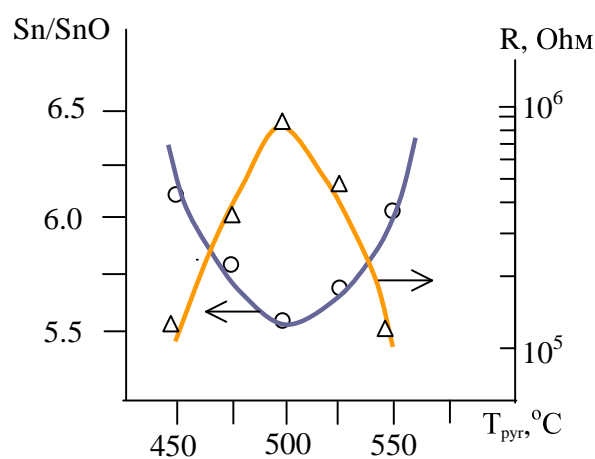

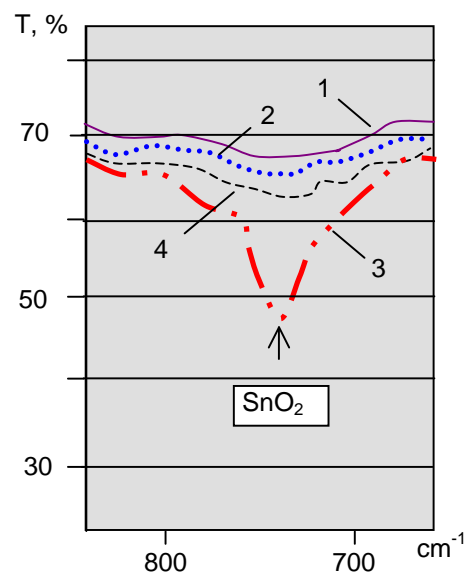Fig.4. Influence of T_{pyr} on phase composition of SnO_2 thin films

Fig.5. IR transmission spectra of SnO_2/Si, deposited at $T_{pyr}(^{\circ}C)$: 1-400; 2-450; 3-500; 4-550.

Hall measurements have shown that in SnO_2 thin films the dependence of concentration of charge carriers on T_{pyr} demonstrates also non-monotonic character with minimum at $T_{pyr}=500^oC$. (better stoichiometry). Values of n are amounted $6.9 \cdot 10^{18}$ cm^{-3} (alcohol solution) and $3.4 \cdot 10^{17}$ cm^{-3} (water solution) correspondingly.

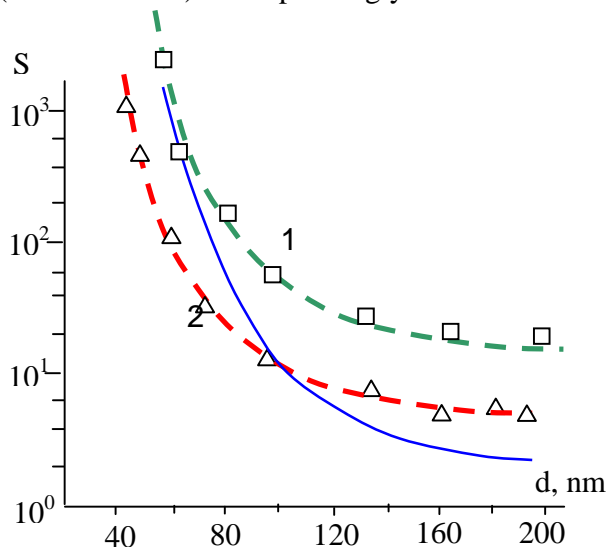Fig.6 Dependence S=f(d) of thin SnO_2 films. ($T_{pyr}=450°C$; $T_m=350°C$ (solid line-modeling, dotted line-experiment 1-n=10^{18} cm^{-3}; 2- n=10^{19} cm^{-3}).

Fig.6 demonstrates dependence of tin dioxide thin film's gas sensitivity to 4 vol.%CO in air for films with different value of n. For comparison, the theoretic-cally calculated curve is also given. One can see that very good coincidence between experimental curves and curve obtained by the results of modeling [5] is observed.

Another conclusion which could be made from these results is that gas sensitivity is decreasing considerably, aspiring to a unity value of sensitivity, at thicknesses greater than 100 nm. The latter means that films with thicknesses, exceeding value of 100 nm are not acceptable for creation of TFGS. At the thicknesses less than 100 nm the sharp growth of S value is observed, however, at the thicknesses less than 30 nm the high non-uniformity of the parameters of deposited films is observed and such films also become unacceptable for TFGS manufacturing.

Conclusions

It was established that thin SnO_2 films deposited by chemical spray pyrolysis method possess high sensitivity to CO (S>10 rel.units) at the thicknesses in the range 30-100 nm and charge carrier concentrations in the range 10^{17}-10^{18} cm^{-3}. Thin tin dioxide films produced through spray pyrolysis can be used successfully for manufacturing of TFGS through group technology of microelectronics.

References

[1] S.Dmitriev, V.Brynzari, G. Korotchenkov, *The 6th Intern. Meeting on Chemical Sensors*, Gaithersburg, Md., USA, July 22-25, 1996, P.268
[2] T.M. Ven, K.Huang, M.Cheu et al.. Thin Solid Films - 1988. - V.158. - P.69-8O.
[3] K.L. Chopra et al.. Phys. of Thin Films. V.12. - N.Y.:Academic Press, 1982. - P.168-232.
[4] V. Vasu, A. Subrahmanyam. Thin Solid Films - 199O. - V.193/194. - P.973-98O.
[5] V.Brynzari, S.Dmitriev, G. Korotchenkov, *Proceedings of the 9th Intern. Conf. on Solid State Sensors and Actuators, Chicago, USA (June 16-19, 1997), IEEE, 1997*

NONLINEAR EXCITATIONS IN CARBON NANOTUBE

A.D. Suprun[1], Yu.I. Prylutskyy[2], I.I. Geru[3], O.V. Ogloblya[2], P. Scharff[4]

*Kiev National Shevchenko University, Departments of [1]Physics and [2]Biophysics,
Vladimirskaya Str., 64, 01033 Kiev, Ukraine
[3]Moldova State University, Chisinau, Republic of Moldova
[4]Technical University of Ilmenau, Institute of Physics, D-98684 Ilmenau, Germany*

Abstract

The possibility of realization of both the cubic and the other power-mode and polynomial types of non-linearity in the Shroedinger equation that describes the quantum excitations for n-dimensional media is shown. This problem is first considered in detail for such system as the single-walled carbon nanotube. The stable solitons are obtained analytically.

1. Introduction

During the electronic excitations in media with different degree of order, relatively stable formations such as solitons appear [1-2]. In contrast to the related excitations of excitons, solitons are more real objects. This is connected with the fact that the excitons leave out of account the influence of electronic excitation on the change in interaction between the structural elements of the medium. A similar change leads to the local deformation inside the lattice. A study of soliton excitations in the novel materials such as the single-walled carbon nanotubes (SWCNT) [3-5] is issue of the day, especially as they are connected also with configurational (conformational) changes in the nanotubes. A change in their form can lead to the appearance of heterojunctions [6-7], which are very important to nanoelectronics.

2. Functional for the electronic excitations

Depending on symmetry, the SWCNT can be metals or semiconductors [2-3]. Therefore the corresponding functional for the electronic excitations in the semiconducting SWCNT takes the form:

$$H(\{A\}) = \sum_{\overline{n},\overline{m}}{}' \left(w_{\overline{n},\overline{m}} + D_{\overline{n},\overline{m}} \cdot \left| A_{\overline{n},\overline{m}} \right|^2 + \sum_{\overline{k},\overline{l}}{}' M_{\overline{k},\overline{l}} \cdot A_{\overline{n},\overline{m}}^* \cdot A_{\overline{n}+\overline{k},\overline{m}+\overline{l}} \right). \qquad (1)$$

Here $\overline{n}, \overline{m}, \overline{k}, \overline{l}$ are the vectors, which indicate the positions of carbon atoms in the nanotube (vectors of lattice). Primes in sum on $\overline{n}, \overline{m}$ mean that $\overline{n} \neq \overline{m}$, and in sum on $\overline{k}, \overline{l}$ mean that these vectors are not equal to zero simultaneously. Factor $w_{\overline{n},\overline{m}}$ describes the pair interaction between the structural elements of the considered space (here carbon atoms) in the absence of excitation ($A_{\overline{n},\overline{m}} = 0$). Factor $D_{\overline{n},\overline{m}}$ describes changes in interaction between carbon atoms in the presence of excitation ($A_{\overline{n},\overline{m}} \neq 0$) and fixed locations of charge carriers (electron in the knot $\overline{n}$ and hole in the knot $\overline{m}$). Factor $M_{\overline{k},\overline{l}}$ represents the additional change in interaction between carbon atoms, but connected with the movement of carri-

ers in the space. $A_{\bar{n},\bar{m}}$ is the wave function which depends on the variables $\bar{n}$ and $\bar{m}$, and determines the distribution of the excitation of the system in the space (nanotube) and in the time. It satisfies the normalization condition:

$$\sum_{\bar{n},\bar{m}} \left| A_{\bar{n},\bar{m}} \right|^2 = 1. \tag{2}$$

Assuming the considered space to be uniform (in this case it indicates the absence of impurities or other defects), it is possible to consider that all enumerated factors in functional (1) depend only on differences in the pairs of their indices. Then functional (1) is reduced to the form

$$H(\{A\}) = \sum_{\bar{N}} \sum_{\bar{n}(\neq 0)} \left(w_{\bar{n}} + D_{\bar{n}} \cdot \left| A_{\bar{N},\bar{n}} \right|^2 + \sum_{\bar{L},\bar{k}}{}' M_{\bar{L},\bar{k}} \cdot A_{\bar{N},\bar{n}}^* \cdot A_{\bar{N}+\bar{L},\bar{n}+\bar{k}} \right), \tag{3}$$

where $\bar{N} = \bar{n} + \bar{m}$ is the doubled value of the geometric center between the carriers (for the difference $\bar{n} - \bar{m}$ is made the replacement simply on $\bar{n}$). Analogously, for the indices $\bar{k}$ and $\bar{l}$: $\bar{L} = \bar{k} + \bar{l}$, and $\bar{k} - \bar{l}$ we have substituted simply on $\bar{k}$. Prime in the sign of sum on $\bar{L}, \bar{k}$ means that these indices cannot be equal to zero simultaneously. If we temporarily designate equilibrium values of variables $\bar{n}, \bar{N}, \bar{k}, \bar{L}$ in the absence of excitation ($A_{\bar{N},\bar{n}} = 0$) through $\bar{n}_0, \bar{N}_0, \bar{k}_0, \bar{L}_0$, then in the presence of excitation ($A_{\bar{N},\bar{n}} \neq 0$) functional (3) will take the form:

$$H(\{A\}) = \sum_{\bar{N}_0} \sum_{\bar{n}_0(\neq 0)} \left(w_{\bar{n}_0 + \bar{\xi}_{\bar{n}_0,\bar{N}_0}} + D_{\bar{n}_0 + \bar{\xi}_{\bar{n}_0,\bar{N}_0}} \left| A_{\bar{N}_0,\bar{n}_0} \right|^2 + \right.$$

$$\left. \sum_{\bar{L}_0,\bar{k}_0}{}' M_{\bar{L}_0,\bar{k}_0} A_{\bar{N}_0,\bar{n}_0}^* A_{\bar{N}_0+\bar{L}_0,\bar{n}_0+\bar{k}_0} \right). \tag{4}$$

Additional displacements $\bar{\xi}_{\bar{n}_0,\bar{N}_0}$ are determined by the presence of excitation. Expanding w and D in series on the components of small displacements $\xi^{\alpha}_{\bar{n}_0,\bar{N}_0}$ (here $\alpha=1,2$), and also by rejecting then indices "0" at the variables $\bar{n}, \bar{N}, \bar{k}, \bar{L}$ (for the purpose of simplification in the notation), we will obtain:

$$w_{\bar{n}+\bar{\xi}_{\bar{n},\bar{N}}} = w_{\bar{n}} + \sum_{\alpha,\beta} U^{\alpha,\beta}_{\bar{n}} \cdot \xi^{\alpha}_{\bar{n},\bar{N}} \cdot \xi^{\beta}_{\bar{n},\bar{N}}, \tag{5}$$

$$D_{\bar{n}+\bar{\xi}_{\bar{n},\bar{N}}} = D_{\bar{n}} + \sum_{\alpha} D^{\alpha}_{\bar{n}} \cdot \xi^{\alpha}_{\bar{n},\bar{N}}. \tag{6}$$

Here $U^{\alpha,\beta}_{\bar{n}}$ and $D^{\alpha}_{\bar{n}}$ are the corresponding force "constants", which are, generally speaking, functions from the distance $\bar{n}$ between the carriers. Substituting (5) and (6) in (4) and minimizing the obtained expression on $\xi^{\alpha}_{\bar{n},\bar{N}}$, we will obtain

$$\xi^{\alpha}_{\overline{n},N} = -\frac{1}{2}\sum_{\beta} \widetilde{U}^{\alpha,\beta}_{\overline{n}} \, D^{\beta}_{\overline{n}} \left| A_{\overline{N},\overline{n}} \right|^{2},$$

(7)

where $\widetilde{U}^{\alpha,\beta}_{\overline{n}}$ is the matrix, reverse with respect to $U^{\alpha,\beta}_{\overline{n}}$ on the superscripts. Substitution of (7) in the functional, which was minimized on $\xi^{\alpha}_{\overline{n},N}$ (obtained of (4) by substitutions (5), (6)) gives the form

$$H(\{A\}) = W + \sum_{\overline{N}}\sum_{\overline{n}(\neq 0)} \left(D_{\overline{n}}\left|A_{\overline{N},\overline{n}}\right|^{2} - \frac{1}{2}G_{\overline{n}}\left|A_{\overline{N},\overline{n}}\right|^{4} + \sum_{\overline{L},\overline{k}}{}' M_{\overline{L},\overline{k}} A^{*}_{\overline{N},\overline{n}} A_{\overline{N}+\overline{L},\overline{n}+\overline{k}} \right),$$

(8)

where $W \equiv \sum_{\overline{N}}\sum_{\overline{n}(\neq 0)} w_{\overline{n}}$ is the energy of the not excited medium and

$G_{\overline{n}} = \frac{1}{2}\sum_{\alpha,\beta} \widetilde{U}^{\alpha,\beta}_{\overline{n}} D^{\alpha}_{\overline{n}} D^{\beta}_{\overline{n}}$. In expression (6) it is possible to consider the following terms of expansion on $\xi^{\alpha}_{\overline{n},\overline{N}}$

$$D_{\overline{n}+\overline{\xi}_{\overline{n},\overline{N}}} = D_{\overline{n}} + \sum_{\alpha} D^{\alpha}_{\overline{n}} \cdot \xi^{\alpha}_{\overline{n},N} + \sum_{\alpha,\beta} D^{\alpha,\beta}_{\overline{n}} \cdot \xi^{\alpha}_{\overline{n},N} \cdot \xi^{\beta}_{\overline{n},N},$$

(9)

where $D^{\alpha,\beta}_{\overline{n}}$ is the force "constant", which makes sense, analogous to $U^{\alpha,\beta}_{\overline{n}}$ "constant". For example, this can be important to maximal precision of the contributions of the second order on $\xi^{\alpha}_{\overline{n},\overline{N}}$. Under the condition $D^{\alpha,\beta}_{\overline{n}} << U^{\alpha,\beta}_{\overline{n}}$, the corresponding minimization leads to the following degree on $\left|A_{\overline{N},\overline{n}}\right|^{2}$

$$H(\{A\}) = W + \sum_{\overline{N}}\sum_{\overline{n}(\neq 0)} \left(D_{\overline{n}}\left|A_{\overline{N},\overline{n}}\right|^{2} - \frac{1}{2}G_{\overline{n}}\left|A_{\overline{N},\overline{n}}\right|^{4} + \frac{1}{3}S_{\overline{n}}\left|A_{\overline{N},\overline{n}}\right|^{6} + \right.$$

$$\left. \sum_{\overline{L},\overline{k}}{}' M_{\overline{L},\overline{k}} A^{*}_{\overline{N},\overline{n}} A_{\overline{N}+\overline{L},\overline{n}+\overline{k}} \right),$$

(10)

where $S_{\overline{n}} = \sum_{\alpha,\beta} 3D^{\alpha,\beta}_{\overline{n}} g^{\alpha}_{\overline{n}} g^{\beta}_{\overline{n}}$ and $g^{\alpha}_{\overline{n}} = \sum_{\beta}\frac{1}{2}\widetilde{U}^{\alpha,\beta}_{\overline{n}}D^{\beta}_{\overline{n}}$. We will further work with this functional, since functional (8) is one of its special cases.

For final obtaining of a strict functional of soliton let us remind that in the sum on $\overline{L}$ and $\overline{k}$ these indices are not equal to zero simultaneously. Choosing separately $\overline{L} = 0, \overline{k} \neq 0$ terms, and $\overline{L} \neq 0, \overline{k} = 0$ terms, and rejecting all the remaining as negligible, and also representing the function $A_{\overline{N},\overline{n}}$ in the form of product $A_{\overline{N},\overline{n}} = \varphi_{\overline{N}} \psi_{\overline{n}}$, transforms the considered functional transforms to the form:

$$H(\{\varphi\},\{\psi\}) = W + \sum_{\overline{N}}\left(\left|\varphi_{\overline{N}}\right|^2 \sum_{\overline{n}\neq 0}\left[\sum_{\overline{k}\neq 0} M_{o,\overline{k}}\,\psi_{\overline{n}}^*\,\psi_{\overline{n}+\overline{k}} + D_{\overline{n}}\left|\psi_{\overline{n}}\right|^2\right] + \sum_{\overline{L}} M_{\overline{L},0}\,\varphi_{\overline{N}}^*\,\varphi_{\overline{N}+\overline{L}}\right) -$$

$$\sum_{\overline{N}}\left(\frac{1}{2}\left|\varphi_{\overline{N}}\right|^4 \sum_{\overline{n}} G_{\overline{n}}\left|\psi_{\overline{n}}\right|^4 - \frac{1}{3}\left|\varphi_{\overline{N}}\right|^6 \sum_{\overline{n}} S_{\overline{n}}\left|\psi_{\overline{n}}\right|^6\right). \qquad (11)$$

In this functional, in the term with the sum on $\overline{L}$, the normalization condition is taken into account

$$\sum_{\overline{n}}\left|\psi_{\overline{n}}\right|^2 = 1, \qquad (12)$$

which follows from condition (2). Since the function $\psi_{\overline{n}}$ describes the internal state of the system of the excited carriers (electron and hole), and factor $D_{\overline{n}}$ actually is reduced to screened Coulomb interaction between them, we can consider the function $\psi_{\overline{n}}$ as eigenfunction relative to the equation

$$\sum_{\overline{k}\neq 0} M_{o,\overline{k}}\,\psi_{\overline{n}+\overline{k}} + D_{\overline{n}}\,\psi_{\overline{n}} = \mathcal{E}\,\psi_{\overline{n}}, \qquad (13)$$

where $\mathcal{E}$ is the eigenvalue of energy. It is not difficult to obtain, in accordance with (12) and

(13), $\displaystyle\sum_{\overline{n}\neq 0}\left(\sum_{\overline{k}\neq 0} M_{o,\overline{k}}\,\psi_{\overline{n}}^*\,\psi_{\overline{n}+\overline{k}} + D_{\overline{n}}\left|\psi_{\overline{n}}\right|^2\right) = \mathcal{E}$. Taking into account this, and also the normalization condition

$$\sum_{\overline{N}}\left|\varphi_{\overline{N}}\right|^2 = 1, \qquad (14)$$

we will obtain soliton functional in the common form

$$H(\{\varphi\}) = W + \mathcal{E} + \sum_{\overline{N}}\left(\varphi_{\overline{N}}^* \sum_{\overline{L}\neq 0} M_{\overline{L},0}\,\varphi_{\overline{N}+\overline{L}} - \frac{1}{2} g\left|\varphi_{\overline{N}}\right|^4 + \frac{1}{3}\sigma\left|\varphi_{\overline{N}}\right|^6\right), \qquad (15)$$

where it is marked: $g = \sum_{\overline{n}} G_{\overline{n}}\left|\psi_{\overline{n}}\right|^4$ and $\sigma = \sum_{\overline{n}} S_{\overline{n}}\left|\psi_{\overline{n}}\right|^6$.

3. Soliton equation and its solutions

Functional (15) is considered as the Hamiltonian system with the pairs of the canonically conjugated variables $\varphi_{\overline{N}}$ and $p_{\overline{N}} = i\hbar\,\varphi_{\overline{N}}^*$, to which it is possible to apply Hamilton's equations:

$$\frac{\partial\varphi_{\overline{N}}}{\partial t} = \frac{\partial H}{\partial p_{\overline{N}}} \equiv \frac{1}{i\hbar}\frac{\partial H}{\partial\varphi_{\overline{N}}^*}; \qquad \frac{\partial p_{\overline{N}}}{\partial t} \equiv i\hbar\frac{\partial\varphi_{\overline{N}}^*}{\partial t} = -\frac{\partial H}{\partial\varphi_{\overline{N}}}. \qquad (16)$$

Substituting in these equations Hamiltonian (15) and taking into account that $M_{\overline{L},0} \equiv M_{-\overline{L},0}$ (since this value depends on $\left|\overline{L}\right|$) we will obtain two complexly conjugated equations. Therefore it is quite enough to consider only one of them:

$$i\hbar\frac{\partial\varphi_{\overline{N}}}{\partial t}=\sum_{\overline{L}>0}M_{\overline{L},0}\cdot\left(\varphi_{\overline{N}+\overline{L}}+\varphi_{\overline{N}-\overline{L}}\right)-g\left|\varphi_{\overline{N}}\right|^{2}\varphi_{\overline{N}}+\sigma\left|\varphi_{\overline{N}}\right|^{4}\varphi_{\overline{N}}. \qquad (17)$$

Generally speaking, this is a soliton equation, formulated in the finite differences. But it is more known in the continuous approximation, when set $\overline{N}\equiv\overline{r}$, where $\overline{r}$ is the vector, which takes the continuum of values. This transition is accomplished by the expansion

$$\sum_{\overline{L}>0}M_{\overline{L},0}\cdot\left(\varphi_{\overline{N}+\overline{L}}+\varphi_{\overline{N}-\overline{L}}\right)\Rightarrow\sum_{\overline{L}>0}M_{\overline{L},0}\cdot\left(2\varphi(\overline{r})+\left|\overline{L}\cdot\nabla\right|^{2}\varphi(\overline{r})\right)\equiv$$
$$M\varphi(\overline{r})+\sum_{\alpha}\sum_{L_{\alpha}>0}\mu_{L_{\alpha}}L_{\alpha}^{2}\frac{\partial^{2}\varphi(\overline{r})}{\partial x_{\alpha}^{2}}, \qquad (18)$$

where $M\equiv\sum_{\overline{L}>0}2M_{\overline{L},0}$, and $\mu_{L_{\alpha}}$ is reduced to the following identity in the two-dimensional case: $\mu_{L_{\alpha}}\equiv\sum_{L_{\beta}}M_{L_{\alpha},L_{\beta};0}$ $(\alpha\neq\beta)$. It is not difficult to see that here it is possible to intro-

duce the effective mass tensor: $\dfrac{\hbar^{2}}{2m_{\alpha}}\equiv-\sum_{L_{\alpha}>0}\mu_{L_{\alpha}}L_{\alpha}^{2}$. Then equation (17) in the continu-

ous approximation is reduced to the following:

$$i\hbar\frac{\partial\varphi}{\partial t}+\sum_{\alpha}\frac{\hbar^{2}}{2m_{\alpha}}\frac{\partial^{2}\varphi}{\partial x_{\alpha}^{2}}-M\varphi+g\left|\varphi\right|^{2}\varphi-\sigma\left|\varphi\right|^{4}\varphi=0. \qquad (19)$$

In certain cases the symmetry of matrix elements $M_{\overline{L},0}$ is such that the effective mass tensor becomes isotropic. But even if not, then, in the last equation, always (if M, g and s are constants) it is possible to carry out scale conversion, so that it is reduced to the classical soliton equation:

$$i\hbar\frac{\partial\varphi}{\partial t}+\frac{\hbar^{2}}{2m}\Delta\varphi-M\varphi+g\left|\varphi\right|^{2}\varphi-\sigma\left|\varphi\right|^{4}\varphi=0. \qquad (20)$$

By simple amplitude-scale conversions it is possible to transform this equation to

$$i\frac{\partial\Phi}{\partial\tau}+\frac{\partial^{2}\Phi}{\partial x^{2}}+\frac{\partial^{2}\Phi}{\partial y^{2}}+f_{0}\Phi+f_{1}\left|\Phi\right|^{2}\Phi+f_{2}\left|\Phi\right|^{4}\Phi=0, \qquad (21)$$

where variables x and y are described by the dimensionless quantities in the units of the dimensional parameter: $x_{0}=\dfrac{\hbar}{|g|}\cdot\sqrt{\dfrac{|\sigma|}{2m}}$. All other values Φ, τ, f_{0}, f_{1} and f_{2} are determined

by the specific relations: $\Phi=A\cdot\varphi$; $t=\tau\cdot t_{0}$; $A=\sqrt{\dfrac{|g|}{|\sigma|}}$; $t_{0}=\hbar\cdot\dfrac{|\sigma|}{|g|^{2}}$; $f_{0}=-\dfrac{M\cdot|\sigma|}{|g|^{2}}$;

$f_{1}=\text{sign}(g)$; $f_{2}=-\text{sign}(\sigma)$. Hyperbolic type generalized solitons first of all are here realized. They can be attributed to the traditional solutions. They depend on the variable of common form $z=a\cdot x+b\cdot y+c$ and are localized in the direction perpendicular to $a\cdot x+b\cdot y+c=\text{const}$ line. These solutions take the form:

$$\Phi(\tau, z) = B \cdot \frac{\exp(i \cdot (q \cdot z - \omega \cdot \tau))}{\sqrt{1 + \beta \cdot ch(\alpha \cdot (z - 2q\tau))}} . \tag{22}$$

Without the limitation of generality variable z lets us select in the simplest form: $z = \frac{x + y}{\sqrt{2}}$. Then by using solution (22) in equation (21) we obtain the following relations for the parameters B, q, ω, β and α, in which this equation becomes identity:

$\omega = q^2 - f_0 - \frac{\alpha^2}{4}$; $\beta = \sqrt{1 + \frac{4}{3}\frac{f_2}{f_1^2} \cdot \alpha^2}$; $B^2 = \frac{\alpha^2}{f_1}$. As one can see, there are three these relations for five parameters. In this case the relations have a form of dependence on the parameters B, β, and ω on the parameter α. Furthermore, the parameter ω depends also on the parameter q (so-called dispersion dependence). The parameter α is determined by the normalization condition (14), and is equal to:

$$\alpha = \pm \frac{f_1 \cdot th\left(\frac{1}{2}\sqrt{-\frac{f_2}{3}}\right)}{\sqrt{-\frac{f_2}{3} \cdot \left(1 + th^2\left(\frac{1}{2}\sqrt{-\frac{f_2}{3}}\right)\right)}} . \tag{23}$$

From the condition $B^2 = \frac{\alpha^2}{f_1}$ follows that the considered type of solitons is realized only in the case of $f_1 > 0$, i.e. actually at $f_1 = 1$ (taking into account the following determination: $f_1 = sign(g)$). This means that hyperbolic type solitons are characteristic only of the systems, which have $g > 0$. In this case σ can have any sign, since the parameter f_2 can take value both 1 and -1.

Besides this solution Lorenz type solitons are realized. The character of these solitons is localized in all directions

$$\varphi(\tau, \vec{r}) = B \cdot \frac{\exp(i \cdot (\vec{q} \cdot \vec{r} - \omega \cdot \tau))}{\sqrt{1 + \beta \cdot |\vec{r} - 2 \cdot \tau \cdot \vec{q}|^2}} , \tag{24}$$

where $\vec{q} = (q_1, q_2)$ and $\vec{r} = (x, y)$. In this case for the parameters B, $\vec{q}$, β and ω we obtain also three relations

$$\omega(q) = q^2 - f_0; \qquad \beta = 3 \cdot \frac{f_1^2}{f_2}; \qquad B^2 = -3 \cdot \frac{f_1}{f_2} , \tag{25}$$

where it is marked: $q^2 \equiv \left|\vec{q}\right|^2 \equiv q_1^2 + q_2^2$. Here we have $f_1 = -1$ and $f_2 = 1$, i.e. in this case $g < 0$, $\sigma < 0$. However this solution does not satisfy the normalization condition (14). But in this case it is important that condition (2) will be executable. It is possible due to satisfaction of condition (12). Therefore, for the SWCNT, Lorenz solitons, presented in Fig.1, can also be of significant interest.
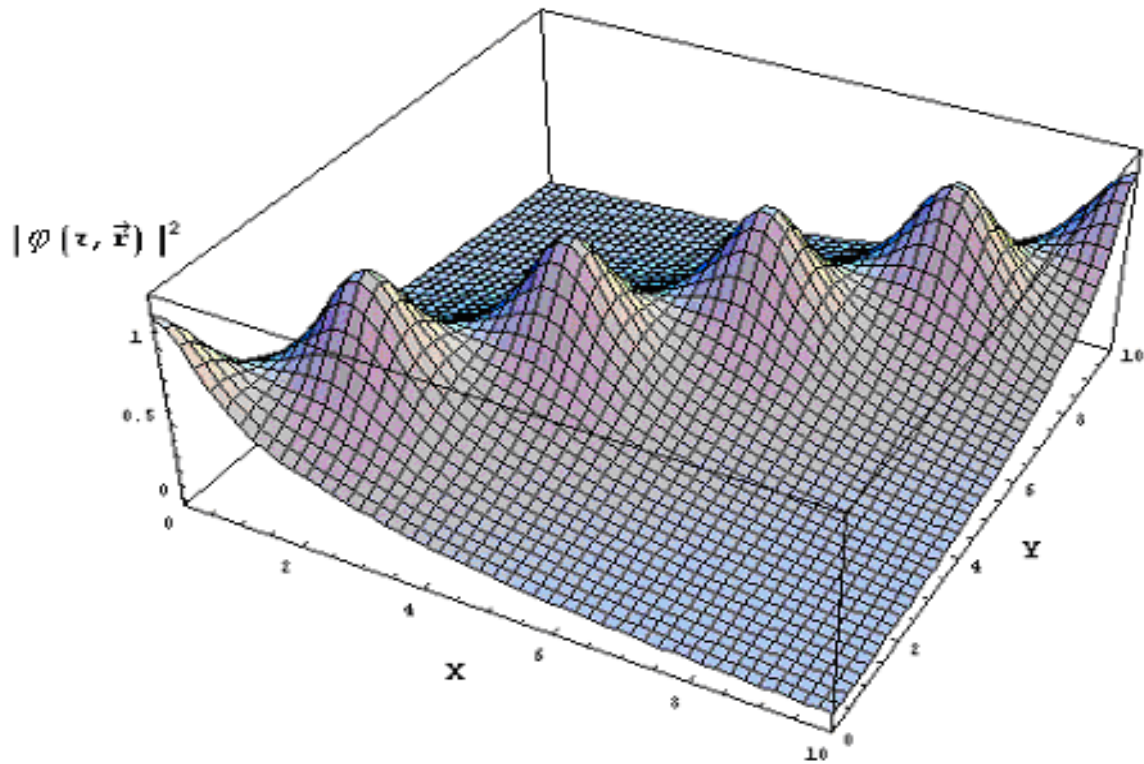

Fig. 1. The image of six consistent Lorenz solitons in the form of joint surface, which is determined by the $\left|\varphi(\tau,\vec{r})\right|^2$ function at the following values of the parameters: $q_1 = q_2 = \overline{0,5}$.

4. Summary

The possibility of the realization of soliton excitations in the single walled carbon nano-tubes with two types of space charge carriers (electron and hole) was considered in this paper. It is shown that the type of the realized soliton depends on the force "constants" $U_{\frac{\alpha,\beta}{n}}$, $D_{\frac{\alpha}{n}}$, determined in formulas (5), (6), and the force "constant" $D_{\frac{\alpha,\beta}{n}}$, determined in formula (9). These force "constants" substantially govern the values and the signs of the parameters g and σ, which determine the type of the realized soliton. It should be noted that these force "constants" determine also the nature of a change in the configuration (conformation) of nano-tubes. Such changes are caused by the appearance of internal stresses in the nanotube, con-

nected with the displacement vector $\xi \frac{\alpha}{n,N}$, determined in (7). In our opinion, the obtained theoretical results can be useful for studying the mechanical and electronic properties of carbon nanotubes.

Acknowledgements

References

[1] M.J. Ablowitz, H. Segur, "Solitons and the Invers Scattering Transform", SIAM, Philadelpia, 1981.

[2] A.D. Suprun, Funct. Mater. 8, 1 (2001).

[3] M.S. Dresselhause, G. Dresselhause, P.C. Eklund, "Science of Fullerenes and Carbon Nanotubes", Academic Press, New York, 1996.

[4] R. Saito, G. Dresselhause, M.S. Dresselhause, "Physical Properties of Carbon Nanotubes", Singapore, Imperial College Press, 1998.

[5] P. Scharff, Carbon 36, 481 (1998).

[6] R. Saito, G. Dresselhause, M.S. Dresselhause, Phys.Rev. B 53, 2044 (1996).

[7] Yu.I. Prylutskyy, O.V. Ogloblya, P.C. Eklund, P. Scharff, Synth. Met.121, 1209 (2001).

ELLIPSOMETRIC STUDIES OF NANOMETRIC CdS AND CdTe FILMS

M. Caraman[1], Ig. Evtodiev[1], E. Cuculescu[1], M. Rusu[2], Iu. Salaoru[2]

[1]*Faculty of Physics, Moldavian State University, Kishinev, Republic of Moldova*
[2]*Faculty of Physics, "Al. I. Cuza", University, Iassy, Romania*

The thickness of the layers CdS and CdTe grown on the Si, Ge, GaAs was determined from the analysis of the polarization ellipse of the reflected light from the surfaces of structures thin layers – substrate. The thermal treatment of the samples CdS-CdTe in the presence of $CdCl_2$ leads to the increasing of the crystalline phase from layers.

Introduction

The modern semiconductor technologies need the samples and multilayer structures with the well determined physical parameters composed by layers of nanometrical thicknesses. The ellipsometry is one of the nondestructive methods used in practice, which the theory of Drude reflection is based on. The performed calculations in many experimental papers [1, 2] demonstrate the possibilities of correct application of Drude equations up to the thicknesses of layers of 50?100 A order, but in some cases up to 5?10 A [3].

The passage of reflected light rays is represented schematically from the surface of the thin layer – substrate structure in fig.1. As the refraction index of the semiconductor materials and dielectric ones is a complex value, the linear polarized light ray obtains elliptical polarization at reflection. The presence of one thin layer of semiconductor or dielectric one on the reflecting surface forms a supplementary phase difference between reflected rays from the external surface and reflected ray from the substrate surface. The state of elliptical polarization is determined univocally with two parameters ψ and Δ [4] which is determined by relations:

Fig.1.

$$tg\psi = \left(\frac{R_p}{R_s} \right)^{1/2} \quad (1)$$

$$\Delta = \delta_p - \delta_s \quad (2)$$

where R_p and R_s are the reflection energetic coefficients, but δ_p and δ_s are the phases of the components p and s of the reflected light from the sample.

The next relation [5] is available in the spectral range of transparence of the thin layer among the Fresnel coefficients of reflection from the surface of structure r_{1p}, r_{1s} and r_{2p}, r_{2s}, the parameters of polarization ellipse Δ and ψ and the thickness d of the layer from the surface:

$$tg\psi \cdot e^{i\Delta} = \frac{r_{1p} + r_{2p}e^{2i\delta}}{1 + r_{1p}r_{2p}e^{-2i\delta}} \cdot \frac{1 + r_{1s}r_{2s}e^{-2i\delta}}{r_{1s} + r_{2s}e^{2i\delta}} \quad (3)$$

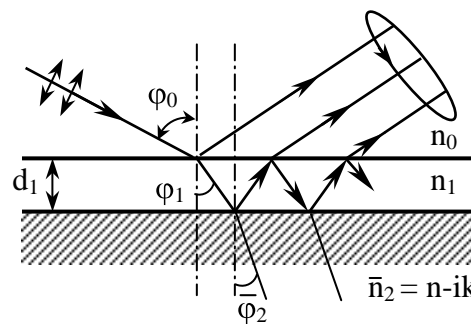The value δ presented with grades is equal to:

$$\delta = \frac{360d}{\lambda}\left(n_1^2 - \sin^2\varphi\right)^{1/2}, \tag{4}$$

where φ is the incident angle of the light ray to the surface of the sample.

The experimental technique and method of researching

The ellipsometrical parameters Δ and ψ were measured by an ellipsometer which optical scheme does not differ principally from the classical model [6] and is represented in fig.2. The wavelengths were selected from the field of transmission of film layer by monochromator MDR-2 from the light beam generated by the Xe lamp (1000 Wt), the thickness and optical constants of which are determined. The monochromatic light beam is polarized by Rochon prism so that the polarization plane of the light makes 45° with respect to the incident plane on the sample. The polarization degree of the reflected light from the surface is analyzed by Glan-Thomson prism and is registered by a selectively amplified photomultiplifier complex FME-51 and adjusted at the modulation frequency of the light beam equal to 325 Hz. Optical scheme is adjusted by He-Ne laser radiation (λ=632 nm).
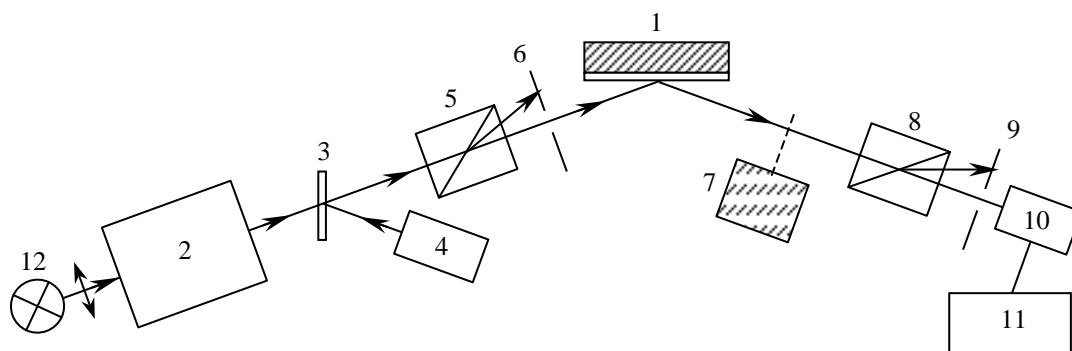

Fig.2. The block-scheme of the ellipsometer. 1 – the sample; 2 – the monochromator MDR-2; 3 – glass plate; 4 – He-Ne laser (LG-52); 5, 8 – Rochon prism; 6, 9 – circular diaphragms; 7 – modulator; 10 – photomultiplifier FME-51; 11 – selective amplifier V6-4.

The samples that are thin layers of CdS deposited on the CdTe substrate were obtained by deposition in the closed volume. The monocrystals of CdS and CdTe grown from the pure spectral components Cd, S and Te were used as the source of vaporization.

The experimental determinations of the refractive index and the thickness of CdS layers that are the components of the CdS-CdTe samples were performed at two wavelengths from the field of optical transparence of the CdS layer. In order to establish the influence of homogeneity of the layer structure of CdS on the optical characteristics, the samples of CdS-CdTe were treated thermally in the presence of $CdCl_2$ during 20 – 30 seconds at the temperature of ≈ 700 K.

Experimental results

As the Fresnel coefficients of reflection and $e^{2i\delta}$ are the complex values then after the selection of real part of equation (3), the theoretical dependences of the ellipse parameters of polarization Δ and ψ on the thickness and the refractive index of the thin layer deposited on the substrate surface of dielectric or semiconductor were calculated. Such calculations were

performed for thin layers of CdS and CdTe grown on the substrate of Si, Ge, GaAs, GaSe and CdTe or CdS respectively.

The diagrams $\Delta - \psi$ for thin layers of CdS and CdTe grown on the substrate of GaAs (a) and Ge (b) are presented in fig.3 and 4. The numerical indications from the graphic show the phase variation obtained as a result of light passage through thin layer with thickness *d*.
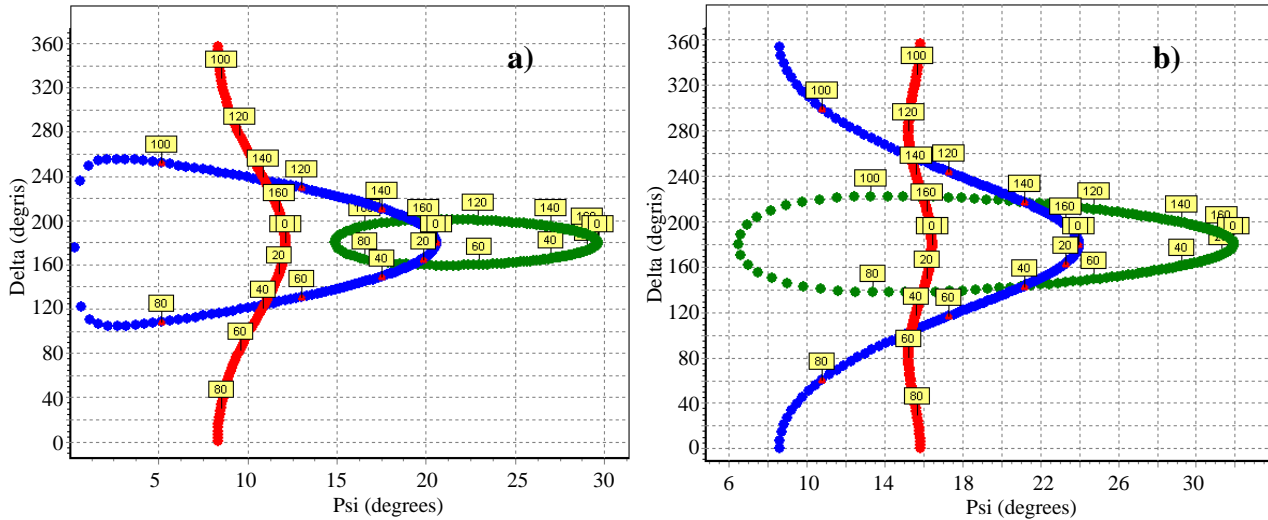

Fig.3. The dependence of the ellipsometric parameters (Δ-Ψ) of the phase difference (δ) for submicronic CdS thin films deposited on: a – GaAs; b – Ge.
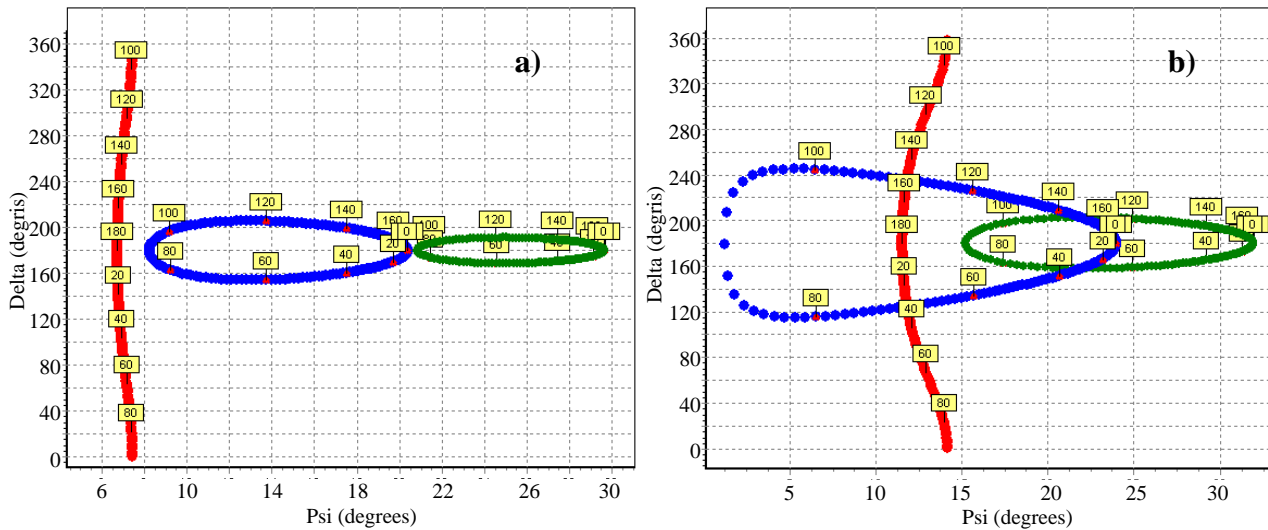

Fig.4. The dependence of the ellipsometric parameters (Δ-Ψ) of the phase difference (δ) for submicronic CdTe thin films deposited on: a – GaAs; b – Ge.

We can easily see from these dependences that with the increasing of the incident angle from 45° till 70° the resolution in the determination of the parameter δ and the thickness is increased.

The diagrams $\Delta - \psi$ for the layers of CdS grown on CdTe and CdTe grown on CdS respectively are presented in fig.5 and 6.

We can see from the analyses of dependences presented in fig.3, 4 and 5, 6 that the variation interval of the parameters Δ and ψ of the polarization ellipse is increased with the

increasing of the refractive index of the substrate for the incident angles smaller than total refraction angle. The diagrams $\Delta - \psi$ are periodical functions of the thickness and are repeated approximately after 2000?2500 A.

If the incident angle is polarized linearly with the angle 45° with respect to the incident plane then selecting the real part and complex from (3) we obtain the commode relations for the determination of the refractive index n and for the wavelengths of the optical transparent range of the layer with the condition k=0.

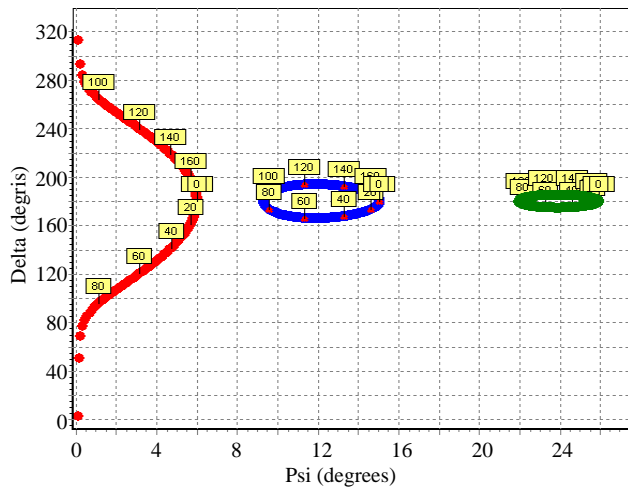$$n = \left[0.5 + \frac{\cos^2 2\psi - \sin^2 2\psi \cdot \sin^2 \Delta}{2(1 - \sin 2\psi \cdot \cos \Delta)^2} \right]^{\frac{1}{2}}. \tag{5}$$

Fig.5. The dependence of the ellipsometric parameters (Δ-Ψ) of the phase difference (δ) for submicronic CdS thin films deposited on CdTe.
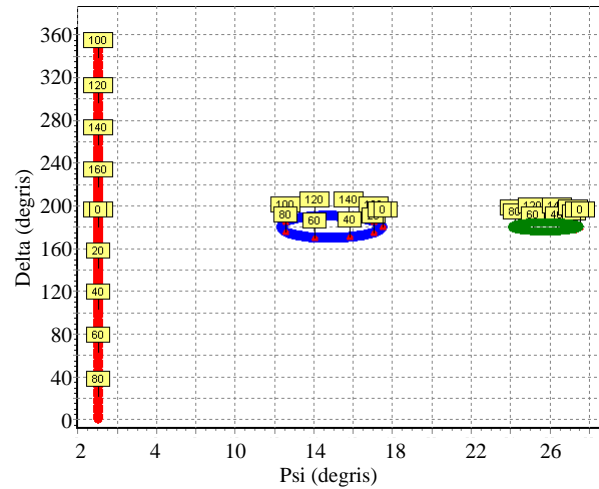
Fig.6. The dependence of the ellipsometric parameters (Δ-Ψ) of the phase difference (δ) for submicronic CdTe thin films deposited on CdS.

The results of experimental determinations of the thickness and refractive index of the samples CdS-CdTe are shown in the table at the wavelengths 0.8 μm and 0.95 μm with the theoretical diagrams $\Delta - \psi = f(\delta)$. The thicknesses of determined layers from interferential structure of the reflected spectra indicated from the respective surface of the samples CdS-CdTe in the range of 500?2500 are also shown in the table. We can also see a good correlation in the determination of the thicknesses of CdS and CdTe layers by ellipsometric method and from the interferential structure of reflection spectra.

Table

λ, nm	CdS on CdTe				CdTe on CdS			
	n	n^*	d, μm	d^*, μm	n	n^*	d, μm	d^*, μm
800	2.383	-	0.053	-	2.721	2.748	0.06	-
	2.385	2.391	0.150	0.17±0.03	2.720	2.750	0.18	0.16±0.04
	2.386	2.390	0.800	0.82±0.01	2.726	2.749	0.78	0.75±0.02
950	2.379	2.380	0.054	-	2.720	2.743	0.06	-
	2.379	2.384	0.150	-	2.720	2.745	0.20	-
	2.380	2.383	0.800	-	2.723	2.745	0.79	-

n^* is the refractive index of layers CdS and CdTe thermally treated in the presence of $CdCl_2$;

117

d^* is the thickness of layer determined from interferential structure of reflective spectra in the range 0.5?2.5 μm.

Conclusions

The dependences of the ellipsometrical parameters Δ and ψ of the phase variation were calculated using the basic equation of ellipsometry as a result of light passage through thin layers of CdS and CdTe by which the refractive index and the thickness of respective layers were determined.

The thermal treatment of the samples CdS-CdTe in the presence of solution $CdCl_2$ leads to the increasing of refractive index both of the layer CdS grown on the substrate of CdTe and thin layer of CdTe grown on CdS. The increasing of refractive index indicates the increasing of the homogeneity degree and crystallization of thin layers of CdS and CdTe.

A good correlation between interferential and ellipsometrical methods of determination of the thickness of thin layers of CdS and CdTe grown on the sublayer of semiconductor was established.

References

[1] A. Sahena Appl. Phys. Lett., 7, 113, N5, 1965.
[2] А. И. Русанов Фазовые равновесия и поверхностные явления. Изд. Химия, 1967.
[3] А. В. Ржанов, К. К. Свиташов Основы эллипсометрии. Новосибирск, Наука, 1979, 422 с.
[4] М. Борн, Э. Вольф Основы оптики. М., 1973.
[5] Р. Аззам, Н. Вашара Эллипсометрия и поляризованный свет. М. Мир, 1981, 583 с.
[6] D. E. Aspnes and A. A. Studna Determination of the properties of thin films by the method of ellipsometry. Appl. Opt., v.14, N1, p.220, 1975.

LASER GAIN SPECTRA OF QUANTUM WELLS AND MULTIPLASMON OPTICAL TRANSITIONS

V. Gurau

State University of Moldova, Department of Physics, Chishinau, MD-2009, Mateevici 60, Republic of Moldova, virgurau@yahoo.com

Abstract

A novel multi-plasmon concept of a light absorption and laser gain of low-dimensional structures are comprehensively discussed. A Generalized Semiconductor Bloch Equations are derived with account of multi-plasmon optical transitions in direct gap quantum wells, using the cumulant expansion method and fluctuation-dissipation theorem. We present results of computer simulations concerning gain spectra of $In_{0.05}Ga_{0.95}As$ quantum wells with account of multi-plasmon optical transitions in two- dimensional systems.

Multi-quantum LO-phonon-plasmon optical transitions are investigated with account of coherent memory effects in quantum wells. It is shown that a red shift of the absorption edge can be caused, not only by known mechanism of band gap shrinkage, but also by multi-plasmon transitions. The electron-hole plasma properties in the active region of the laser device and its interaction with the optical field are studied on a microscopic level using obtained Generalized Semiconductor Bloch Equations.

The comparison with other theories and experimental data measured in $In_{0.05}Ga_{0.95}As$ quantum wells is performed. The gain value $g=50$ cm^{-1} in 8 nm $In_{0.05}Ga_{0.95}As$ quantum wells is obtained at a surface density of electrons $nd_0=1.64 \cdot 10^{-12}$ cm^{-2}.

1. Microscopic theory

The key step to understand the physical mechanisms governing semiconductor laser devices and to develop models capable to predict accurately the relevant experimental properties, is to investigate the potential for further progress in design of a wide variety of semiconductor lasers and light emitting diodes. The electron-hole plasma properties in the laser device active region and its interaction with the optical field are studied in this paper on a microscopic level.

The Coulomb interaction in the electron-hole plasma leads not only to the band gap energy renormalization and to the enhancement of the transition matrix element [1-5], but also causes, due to correlations, multi-plasmon optical transitions that have been investigated experimentally and theoretically in works [6-10]. Here we consider interband light absorption and radiation in quantum wells in two-band approximation, with account of electron-hole pair strong coupling with plasmons. Also, as for three-dimensional systems [6-10], we use the cumulant expansion method and fluctuation dissipation theorem, allowing to express correlation function density - density through a structure factor.

Generalizing the results of papers [6-10] at low-dimensional structures, we find for the coefficient of light interband absorption in the symmetric quantum wells of width d_0 the following expression:

$$\alpha(\omega) = \alpha_0 \frac{\omega_g}{\omega} \sum_N \int_0^\infty \{1 - f_N^e(\omega_{k_\perp}) - f_N^h(\omega_{k_\perp})\} C(k_\perp) \mathrm{Re} \int_0^\infty e^{i\left(\omega - \omega_g - \omega_N - \omega_{k_\perp}\right)t - g(t)} dt \, d\omega_{k_\perp} \quad (1)$$

Gain spectrum is determined by a known relation $g(\omega) = -\alpha(\omega)$. Here $\hbar\omega_g = E_g$ is the band gap of semiconductor $\omega_{k_\perp} = \hbar k_\perp^2 / 2m_r$, $m_r = m_e m_h / (m_e + m_h)$ is the reduced electron and a hole mass. f_N^e and f_N^h are Fermi-Dirac distributions of electrons and holes. The successions of energy subbands are labeled by the quantum numbers N=1,2,3… The constant α_0 looks like:

$$\alpha_0 = \frac{2^{5/2} e^2 P_{cv}^2 m_r^{3/2}}{cn m_0^2 \hbar^{5/2} \omega_g} \left(\frac{\hbar}{2m_r d_0^2} \right)^{1/2} \quad (2)$$

Here c is the speed of light, and n is refraction index, m_0 is mass, e is electron charge, P_{cv} is matrix element of the momentum projection on light polarization direction.

Functions $C(k_\perp)$ and $g(t)$ characterize the electron and hole interaction with plasma and lattice vibrations.

Without taking into account a Coulomb interaction, in free carrier approximation $C(k_\perp) = 1$ and $g(t) = 0$ and we obtain the known result for the coefficient of interband absorption in quantum wells as a superposition of step functions [1-5]. At low concentrations of plasma Coulomb or Sommerfeld factor $C(k_\perp)$ looks like [1]:

$$C(k_\perp) = \frac{\exp\{q(k_\perp)\}}{\cosh\{q(k_\perp)\}}, \quad q(k_\perp) = \frac{\pi}{a_B k_\perp}, \quad a_B = \frac{\hbar^2 \varepsilon_0}{m_r e^2}, \quad (3)$$

Let's consider, that for a screened two-dimensional exciton, $C(k_\perp)$ also looks like (3), but q we shall calculate with account of interaction with plasma. Using screened Coulomb interaction as perturbation, we find:

$$q(k_\perp) = \frac{2}{\pi} \frac{\lambda_0}{a_B} \int \frac{1}{1 + \lambda_0 |k_\perp' - k_\perp|} \frac{dk_\perp'}{k_\perp'^2 - k_\perp^2} = 4 \frac{\lambda_0}{a_B} \mathrm{Re} \frac{1}{\sqrt{1 - 4\lambda_0 k_\perp^2}} \ln \frac{1 + \sqrt{1 - 4\lambda_0 k_\perp^2}}{2\lambda_0 k_\perp} \quad (4)$$

When the screening length λ_0 satisfies the inequality $\lambda_0 k_\perp \gg 1$, function $q(k_\perp)$ (4) transfers in $q(k_\perp) = \pi/a_B k_\perp$ (3). According to expression (4), plasma screening decreases the influence of Coulomb electron and a hole attraction on the transition probability. As a result of screening, near to the light absorption threshold ($k_\perp = 0$), the power dependence $q \sim 1/k_\perp$ (3) is replaced logarithmic (4). The screening length is determined by the expression:

$$\frac{1}{\lambda_0} = \frac{2}{a_B} \left\{ \frac{m_e}{m_r} \sum_N f_N^e(0) + \frac{m_h}{m_r} \sum_N f_N^h(0) \right\} \quad (5)$$

At performance of the inequality $\hbar^2 k_\perp^2 / 2m \, k_0 T \ll 1$ the screening length depends on electron and hole number, which momentum $\hbar k_\perp$ along the interface is equal to zero.

In case of electron - hole pair weak interaction with plasma and lattice oscillations, the main contribution to integral on time (1) is given by values $t \to \infty$, but absorption coefficient $\alpha(\omega)$ can be represented as a superposition of Lorentzian lineshape functions. At a strong e-h pair coupling with plasma, the limit of small t is actual, but function g(t) can be represented by expression:

$$g(t) = \frac{1}{2}\sigma t^2 + N_{LO} e^{i\omega_{LO} t}, \, N_{LO} = \alpha_e \left(1 + \sqrt{\frac{m_h}{m_e}}\right) n(\omega_{LO}) \tag{6}$$

Here the weak coupling with longitudinal optical phonons is taken into account. α_e is Frohlich coupling constant for electrons, n (ω_{LO}) is phonon number, and σ is the second moment of absorption band that looks like:

$$\sigma = \frac{2}{\pi \hbar} \sum_{\kappa_\perp} V_{\kappa_\perp} \int_0^\infty \mathrm{Im}\left\{\frac{\varepsilon_0}{\varepsilon^*(\kappa_\perp, \omega)}\right\} cth \frac{\hbar\omega}{2k_0 T} d\omega \,, \quad V_{\kappa_\perp} = \frac{2\pi e^2}{\varepsilon_0 A \kappa_\perp} \tag{7}$$

Two-dimensional Coulomb interaction $V_{\kappa_\perp}$ (7) is dynamically screened by plasma, which oscillation frequencies are determined by zeros of the dielectric function $\varepsilon(k_\perp, \omega)$.

At high temperatures $k_0 T > \hbar \omega_p$, $\omega_p = \left(\frac{4\pi n e^2}{\varepsilon_0 m_r}\right)^{1/2}$, using the approximation

$cth \frac{\hbar\omega}{2k_0 T} \approx \frac{2k_0 T}{\hbar\omega}$ and a sum rule one obtains :

$$\sigma = \frac{e^2 k_0 T}{\hbar^2 \varepsilon_0} \int_0^\infty d\kappa_\perp \left(1 - \frac{\varepsilon_0}{\varepsilon(\kappa_\perp, 0)}\right) = \frac{4^{5/3} \pi^{4/3}}{3^{3/2} \hbar^2} Ry \, k_0 T \left\{\frac{d_0 a_B^2}{m_r}(m_e + m_h) n\right\}^{1/3} \tag{8}$$

Here n is the concentration of plasma. Substituting g (t) (6) in expression (1) for the absorption coefficient and integrating on time, we find with account of LO-phonon satellites:

$$g(\omega) = \sqrt{\frac{\pi}{2\sigma}} \alpha_0 \frac{\omega_g}{\omega} \sum_{N0}^\infty \int C(k_\perp) \{f_N^e(k_\perp) + f_N^h(k_\perp) - 1\} \sum_{j=0}^\infty \frac{(N_{LO})^j}{j!} \exp\left\{-\frac{(\omega - \omega_g - \omega_N - \omega_{k_\perp} + j\omega_{LO})^2}{2\sigma}\right\} d\omega_{k_\perp} \tag{9}$$

The strong electron and hole coupling with plasmons is valid at performance of the inequality :

$$k_0 T Ry < (\hbar\omega_p)^2 \quad \left(Ry = \frac{e^2}{2\varepsilon_0 a_B}\right) \tag{10}$$

2. Results and discussion

The light gain frequency dependence in case of strong charge carrier interaction is determined by processes of absorption and radiation of several oscillation quanta of two-dimensional plasma and several optical phonons.
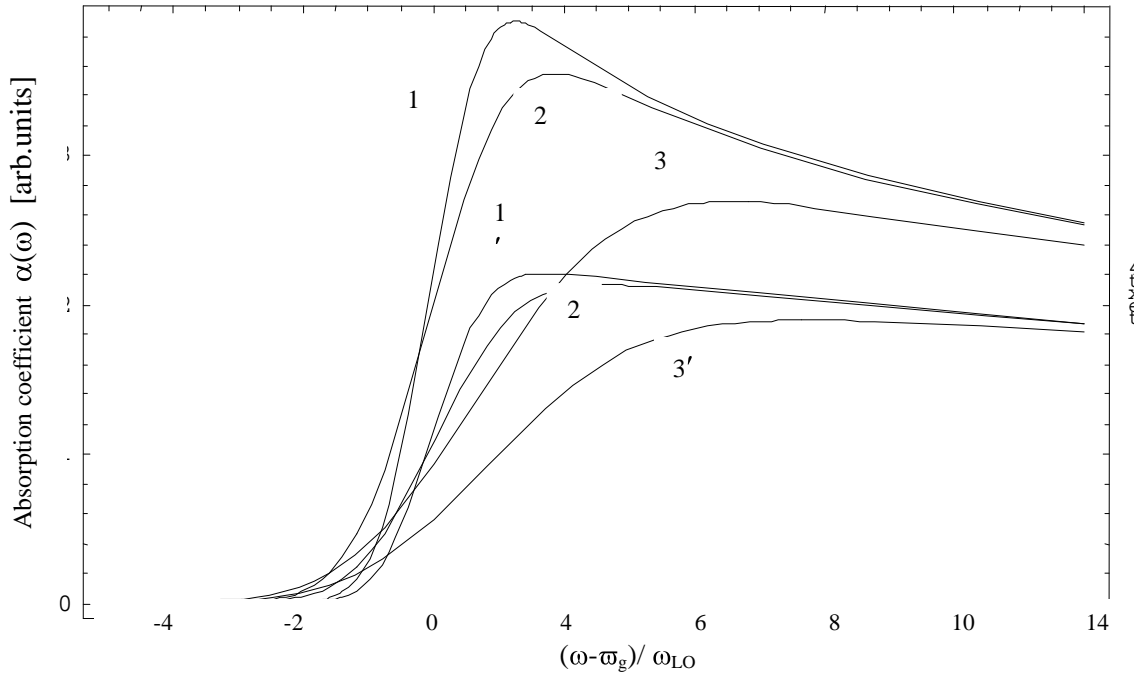

Fig.1. Absorption coefficient $\alpha(\omega)$ frequency dependence of 10 nm GaAs quantum well at T=300K and at different plasma concentrations $1,1'$- n $=10^{16}$cm^{-3}, $2,2'$- n $=10^{17}$cm^{-3} and $3,3'$- n$=10^{18}$cm^{-3}, $\hbar\varpi_g=E_g+\hbar^2\pi^2/2m_r d_0^2$.

Figure.1 is a plot of the absorption spectra for different plasma concentration. In the absence of doping, the total carrier density is the same for electrons and holes. For each of two groups the top curves $1,1'$ are for n $=10^{16}$cm^{-3}, the middle $2,2'$ for n $=10^{17}$cm^{-3} and the bottom $3,3'$ for n$=10^{18}$cm^{-3}. Curves 1,2,3 are the absorption spectra calculated with account of Sommerfeld enhancement factor, $1', 2', 3'$ at C $(k_\perp) = 1$. The attractive Coulomb interaction between electrons and holes is responsible for the absorption increase, when compared to the free-carrier approximation C $(k_\perp) = 1$, but plasma screening leads to the decrease in it. At low plasma concentrations n $= 10^{16} - 10^{17}$ cm^{-3} the absorption coefficient $\alpha(\omega)=-g(\omega)$ (9) looks like a step. With growth of plasma concentration n, the frequency dependence is flattened, and the absorption threshold is shifted in the long-wave region of a spectrum. These features are represented in figure1. And at last, at n $\cong 2\cdot 10^{18}$ cm^{-3} there is an amplification.

Results of numerical calculation of laser amplification spectrum of 8 nm In $_{0.05}$Ga $_{0.95}$ As quantum well under formula (9), using (3), (4) and (8) formulas, at a surface plasma density nd$_0$ = 1.56, 1.60, 1.64$^.$ 10 ^{12} cm $^{-2}$ are shown in figure 2. Apparently from the figure, the theoretical results and experimental data [11] shown on a parenthesizing of figure 2, are in agreement between themselves.The gain value g = 50 cm $^{-1}$ is obtained at nd$_0$=1.64 $^.$ 10 ^{12} cm $^{-2}$, that approximately is twice less, than in the theory [11]. The experimental value of n in paper [11] is not given. Injection currents have been 5, 7.5, 10, 15, 20 mA [11].
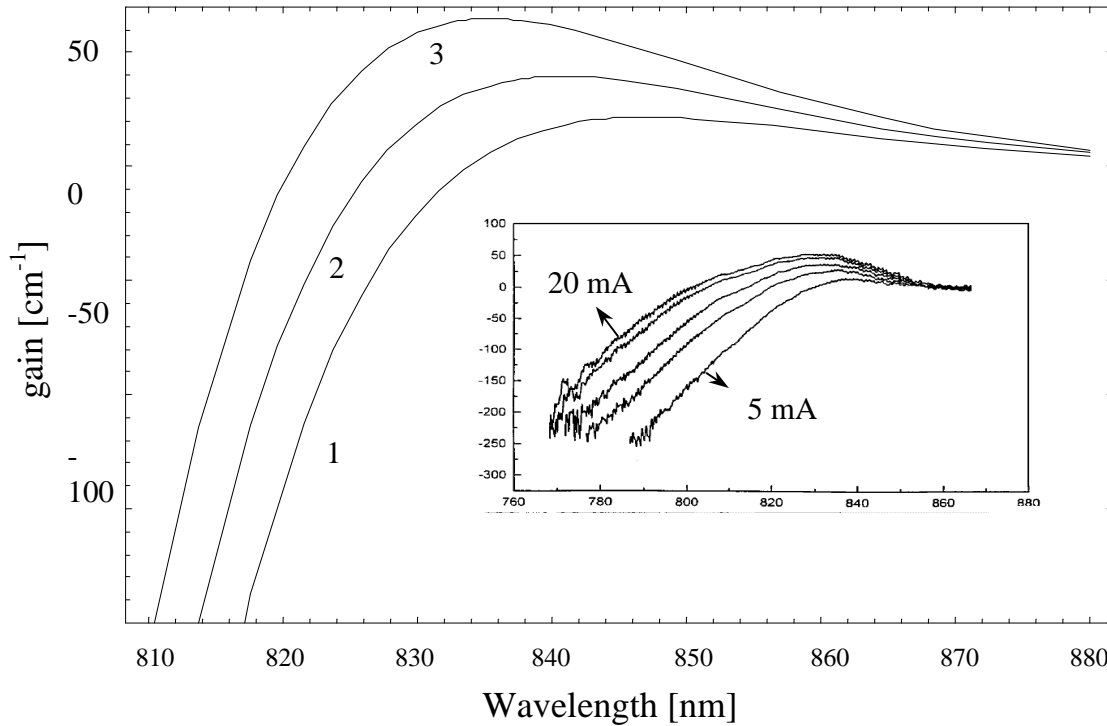

Fig.2. Laser gain spectra designed unde formula (9) with account of transitions between two subbands (N = 1) and functions (3), (4) and (8) at the following values of parameters: T = 300 K, m$_e$ = 0,0648 m$_o$, m$_h$ = 0,476 m$_o$, E$_g$ = 1,42 eV, ℏω$_{LO}$=35meV, α$_e$=0,07, ε$_0$=13,13 ε$_\infty$=11,1. Surface density of electrons are 1-1.56, 2-1.60, 3-1.64×10^{12}см$^{-2}$. Experimental gain spectra are measured at the following injection currents 5, 7.5, 10, 15, 20 mA [11].

Two - dimensional plasma approach is valid for a narrow quantum well. For an arbitrary width well one obtains:

$$\omega^2_p(\kappa_\perp) = \frac{4\pi n e^2}{\varepsilon_0 m_r}\left(1 - e^{-\frac{\kappa_\perp d_0}{2}}\right) \tag{11}$$

For $\kappa_\perp d_0 < 1$ formula (11) gives known result for two-dimensional plasma $\omega^2_p = 2\pi n e^2 d_0 \kappa_\perp / \varepsilon_0 m_r$ [1-5], whereas at $\kappa_\perp d_0 > 1$ plasma behaves as volumetric. In a

three-dimensional case plasma oscillations are similar to longitudinal optical lattice oscillations and multi-plasmon processes determine an equidistant thin structure of emission bands [6-10]. Thus, the multi-plasmon satellites of radiation lines, under condition of plasma oscillation existence $\omega\tau\square_1$ where τ is the plasmon lifetime , may be also allowed in case of wide quantum wells. Optical properties of wide quantum wells have been explored in papers [12-14]. Gossard with co-authors [14] have found out, that photoexcitation spectra of wide (4000 E) $GaAs/Al_xGa_{1-x}As$ quantum wells in which x was incremented from zero near the interface, up to x = 0,3 in the middle of the well, consist of a series of equidistant peaks, parted energy distance about 3 meV. This equidistant structure has been attributed by authors of paper [14] to the parabolic shape of the quantum well and to the equidistant electron and hole energy spectrum . In our opinion the equidistant structure may be caused by resonant radiation of several plasmons alongside with a photon. For the benefit of our guess quantity of plasmon energy $\hbar\omega_p \cong 3$ meV meets to a surface density of electrons $nd_0 \cong 10^{12}$ cm^{-2} given in paper [14] speaks, first. Except for that in work [14] the magnification of distance between peaks was observed at a doping of donor silicon strata which can be also easily explained by the multi-plasmon mechanism of radiation, namely - magnification of energy plasmon with increasing of an electron plasma concentration.

References

[1] H.Haug and S.W.Koch, *Quantum Theory of the Optical and Electronic Properties of Semiconductors*, (World Scientific 1990, Second edition), 1993.

[2] W.W.Chow, S.W.Koch, M.Sargent, *Semiconductor Laser Physics.* (Springer, Berlin, Heidelberg), 1994.

[3] M.Kira, W.Hoyer, S.W.Koch, *Phys. Stat. Sol.* (*b*), V.238,N3, P.443-450, (2003).

[4] G.Bastard. *Wave mechanics applied to semiconductor heterostructures*, (Ed. de Phys., Lesulis), 1988.

[5] A.Shik. *Quantum Wells*,(World Scientific), 1988.

[6] A. A. Klyukanov, N. A. Loiko, I. V. Babushkin, V. Gurau, *Proceedings of SPIE*, V. 47-48, p. 301-312, (2002)

[7] A. A. Klyukanov, N. A. Loiko, I. V. Babushkin, *Laser Physics* ,V.11, N.3, 318, (2001).

[8] В.С.Вавилов, А.А.Клюканов, К.Д.Сушкевич, М.В.Чукичев, А.З.Ававдех, Р.Р.Резванов, *ФТТ*, Т.41, N.7, 1176, (1999) .

[9] В.С.Вавилов, А.А.Клюканов, К.Д.Сушкевич, М.В.Чукичев, А.З.Ававдех, Р.Р.Резванов, *ФТТ*, Т.43, N.5, 776, (2001).

[10] А.А. Клюканов. *ФТТ*, Т.29. С.1529, (1987).

[11] C. Ellmers, M.Hofmann, W.W.Ruhle, A. Girndt, F.Jahnke, W.W.Chow, A. Knorr, S.W.Koch, C Hanke, L.Korte, C.Hoyler, *Phys. Stat. Sol. (b)*, V.206, P.407-412, (1998).

[12] I.H. Burnett, H.H. Cheong, W. Paul, P.F. Hopkins, A.S. Gossard, *Phys.Rev. B.*, V.48, N.11, pp.7940-7943, (1993-I).

[13] H. Fritze, W. Chen, A.V. Nurmiko, J. Jo, M. Santos and Sheyegan, *Phys.Rev. B*. V.48, N20, 15103 – 15111, (1993-II).

[14] I.H. Bunett, H.H. Cheong, W. Paul, P.F. Hopkins, E.G. Gwinn, A.I. Rinberg, R.M. Westervelt, M. Sundaram, A.S. Gossard, *Phys.Rev. B*. V.43, N.14, pp.12033-12035, (1991).

MORPHOLOGY STUDY AND CATHODOLUMINESCENCE MICROANALYSIS OF PHOTOELECTROCHEMICALLY ETCHED GaN EPILAYERS

V. Popa

Technical University of Moldova, MD-2004, Chisinau, Republic of Moldova

1. Abstract

Photoelectrochemical etching of GaN in different solutions such as KOH, $HF/H_2O_2/C_2H_5OH$ and oxalic acid was performed. The results of scanning electron microscopy cathodoluminescence analysis of the etched samples are presented.

2. Introduction

GaN and related nitrides are considered promising materials for numerous applications such as the creation of full-color display systems, data storage devices, solar-blind ultraviolet detectors, new sensor technologies, wireless communications, solid-state lighting and high-power microwave generation for radar, etc. Note that nitride-based light-emitting diodes and lasers have been successfully commercialized. Further elaboration of novel device structures on GaN and related materials depends upon the progress in growth technologies and material processing. Considerable efforts are focused nowadays to the study of etching processes in III-group nitrides, most processing being currently done by dry plasma etching. High etching rates are observed under high-density plasma conditions. There are however, important disadvantages to dry etching, including the generation of processing-induced damage and difficulties in obtaining smooth etched sidewalls, which are required for high-performance nitride-based laser diodes and other devices. Increasing attention is being paid therefore to wet etching of III-group nitrides.

Many research groups proposed different acids and bases for GaN wet etching using Hg arc lamp or HeCd laser as UV light sources. There are two mechanisms during interaction of GaN surface with solution, one of them is direct chemical reaction between dislocations and solution, the other one is gallium oxide formation on GaN surface during UV expose and its subsequent dissolution. The first mechanism seems to be highly dependent upon solution concentration and crystal orientation [1], when for the second mechanism the etch rate is dependent on the kinetics of the solution. Adjusting the UV power, it is possible to control the share of each mechanism in the etch rate and, as a result, to define the final morphology.

3. Experiment
3.1. PEC etching in KOH solution

During PEC etching using KOH as etchant solution, we use epilayers of GaN grown by low-pressure MOCVD on sapphire using trimethylgallium and ammonia as source materials. A buffer layer of about 25-nm thick GaN was first grown at 510°C, while the top n-GaN layer with 1.3-2.0 μm thickness was grown at 1100°C. The concentration of free electrons in the top n-GaN layer was $1.7 \times 10^{17} \text{cm}^{-3}$.

Ti/Al/Ti/Au ohmic contacts with the thickness 300/900/500/1500 A respectively were deposited by e-beam evaporation followed by rapid thermal annealing (RTA) process at 800°C for 30 seconds in nitrogen atmosphere.

The photoelectrochemical etching of samples was carried out in 0.05 M aqueous solution of KOH under in situ UV illumination provided by focusing the radiation of 50-200W Hg or Xe lamps on the GaN surface exposed to electrolyte. In experiments using Hg lamp the current between the sample and Pt electrode decreased from 4 to 0.1 mA in 10 minutes and did not depend on radiation power density, while under Xe lamp excitation the current was directly proportional to the radiation power density and was almost constant during the process. The difference between these two UV sources comes from different kinds of spectral characteristics and as a result different morphologies were obtained (Fig.1).
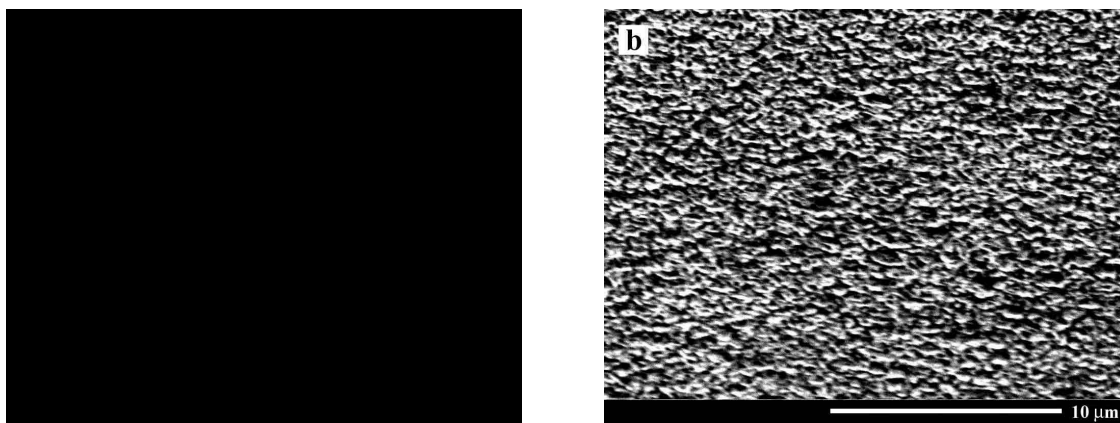

Fig.1. Samples etched for 10 min in 0.05M KOH at 100W using Hg (a) and Xe (b) lamps.

Note that the etching process using Xe lamp gives more uniform morphology near the ohmic contact and in the middle of the sample than that based on use of the Hg lamp. The I-V characteristics taken from resistive samples after PEC etching show a nonlinear behavior.

Fig. 2 shows the CL spectra of columnar and bulk GaN at 80 K. Both spectra consist of near-band-edge peaks, CL band at 3.28 eV related to non-equilibrium carrier recombination via donor acceptor pairs (DAP), phonon replicas of DAP-related band, and a broad band with the maximum at 2.15 eV (the so-called "yellow" luminescence). One can see that porosity induces an upward frequency shift of the near-band-edge peak. Apart from that, it results in a sharp diminution of the intensity of yellow emission. Monochromatic CL images taken

Fig. 2. CL spectra of bulk and nanostructured GaN at T = 80 K.

from the same areas of the samples exhibited an anti-correlation in the spatial distribution of near-band-edge and yellow CL (Fig. 3). During irradiation exposure, attenuation of near-
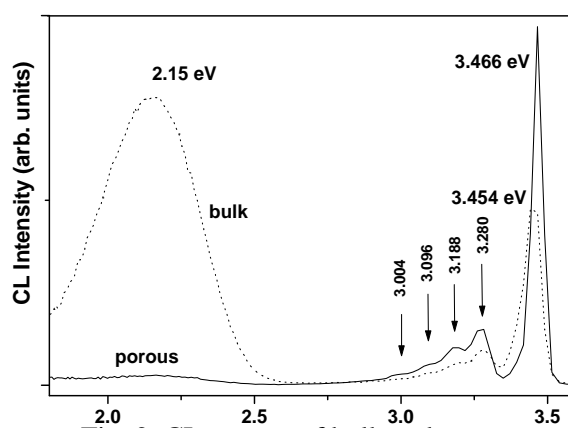
band-edge and visible CL by the electron beam was evidenced, the effect being more pronounced for the UV emission.
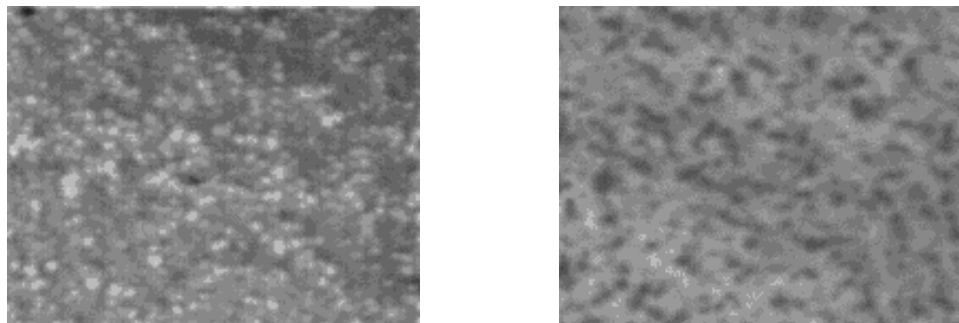

Fig. 3. UV (left) and yellow (right) monochromatic CL images taken from PEC etched GaN at T = 80 K. The image width equals 40 μm.

3.2. PEC etching in HF /H_2O_2/C_2H_5OH solution

Porous Si can be generated using Pt-assisted electroless etching in ethanol:HF:H_2O_2 (1:1:1) [2]. In this process, a thin discontinuous layer of Pt (d < 8 nm thickness) is patterned onto the surface. This approach has been used for porous GaN obtaining.

On n+n GaN layers (Si as dopant) with the thickness of 2 and 1 μm respectively with carrier concentrations of 5×10^{18} and 2×10^{17} cm^{-3} Pt islands were patterned using electrochemical deposition based on short impulses (0.1 μs duration, 1 μs period and 10V amplitude) applied during 20 seconds as a result uniform island morphology was achieved, see Fig.4.

Fig.4. Pt islands on GaN surface.

Catalytic reduction of H_2O_2 at the Pt islands combined with UV illumination injects holes into the valence band, as a result local polarization is reached which initiates local etching, developing with time in a porous structure.

After precleaning procedure, the samples were dipped in a stirred solution of HF/H_2O_2/C_2H_5OH at room temperature and subjected to UV illumination from a 200W Xe lamp. No current was observed in dark so there was no chemical decomposition in HF solution. When the light is switched on, then a current of about 50 μA emerges, which drops to 10 μA after 30 minutes, at the same time, when the light is switched, the current increases up to 30 μA and then diminishes up to zero in about 10 minutes.

The fabricated porous structures were then cleaved and cross-sectional images were taken by SEM. Fig.5 shows a porous layer with the thickness of 0.8 μm exhibiting pores stretching perpendicularly to the initial surface.

Fig.5. SEM image of porous GaN
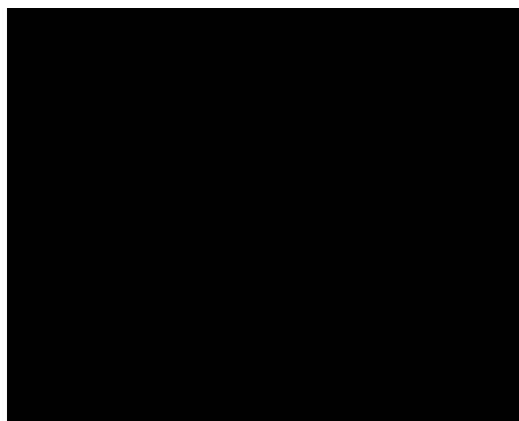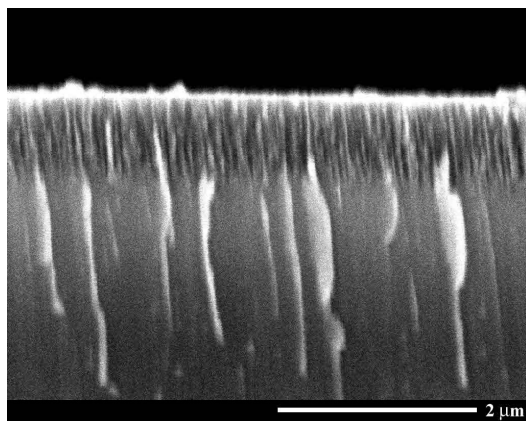
3.3. PEC etching in oxalic acid

Oxalic acid ($H_2C_2O_4 \times 2H_2O$) can be used for GaN defect characterization [6]. Etching in this solution under UV illumination resulted in a porous structure of GaN. For the electrolyte preparation, 5 grams of oxalic acid were dissolved in 300 ml of water. Potential of 10 V was applied between the sample and Pt electrode. At room temperature and UV expose, the initial current of 120 μA increased up to 250 μA after 5 minutes and reached the value of 550 μA in 7 minutes. Intensive hydrogen bubbles were observed on GaN surface during the experiment.
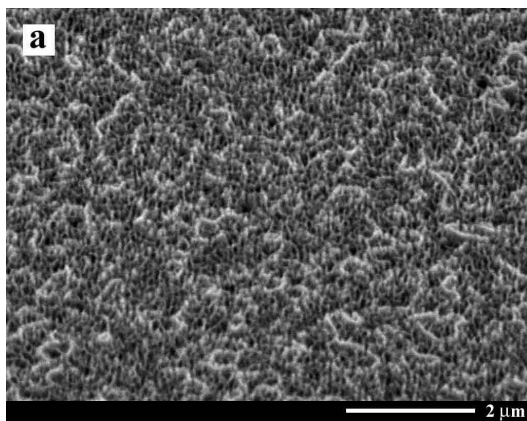

Fig.6. SEM images taken from GaN surface etched in oxalic acid,
top view **(a)** and cross-sectional view **(b)**

4. Conclusion

PEC etching in KOH solution under UV Xe-lamp illumination of GaN results in smooth morphology, while columnar structures are obtained at relatively low power UV irradiation from Hg lamp when etching occurs in the same solution.

Uniform porous layers with high density of pores were obtained in HF/H_2O_2/ C_2H_5OH solution under UV irradiation.

Acknowledgements

References

[1] C.H. Ko et al., Mat. Sci. Eng., B96, 43-47 (2002)
[2] S.Chattopadhyay, X.Li and P.W.Bohn, J.Appl.Phys. 91, 6134 (2002)
[3] Diego J.Diaz et al., J. Vac. Sci. Technol., B20(6) (2002)
[4] C.Youtsey, I.Adesida, G.Bulman, Appl. Phys. Lett. 71, 15 (1997)
[5] Xiuling Li et al., Appl. Phys. Lett. 80, 6 (2002)
[6] Sri Priya Sundararajan, D.Crouse, Yu-Hwa Lo, J. Vac. Sci. Technol., B20(4) (2002)

TO THE 50TH ANNIVERSARY
OF ACADEMICIAN VALERIU KANTSER
PROFESSOR, DOCTOR HABILITY IN PHYSICS AND MATHEMATICS,
MOLDOVA STATE PRIZE LAUREATE

V.Kantser was born in 1955. In 1977 he has graduated with honours from the State University of Moldova and has begun his working activities as an engineer in the IAP of the ASM immediately after graduating. In 1977-1980 he is a post-graduate student of the "P.N.Lebedev" Physical Institute (Moscow, Russia). Since 1980 V.Kantser is a doctor, and since 1990 - doctor hability in physics and mathematics. In 1995 he was elected Associate Member of the ASM and in 2000 - Full member of the ASM. After post-graduate studentship and defence of thesis of doctor until now V.Kantser develops his basic activities in the frames of the IAP ASM. At the beginning he is an inferior research scientist (1981-1983), then a superior research scientist (1983-1989), from 1989 to 1991 - a coordinating research scientist, and since 1991 V.Kantser is a general research scientist. Since 1992 he is Head of laboratory of low temperature physics and Deputy director of ILSSE IAP, and from 1997 to 2000 he is Deputy director of the IAP. Since 2000 V.Kantser is Head of Division of Physical and Engineering Sciences of ASM and Director of the International Laboratory of Superconductivity and Solid State Electronics. Since 1988 he works pluralistically at the State University of Moldova, where since 1998 he is a University professor.

Scientific direction developed by V.Kantser contains identification, investigation and development of methods for characterization of physical processes and phenomena in electron systems with many groups of quasiparticles, anisotropy and nonparabolicity of spectrum, electron instability and other peculiarities. These properties are characteristic of semimetals,

narrow band semiconductors, high temperature superconductors (HTS) and quantum structures on their basis.

Acad.V.Kantser is known in scientific community of the country and abroad as a researcher of high professional bearing in the field of physics and solid state electronics. Aria of his investigations constituted for a period of more than two decades of scientific activities is extended by both range of abordate physical effects and phenomena (electron phase transitions, electron structure and quasiparticles, phenomena of transport and tunnelling, effects of quantification and interface, etc.) and range of studied materials and systems of solid state: semiconductors, semimetals and superconductors, including quantum structures of reduced dimensionality based on them.

High skill, wide horizon of knowledge and self-abnegation in theoretical and experimental researches have given him a possibility to obtain valuable scientific results in the field of solid state physics and electronics. Generalization of variational methods of investigation of electron anisotropic transport phenomena allowed him to explain and describe in the frames of united concept galvano- and thermomagnetic properties of semimetals and narrow band semiconductors, to identify new peculiarities of electron transport in anisotropic systems, which were experimentally confirmed later. Results of these investigations were published in series of works, cited widely in scientific literature and generalized in monograph "Transport phenomena in bismuth and its alloys".

In cycle of the theoretical studies of cooperative properties of the system of electrons and holes in semimetals and narrow band semiconductors V.Kantser has predicted and investigated a new magnetic phase - orbital ferromagnetism, he has proposed first microscopic model of extrinsic electron ferroelectrics. For description of interconnected electron phase transitions Landau functional with three order parameters was proposed, which later was used for description of different systems with many types of ordering. In 1982 this cycle of works was mentioned with Prize of Youth of Moldova in the field of science and technique.

On the basis of systematic analysis of nature of valence bonds and of crystalline structure there was proposed an idea of common genesis by Peierls electron instability of electron spectrum of semimetals of bismuth type and its more complex isoelectron analogues, and there was developed theory of electron structure of compounds $A^3B^5C_2^6$ and multiple alloys on their basis. In its frames for the first time there was identified the effect of electron spectrum inversion for solid solutions of materials with different symmetry, and there was found a new group of semiconductor alloys with band inversion through zero gap state. A new effect - double inversion of band spectrum in anisotropic materials was predicted. Later a whole series of the obtained theoretical results was experimentally confirmed, including some experimental researches carried out by acad. V.Kantser. These results were widely published and remarked by specialists in the field, they were generalized in correlation with data of experimental investigations in monograph "Ternary narrow band semiconductors $A^3B^5C_2^6$ and their solid solutions". In 1992 these results have been appreciated by the Prize of the ASM.

Investigations concerning physical processes and effects in quantum structures (heterojunctions, quantum wells, superlattices, constrictions and mesoscopic microstructures) formed on the basis of semiconductors and semimetals are of special importance. In this major aria of research there was developed a new direction in physics of quantum solid state structures concerning effects and peculiarities appearing at quantification, tunnelling, transport of quasiparticles with anisotropic characteristics, nonparabolicity and spectrum inversion, spatial variation of nonpotential parameters characterizing structure, resonance

states of impurities, spintronics effects. Thus, a new mechanism of appearance of electron systems with reduced dimensionality conditioned by generation of interface states was identified. There were found many variants of genesis of these states, including by kinetic potentials conditioned by spatial variation and anisotropy of the effective mass, by appearance of piezopolarization fields. It was established that in quantum wells and superlattices in function of geometric factors and structure parameters there appear effects of inversion of interface electron bands, it was shown that characteristics of these states generated by anisotropy, vectorial fields are essentially modified in function of crystallographic orientation of the structure. There were identified effects of anisotropic tunnelling, kinetic delay, resonance tunnelling by interface states, strong interaction of the latter with impurity resonance states. It was shown that these found electronic properties lead to appearance of new effects: interface magnetism, magnetoelectric and photovoltaic effects, new effects of interaction with magnetic and electric fields. This range of results opens new possibilities in physics and engineering of quantum solid state structures, on their basis new principles of design of electron quantum devices are elaborated. Advanced degree of these studies is confirmed in particular by winning of rigid competition of INTAS projects in 1997 and 2001, in its frames new aspects of thermoelectricity based on physics of the mentioned low dimensional structures were developed. In 2004 these results were mentioned with the National Award of the Republic of Moldova.

Together with discovery of high temperature superconductivity (HTS) in the IAP there was initiated and developed a number of researches in this field coordinated by acad. V.Kantser. During 1987-1992 these researches were carried out within the framework of the Program projects of the former Soviet Union. V.Kantser directly participated in elaboration of technology for magnetron deposition of HTS this layers, in which the effects of mixed phase and dimensional effects are studied. In HTS ceramics based on bismuth there was studied the influence of magnetic and other impurities on critical parameters, thermoelectric and other electrophysical properties. In the context of fundamental investigations of HTS theoretical investigations concerning processes and effects conditioned by coupling of d type in quantum structures with HTS are of special interest. In the context of these studies it was shown that anisotropic and specific nature of the order parameter of d type realized in HTS leads to appearance of a number of new phenomena non-characteristic of classical superconductors: interface states of quasiparticles, genesis of new ordering and instabilities at the interface and on the surface of HTS, tunnelling by states and interface, effect of quasiparticle spectrum splitting under action of exchange fields, magnetic fields.

An important direction of researches in the laboratory conducted by V.Kantser is physics of defects of semiconductors of group A^4B^6 and structures on their basis. There was elaborated a technology for obtaining of intrinsic and doped semiconductors PbTe and their derivatives, there were developed several epitaxial methods for obtaining of thin layered structures, including molecular beam epitaxy. Study of photoelectric properties of materials of PbTe type doped with indium and gallium has shown that due to nonspecific character of impurities they show increased photosensibility and may be related even to isolation state. It was demonstrated that specific peculiarities and sensitivity of carriers due to different factors lead to flexible character of the impurity states. There was realized a number of structures and sensible elements in infrared with parameters exceeding those of existing prototypes, and these researches served as a basis for elaboration of new infrared photodetectors in the frames of some technical-applied projects.

High level of the carried out researches is attested through inclusion of the collective of researchers conducted by V.Kantser in different programs of international collaboration with

INTAS, MRDA, BMBF, etc. with partners from England, France, Germany, Israel, Ukraine, etc. A number of activities of V.Kantser deal with materialization of research results in devices and products. Among them the following may be mentioned: new technological and constructive solutions of medium and far infrared phototransducers; different variants of pressure, temperature and presence detectors; methods and devices for cooling - thermoelectric microrefrigerators and Joule-Thompson planar refrigerators; thin layer technologies and realization on their basis of electron hybrid devices; devices SQUID based on HTS. A part of technologies and electronic devices is realized up to the level of prototype and specifications. Several products were assimilated and put in production at the factory «Topaz» from Chisinau, an electron device for electroenergetics is under assimilation.

Acad.V.Kantser has published more than 300 scientific works, including 6 monographs, he has 12 patents, he participated many times at international conferences presenting original communications and invited reports. V.Kantser is a reviewer in different international journals, he is a member of the Program committee of some conferences, is an independent expert of international programs INTAS and Copernicus. He is a member of the International Academy of Thermoelectricity, Associate member of Romanian-American Academy of art and science, member of Scientific Council of the JINR, Dubna, Russia. All this certifies high degree of the carried out investigations and international recognition. Intense research activities of acad. V.Kantser briefly mentioned above, are strongly connected to training of young researchers. Four young researchers of the laboratory for already several years work in centers abroad. Under supervision of V.Kantser 6 theses of doctor, 2 theses of doctor hability were defended, and 4 theses of doctor are ready for defending, 3 young persons are post-graduate students of the ILSSE. During the whole period of his activities in the IAP V.Kantser was implied in university training in educational institutions. First in the Pedagogical Institute of Tiraspol, then at the Technical University of Moldova, and during more than 15 last years - at the State University of Moldova (SUM). At present at the SUM he pluralistically is engaged as university professor with three courses. V.Kantser has published two books for students and post-graduates: "Solid State Physics" (1992) and "Introduction into superconductivity" (1999). He was invited with courses of lectures to different Universities of Romania, to the International Center of Theoretical Physics of Triste (Italy), Warwick University (England), Augsburg University (Germany).

Acad. V.Kantser combines successfully wide activities of scientific research and scientific-organizing and public work. He is director of the Center ILSSE IAP and solves many problems of maintaining of researches, extending collaboration of the ILSSE with other institutions from Moldova and abroad, promoting new forms of organization of research. He coordinates activities of the ILSSE for realization of projects of the republican programs and a number of contracts, including those with scientific institutions from Romania.

Being academician coordinator of the Division of Physics and Engineering of the ASM and due to his active position V.Kantser is engaged in different actions on the level of the ASM and on the national level. V.Kantser is the president of the Society of Physicists of Moldova, president of the Republican consultative council of experts of the Ministry of Education and Science, he is member of Council of experts in physics in the frames of the Supreme Attestation Committee, member of Specialized Councils "Theoretical physics" and "Solid state physics". V.Kantser is editor-in-chief of the "Moldavian Journal of the Physical Sciences", member of the editorial board of the international journal "The Annals: Metallurgy and Material Science", of the republican journals "Physics and Modern Technologies" and "Intelectus". He actively participated in elaboration of different documents, programs, legislative and normative statements concerning scientific activities, reforms in the sphere of

research and education. Acad. V.Kantser has represented the Academy of Sciences at some International meetings concerning aspects of development of international collaboration. During the whole period of his scientific activities he participated in organization of different conferences, seminars and scientific meetings. He is the head of the republican physical seminar.

V.Kantser carries merited authority with physicists of Moldova. He has celebrated his fiftieth anniversary in the prime of his creative power. His is full of energy and plans for development of physical-technical science in the Republic. We wish him success. La mult ani!

Society of Physicists of Moldova,
Editorial Board of the "Moldavian Journal of the Physical Sciences"